UNIVERSIDAD DE NAVARRA
ESCUELA SUPERIOR DE INGENIEROS
SAN SEBASTIÁN



Characterization and Optimization of Wireless Links for Implantable Applications and Inkjet Printing Technology Feasibility Study

DISSERTATION

submitted for the degree of Doctor of Philosophy by

Iñaki Ortego Isasa

Under the supervision of

Dr. Daniel Valderas Gázquez
Dr. Juan Ignacio Sancho Seuma

San Sebastián, December 2014

Acknowledgements

With these lines I would like to express my sincere gratitude to all institutions and individuals who have made this research work possible.

Gracias a Tecnun-CEIT y al Gobierno Vasco por financiarme y haberme dado la oportunidad de disfrutar de la investigación en estos cuatro años.

Hay tantas personas involucradas de alguna forma u otra que han hecho que este trabajo se realice, que el sentido común me dice que haga un agradecimiento colectivo para no dejarme a ninguna, pero la vida es riesgo así que… empecemos.

En primer lugar, me gustaría agradecer a mis directores de tesis, Daniel Valderas e Iñaki Sancho por su dedicación y por el haberme guiado durante estos últimos años. Especialmente, me gustaría destacar, que ha sido un verdadero placer trabajar codo con codo con Dani. Creo que hemos formado un gran equipo. Tu paciencia y forma de ser me han influenciado mucho durante estos años.

En segundo lugar, este trabajo no se hubiera realizado sin la inestimable ayuda de Kami Benli, Ainara Bujanda y Guillermo Aramendia. Sin vosotros esta tesis no sería lo que es, así que muchísimas gracias de corazón.

Me gustaría recordar a todos los compañeros de la familia Tecnun-Ceit que me habéis acompañado durante todos estos años. A todos los doctorandos, algunos ya doctores, con los que he podido compartir grandes momentos, y en definitiva los que habéis conseguido que mi estancia aquí sea tan agradable.

Merecen especial mención, Jurgi, por aguantarme tantos años, Ane Miren… que decir de ella, cuántas comidas te debo ya? y David Del Rio, que ha sido un compañero de despacho inmejorable.

Muchas gracias también a mi Meal-Group, sobre todo por tener la paciencia de esperarme a que acabe de comer y de tener que soportar mis charlas durante la comida. Gonzalo, siempre será un placer compartir contigo todas esas aficiones e intereses musicales y científicos. Saioa, sabes que los ordenadores no son lo mío, y el puenting tampoco, pero estaré encantando de tomar un café. Jon, siempre será un placer meterme con el Athletic en tu presencia. Mikel y Aitziber, espero que me invitéis a la boda y que algún día el señorito me de una clase de crossfit y me invite a un capuccino. Por último Bea, sobran las palabras, gracias por tus consejos y por haberme ayudado tanto durante estos años no sólo en lo profesional sino también en lo personal.

Muchas gracias también a Aitor Arriola, por prestarse siempre a ayudar de forma desinteresada y por haberme dejado utilizar mi querida sonda dieléctrica.

I would like also to thank Queen Mary University of London, for giving me the possibility of being working there for three months. Thanks to Prof. Chen and Frank, for their support and especially to Massimo Candotti. I learned a lot in the anechoic chamber and without his help, it would be impossible to make the measurements presented in this research work.

Gracias a Ana, por sus enseñanzas del mundo del Yoga y abrirme los ojos para ver el mundo desde otro punto de vista, gracias a ti he entendido otra forma de ver las cosas y me siento muy diferente.

No puedo olvidarme de mi kuadri, que siempre están allí apoyándome, sea en Sagües, en Larrabetzu o en cualquier otra parte, ya sabéis que os aprecio

mucho. Eskerrik asko a otros compañeros de viaje de estos últimos cuatros años, a Lauroba taldea, Xabier Zurbano, Naiara, Jan, Ivan Markusek, Simon Stastny…

Hay una persona que me ha acompañado en los últimos años muy de cerca, y que ha sido sin duda un apoyo fundamental en mi vida, Ainitze. Que puedo decir, si numerara todas las cosas en las que me has ayudado, necesitaría más hojas que las que contiene esta tesis, así que me limitaré a decirte que muchísimas gracias por todo, de corazón. Las personas evolucionamos con los años y te aseguro que has tenido una gran influencia en mi vida y que me has ayudado a encontrar fuerzas en esos momentos en los que andamos perdidos como pollos sin cabeza.

Eta azkenik, nere familia…. Nondik hasi? Eskerrik asko baserriko familia guztiari, urte hauetan zehar pasatako momentu on guztiengatik eta bazkari goxoengatik. Begira Aitona, hau da, hainbeste urtetan egin dudan lanaren laburpena, emango dizut kopia bat irakurtzeko, lasai. Eskerrik asko ere Azkoitiko familiari, eta lasai primas, seguraski estudiatzen jarraituko dut eta… Doktorautza hasi nuenean, bederatzi izaten ginen Tolosan ospakizunetan, tamalki, orain bi fisikoki ez daude, baina hementxe somatzen ditut nere ondoan. Eskerrik asko Tolosako familiari eta bereziki aitona eta amonari, beti bihotzen edukiko zaituztet eta. Eta bukatzeko, dudarik gabe nere hirukote garrantzitsuena, Ainhoa, eskerrik asko eta barkatu batzutan merezi ez dezun erantzunak jasotzeagatik, baina badakizu nolakoa naizen, Aita, emandako sustoaren ondoren, etxean zauden egun bakoitza opari bat delako, eta Ama, zer esan, zu gabe benetan ez nintzen izango orain naizena. Eskerrik asko bihotzez.

Muxu handi bat guztioi, eta mila esker

Muchas gracias a todos,

Thanks to all

Abstract

In this research work the characterization and optimization of wireless links for implanted applications and the feasibility of using inkjet printing technology as fabrication process for implantable antennas are studied.

The basic concepts of biolectromagnetics that are necessary to study the communications in implantable devices are analyzed describing the main electromagnetic properties of human tissues, the mathematical model that represents these properties and different voxel models that correspond to the human body.

There are two different ways to communicate with implants, based on near field or far field approaches. Most of the research and already implemented implanted applications are based on the near field one. A methodology including an analytic description, circuital and 3D simulations, and measurements is carried out to study and identify the optimum topology for implanted applications based on inductive coupling. With this methodology, the needed compensations, bifurcation-free conditions and efficiency analysis are studied. The SS topology offers great advantages for implanted applications since the resonance frequency of the primary circuit is independent from the coupling coefficient.

The feasibility of implementing an implanted coil-antenna in a flexible substrate by using inkjet printing technology is also studied. In this context, the

advantages and limitations of inkjet printing technology to design implantable flexible antennas are described. It is considered as a very promising technique for the fabrication of completely biocompatible and flexible implanted antennas.

Communications with implanted devices based on far field approach are also analyzed. A strategy to reliably characterize for far field implanted communication links based on a combination of analytical, computational and experimental methods is made. A characterization of plane wave attenuation in homogeneous phantom is done in an anechoic chamber and the frequency limits of cost effective sugar based tissue simulating liquids are studied.

Different human body simulation models are used to study the effect of the human tissue distribution on implanted applications focusing the attention on subcutaneous ones. An analytical approach is used to compare the results with heterogeneous planar phantom models with two and three layers. The effect of skin and fat/SAT tissues in the E-field behaviour is studied with a four layered planar homogeneous model. The thicknesses of these layers and the difference between using fat or SAT changes the E-field behaviour for subcutaneous implanted devices. Finally, a voxel phantom model simulation study is developed using Virtual Family from IT'IS foundation and CST Voxel Family. The suitability of using heterogeneous layered planar phantoms for subcutaneous implanted devices is demonstrated by comparing this model with the corresponding voxel model.

Glossary

AC	Alternating current
ANP	Advanced Nano Products
ARPANSA	Australian Radiation Protection and Nuclear Safety Agency
AUT	Antenna under test
CST	Computer Simulation Technology
CT	Computed Tomography
DGBE	Di-ethylene Glycol Butyl Ether
DMP	Dimatix material printer
DOD	Drop-on-demand
DS	Design Studio
EM	Electromagnetic
EMF	Electromagnetic field
ERP	Equivalent radiated power
ETSI	European Telecommunications Standards Institute
FCC	Federal Communications Commission
FDTD	Finite difference time domain method
FEM	Finite elements method
FIT	Finite integration technique
ICNIRP	International Commission on Nonionizing Radiation
IEEE	Institute of Electrical and Electronic Engineers
ISM	Industrial, Scientific and Medical
IT'IS	Information Technologies in Society
MEMS	Microelectromagnetical systems
MICS	Medical Implant Communication System

MIRD	Medical Internal Radiation Dose
MIT	Massachusetts Institute of Technology
MoM	Method of moments
MR	Magnetic Resonance
MRI	Magnetic Resonance Imaging
MWS	Microwave Studio
NFC	Near Field Communication
NLM	National Library of Medicine
NRPB	National Radiological Protection Board
PCB	Printed Circuit Board
PDMS	Poly Disemthyl Siloxane
PET	Polyethylene Terephthalate
PP	Parallel-parallel
PS	Parallel-series
PZT	Zirconate titanate
RF	Radio Frequency
RFID	Radio Frequency Identification
SA	Specific energy absorption
SAM	Specific Anthropomorphic Mannequin
SAR	Specific energy absorption rate
SAT	Subcutaneous Adipose Tissue
SP	Series-parallel
SS	Series-series
TBW	Total Body Water
UHF	Ultra high frequency
USD	United States' Dollar

Table Of Contents

1 INTRODUCTION 23

1.1 IMPLANTED MEDICAL DEVICES 24
1.2 SCOPE AND STRUCTURE OF THE WORK 27

2 BIOELECTROMAGNETICS 31

2.1 ELECTROMAGNETIC PROPERTIES OF HUMAN BODY 32
2.1.1 Electrical characterization of human tissues 32
2.1.2 Dielectric dispersion 37
2.1.3 Human tissue distribution 40
2.2 MATHEMATICAL MODELS OF HUMAN BODY 44
2.3 PHANTOMS 48
2.3.1 Physical phantoms 49
2.3.2 Phantom simulation 56
2.4 BIOLOGICAL EFFECTS AND EXPOSURE LIMITS 63
2.4.1 Biological effects 63
2.4.2 Radio frequency exposure limits 65

3 COMMUNICATION WITH IMPLANTS 69

3.1 NEAR FIELD SYSTEMS 70
3.1.1 Inductive coupling 70
3.1.2 Concept of resonance 73

3.1.3 Maximum power transfer vs. maximum power transfer efficiency....80
3.2 ELECTROMAGNETIC PROPAGATION IN HUMAN BODY....84
3.3 STANDARDS AND PROTOCOLS FOR COMMUNICATION WITH IMPLANTABLE DEVICES....87
3.3.1 9-315 kHz band....88
3.3.2 402-405 MHz band (MICS)....88
3.3.3 ISM bands....89

4 INKJET PRINTING TECHNOLOGY....91

4.1 SUBTRACTIVE ETCHING....92
4.2 INKJET PRINTING TECHNOLOGY....94
4.2.1 Different technologies....95
4.2.2 Inks....96
4.2.3 Substrates....97
4.2.4 Sintering process....98

5 OBJECTIVES....101

5.1 NEAR FIELD APPROACH PARTIAL OBJECTIVES....101
5.2 FAR FIELD APPROACH PARTIAL OBJECTIVES....102
5.3 INKJET PRINTING TECHNOLOGY OPTIMIZATION FOR IMPLANTED APPLICATIONS....103

6 METHODOLOGY....105

6.1 NEAR FIELD APPROACH....105
6.1.1 Analytical approach....106
6.1.2 Simulation....114
6.1.3 Measurements....117
6.2 FAR FIELD APPROACH....118
6.2.1 Analytical approach....119
6.2.2 Simulation....123
6.2.3 Measurements....130

6.3 INKJET PRINTING IMPLEMENTATION 139
6.3.1 Used equipment and materials 139
6.3.2 Fabrication process description 142

7 INKJET PRINTING TECHNOLOGY ANALYSIS 151

7.1 RESOLUTION STUDY 152
7.1.1 Minimum printable width 152
7.1.2 Thickness estimation 156
7.2 INK'S CHARACTERIZATION 158
7.2.1 Electrical resistance estimation 160
7.2.2 Ink conductivity estimation 161

8 NEAR FIELD IMPLANTED WIRELESS LINKS OPTIMIZATION 163

8.1 COIL IMPLEMENTATION AND CHARACTERIZATION 164
8.2 TOPOLOGY ANALYSIS 168
8.2.1 Effects of secondary resonant circuit on primary 168
8.2.2 SP topology (Methodology validation) 174
8.2.3 Final results of all topologies 188
8.3 EFFICIENCY ANALYSIS 191
8.3.1 Efficiency in SS topology 192
8.3.2 Efficiency in SP topology 194
8.4 INKJET PRINTING IMPLEMENTATION AND ANALYSIS 201
8.4.1 Compensation 202
8.4.2 Quality factor 205
8.4.3 Bifurcation phenomena 208
8.4.4 Efficiency analysis 210
8.5 CASE STUDY: SENSOR-ANTENNA APPROACH 212

9 FAR FIELD IMPLANTED WIRELESS LINKS OPTIMIZATION 217

9.1 HOMOGENEOUS PHANTOM CHARACTERIZATION 218
9.1.1 Sugar based phantom analysis 218

9.1.2 Characterization of plane wave attenuation in homogeneous phantoms....221
9.2 HETEROGENEOUS LAYERED PLANAR PHANTOM ANALYSIS....236
9.2.1 Checking simulation methodology....237
9.2.1 Heterogeneous four layered planar phantom analysis....240
9.3 VOXEL PHANTOM ANALYSIS....249

10 CONCLUSIONS AND AREAS FOR FURTHER RESEARCH....261

10.1 INKJET PRINTING TECHNOLOGY....261
10.2 NEAR FIELD SYSTEMS....262
10.3 FAR FIELD SYSTEMS....266
10.4 AREAS FOR FURTHER RESEARCH....269

11 REFERENCES....273

I. APPENDIX A: MATERIAL MAPPING....285

II. APPENDIX B: TOPOLOGY ANALYSIS RESULTS....289

III. APPENDIX C: CST VOXEL FAMILY....297

IV. APPENDIX D: PUBLICATIONS....305

List of Figures

Figure 1.1: Example of an implanted pacemaker. (a) Double-chamber (double-lead) pacemaker. (b) Electrode electrically stimulating heart muscle. (c) Single-chamber (single-lead) pacemaker [10] 26

Figure 2.1: Polarization effect 33

Figure 2.2: Dielectric permittivity and electrical conductivity of muscle-like biological material as a function of frequency [12] 39

Figure 2.3: Polarization phenomena [13] 39

Figure 2.4: Water content in different parts of the human body 41

Figure 2.5: Skin composition 42

Figure 2.6: Duke's human torso. (a) SAT (blue colour) + Fat tissue (yellow colour). (b) Skin (yellow colour) + SAT (blue color) 43

Figure 2.7: Normalized permittivity $\varepsilon' - \varepsilon\infty\varepsilon s - \varepsilon\infty$, loss factor $\varepsilon''\varepsilon s - \varepsilon\infty$, and conductivity $\omega\varepsilon 0\varepsilon''\varepsilon s - \varepsilon\infty$ for a single time constant relaxation plotted against ffr [11] 45

Figure 2.8: Measured (blue) and modelled (red) data for permittivity (solid lines) and conductivity (dotted lines) of skin dry 47

Figure 2.9: SAM-V4.5BSE 49

Figure 2.10: Open-ended coaxial line: (a) topology; (b) measured S-parameters [13] 53

Figure 2.11: Parallel plate method [13] 54

Figure 2.12: Waveguide resonator: (a) topology; (b) resonance shift [13] 55

Figure 2.13: Filled rectangular waveguide: (a) topology; (b) measured S-parameters [13] 55

Figure 2.14: Free-Space method for material characterization [13]....56

Figure 2.15: Summary of measurements techniques [13] 56

Figure 2.16: Head's multilayer planar block model. 1. Skin and fat. 2. Muscle. 3. Skull exterior. 4. Nasopharyns / mouth + tongue (depending on the part of the head one is focusing on). 5. Dura mater outer + veins. 6. Dura mater outer. 7. Cerebrum. 8. Cerebellum. 9. Ventricles + Putamen + Glands + Nerves. 58

Figure 2.17: MIRD phantom developed in 1980s....59

Figure 2.18: Voxel model of a woman head [29]....60

Figure 2.19: Virtual Family created by IT'IS foundation. From left to right: Duke, Ella, Billie and Thelonious 61

Figure 2.20: CST voxel family 62

Figure 3.1: Inductive coupling scheme....71

Figure 3.2: Measured (points) and calculated (lines) coupling factors for two planar coils with 30 mm diameter [52] 73

Figure 3.3: Series resonance circuit....74

Figure 3.4: Current and voltage behaviour in series resonance circuit....75

Figure 3.5: Parallel resonance circuit 75

Figure 3.6: Current and voltage behaviour in parallel resonance circuit....76

Figure 3.7: Purely resistive circuit for power and efficiency analysis 80

Figure 3.8: Change in total power, power transferred to the load and efficiency of resistive load for a system with $Vin = 100\,V$ and $Rin = 50\,\Omega$ 82

Figure 3.9: Typical arrangement of an inductively coupled power transfer system [52] 83

Figure 3.10: Electric field behavior in a lossy medium 85

Figure 3.11: Skin depth behaviour with frequency for different human tissues using 4 Cole-Cole model....86

Figure 3.12: ISM Spectrum in different world regions 90

Figure 4.1: Process flow of the chemical etching (photolithography) process [77] 93

Figure 4.2: Illustration of the ink jet (drop on demand) printing process 95

Figure 4.3: Sintering process....98

Figure 6.1: Four basic topologies 106
Figure 6.2: Rectangular planar spiral inductor 107
Figure 6.3: Two conductor segments for mutual inductance calculation 109
Figure 6.4: Phasor model: (a) Coupling circuit. (b) Equivalent coupling circuit. (c) Primary circuit with reflected impedance 110
Figure 6.5: Primary circuits with reflected impedance: (a) Series compensated primary; (b) Parallel compensated primary....112
Figure 6.6: Design Studio model of SP Topology: (a) Real circuit; (b) Phasor model....115
Figure 6.7: CST 3D model of the inductor....117
Figure 6.8: Setup for the measurements....117
Figure 6.9: System for controlling the distances between the coils 118
Figure 6.10: Wave reflection and transmission at normal incidence on a planar interface [67]....120
Figure 6.11: Reflection and transmission coefficients for wave propagation in 3 layers dielectric slab. (a) Referred to impedance and intrinsic reflection coefficient. (b) Ray-tracing model [67]....121
Figure 6.12: Normal wave propagation through N layers sandwiched between two media [67]....122
Figure 6.13: Screen shot of the macro to define the biological properties in CST MWS....124
Figure 6.14: Electric dispersion for Muscle using CST MWS macro for defining human material properties 125
Figure 6.15: Screen shot of the simulation set-up....128
Figure 6.16: Screen shot of the simulation set-up: (a) Plane wave excitation; (b) Waveguide port....128
Figure 6.17: Definition of the curve and probes to evaluate the electric field ..129
Figure 6.18: 85070E dielectric probe and recommended set up scheme [102]....130
Figure 6.19: Set up for measuring the dielectric properties of liquid phantoms. (a) PNA. (b) Dielectric probe. (c) Platform to move the sample. (d) Tank to store the phantom. (e) Heater and mixer to fabricate the phantom....132
Figure 6.20: Antennas used for the measurements: (a) Antenna 1, (b) Antenna 2 133

Figure 6.21: Simulated antenna gain (dBi) in relation to phantom height z (zblock=z/2 mm) for 402 MHz (vertical polarization, horizontal plane) 135

Figure 6.22: Semi-anechoic chamber of Queen Mary University of London ...136

Figure 6.23: Transmitting horn antenna 136

Figure 6.24: Plane of the anechoic chamber set-up.....137

Figure 6.25: Antenna under test location: (a) Phantom general location overview. (b), (c) Designed system to move the antenna into the phantom. ...138

Figure 6.26: Dimatix Material Printer 2800 139

Figure 6.27: Cartridge.....140

Figure 6.28: Applied voltage and waveform each nozzle: (a) Voltage value and (b) waveform.....143

Figure 6.29: Drop Watcher 144

Figure 6.30: Spit-Purge-Blot-Spit cleaning cycle.....146

Figure 6.31: Resolution with DMP2800 printer: (a) cartridge angle of 90º and (b) cartridge angle of 30º [108] 147

Figure 6.32: Cartridge alignment scale system [108].....147

Figure 6.33: Fiducial Camera 148

Figure 7.1: Designed pattern for resolution study 152

Figure 7.2: Printed pattern for resolution study 153

Figure 7.3: Images of the tracks taken by the fiducial camera. (a) 500 µm line. (b) 75 µm line 154

Figure 7.4: Images of the 75 µm line taken by the fiducial camera after 30min@200ºC sintering process 155

Figure 7.5: Obtained profiles for different number of layers under same sintering conditions 157

Figure 7.6: Designed plate and printed structure for measuring the electrical resistance 159

Figure 7.7: Set-up: (a) General overview and (b) Connection system.....159

Figure 7.8: Electrical Resistance vs. time for different number of layers 160

Figure 8.1: Fabricated prototypes. (a) Subtractive etching method. (b) Inkjet printing technology.....164

Figure 8.2: Calculation of R and Q for different thickness.....167

Figure 8.3: (a) Non resonance-Series circuit; (b) Equivalent coupling circuit; (c) Primary circuit with reflected impedance.....169

Figure 8.4: (a) Non resonance- Parallel topology; (b) Equivalent coupling circuit; (c) Primary circuit with reflected impedance 170

Figure 8.5: Frequency vs. $ReZr$ for a system with $fc = 17.05MHz$. ($RL = 300\Omega$) 173

Figure 8.6: Frequency vs. $ReZr$ for a system with $fc = 8{,}52MHz$. ($RL = 150\Omega$) 173

Figure 8.7: Frequency vs. $ReZr$ for a system with $fc = 13{,}56MHz$. ($RL = 240\Omega$) 174

Figure 8.8: Series-Parallel topology 174

Figure 8.9: Equivalent circuit of SP topology: (a) Equivalent coupling circuit. (b) Primary circuit with reflected impedance 175

Figure 8.10: Design Studio (CST) model for series-parallel topology: (a) Real model; (b) Phasor model....179

Figure 8.11: $S11$ parameter: (a) Real part; (b) Imaginary part 181

Figure 8.12: Comparison of the imaginary part of S11 with compensated and non compensated primary....182

Figure 8.13: Comparison of the imaginary part of S11 with compensated and non compensated primary (k=0,2)....183

Figure 8.14: (a) Representation of the SP topology scheme combining Design Studio and 3D model from CST MWS. (b) 3D model from CST MWS....185

Figure 8.15: Comparison of the simulated and measured of S11 for different distances: (a) Real Part of S11; (b) Imaginary part of S11 187

Figure 8.16: Behaviour of the limit coupling factor for bifurcation free system with RL....191

Figure 8.17: (a) SS topology circuit scheme. (b) Equivalent coupling circuit. (c) Primary circuit with reflected impedance....192

Figure 8.18: (a) SP topology circuit scheme ((b) Equivalent coupling circuit. (c) Primary circuit with reflected impedance....194

Figure 8.19: Effect of the coupling factor in the efficiency for both compensations. (-) stable (*) unstable....196

Figure 8.20: Frequency vs. efficiency for a system with $fc = 17.07MHz$. ($RL = 300\Omega$)....198

Figure 8.21: Frequency vs. Efficiency for a system with $fc = 8{,}53MHz$. ($RL = 150\Omega$)....198

Figure 8.22: Frequency vs. $ReZr$ for a system with $fc = 13{,}56MHz$. ($RL = 240\Omega$)....199

Figure 8.23: Efficiency behaviour with load resistance 200

Figure 8.24: Effect of Rs in the primary compensation capacitance:(a) k=0,05. (b) k=0,6. Continuous line represents $RL = 50\Omega$ and dotted line $RL = 200\Omega$ 204

Figure 8.25: Effect of Rs in the secondary quality factor for different loads 206

Figure 8.26: Effect of Rs in the primary quality factor for different loads (a) k=0,05. (b) k=0,6 207

Figure 8.27: Effect of Rs in the boundary coupling coefficient for bifurcation free system for all topologies with different load impedances. $RL = 50\Omega$ (-), $RL = 100\Omega$ (--), $RL = 200\Omega$ (*-) 209

Figure 8.28: Effect of Rs in the efficiency for different load impedances (-) 50Ω. (--) 100Ω, (*)200 Ω 211

Figure 8.29: Effect of Rs in fc for different coupling and load impendances (-) 50Ω. (--) 100Ω, (*)200 Ω 212

Figure 8.30: Behaviour of the imaginary part of S11 with coupling coefficient. (a) Series primary compensation. (b) Parallel primary compensation 214

Figure 8.31: Shift of the S11 imaginary part with Cs (k=0,05) 215

Figure 8.32: Shift of the S11 imaginary part with Cs (k = 0.6) 215

Figure 9.1: Measured real part of permittivity for different sugar concentration liquids 219

Figure 9.2: Measured imaginary part of permittivity for different sugar concentration liquids 219

Figure 9.3: Measured conductivity for different sugar concentration liquids 220

Figure 9.4: Measurements with antenna 1 horizontal polarization 222

Figure 9.5: S21 dB vs. frequency: (a) f=402 MHz, (b) f=868 MHz, (c) f=2.45 GHz and (d) f=5.8 GHz. Antenna 1 (Ant1), Antenna 2 (Ant2), horizontal polarization (H) and vertical polarization (V). 224

Figure 9.6: S11 parameter for both antennas. (a) f=402 MHz; (b) f=868 MHz 227

Figure 9.7: Simulated homogeneous phantom model 228

Figure 9.8: Simulation vs. Measurements (a) f=402 MHz, (b) f=868 MHz, (c) f=2.45 GHz and (d) f=5.8 GHz. 230

Figure 9.9: Effect of the conductivity at 5.8 GHz 231

Figure 9.10: Conductivity behaviour with frequency for different materials 232

Figure 9.11: Effect of boundary conditions in x and y directions: (a) f=402 MHz and (b) f= 868 MHz 234

Figure 9.12: Effect of boundary conditions in x and y directions at f=2.45 GHz....235

Figure 9.13: Frequency behaviour of the reflection coefficient 237

Figure 9.14: Comparison between analytical and simulation approach....238

Figure 9.15: Frequency behaviour of the reflection coefficient 239

Figure 9.16: Comparison between analytical and simulation approach....239

Figure 9.17: Simulation set up: (a) General overview and (b) Definition of two ports and central line to evaluate the fields. 240

Figure 9.18: Dielectric properties of fat and SAT tissues: (a) Dielectric constant; (b) Conductivity 242

Figure 9.19: E-field frequency behaviour for subcutaneous implants for different fat (solid line) and SAT (dotted line) thicknesses 243

Figure 9.20: E-field frequency behaviour at the interface between fat/SAT and muscle layer: (a) fat and (b) SAT 245

Figure 9.21: Skin's thickness effect in E-field's frequency behaviour for different SAT thicknesses: (a) 2 mm, (b) 8 mm and 16 mm....248

Figure 9.22: Duke's torso simulation set-up 250

Figure 9.23: E-field behaviour along the central line 250

Figure 9.24: E-field behaviour along the central line in air-phantom interface zoom in 251

Figure 9.25: Tissue distribution of Duke's Torso 252

Figure 9.26: Comparison between Duke voxel model (solid lines) and its equivalent four layered planar phantom model (dotted lines) 253

Figure 9.27: E-field behaviour along central line for Ella model: (a) full range and (b) air-phantom interface zoom in 255

Figure 9.28: E-field behaviour along central line for Billie model: (a) full range and (b) air-phantom interface zoom in 256

Figure 9.29: E-field behaviour along central line for Thelonious model: (a) full range and (b) air-phantom interface zoom in....257

Figure 10.1: Printed prototypes in PDMS substrate: (a) With no treatment and (b) with oxygen plasma treatment (30s, 100 W)....272

Figure B.1: Change in $ImYn$ for different Qsvalues 293

Figure B.2: Change in $ImYn$ for different Qsvalues 295

Figure C.1: E-field behaviour along central line for Baby voxel model: (a) full range and (b) air-phantom interface zoom in.....298

Figure C.2: E-field behaviour along central line for Child voxel model: (a) full range and (b) air-phantom interface zoom in.....299

Figure C.3: E-field behaviour along central line for Donna voxel model: (a) full range and (b) air-phantom interface zoom in.....300

Figure C.4: E-field behaviour along central line for Emma voxel model: (a) full range and (b) air-phantom interface zoom in.....301

Figure C.5: E-field behaviour along central line for Gustav voxel model: (a) full range and (b) air-phantom interface zoom in.....302

Figure C.6: E-field behaviour along central line for Laura voxel model: (a) full range and (b) air-phantom interface zoom in.....303

Figure C.7: E-field behaviour along central line for Katja voxel model: (a) full range and (b) air-phantom interface zoom in.....304

List of Tables

Table 2.1: Typical thickness of human body layers for different locations and ages [14]. 41

Table 2.2: Parameters of the Cole-Cole model for different tissues [19] 47

Table 2.3: Suggested recipes for achieving target dielectric parameters for head tissue-equivalent liquids [22] 51

Table 2.4: Examples of commercial software packages offering full wave, three-dimensional solutions to EMF exposure problems 57

Table 2.5: Virtual family's physical characteristics 61

Table 2.6: CST voxel family´s physical characteristics 62

Table 2.7: MPE Limits for controlled environments....67

Table 2.8: MPE Limits for uncontrolled environments....67

Table 3.1: Obtained total power and efficiency for different $\boldsymbol{RL}$ values....82

Table 7.1: Dimension of the printed pattern for resolution study....152

Table 7.2: Obtained line's width for different sintering times at 200ºC and 1 layer prototypes 153

Table 7.3: Obtained line's width for different number of layers prototypes with 30min@200ºC sintering process....155

Table 7.4: Obtained thickness for different number of layers....157

Table 7.5: Printed prototype's dimensions 159

Table 7.6: Electrical Resistance depending on the number of layers 161

Table 7.7: Decrement of the electrical resistance in percentage with respect to one layer 161
Table 7.8: Obtained conductivity values with 30min@200ºC sintering process 162
Table 8.1: Nominal dimensions of ID-1 card type 164
Table 8.2: Fabricated prototypes.....165
Table 8.3: Obtained results: Analytical (A), Simulation (S) and Measurement (M) 165
Table 8.4: Conductivity and skin depth calculation for the used materials 166
Table 8.5: Parameters of the circuit under study.....172
Table 8.6: Parameters used in the simulation.....180
Table 8.7: Main parameters of the material used in CST 3D simulation.....184
Table 8.8: Real circuit components values used in SP topology 186
Table 8.9: Parameters of the circuit under study.....197
Table 8.10: Parameters of the circuit 202
Table 9.1: Fabricated phantom recipes for the frequencies of interest.....220
Table 9.2: Physical dimensions of the proposed phantom.....240
Table 9.3: Wavelength for different tissues and frequencies 246
Table 9.4: Computer's features 253
Table 9.5: Simulation properties for the phantom models.....254
Table 10.1: Main characteristics of each topology 263
Table A.1: Material mapping.....285

Chapter 1

Introduction

The rapid technological advances in electronics, electro-optics, and computer science have profoundly affected our everyday lives. They have also set the stage for an unprecedented drive toward the improvement of existing medical devices and the development of new ones. These new devices will perform in vivo diagnostic and therapeutic intervention, improving the quality of life for many patients. At this respect, “Implantable Electronics” has been defined as one of the ten emerging technologies in 2010 by MIT [1].

In this context, the study of interaction between Electromagnetic (EM) fields and biological tissues often referred to as bioelectromagnetics, has become a major research topic. It is an interdisciplinary science since it involves physics and engineering with life sciences. Its applications go from diagnostic purposes (MRI), therapeutic use (regeneration of tissues, bone non-unions treatment and miotic control of tissues and cells, for example) to cancer research and

psychological disturbances research. A large amount of research has been performed on the biological effects which are caused by exposure to RF radiation [2–6].

Understanding the underlying interaction mechanisms caused by EM fields is necessary for assessing the possible impact on biological tissues and being able to design medical devices for improving quality of life of patients [7]. This is is a complicated subject due to the complex nature of biological objects.

1.1 Implanted medical devices

One of the priorities for sustaining high standards of medium to long term health care, is to provide an effective monitoring system thus reducing the need for multiple consultations and hospital visits. If efficiently implemented, diagnostics via a remote medical telecare communication system would give instant access to patience condition without the need for personal contact or even permanent hospitalization. In a world with an increasing aged population, medical telemetry over wireless networks has attracted much attention and will provide long term monitoring whilst giving medical personnel freedom from constant local patient contact.

Implanted biosensors constitute an essential area for present and future telemetry research. The major problem with this kind of applications is due to the losses introduced by the body, which rise dramatically at RF frequencies and beyond and hinders the communication link. Thus, the absorption of EM radiation by the human body barely allows any communication when the antenna is deeply implanted.

In general, two different approaches can be used for communications with medical devices: near field approach and far field approach.

In near field coupling:

- Radiofrequency electric and magnetic fields are decoupled, independent, and non uniform.
- Wave impedance varies from point to point.
- The RF electric and magnetic fields are in the time quadrature (90º out of time phase)
- Maxima of electric and magnetic fields occur at different locations as in a standing-wave field.

In far field communications:

- E and H are coupled e.g. E is perpendicular to H and both are perpendicular to the direction of motion.
- Coupling is characterized by plane wave RF field interaction.
- Electric and magnetic fields of the outgoing wave are in time phase with each other.
- Electric and magnetic field are uniquely defined and are related through the intrinsic impedance of the medium (120π ohms in air)
- Determination of electric field behavior is sufficient to characterize the interaction.

Depending on the application each approach has its advantages or disadvantages. The working principle of these two approaches is different. In near field approach, the communication is based on inductive coupling, there is no radiation in contrast to far field approach, where the communication is based on electromagnetic radiation.

Most of the research today has tended to focus on systems based in near field approach since they are reliable for setting inductive link between in-body and on-body transceivers, e.g., for pacemakers, RFID links and electrical

stimulation of muscles. The main advantage of these kinds of systems is that as they are based on inductive coupling, the effect of the human body in the communication is not very high since human body tissues are not magnetic.

Most of them use resonant structures in primary and secondary sides for transferring power wirelessly [8]. There are very few empirical studies about inductive coupling to transfer power to implantable devices without battery. One of them can be found in [9] where some measurement are realized in a Cadaver Head.

Implantable devices such as pacemakers and defibrillators (Figure 1.1), neural recording and stimulation devices, and cochlear and retinal implanted require methods to recharge their batteries and transmit data both to and from the device [10].

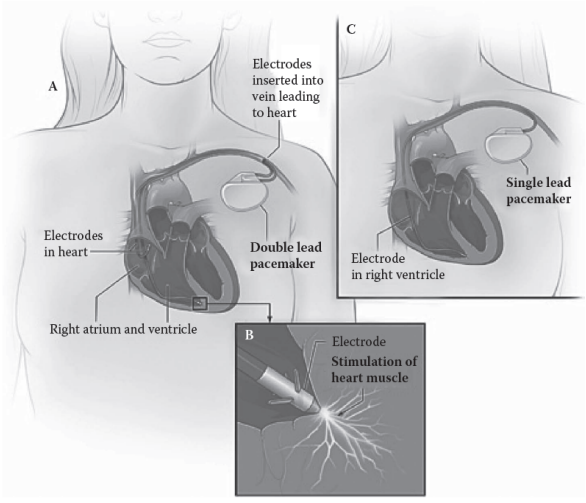

Figure 1.1: Example of an implanted pacemaker. (a) Double-chamber (double-lead) pacemaker. (b) Electrode electrically stimulating heart muscle. (c) Single-chamber (single-lead) pacemaker [10]

Inductively coupled applications are usually limited to transcutaneous links rather than transmission through larger, more lossy regions of the body [10]. Nevertheless, three major problems still arise: their magnetic-coupling intrinsic

short range, the critical positioning required for the two coils, which restrict the versatility of a wireless continuous monitoring system as it is nowadays demanded; and the exhibited low data rate. Therefore, it appeared reasonable to attempt an optimization of current systems based on inductive coupling.

Besides, one of the most important constraints in the design of implantable antennas is the required small size, conformability and isolation from the human body. Several new manufacturing processes allow the fabrication of flexible biocompatible antennas that will open an countless number of new applications and that will revolutionize the current medical implanted devices. In this research the feasibility of Inkjet Printing Technology for implanted applications is studied.

1.2 Scope and structure of the work

In this research work a characterization and optimization of wireless links and a feasibility study of inkjet printing technology for the fabrication of implanted coil antennas is addressed. To achieve this, it is necessary to make and extensive literature overview about bioelectromagnetics, communication systems and inkjet printing technology.

The structure that is followed in this research work is the following one:

Chapter 2: Biolectromagnetics

In this chapter the basic concepts of Biolectromagnetics that are necessary to design implantable devices are explained. The electromagnetic properties of human body and the mathematical models to represent them are analyzed. The existing phantom models are described and the biological effects and current exposure limits standards are presented.

Chapter 3: Communication with implants

This chapter is focused on the communication with implants explaining the basic concepts of communication based in near field approach (inductive coupling) and far field approach (electromagnetic radiation). The standards and protocols for communication with implants are also described.

Chapter 4: Inkjet Printing Technology

This chapter presents the main features of this new technique for the fabrication of flexible implanted antennas. Traditional fabrication techniques are also explained, to show the main differences with inkjet printing technology.

Chapter 5: Objectives

This chapter states the main objective of the research work and divides it into partial objectives.

Chapter 6: Methodology

This chapter is focused on the procedure that is followed in chapters 7, 8 and 9 for the characterization of inkjet printing fabrication process and implanted wireless links based on near field and far field approach respectively.

Chapter 7: Inkjet printing technology analysis

This chapter shows the characterization and optimization of inkjet printing technology for the fabrication of implantable antennas by making a resolution study and characterizing the used ink.

Chapter 8: Near field implanted wireless links optimization

This chapter is focused on the characterization and optimization of systems based on inductive coupling for communication with implants. The feasibility of using inkjet printing technology for the fabrication of the implanted coil antennas is also addressed.

Chapter 9: Far field implanted wireless links optimization

This chapter presents the main concerns for the design of reliable implanted devices based on electromagnetic radiation, especially for subcutaneous implanted applications. A comparison between different phantom models is addressed.

Chapter 10: Conclusions

The main conclusions and areas for further research are put forward in Chapter 10.

Chapter 2

Bioelectromagnetics

In this chapter the basic bioelectromagnetic concepts that are necessary to design an implantable communication system are presented. The objective is to describe only the main properties of human body that have influence on these kinds of communications. First of all, main electromagnetic properties of human body are described and human tissue distribution is briefly analyzed. Secondly, mathematical models that have been used to reproduce the human body's behavior are explained. Once these models have been explained the different phantom models for human body representation are shown. Finally, some comments about the possible biological effects and current regulation about exposure limits are addressed.

2.1 Electromagnetic properties of human body

The dielectric properties of biological tissues result from the interaction of electromagnetic radiation with its constituents at the cellular and molecular level. The mechanisms of the interaction are well understood and discussed in several articles. The interaction of the human body with electric fields is complex. However, there is no direct interaction with the magnetic component of electromagnetic fields at low field strength [11]. For most biological materials, the magnetic permeability is close to that of the free space. Although recent studies about nervous tissue put in doubt this statement. This later issue is outside the scope of this work, but more information could be found in [11]. Nevertheless, the body is so weakly magnetic that generally μ_r is assumed to be 1, except for magnetic resonance imaging and spectroscopy applications where a very large magnetic field is used [10].

Therefore, the attention will be focused on the proper electrical characterization of human body.

2.1.1 Electrical characterization of human tissues

Human tissues can be considered as linear non-magnetic lossy materials. In order to understand and define properly the main electrical characteristics of human tissues several aspects of the material's composition are required.

The atom is composed of subatomic particles. Between all of them the three main ones are neutrons, protons and electrons. Protons and electrons and electrically charged. While the first one is positively charged, the second one is negatively charged. However, neutrons are electrically neutral.

Protons and neutrons are packed together in the atomic nucleus, at the centre of the atom which is positively charged. Electrons form a "cloud" of negative charge around the nucleus. The attraction forces keep the electrons in the vicinity of the atomic nucleus.

An atom is neutral in electrical charge, which means that its protons must be balanced by an equal number of electrons.

When an electric field is applied to a dielectric material, electric dipoles are created in the material, the nucleus of the atom is pushed in the direction of the field and the electrons "cloud" just in the opposite way. The atom will have now a dipole moment. These dipoles increase the electric displacement flux, **D** by a factor called Electric Polarization (***P***).

$$\boldsymbol{D} = \varepsilon \boldsymbol{E} = \varepsilon_0 \boldsymbol{E} + \boldsymbol{P} \qquad \textbf{2.1}$$

where:

$$\boldsymbol{P} = \alpha_p \boldsymbol{E} = \varepsilon_0 \chi_e \boldsymbol{E} \qquad \textbf{2.2}$$

α_p is the atomic polarizability constant and χ_e is the electric susceptibility which is the proportionality constant between the applied electric field and the electric flux caused by the presence of a dielectric material.

The atom must reach again a balance state. If the shape of the atom is supposed to be spherical, the equilibrium is reached when the nucleus of the atom is displaced a distance *d* from the centre of the sphere (Figure 2.1). The external **E** field, which pushes the nucleus of the atom in the same direction to the applied field, exactly balances the generated internal field pulling it to the left.

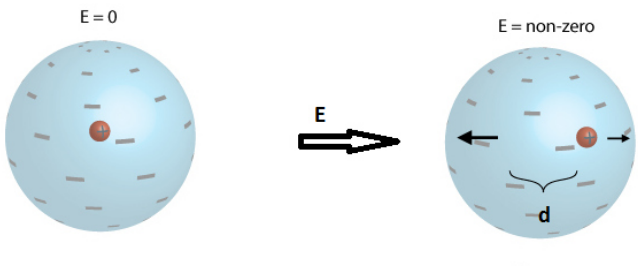

Figure 2.1: Polarization effect

There are three types of electric dipoles:

- Permanent dipoles
- Instantaneous dipoles
- Induced dipoles

In all biological materials there exists at least one type of these electric dipoles. When an external field is applied to the biological material, the dipoles align with the field.

Combining equations 2.1 and 2.2, the electric flux density, **D** can be expressed therefore as:

$$\boldsymbol{D} = \varepsilon_0(1 + \chi_e)\boldsymbol{E} \qquad \textbf{2.3}$$

Usually $1 + \chi_e$ is denoted as the relative permittivity of the material $\hat{\varepsilon}_r$. The previous equation can be rewritten as:

$$\boldsymbol{D} = \varepsilon_0\hat{\varepsilon}_r\boldsymbol{E} \qquad \textbf{2.4}$$

The relative permittivity is in general a complex quantity and the reason to be complex is found in the fact that the relative permittivity has a lot to do with the losses of the material when an electric field is applied to it. The best way to understand the latter concept is considering an alternating electric field applied to a dipole. When the field incises in the dipole, it rotates to align itself with the field. As time goes by, the electric field changes its direction and the dipole must rotate to align itself with the new direction of the electric field and in that way to remain with the correct polarity. As it rotates, some amount of energy is lost generating heat because of the friction. There will be a point, as the frequency of the electric field increases, in which the dipole will not be able to follow the orientation of the applied electric field, and the dipole will be out of phase with the incident electric field generating some losses. The imaginary part of the relative permittivity will show how large the losses in function of the frequency are.

Therefore, the relative permittivity of a lossy material can be defined as:

$$\hat{\varepsilon} = \varepsilon_0 \hat{\varepsilon}_r = \varepsilon' - j\varepsilon'' \, [F/m] \quad \textbf{2.5}$$

where

$$\varepsilon' = \varepsilon_0 \varepsilon_r \quad \textbf{2.6}$$

$$\varepsilon'' = \varepsilon_0 \frac{\sigma_a}{\omega \varepsilon_0} \quad \textbf{2.7}$$

where σ_a is the conductivity due to the applied alternating field.

According to the Maxwell's equations, specifically to the fourth Maxwell equation, the generalized version of the Ampere's law can be written as:

$$\boldsymbol{\nabla} \times \boldsymbol{H} = \boldsymbol{J} + j\omega \boldsymbol{D} \quad \textbf{2.8}$$

where ω is the angular frequency of the field measured in radians per second and $\boldsymbol{J}$ is the electric current density measured in amperes per square meter, which can be at the same time divided into two terms

$$\boldsymbol{J} = \boldsymbol{J}_i + \boldsymbol{J}_c \quad \textbf{2.9}$$

where $\boldsymbol{J}_i$ corresponds to the electric current density produced by an independent source to the applied electric field and $\boldsymbol{J}_c$ is the conduction electric current density, that is directly proportional to the strength of the electric field and can be expressed as:

$$\boldsymbol{J}_c = \sigma_s \boldsymbol{E} \quad \textbf{2.10}$$

where σ_s is the static conductivity of the material which is defined as:

$$\sigma_s = -q\mu_e \quad \textbf{2.11}$$

μ_e is the mobility of the electrons in a particular material and q is the charge of the electron. This conductivity can also have an imaginary part in order to account to the delay in the conduction response of large ions; it has not been included here for simplicity.

Therefore, the 4th Maxwell equation can be redefined as:

$$\nabla \times \boldsymbol{H} = \boldsymbol{J_i} + \boldsymbol{J_c} + j\omega \boldsymbol{D} \quad \textbf{2.12}$$

$$\nabla \times \boldsymbol{H} = \boldsymbol{J_i} + \sigma_s \boldsymbol{E} + j\omega(\varepsilon' - j\varepsilon'')\boldsymbol{E} \quad \textbf{2.13}$$

Regrouping the equation above,

$$\nabla \times \boldsymbol{H} = \boldsymbol{J_i} + (\sigma_s + \omega\varepsilon'')\boldsymbol{E} + j\omega\varepsilon' \boldsymbol{E} \quad \textbf{2.14}$$

The term $\sigma_s + \omega\varepsilon''$ is called effective conductivity σ_e and it is the value that usually is given in all the datasheets and in the data base of dielectric properties of body tissues done by Gabriel et al. in the Italian Institute for Applied Physics. σ_s is the static conductivity of the material and $\omega\varepsilon''$ is the conductivity of the material generated due to the applied alternating field. Consequently, the effective conductivity can be expressed as:

$$\sigma_e = \sigma_s + \omega\varepsilon'' = \sigma_s + \sigma_a \quad \textbf{2.15}$$

From the last expression of the fourth Maxwell's equation, the loss tangent of a material can be defined as the ratio between the term that expresses the losses associated to the electric field and the lossless term associated to the electric field. That is:

$$\tan\delta = \frac{\sigma_s + \omega\varepsilon''}{\omega\varepsilon'} \quad \textbf{2.16}$$

As conclusion, the fact that human tissues can be considered as linear non-magnetic lossy materials with electrical permittivity ε_r and effective conductivity σ_e can be stated The permittivity and conductivity are frequency-dependent in biological tissues. The complex relative permittivity of a lossy material can be expressed as [7]:

$$\hat{\varepsilon}_r = \varepsilon_r' - j\varepsilon_r'' = \varepsilon_r - j\frac{\sigma_e}{\omega\varepsilon_0} \quad \textbf{2.17}$$

σ_e is the effective conductivity of the material which, depending on the nature of the sample, may include a contribution from a frequency-independent ionic conductivity σ_i .

2.1.2 Dielectric dispersion

Typically, dielectric constants decrease and conductivities increase with increasing frequency. The behavior of biological media is frequency dependent due to the dramatic change that membrane capacitance undergoes as the frequency increases.

At low frequencies, biological materials exhibit very high dielectric constants due to biological tissues are composed of macromolecules, cells, and other membrane-bound substances [12]. Cell membranes have a relatively high capacitance at low frequencies. They become progressively short-circuited for frequencies above 1 kHz, facilitating the participation of intracellular fluid in electric current conduction. This causes conductivity to increase with increase in frequency.

As frequency increases, insufficient time is allowed during each cycle to permit complete charging of cells membranes. The total charges per cycle must decrease, together with membrane capacitance, with increasing the frequency. This behavior gives rise to decrease in the dielectric constant between 10 kHz and 30 MHz.

For still higher frequencies, the change in membrane capacitance stabilizes until the rotational and vibrational properties of polar molecules of water become significant.

There are three main dispersion regions in the dielectric spectrum of a biological tissue α, β and γ, although the δ dispersion can also be found for some materials. The dispersions are rather broad, indicating the possible

overlap of discrete relaxations arising from the polarization mechanisms encountered in the complex biological environment.

- *α Dispersion*

The alpha or low frequency dispersion is characterized by very high permittivity values and can be attributed, at least partially, to counterion (the ion that accompanies an ionic species in order to maintain electric neutrality) diffusion effects. Such large dispersions are predicted by theories of ionic diffusion in heterogeneous media. Also other mechanisms were postulated to contribute to the alpha dispersion; many relate to interactions in the vicinity of the cell membrane [11].

- *β Dispersion*

The β dispersion occurs at intermediate frequencies and originates mostly from the capacitive charging of the cellular membranes and those of membrane-bound intracellular bodies. This phenomenon, also known as interfacial polarization, has been studied theoretically and experimentally [11].

- *γ Dispersion*

The Gamma dispersion is due to the dipolar polarization of water molecules [11].

- *δ Dispersion*

Tissues and other biological materials may exhibit dispersions other than the three main ones. The δ dispersion, identified in some protein solutions between the β and γ dispersions may also occur in tissue in the hundreds of megahertz range; when present, its magnitude is small compared to the adjacent ones. Possible mechanisms include the dipolar relaxation of bound water, relaxation of small dipolar segments or side chains of biological molecules, and counterion diffusion along small regions of the charged surface. Under these conditions it is difficult to isolate and, in view of the multiplicity of possible mechanisms, difficult

to interpret. It is often treated as the tail end of the *β* dispersion or a broadening of the *γ* dispersion [11].

In Figure 2.2, the aforementioned dispersions are shown.

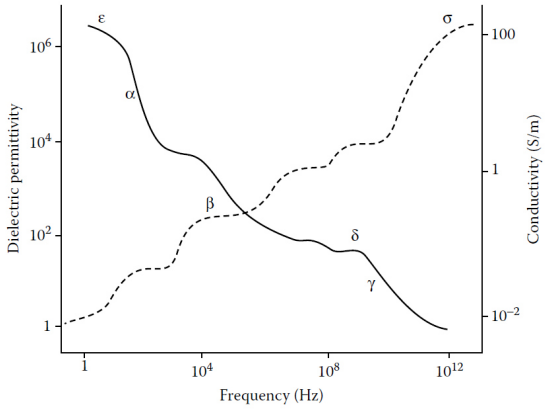

Figure 2.2: Dielectric permittivity and electrical conductivity of muscle-like biological material as a function of frequency [12]

It is important to note that all the previous dispersion phenomena are related to the aligment of the molecular dipolar moments to an applied field (dipolar polarization). A relaxation effect is usually associated with this kind of polarization. However, at higher frequencies, resonant effects appear due to atomic and electronic polarizations (Figure 2.3).

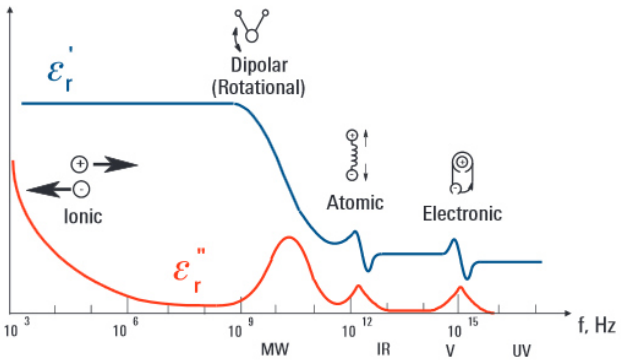

Figure 2.3: Polarization phenomena [13]

Atomic polazation occurs when adjacent positive and negative ions are separated by the applied electric field, while electronic polarization appears when the electric field displaces the nucleus of the atom from the electrons that sorrund it [13]. These phenomena show up at frequencies that are higher than the ones that will be studied in this thesis so they are outside the scope of the presented work.

2.1.3 Human tissue distribution

The human body is a combination of very different number of tissues with different properties and functions. Tissue distribution is highly dependent on each person, gender and age [14]. A visual distribution of the tissues inside the human body can be obtained from the results of the Visible Human Project [15].

The different tissues in the human body can be grouped in two general types: high-water content tissue with high permittivity and losses (skin and muscle for example) and low-water content tissues which have lower permittivity and losses (fat and bone for example). In Figure 2.4 an illustration that shows different parts of the body and their water content is presented.

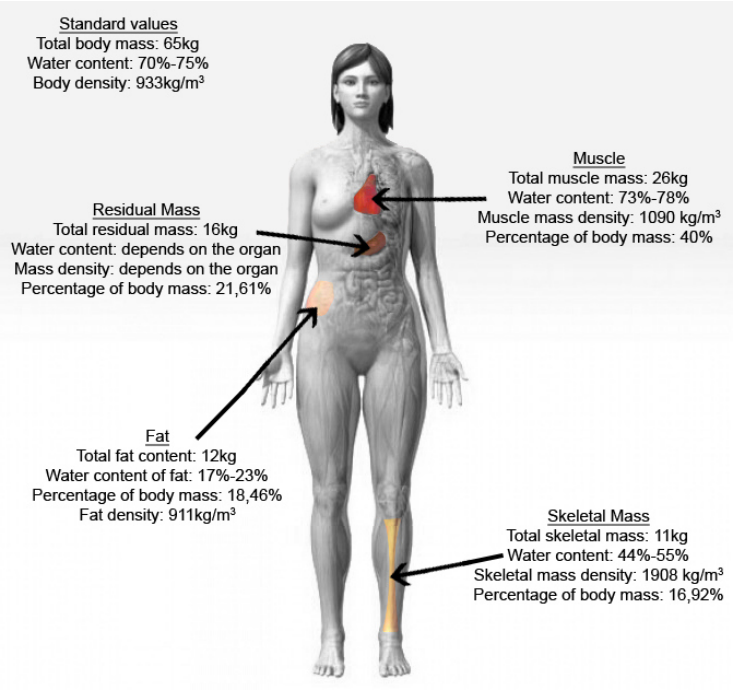

Figure 2.4: Water content in different parts of the human body

There are also some studies about how the age affects the dielectric properties of the human body. In general, the main changes are due to the decrease in the content of the Total Body Water (TBW) with the age and the hormonal changes in women [16].

In Table 2.1 the typical thickness of the tissues is shown for different parts of the human body [14].

Table 2.1: Typical thickness of human body layers for different locations and ages [14].

Tissue	Frontal Thorax		Frontal Abdomen		Rear Thorax		Rear Abdomen		Spine	
	Child	Adult	Child	Adult	Child	Adult	Child	Adult	Child	Adult
Skin	0.6-1.0	0.8-2.6	0.6-0.8	1.0-2.6	0.4-1.0	1.4-2.6	0.4-1.0	1.4-2.6	0.4-1.0	1.4-2.6
SAT	0.0-16.0	1.4-23.2	0.0-16.2	1.6-22.2	0.0-10.8	0.6-15.0	0.0-13.2	2.4-21.2	0.0-13.2	2.4-21.2
Breast Tissue	-	0.0-30.0	-	-	-	-	-	-	-	-
Muscle	0.0-30.0	0.0-30.0	0.0-30.0	0.0-30.0	0.0-30.0	0.0-30.0	0.0-30.0	0.0-30.0	-	-
Bone	0, 4.4-4.8	0, 5.6-6.6	-	-	4.4-4.8	5.6-6.6	4.4-4.8	5.6-6.6	17.0-17.6	24.4-30.4
CSF	-	-	-	-	-	-	-	-	2.6-6.4*	2.6-6.4
Viscera (Termination)	Heart, Lung Liver, Thymus		Intestines		Lung Liver		Kidney Spleen		Spinal Cord	

As it has been mentioned at the beginning of this chapter, it is out of scope of this thesis to study deeply all the electrical properties and the biological effects that are produced by the different tissues. Therefore, the attention will be focused on the first three layers that are also the most critical for the communication with implanted devices: skin, fat and muscle.

- Skin: human skin is a laminar tissue made up of three main layers (see Figure 2.5)

  - The *epidermis*, the outermost layer of skin, provides a waterproof barrier and creates our skin tone.
  - The *dermis*, beneath the epidermis, contains tough connective tissue, hair follicles, and sweat glands.
  - The deeper subcutaneous tissue (*hypodermis*) is made of sat and connective tissue.

  The dielectric properties of composite skin are a mixture of the properties of all previous layers. Skin is in the group of high water content tissues.

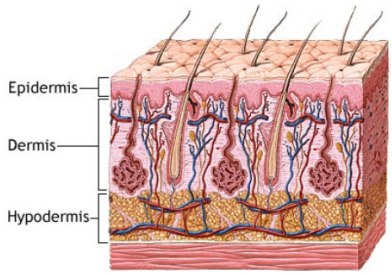

Figure 2.5: Skin composition

- Fat and SAT: SAT is the Subcutaneous Adipose Tissue or averaged fat, and it is the layer between the skin and the muscle. Whereas, fat (not infiltrated) is located around different areas in the body, not only between skin and muscle tissues. Both tissues are low-water content

tissues, however, SAT could be considered to be a mixture of blood (high water content) and fat, and consequently its dielectric constant and conductivity are higher than the ones of the fat. As it will be discussed later, these differences may affect the performance of a hypothetical implanted communication link.

In most of the research articles, fat (not infiltrated) is used as material, however, SAT (Subcutaneous Adipose Tissue or averaged fat) should be used depending on the body location. Differences have been also found in different phantom models. In Figure 2.6, SAT vs. fat is shown for human torso in Duke's torso from Virtual Family (IT'IS foundation).

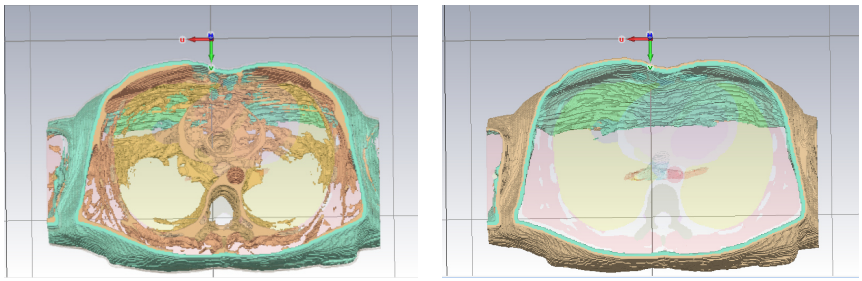

(a) **(b)**

Figure 2.6: Duke's human torso. (a) SAT (blue colour) + Fat tissue (yellow colour). (b) Skin (yellow colour) + SAT (blue color)

Anyway, regardless of the used model, in both cases, either SAT or FAT are located between the skin and muscle and its water content is lower than the other two layers. Due to this drastic change in the medium properties, as it will be discussed later; a standing-wave pattern can be created in this layer, which is not desirable since it leads to the absorption of the signal [14].

- Muscle: is a high water content medium and consequently quite lossy. As it has been shown in Table 2.1, maximum thickness close to 30 mm can be considered, although thicknesses as high as 60 mm have been

reported in literature. Therefore, depending on the working frequency, the RF signals will be strongly attenuated in the muscle layer by the time they reach the internal organs [17].

2.2 Mathematical models of human body

The dielectric properties of biological materials and their frequency behavior have been extensively studied in the last century. The main objective of these studies was to set a credible database of dielectric properties of human body tissues. In order to simplify the insertion of body properties in Maxwell Equation solvers it is useful to obtain mathematical models from the measurement results [18]. From the previous section it can be clearly seen that human tissues are very dispersive; the underlying basic mechanism that accounts for this dispersion is a multi-band relaxation phenomenon which takes place during dipolar polarization when an electric field is applied to the different human body tissues. In its simplest form, each of these relaxation regions, that is the manifestation of a polarization mechanism, can be characterized by a single time constant τ by Debye's first order equation [19]:

$$\hat{\varepsilon}_r = \varepsilon_\infty + \frac{\varepsilon_s - \varepsilon_\infty}{1 + j\omega\tau} \quad \textbf{2.18}$$

where ε_s is the real part of the relative permittivity at zero frequency (static), ε_∞ is real part of the relative permittivity at infinite frequency (optical).

From the previous expression, the real and imaginary parts of the permittivity can be described as:

$$Re\{\hat{\varepsilon}_r\} = \varepsilon_\infty + \frac{\varepsilon_s - \varepsilon_\infty}{1 + (\omega\tau)^2} \quad \textbf{2.19}$$

$$Im\{\hat{\varepsilon}_r\} = \varepsilon_\infty + \frac{(\varepsilon_s - \varepsilon_\infty)\omega\tau}{1 + (\omega\tau)^2} \quad \textbf{2.20}$$

The relaxation time corresponds to a relaxation frequency $f_r = {}^{1}/_{2\pi\tau}$. At that frequency, the permittivity and conductivity is halfway between its limiting values and the loss factor at its highest (Figure 2.7).

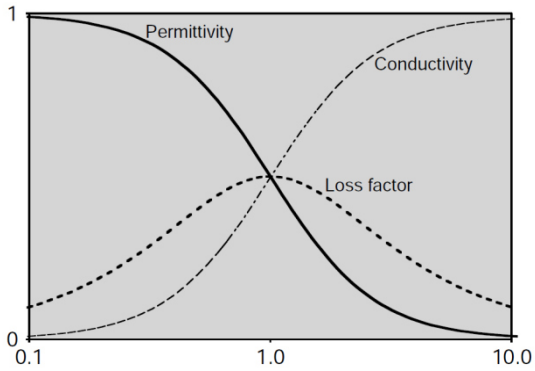

Figure 2.7: Normalized permittivity $(\varepsilon' - \varepsilon_\infty)/(\varepsilon_s - \varepsilon_\infty)$, loss factor $\varepsilon''/(\varepsilon_s - \varepsilon_\infty)$, and conductivity $\omega\varepsilon_0\,\varepsilon''/(\varepsilon_s - \varepsilon_\infty)$ for a single time constant relaxation plotted against f/f_r [11]

Below the relaxation frequency the electric field is slow enough so that the dipoles can follow the field variations; consequently, the polarization develops fully and the loss is directly proportional to frequency [13]. As the frequency increases, $Im\{\hat{\varepsilon}\}$ continues to increase but the storage starts to decrease as dipoles start delaying from the electric field. Above the relaxation frequency, both terms decrease, because the dipole rotation cannot follow the electric field anymore.

The biological materials have multiple dispersions and distributions of relaxation time, therefore the Debye model, which exhibits only a single relaxation time, is not accurate enough.

The currently most comprehensive, complete, and best known database of RF dielectric properties of body tissues is based on the work of Gabriel et al., which

provides dispersive parameter models for several important body tissues [19–21].

Previous to this work most data was obtained from measurements from animals. The data that is used to construct the proposed mathematical model are those that correspond more closely lo living human tissues. Consequently, human tissue and in vivo measurements were selected in preference to animal tissues and in vitro. For in vitro measurements, data obtained at temperatures closest to that of the body and the nearest to time after death were used when available [20].

Based on these measurements, Gabriel et al. proposed a parametric model using a Cole-Cole analysis for several body tissues in the frequency range from 10 Hz to 100 GHz. The experimental spectrum is modeled with four dispersion regions.

Cole-Cole model is a variation of Debye's equation taking into account broader dispersions. The complex permittivity of a tissue can be modeled with a four Cole-Cole model and an ionic conductivity term (which is the contribution of ionic conductivity and lower frequency polarization mechanisms).

$$\hat{\varepsilon} = \epsilon_\infty + \sum_{n=1}^{4} \frac{\Delta\varepsilon_n}{1 + (j\omega\tau_n)^{(1-\alpha_n)}} + \frac{\sigma_i}{j\omega\varepsilon_0} \qquad \textbf{2.21}$$

The values for the different parameters in the model where statistically fitted for each tissue and each dispersion region. In Table 2.2, the values of these parameters for different biological tissues are summarized.

Table 2.2: Parameters of the Cole-Cole model for different tissues [19]

Tissue type	ε_∞	$\Delta\varepsilon_1$	τ_1 (ps)	α_1	$\Delta\varepsilon_2$	τ_2 (ns)	α_2	$\Delta\varepsilon_3$	τ_3 (μs)	α_3	$\Delta\varepsilon_4$	τ_4 (ms)	α_4	σ
Blood	4.0	56.0	8.38	0.10	5200	132.63	0.10	0.0			0.0			0.7000
Bone (cancellous)	2.5	18.0	13.26	0.22	300	79.58	0.25	2.0×10^4	159.15	0.20	2.0×10^7	15.915	0.00	0.0700
Bone (cortical)	2.5	10.0	13.26	0.20	180	79.58	0.20	5.0×10^3	159.15	0.20	1.0×10^5	15.915	0.00	0.0200
Brain (grey matter)	4.0	45.0	7.96	0.10	400	15.92	0.15	2.0×10^5	106.10	0.22	4.5×10^7	5.305	0.00	0.0200
Brain (white matter)	4.0	32.0	7.96	0.10	100	7.96	0.10	4.0×10^4	53.05	0.30	3.5×10^7	7.958	0.02	0.0200
Fat (infiltrated)	2.5	9.0	7.96	0.20	35	15.92	0.10	3.3×10^4	159.15	0.05	1.0×10^7	15.915	0.01	0.0350
Fat (not infiltrated)	2.5	3.0	7.96	0.20	15	15.92	0.10	3.3×10^4	159.15	0.05	1.0×10^7	7.958	0.01	0.0100
Heart	4.0	50.0	7.96	0.10	1200	159.15	0.05	4.5×10^5	72.34	0.22	2.5×10^7	4.547	0.00	0.0500
Kidney	4.0	47.0	7.96	0.10	3500	198.94	0.22	2.5×10^5	79.58	0.22	3.0×10^7	4.547	0.00	0.0500
Lens cortex	4.0	42.0	7.96	0.10	1500	79.58	0.10	2.0×10^5	159.15	0.10	4.0×10^7	15.915	0.00	0.3000
Liver	4.0	39.0	8.84	0.10	6000	530.52	0.20	5.0×10^4	22.74	0.20	3.0×10^7	15.915	0.05	0.0200
Lung (inflated)	2.5	18.0	7.96	0.10	500	63.66	0.10	2.5×10^5	159.15	0.20	4.0×10^7	7.958	0.00	0.0300
Muscle	4.0	50.0	7.23	0.10	7000	353.68	0.10	1.2×10^6	318.31	0.10	2.5×10^7	2.274	0.00	0.2000
Skin (dry)	4.0	32.0	7.23	0.00	1100	32.48	0.20	0.0			0.0			0.0002
Skin (wet)	4.0	39.0	7.96	0.10	280	79.58	0.00	3.0×10^4	1.59	0.16	3.0×10^4	1.592	0.20	0.0004
Spleen	4.0	48.0	7.96	0.10	2500	63.66	0.15	2.0×10^5	265.26	0.25	5.0×10^7	6.366	0.00	0.0300
Tendon	4.0	42.0	12.24	0.10	60	6.37	0.10	6.0×10^4	318.31	0.22	2.0×10^7	1.326	0.00	0.2500

In Figure 2.8 the comparison between the modeled and measured permittivity and conductivity values taking as an example the skin is shown.

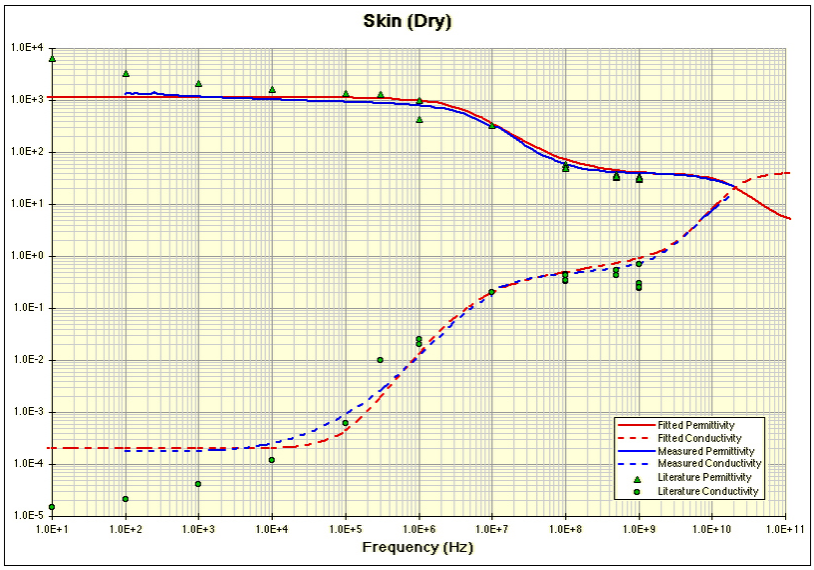

Figure 2.8: Measured (blue) and modelled (red) data for permittivity (solid lines) and conductivity (dotted lines) of skin dry

The good matching obtained with the proposed model can be seen in the previous graph. The parameters of all the rest of tissues and the full explanation of the measurements and calculations procedures can be found in [7], [19–21].

2.3 Phantoms

A phantom is a physical or numerical model with the same electrical characteristics as the human body. The aim of these models is to explore the interaction between the human tissue and the electromagnetic waves.

Most of the research in RF and Microwave frequency range has been focused on dosimetry calculations. Dosimetry is the science of quantifying the three dimensional distribution of electromagnetic fields inside tissues and organs of biological bodies [11].

The distribution of induced fields in human body depends on several parameters such as: frequency, size and shape of the body, incident field strength and angle, tissue distribution…

Phantom models in bioelectromagnetics have progressed from the spherical models of human used during the 1970s to ultrahigh resolution phantoms such as the ones developed by IT'IS foundation and joined together in Virtual Population voxel-based model. These models are used by several electromagnetic computer simulation software. In this section an analysis of the different phantom types will be addressed.

Phantom models can be classified according to different criteria:

- Nature: physical and numerical
- Composition: homogeneous and heterogeneous.
- Geometry: planar, spherical, cylindrical and voxel models.

The choice between homogeneous and heterogeneous or simple geometry or voxel models, depends on the accuracy required by the application.

In the following sections the main options for simulation and fabrication of phantoms will be explained.

2.3.1 Physical phantoms

Several kinds of materials can be used to replicate the electric properties of the different human body tissues. Some references can be found in different international standards on RF dosimetry [22].

2.3.1.1 Classification of physical phantoms

Basically the physical phantoms can be classified according to their composition as solid-dry, solid-wet, semisolid gel and liquid phantoms.

a) Solid dry phantoms

Solid dry phantoms are expensive to manufacture since they require special equipment and procedures. One of the most cumbersome solid dry phantom is SAM (Specific Anthropomorphic Mannequin) voxel model (Figure 2.9).



Figure 2.9: SAM-V4.5BSE

It is the most widely used homogeneous head phantom, which has been proposed by the IEEE (2003) and IEC (2005) standards for compliance testing in mobile phone industry.

b) Liquid phantoms

On the other hand, liquid phantoms are basically a tank filled with tissue-simulating liquid. This liquid is usually water plus several additional elements in order to control the permittivity and conductivity.

Conductivity describes how well electric current propagates, and is dependent on the number of ions in the solution. This means that adding a substance which increases the number of ions in the solution also increases the conductivity. Typically, salt (NaCl) can be added since both Na+ and Cl- ions will increase the conductivity. The lowest conductivity possible in water is obtained when there are no ions present, i.e. deionized water.

Moreover, the dielectric permittivity is a measurement on how polar a substance is. If the molecules in the substance are polar or highly polarizable the permittivity is high [45]. Water molecules are very polar and hence water has a high permittivity. In order to reduce permittivity, a non-polar molecule, for example sugar, can be added.

Most common recipes add sugar for low frequencies and either Diacetin or Di-ethylene Glycol Butyl Ether (DGBE) for higher frequencies in order to control the permittivity [23].

In Table 2.3, some recipes based on the aforementioned materials for head tissue are shown.

Table 2.3: Suggested recipes for achieving target dielectric parameters for head tissue-equivalent liquids [22]

Frequency (MHz)	300	450			835		900			1450	1800			1900			1950	2000	2100		2450			3000
Recipe #	1	1	3		1	1	2	3	1	1	2	2	3	1	2	4	1	1	2	2	3	1		
Ingredients (% by weight)																								
1,2-Propanediol							64.81																	
Bactericide	0.19	0.19	0.5	0.1	0.1			0.5					0.5								0.5			
Diacetin			48.9					49.2					49.43								49.75			
DGBE									45.41	47	13.84	44.92		44.92	13.84	45	50	50	7.99	7.99		7.99		7.99
HEC	0.98	0.98		1	1																			
NaCl	5.95	3.95	1.7	1.45	1.48	0.79	1.1	0.67	0.36	0.35	0.18	0.64	0.18	0.35				0.16	0.16		0.16		0.16	
Sucrose	55.32	56.32		57	56.5																			
Triton X-100										30.45				30.45					19.97	19.97		19.97		
Water	37.56	38.56	48.9	40.45	40.92	34.4	49.2	53.82	52.64	55.36	54.9	49.43	54.9	55.36	55	55	50	50	71.88	71.88	49.75	71.88	71.88	
Measured dielectric parameters																								
ε'	46	43.4	44.3	41.6	41.2	41.8	42.7	40.9	39.3	41	40.4	39.2	39.9	41	40.1	37	36.8	41.1	40.3	39.2	37.9			
σ (S/m)	0.86	0.85	0.9	0.9	0.98	0.97	0.99	1.21	1.39	1.38	1.4	1.4	1.42	1.38	1.41	1.4	1.51	1.55	1.88	1.82	2.46			
Temp. (°C)	22	22	20	22	22	22	22	20	22	22	22	20	21	21	20	22	22	20	20	20	20			
Target dielectric parameters																								
ε'	45.3	43.5		41.5		41.5		40.5	40								39.8		39.2		38.5			
σ (S/m)	0.87	0.87		0.9		0.97		1.2	1.4								1.49		1.8		2.4			

According to Table 2.3, focusing the attention on sugar and salt based phantoms, a very small concentration of salt results in a great increase in conductivity, while the concentration of sugar needs to be higher in order to get a comparable change in permittivity.

As it can be seen, these recipes also include a bactericide in order to prevent material's breakdown and extend its life.

In this thesis, liquid phantoms are used since they are easy to produce with low-cost materials and procedures. Moreover, these kind of phantoms allow the movement of an antenna inside them, which is a key factor in this research.

The main disadvantage of liquid phantoms is the limited range of frequencies where the liquid can maintain its properties. The liquid made out of water, sugar and salt, gives a permittivity and conductivity which has a better linear behavior than real human body tissues.

Other disadvantages include the difficulty of handling the liquid and the container, in addition to the impact of the electrical properties of the container, which is usually made of Fiberglass of Polyurethane.

c) Semisolid gel phantoms

Liquid phantoms are suitable for homogeneous phantoms but when heterogeneous ones are needed, it is difficult to keep the materials of different compositions from mixing one with each other. Therefore; solid, semi-solid or gel phantoms must be used. Once a liquid phantom is fabricated, agar substance can be added in order to become the solution gelatinous. Depending on the concentration of agar, different viscosities can be obtained. However, the relative dielectric constant values decrease as the concentration of gelatin increases and the agar also affects the obtained conductivity. The study of gel phantoms is out of the scope of this thesis. A deeper analysis on the effect of agar in these kind of phantoms is addressed in [24].

Several manufactures also provide off-the-shelf tissue-simulating liquids [25][26].

2.3.1.2 Dielectric characterization of materials

It is very important to characterize the electromagnetic properties of the physical phantoms. There are different measuring techniques for the characterization of the dielectric properties of materials. In this section some of the most importants are presented.

a) Open-Ended Coaxial Line

The open-ended coaxial probe is a cut off section of a transmission line (Figure 2.10). The material is measured by immersing the probe into a liquid or touching it to the flat face of a solid material (preferably soft or powder-made). The fields at the probe end “fringe” into the material and change as they come into contact with the material under test. The reflected signal (S11) can be measured and related to $\varepsilon_r{}^*$.

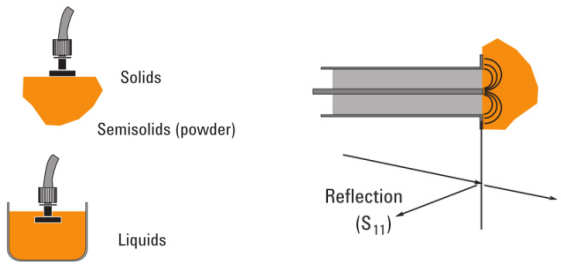

Figure 2.10: Open-ended coaxial line: (a) topology; (b) measured S-parameters [13]

The main advantage of this method is its suitability for measuring liquids and its simplicity for broadband characterization of material properties, although the accuracy of the result is more limited compared to other methods. The main disadvantage is the possible air-gaps that can be produced between the material and the probe. These air-gaps have influence in the measurement

results. Consequently, a very flat surface is required when the material under test is solid.

b) Parallel plate

The parallel plate method involves sandwiching a thin sheet of the material under test between two electrodes to form a capacitor (Figure 2.11). The measured capacitance is then used to calculate permittivity. It is typically used at frequencies below 1 GHz, and it requires the use of an impedance analyzer.

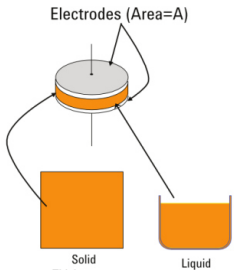

Figure 2.11: Parallel plate method [13]

c) Resonant cavity

This method uses a resonant cavity for the sample holder, and a network analyzer to measure the resonant frequency and quality factor of the cavity, both empty and with the sample present (Figure 2.12a). When a piece of material is placed inside the cavity, the center frequency and the quality factor of the cavity will be affected (Figure 2.12b). From this, electric and magnetic properties of the material under test can be calculated. This method has the best loss factor resolution and it is very accurate. However, the fact that is a narrowband method is the main drawback.

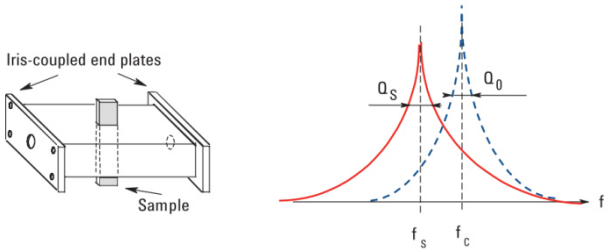

(a) **(b)**

Figure 2.12: Waveguide resonator: (a) topology; (b) resonance shift [13]

d) Transmission line

This method involves placing the material under test inside a portion of an enclosed transmission line (Figure 2.13). The line is usually a section of rectangular waveguide or coaxial line. ε_r^* and μ_r^* are computed from the measurement of the reflected signal (S11) and transmitted signal (S21).

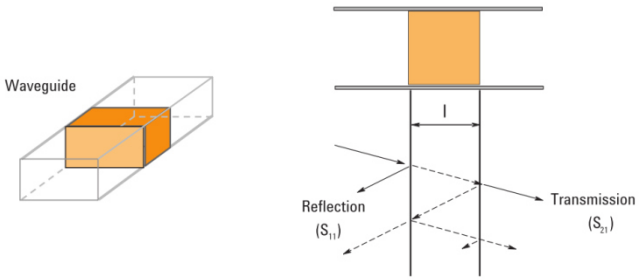

(a) **(b)**

Figure 2.13: Filled rectangular waveguide: (a) topology; (b) measured S-parameters [13]

e) Free-Space

This method consists of placing the material under test between two directive antennas to focus microwave energy at or through a slab or sheet of this material (Figure 2.14). In that way, both its electric and magnetic properties can

be obtained. This method is non-contacting and can be applied to materials to be tested under high temperatures and hostile environments.

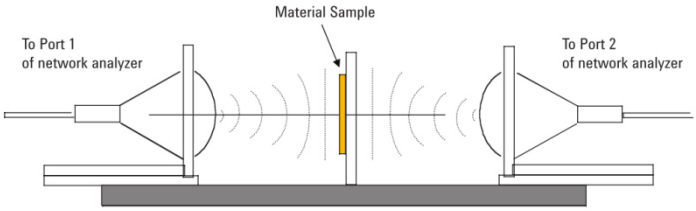

Figure 2.14: Free-Space method for material characterization [13]

To sum up, a comparison of the methods is shown in Figure 2.15.

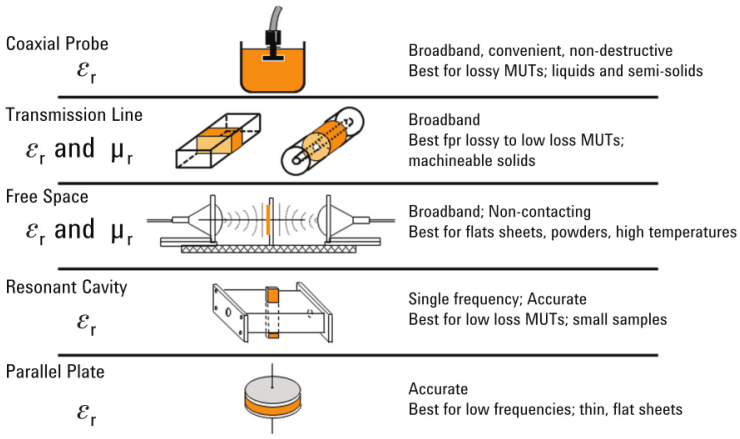

Figure 2.15: Summary of measurements techniques [13]

2.3.2 Phantom simulation

2.3.2.1 Simulation techniques

The numerical methods used to evaluate the power absorption into biological bodies are basically four: method of moments (MoM), the finite integration technique (FIT), the finite difference time domain (FDTD) method and the finite elements method (FEM).

FDTD and FIT solve Maxwell's equation in time domain in contrast to MoM and FEM. FIT method is a consistent formulation for the discrete representation of Maxwell's equations on spatial grids [27]. First proposed by Weiland [28] in 1977, the finite integration technique can be viewed as a generalization of the FDTD method. These two methods are particularly well suited to bioelectromagnetics because they can efficiently model the heterogeneity of the human body with high resolution and frequency-dependent properties [10].

There are different commercial software available in the market offering full wave, three dimensional solutions to EMF exposure problems (Table 2.4).

Table 2.4: Examples of commercial software packages offering full wave, three-dimensional solutions to EMF exposure problems

Product	*Numerical technique*	*Manufacturer*
CONCERTO	*FDTD*	*Vector Fields*
EMPIRE XCcel	*FDTD*	*IMST GmbH*
FIDELITY	*FDTD*	*Zeland Software*
GEMS	*FDTD*	*2COMU*
SEMCAD X	*FDTD*	*SPEAG*
XFDTD	*FDTD*	*Remcom*
HFSS	*FEM*	*Ansoft*
Microwave Studio	*FIT*	*CST*
FEKO	*MoM/FEM*	*Electromagnetic Software and Systems*

2.3.2.2 Phantom models

Originally, when the consequences of radiation were first noticed in the 1960s, the scientific community decided to create some simple phantoms to test the effects of ionizing radiation.

Spherical models were used to represent the biological models when bioelectromagnetics research world was starting to take off. Spheres obviously do not represent the shape of humans or animals very accurately, but much useful information that served as a basis for calculations in more realistic models was obtained from them. Using the data obtained from these models, the Maxwell equations could be solved and mathematical expressions and

results for the internal H and E fields could be obtained. At the 70's, thanks to spherical models valuable information was obtained in order to understand the characteristics of E and B fields inside the human and animal bodies.

Later, other models with more realistic shapes were used in both experimental measurements and calculations. A very common approach is to use block models of the body of interest. A block model consists on cubical mathematical cells arranged to approximate the shape of the human and animal's bodies. As an example, a head's multilayer planar block model is shown in Figure 2.16.

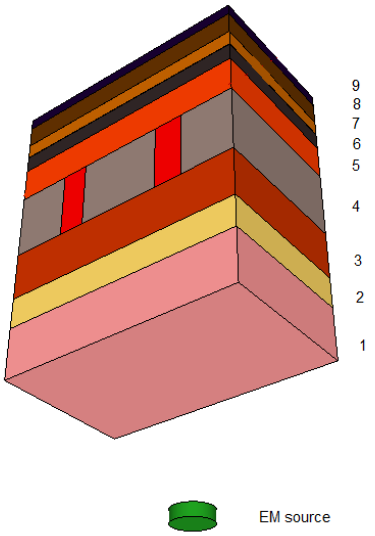

Figure 2.16: Head's multilayer planar block model. 1. Skin and fat. 2. Muscle. 3. Skull exterior. 4. Nasopharyns / mouth + tongue (depending on the part of the head one is focusing on). 5. Dura mater outer + veins. 6. Dura mater outer. 7. Cerebrum. 8. Cerebellum. 9. Ventricles + Putamen + Glands + Nerves.

The first phantom models were based on MIRD (Medical Internal Radiation Dose). These human models had 22 organs and 100 sub-regions (Figure 2.17).

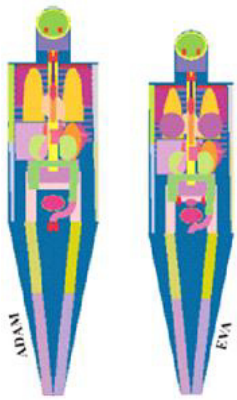

Figure 2.17: MIRD phantom developed in 1980s

A second generation phantoms were created thanks to new advanced techniques such as, CT (Computed Tomography), MRI (Magnetic Resonance Imaging) or cryogenic images. High quality images could be obtained to reconstruct the full human body in 3-D. These new structures would be known as volumetric pixel; today known as voxels.

The resolution in each slice is in the order of several millimeters. MRI technology allows the correct and accurate detection of soft tissues. The correct detection of this kind of tissues is of great importance because it is essential for the calculation of the reflections and the interferences produced by these kinds of materials. Furthermore, MRI is selected owing to the proper positioning of the internal organs and the possibility to determine the density of each organ that make this technique optimum to describe the shape of the body.

MRI data are generally superior to CT data in identifying interior tissues because of the high contrast images of the soft tissues [12]. With these voxels, dosimetry studies are much more accurate (Figure 2.18).

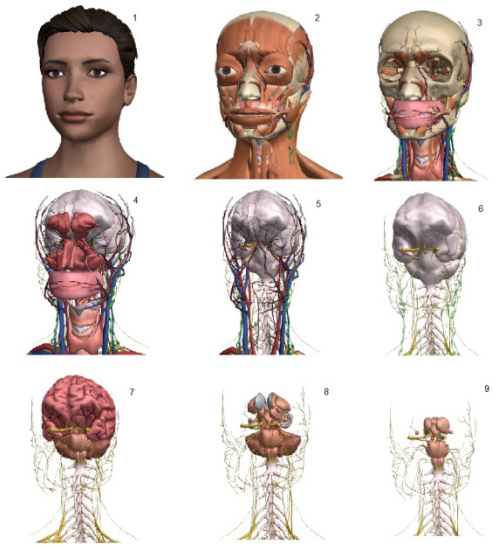

Figure 2.18: Voxel model of a woman head [29]

There are a number of companies and research centres that have developed different phantom models. In current study the virtual family of IT'IS foundation is deeply analyzed. Other some important models are also mentioned in this section.

a) Virtual Family (IT'IS foundation)

The Foundation for Research on Information Technologies in Society (IT'IS) is a nonprofit research foundation dedicated to improving and advancing the quality of people's live. This foundation has created a very accurate voxel models, the so called Virtual Family (Figure 2.19), by using Magnetic Resonance Imaging (MRI) technique [29].

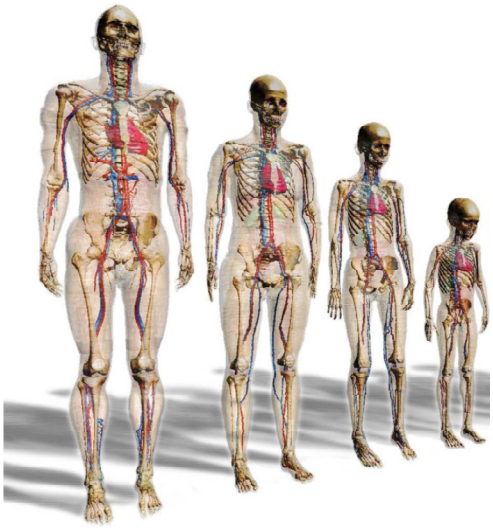

Figure 2.19: Virtual Family created by IT'IS foundation. From left to right: Duke, Ella, Billie and Thelonious

Virtual family's offers different voxel resolutions for each model:

$$5x5x5\ mm^3, 2x2x2\ mm^3, 1x1x1\ mm^3\ \&\ 0.5x0.5x0.5\ mm^3.$$

The physical characteristics of each voxel are summarized in Table 2.5.

Table 2.5: Virtual family's physical characteristics

Name	*Age*	*Gender*	*Height[cm]*	*Weight [kg]*	*Corporal Mass Index [kg/m2]*
Duke	*34*	*Male*	*177*	*72.4*	*23.1*
Billie	*11*	*Female*	*147*	*35.4*	*16.4*
Ella	*26*	*Female*	*163*	*58.7*	*22.1*
Thelonious	*6*	*Male*	*117*	*19.3*	*14.1*

b) CST voxel family

CST offers accurate, efficient computational solutions for electromagnetic design and analysis. CST has developed their own human models, the so

called CST Voxel Family [30]. The main information about the phantoms is described in Table 2.6 and Figure 2.20.

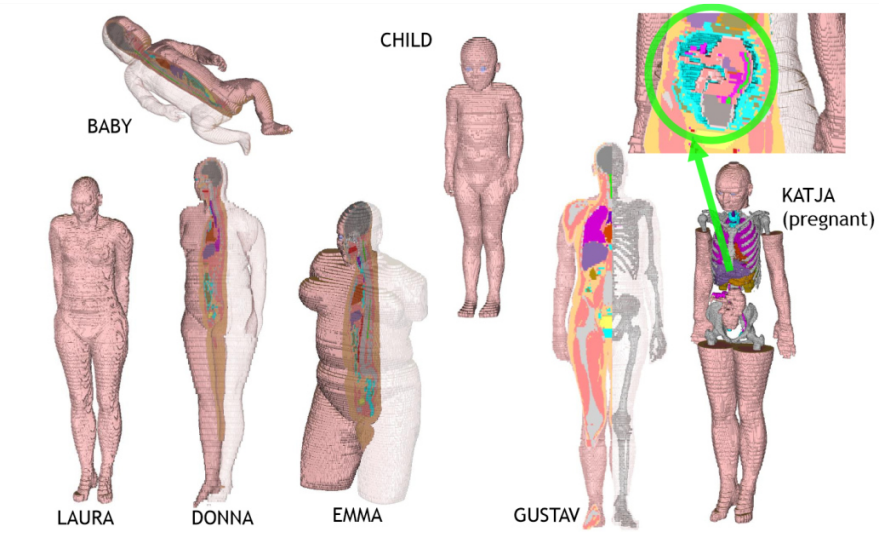

Figure 2.20: CST voxel family

Table 2.6: CST voxel family´s physical characteristics

Model	*Age*	*Gender*	*Height[cm]*	*Mass[kg]*	*Resolution[mm^3]*
Baby	*8 weeks*	*Female*	*57*	*4.2*	*0.85x0.85x2.0*
Child	*7 years*	*Female*	*115*	*21.7*	*1.54x1.54x1.6*
Donna	*40 years*	*Female*	*176*	*79*	*1.875x1.875x2.0*
Emma	*26 years*	*Female*	*170*	*81*	*0.98x0.98x1.0*
Gustav	*38 years*	*Male*	*176*	*69*	*2.08x2.08x2.0*
Laura	*43 years*	*Female*	*163*	*51*	*1.875x1.875x1.25*
Katja	*43 years*	*Pregnant*	*163*	*62*	*1.775x1.775x1.21*

c) Visible human project

The visible Human Project is an initiative run by U.S. National Library of Medicine (NLM) which consists of database of Computed Tomography (CT), Magnetics Resonance (MR) and high resolution pictures obtained from human cadavers. Several institutions taking part in this project have made the results available for research purposes. The Visible Human Project [15] developed the Hugo model. It is more complex than the CST Voxel Family but still has not got as many tissues as the Virtual Family from IT'IS foundation.

2.4 Biological effects and exposure limits

In this section some basic explanations about the possible health effects related with EM radiation are shown, explaining the concept of SAR (Specific Absorption Rate) and bio-heat equation. Besides, some comments about regulation for maximum RF exposure limits are mentioned.

2.4.1 Biological effects

Radio frequency electromagnetic (RF) fields have been used for various purposes for a very long time, for example in radio and TV transmission, microwave ovens, and during the last decades also in mobile telecommunications. Since RF fields have the ability to cause heating in the exposed individuals, there are concerns about possible health implications.

The interaction of RF fields with living systems can be considered at the molecular, sub-cellular, cellular, organ or system level, as well as the entire body. Biological effects due to exposure to radiofrequency radiation are differentiated into three levels [31]: high-level (thermal) effects, intermediate-level (athermal) effects, and low-level (non-thermal) effects.

In order to study the thermal effects, the Specific Absorption Rate (SAR) in combination with Bio-Heat equations are used in most cases.

SAR is defined as transferred power divided by the mass of the object. Specific refers to the normalization to mass, and absorption rate to the rate of energy absorbed by the object [10]. For sinusoidal steady-state EM fields the time-average SAR is given by:

$$SAR = \frac{\sigma_e |E_{rms}|^2}{\rho} \ [W/kg] \qquad \textbf{2.22}$$

where ρ is the mass density of the object in kg/m^3, E_{rms} is the root mean square (rms) value of the electric field.

The bio-heat equation was originally proposed by Pennes in 1948 to analyze temperature distributions in a resting forearm [32]. It is an analytical model that describes the temperature distribution inside the body as follows [2].

$$\rho c \frac{\partial T}{\partial t} = \nabla \cdot (k \nabla T) + \rho Q + \rho S - \rho_b c_b \rho \omega (T - T_b) \qquad \textbf{2.23}$$

where T is the temperature, t is the time, ρ is the volume density of mass, c is the specific heat capacity, k is the thermal conductivity, ω is the volumetric blood perfusion rate, Q is the metabolic heat generation rate, S is the specific absorption rate (SAR) and the subscript *b* denotes a blood property.

Subsequently, it has been modified to study the phenomena of heat transport and exchange for the whole body [33], it can be expressed in many different ways [10]:

$$\frac{\partial(\Delta T)}{\partial t} = \frac{1}{4186c}(W_{em} + W_m - W_c - W_b) \qquad \textbf{2.24}$$

where *c* is the specific heat of the tissue, W_{em} is the rate of electromagnetic power deposition in the tissue, W_m is the metabolic heating rate and W_c and W_b are the thermal dissipation by conduction and blood flow respectively.

The only well documented effects of exposure to RF fields are heating effects. The heating effect depends on the absorption of RF fields, but in general, the

greater the absorption rate, the more likely it is that significant heating occurs [34].

SAR is a suitable parameter for characterizing the absorption of RF fields in the body when discussing thermal effects but this parameter might, however, not be the appropriate one to use when discussing possible non-thermal effects.

SAR is a measure of the momentary, time independent absorption in the body. Non-thermal effects might not be time independent and it could therefore be necessary to incorporate the time factor in the concept of dose.

At that point is where the specific absorption (SA) plays an important role. The SA is time dependant and it is defined as the quotient of the incremental energy (dW) absorbed by an incremental mass contained in a volumen of a given density ($\rho \cdot dV$). The specific absorpton can be derived from the integral of the energy over the pulse duration as [35]:

$$SA = \frac{dW}{\rho \cdot dV} = \sum_{i=1}^{n} \frac{\sigma_e |E|^2 \partial t}{\rho \cdot dV} \; [Joules/kg] \qquad \textbf{2.25}$$

2.4.2 Radio frequency exposure limits

The development of protection guidelines is a complex process that starts form a comprehensive review of the scientific literature, including studies describing thermal and nonthermal effects, short and long-term exposures, biological and health end points, and epidemiological and human studies [31]. The next step is the identification of the critical effects, that is, the established adverse health effects that occur at the lowest level of exposure. The exposure levels that are harmful, or are considered likely to be harmful, to human health are determined.

Several decades of research in the area of bioelectromagnetics have led to a scientific consensus on the safety of EM fields. Many institutions and organizations throughout the world have recommended safety limits for EMF (Electric and Magnetic Field) exposure. These include the Institute of Electrical

and Electronic Engineers (IEEE) [36–39], the National Radiological Protection Board (NRPB) of the United Kingdom [40–42], the International Commission on Nonionizing Radiation Protection (ICNIRP) [43–45], the Swedish Radiation Protection Institute [46], Health Canada [47], and the Australian Radiation Protection and Nuclear Safety Agency (ARPANSA) [48].

The differences in RF safety standards are due to different philosophical approaches to public health standards development, different scientific approaches and interpretations of the scientific data, and different jurisdictions in various countries [49]

The IEEE defines different standards to regulate the exposure of human bodies to electromagnetic waves. Since 1960 the IEEE has standards to regulate RF safety issues. The first one was *UASI C95: Radiation hazards project and committee chartered.* In 1966 the *ANSI C95.1-1966* was defined, and with different modifications done in 1974 and 1982 it was valid until 1991, when *IEEE C95.1-1991* was defined. The latter was revised in 2005 and after that revision in April 2006 *IEEE C95.1-2005* was published. In 2010 IEEE dosimetry new rules started to appear with the new standard *IEEE 1528.1*. This standard has been revised 5 times and from these revisions *IEEE 1528.2, IEEE 1528.3, IEEE 1528.4* and *IEEE 1528-2013* have been established in chronological order from 2010 to 2013. Whilst the *IEEE 1528* is focused on the SAR evaluation procedures, the *IEEE C95.3* is more focused on RF evaluation procedures. Therefore both standards coexist in the dosimetry regulation field [50].

Maximum Permissible Exposure (MPE) limits defined in IEEE C95.1-2005 for controlled environments and uncontrolled environments are shown in Table 2.7 and 2.8.

Table 2.7: MPE Limits for controlled environments

Frequency (MHz)	Power Density (W/m^2)
0.1–1.0	9,000
1.0–30	$9{,}000/f^2$
30–300	10
300–3,000	f/30
3,000–300,000	100

Table 2.8: MPE Limits for uncontrolled environments

Frequency (MHz)	Power Density (W/m^2)
0.1–1.34	1,000
1.34–30	$1{,}800/f^2$
30–400	2.0
400–2,000	f/200
2,000–100,000	10
100,000–300,000	Increases from 10 to 100

Chapter 3

Communication with implants

In this chapter the basics of the communications with implantable devices are described. The chapter is divided into three sections. In the first one, the basic principles of the systems based on inductive coupling are explained (near field systems). In the second one, the behavior of the electromagnetic wave propagation in human bodies is explained to understand the main concerns that must be considered to design an implanted system (far field approach). Finally, some guidelines about the current regulation for implanted communications are addressed.

3.1 Near field systems

In this section the basic aspects of near field systems are explained in order to characterize the most used way of communication in implanted applications.

The inductive links in biomedical implants are loosely coupled due to the presence of air, skin, fat, muscle… and other tissues between the two coils, and therefore the power transfer efficiency is limited [51].

Besides, in biomedical applications the sizes of the coils are limited by the strict form factor requirements contrary to applications such as wireless chargers for mobile devices, in which the size constraints are liberal compared to the implanted cases.

Consequently, a small increase in efficiency is very valuable. The increase in efficiency is also valuable to decrease the overheating of the tissues due to electromagnetic radiation levels.

It is important to define and study the main principles of this kind of system to improve the current applications. In this section the main principles concerning near field systems are analyzed: inductive coupling, concept of resonance, and concept of maximum power transfer and maximum power transfer efficiency.

3.1.1 Inductive coupling

The basic principle of an inductively coupled power transfer system is shown in Figure 3.1. It consists of a transmitter coil L_p and a receiver coil L_s, both coils forming a system of magnetically coupled inductors. In the transmitter coil an alternating current generates a magnetic field which induces a current in the receiver coil.

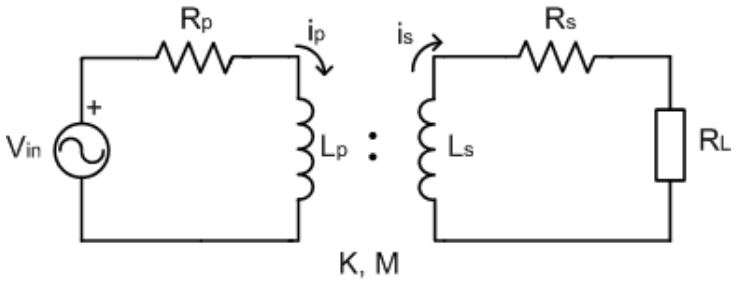

Figure 3.1: Inductive coupling scheme

where:

- V_{in}: input voltage
- R_p: internal resistance of the primary inductance
- R_s: internal resistance of the secondary inductance
- L_p: primary inductance
- L_s: secondary inductance
- R_L: load resistance

Whenever V_{in} is powered with an alternating current, changing magnetic field in L_p induces an opposing electro-motive-force (EMF) in L_s according to Faraday-Lenz law. The induced EMF (in Volts) can be quantified by equation 3.1:

$$\epsilon = -M\frac{di}{dt} \qquad \textbf{3.1}$$

where

- ϵ: Induced electromotive force in the secondary inductor
- *i*: Current in the inductor
- *M*: Mutual inductance

The mutual inductance between both coils is defined as:

$$M = k\sqrt{L_p L_s} \quad \textbf{3.2}$$

where *k* is the coupling coefficient, and is only dependent on geometry, distance and angle between inductors. If the receiver coil is at a certain distance from the transmitter coil, only a fraction of the magnetic flux, which is generated by the transmitter coil, penetrates the receiver coil and contributes to the power transmission. The more flux reaches the receiver, the better the coils are coupled. The grade of coupling is expressed by the coupling factor *k*. It satisfies the following relation:

$$0 \leq k \leq 1 \quad \textbf{3.3}$$

k=1 expresses perfect coupling, i.e. all flux generated penetrates the receiver coil. k=0 expresses a system, where transmitter and receiver coils are independent of each other and none of the magnetic lines created in one coil go through the other one.

The coupling factor is determined by the distance between the inductors and their relative size. It is further determined by the shape of the coils and the angle between them. If coils are axially aligned, a displacement causes a decrease in *k*. Figure 3.2 shows this effect for an exemplary arrangement of planar coils with 30mm diameter. It shows the measured and calculated coupling factor for parallel coils at different misalignment distances at the horizontal axis.

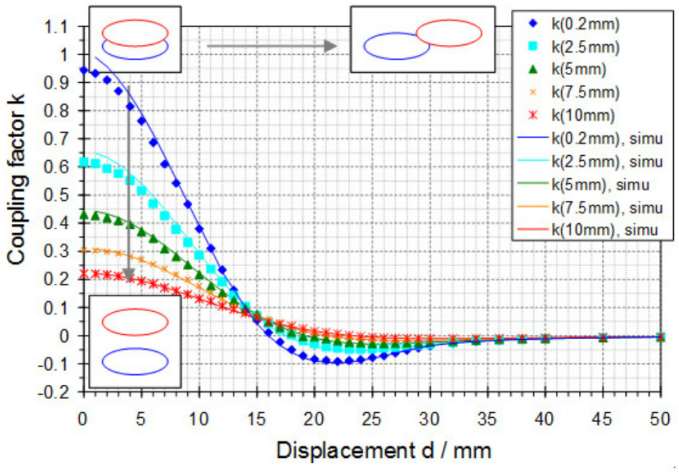

Figure 3.2: Measured (points) and calculated (lines) coupling factors for two planar coils with 30 mm diameter [52]

3.1.2 Concept of resonance

Power transfer can be done via inductive coupling. However, adding capacitances at primary and/or secondary sides of the circuit, can improve the power transfer.

Resonance is achieved when the source sees the load as purely resistive; it means that, the reactive part of the inductor is canceled by the reactive part of a capacitor. When this condition is achieved, energy stored in magnetic field of the inductor flows to the capacitor, and is stored as electrical energy in the electric field of the capacitor. In a lossless resonance, this achieves an infinite charge/discharge of the inductor and the capacitor. In real world problems, there is always some energy that is dissipated in the resistances between components, thus the effectiveness of the resonance is reduced. According to the type of the resonance (series or parallel), current or voltage can be maximized, achieving higher energy transfer in the specified frequency.

3.1.2.1 Series resonance

The circuit that is studied is shown in Figure 3.3.

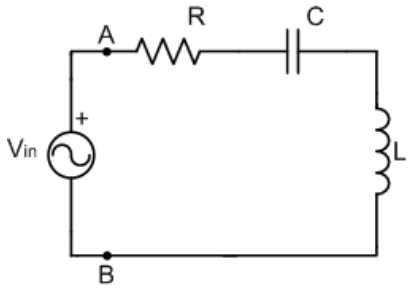

Figure 3.3: Series resonance circuit

The impedance between A and B points is defined as Z (equation 3.4).

$$Z = R + jL\omega + \frac{1}{jC\omega} = R + j(L\omega - \frac{1}{C\omega}) \quad \textbf{3.4}$$

The resonance condition is obtained when the imaginary part of Z is equaled to zero (equations 3.5 and 3.6):

$$Im\{Z\} = 0 \rightarrow C\omega - \frac{1}{L\omega} = 0 \quad \textbf{3.5}$$

$$\omega = \omega_0 = \frac{1}{\sqrt{LC}} \quad \textbf{3.6}$$

At resonance, minimum of voltage and maximum of current is achieved (Figure 3.4)

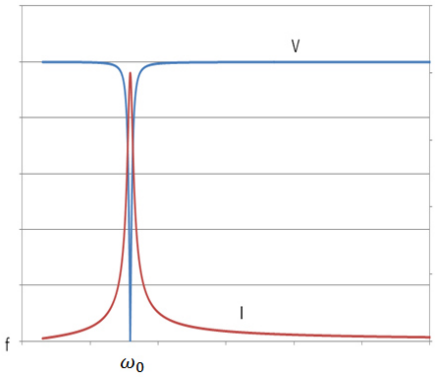

Figure 3.4: Current and voltage behaviour in series resonance circuit

3.1.2.2 Parallel resonance

The circuit that is studied is shown in Figure 3.5.

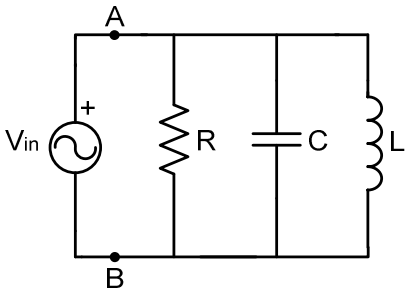

Figure 3.5: Parallel resonance circuit

The admittance between A and B points is defined as Y (equation 3.7).

$$Y = \frac{1}{R} + \frac{1}{jL\omega} + jC\omega = \frac{1}{R} + j(C\omega - \frac{1}{L\omega}) \quad \textbf{3.7}$$

The resonance condition is obtained when the imaginary part of Y is equaled to zero (equations 3.8 and 3.9).

$$Im\{Y\} = 0 \rightarrow C\omega - \frac{1}{L\omega} = 0 \quad \textbf{3.8}$$

$$\omega = \omega_0 = \frac{1}{\sqrt{LC}} \quad \textbf{3.9}$$

At resonance, maximum of voltage and minimum of current is achieved (Figure 3.6).

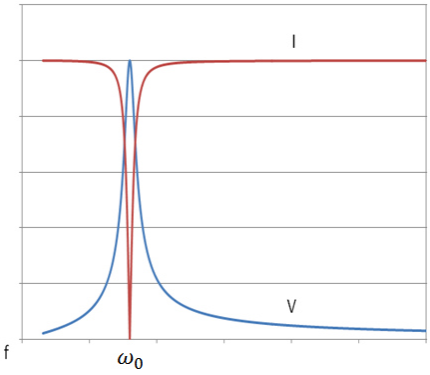

Figure 3.6: Current and voltage behaviour in parallel resonance circuit

3.1.2.3 Quality factor

An important parameter of a resonant circuit is the quality factor Q, which is defined as [53]:

$$Q = \omega_0 \frac{average\ enery\ stored}{energy\ loss/second} \quad \textbf{3.10}$$

a) Quality factor of a series resonant circuit

In the circuit of the Figure 3.3 the power dissipated by the resistor is:

$$P_{loss} = \frac{1}{2}|I|^2 R \quad \textbf{3.11}$$

The average magnetic energy stored in the inductor is:

$$W_m = \frac{1}{4}|I|^2 L \quad \textbf{3.12}$$

The average electric energy stored in the capacitor C is:

$$W_e = \frac{1}{4}|V_C|^2 C = \frac{1}{4}|I|^2 \frac{1}{\omega^2 C} \quad \textbf{3.13}$$

being V_C the voltage across the capacitor.

The resonance occurs when $W_e = W_m$, thus the quality factor can be written as:

$$Q = \omega_0 \frac{W_m + W_e}{P_{loss}} = \frac{2W_m}{P_{loss}} = \frac{L\omega_0}{R} \quad \textbf{3.14}$$

b) Quality factor of a parallel resonant circuit

In the circuit of the Figure 3.5 the power dissipated by the resistor is:

$$P_{loss} = \frac{1}{2}\frac{|V|^2}{R} \quad \textbf{3.15}$$

The average magnetic energy stored in the inductor is:

$$W_m = \frac{1}{4}|I_L|^2 L = \frac{1}{4}|V|^2 \frac{1}{\omega^2 L} \quad \textbf{3.16}$$

where I_L is the current across the capacitor. The average electric energy stored in the capacitor C is:

$$W_e = \frac{1}{4}|V|^2 C \quad \textbf{3.17}$$

The resonance occurs when $W_e = W_m$, thus the quality factor can be written as:

$$Q = \omega_0 \frac{W_m + W_e}{P_{loss}} = \frac{2W_m}{P_{loss}} = \frac{R}{L\omega_0} \quad \textbf{3.18}$$

c) Quality factor as a figure of merit

The ratio of the inductance *L* to the resistance *R* of a coil remains constant for different winding arrangements in the same volume and shape. It makes sense to define this value as a figure of merit to distinguish different coil structures. The quality factor Q_L is defined by this ratio.

The voltage, which is induced by the same current in an inductor scales with the frequency *f* and thus the apparent power in the device. The general definition of the quality factor is based on the ratio of the apparent power to the power losses in a device. From this definition, the quality factor of a coil results in:

$$Q_L = \frac{L\omega}{R_{int}} \qquad \textbf{3.19}$$

where R_{int} is the internal resistance of the coil. The quality factor Q_L can have a value between 0 and infinity. But technically it is difficult to obtain values far above 1000 for coils. For mass production values around 100 can be expected. These values have to be considered as the typical order of magnitude.

The quality factor is only dependent on the shape and size of the coil and on the used materials for a fixed operating frequency. For typical technologies (e.g. wire-wound coils, PCB coils) typical quality factors can be given.

As it is explained later, lower Q factors are achieved with inkjet printing technology, typically around 10. However, for some applications this quality factor is good enough and inkjet printing is an interesting manufacturing process since a great degree of freedom for flexible antenna designs is reached [54].

The Q_L defined is a characteristic of the resonant circuit itself, in the absence of any loading effects caused by external circuitry, usually a load impedance (R_L). This Q_L factor is also known as unloaded Q.

In practice, however, this resonant circuit is coupled to other circuitry, which has always the effect of lowering the overall, or loaded Q, which is denoted as *Q*, of the circuit [53], and that has been calculated previously.

3.1.2.4 Bifurcation phenomena

One of the most important design checks in resonant circuits is to ensure that the system is stable under all load conditions. Bifurcation phenomena appear when in a resonant circuit the resonance condition is achieved not only for the desired frequency. When the imaginary part of the impedance seen by the source is zero for other frequencies apart from $\omega = \omega_0$, it is said that the system is working with bifurcation.

For most applications, as they are focused on maximum power transfer or maximum efficiency transfer, bifurcation free systems are preferred [55]. In most cases, bifurcation-free operation is assumed without making the corresponding checking.

A rule of thumb is that if the primary quality factor (Q_p) is much higher than the secondary quality factor (Q_s), the system generally exhibits stable characteristics, whereas if $Q_s > Q_p$, a thorough system stability analysis is needed to be undertaken.

To the date, some analysis has been undertaken to determine the bifurcation criterion for some specific topologies and applied to particular applications [56–58]. A general methodology to study the bifurcation phenomena for all topologies is addressed in [55], [59] and the obtained conditions are summarized in equations 3.20, 3.21 and 3.22 for different topologies:

- SS topology:

$$Q_p > \frac{4{Q_s}^3}{4{Q_s}^2 - 1} \qquad \textbf{3.20}$$

- SP/PP topology:

$$Q_p > Q_s + \frac{1}{Q_s} \qquad \textbf{3.21}$$

- PS topology:

$$Q_p > Q_s \quad \textbf{3.22}$$

In this thesis, the four topologies are represented as SS/SP/PS/PP, where the first alphabet denotes the type of compensation in the primary side and the second alphabet denotes the type of resonance used in the secondary side.

3.1.3 Maximum power transfer vs. maximum power transfer efficiency

In order to explain these two concepts the circuit of Figure 3.7 is analyzed.

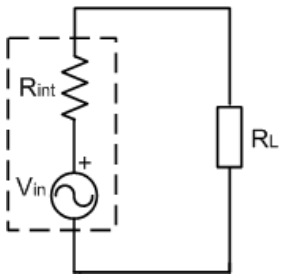

Figure 3.7: Purely resistive circuit for power and efficiency analysis

where:

- V_{in}: Voltage source
- R_{int}: Internal resistance of the source
- R_L: Resistive load

The power consumed in each resistance is analyzed to understand the behavior.

$$P_{R_{int}} = R_{int}\left(\frac{V_{in}}{R_{int} + R_L}\right)^2 \quad \textbf{3.23}$$

$$P_{R_L} = R_L\left(\frac{V_{in}}{R_{int} + R_L}\right)^2 \quad \textbf{3.24}$$

Therefore the total power (*P*) delivered from the voltage source is deduced by:

$$P = P_{R_{int}} + P_{R_L} \quad \textbf{3.25}$$

The efficiency of the power transfer is derived as the ratio of total energy that is delivered to the load to the total energy that is derived from the source in one complete cycle (equation 3.26).

$$efficiency = \frac{P_{R_L}}{P} \quad \textbf{3.26}$$

The maximum power transfer condition, however; is obtained when P_{R_L} is maximized (equation 3.27):

$$\frac{\partial P_{R_L}}{\partial R_L} = \frac{{V_{in}}^2}{(R_{in} + R_L)^2} - \frac{2R_L{V_{in}}^2}{(R_{in} + R_L)^2} = 0 \quad \textbf{3.27}$$

This equation is satisfied when $R_L = R_{in}$, this is, maximum power is transferred from the source to the load when the resistance of the load is equal to the internal resistance of the source.

With this condition the obtained efficiency is not maximum, it is just 50%. If the resistance of the load is made larger than the resistance of the source, then the efficiency is higher, since a higher percentage of the source power is transferred to the load, but the magnitude of the load power is lower since the total circuit resistance goes up.

If the load resistance is smaller than the source resistance, then most of the power ends up being dissipated in the source, and although the total power dissipated is higher, due to a lower total resistance, it turns out that the amount dissipated in the load is reduced.

In Figure 3.8 and Table 3.1, the behavior for a system with V_{in}=100 V and R_{in}= 50Ω is summarized.

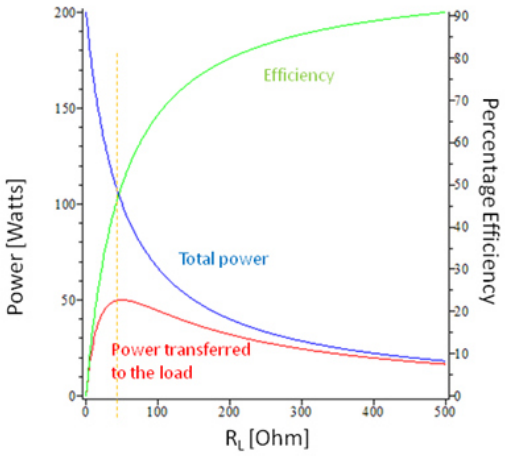

Figure 3.8: Change in total power, power transferred to the load and efficiency of resistive load for a system with $V_{in} = 100\ V$ and $R_{in} = 50\ \Omega$

Table 3.1: Obtained total power and efficiency for different R_L values

$R_L(\Omega)$	$P_{R_{in}}(W)$	$P_{R_L}(W)$	$P(W)$	*Efficiency (%)*
0	*200*	*0*	*200*	*0*
50	*50*	*50*	*100*	*50*
100	*22.22*	*44.4*	*66.6*	*66.6*

The efficiency and power transfer are also affected by the distance, size and relative sizes between the coils. In Figure 3.9 this effect in two circular coils is shown.

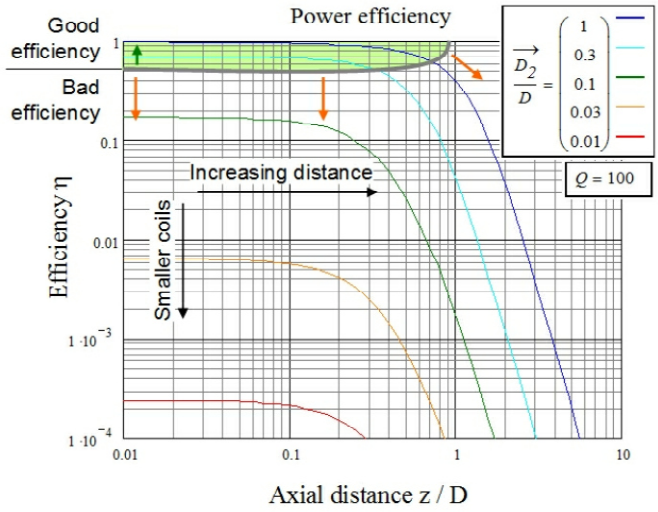

Figure 3.9: Typical arrangement of an inductively coupled power transfer system [52]

The efficiency of the power transfer and the magnitude of the power transferred to the load can be improved using resonant tuning and matching techniques at the primary and secondary sides respectively [55][60][61].

The theorem can be extended to AC circuits that include reactance, and states that maximum power transfer occurs when the load impedance is equal to the complex conjugate of the source impedance.

Several studies about the efficiency and power transfer capability of resonant circuits are found in the literature [3], [62–64]. There are different ways to study the efficiency in these kinds of systems.

From the plethora of existing literature on design and optimization of wireless inductive power links, almost in most of them series-parallel topology is used to transfer power efficiently and most of the design and optimization efforts have been directed towards this method [65].

In this thesis an efficiency analysis for all topologies is addressed and a description of the main advantages of each topology is explained for implanted applications.

3.2 Electromagnetic propagation in human body

In this section the electromagnetic propagation in human body is analyzed. Human body is composed of different tissues with different electrical properties. The human body tissues can be considered as lossy materials and consequently in this section, the main characteristics of the propagation of electromagnetic waves in human tissues are addressed.

In a rectangular coordinate system, the general solution for $E(x,y,z)$ can written as:

$$E(x,y,z) = \hat{a}_x E_x(x,y,z) + \hat{a}_y E_y(x,y,z) + \hat{a}_z E_z(x,y,z) \quad \textbf{3.28}$$

If it is assumed that the wave is propagating in z direction and that the E-field has only a component in x direction, the equation can be rewritten as:

$$E(z) = \hat{a}_x E_x(z) = \hat{a}_x (E_0^+ e^{-\gamma z} + E_0^- e^{+\gamma z}) \quad \textbf{3.29}$$

where $\hat{\gamma}$ is the complex propagation constant that is defined as follows:

$$\hat{\gamma} = \alpha + j\beta \quad \textbf{3.30}$$

where α is defined as the attenuation constant and β is the phase constant:

$$\alpha = \omega\sqrt{\mu\varepsilon'}\left\{\frac{1}{2}\left[\sqrt{1+\left(\frac{\sigma_e}{\omega\varepsilon'}\right)^2}-1\right]\right\}^{1/2} Np/m \quad \textbf{3.31}$$

$$\beta = \omega\sqrt{\mu\varepsilon'}\left\{\frac{1}{2}\left[\sqrt{1+\left(\frac{\sigma_e}{\omega\varepsilon'}\right)^2}+1\right]\right\}^{1/2} rad/m \quad \textbf{3.32}$$

The attenuation constant accounts for the exponential decay of the wave amplitude when it goes through a lossy medium, as in the human body. In lossy

media, as the transmitted field propagates in the tissue, RF energy is extracted from the field and spread along the medium, resulting in a progressive reduction of power density of the field (Figure 3.10).

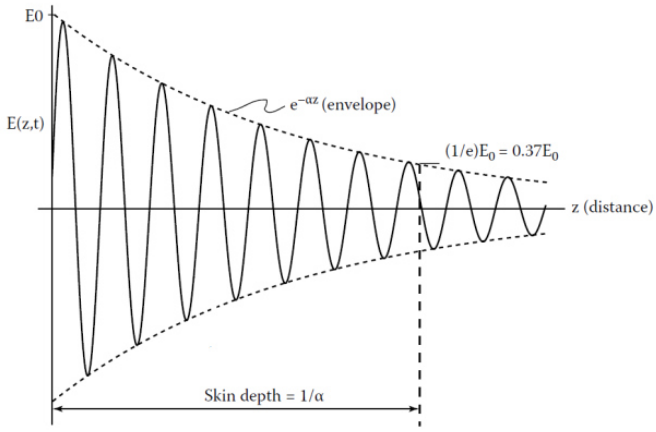

Figure 3.10: Electric field behavior in a lossy medium

Skin depth is a parameter that defines the distance inside the material where the propagating electric field is attenuated by a factor of e^{-1}. Therefore, for a wave propagating in a lossy medium, the skin depth can be expressed as [53]:

$$\delta_s = \frac{1}{\alpha} \qquad \textbf{3.33}$$

It is important to note that the full expression of the attenuation constant must be used (equation 3.31). No approximation can be made, because in the case of biological tissues the real and imaginary parts of the permittivity are of the same order of magnitude [66].

From equations 3.31 and 3.33, it can be also concluded that the fields penetrate less in the tissues when either the frequency of the signal and/or the conductivity of tissue are higher.

In Figure 3.11, the frequency behavior of the skin depth in skin, fat, sat and muscle tissues is shown.

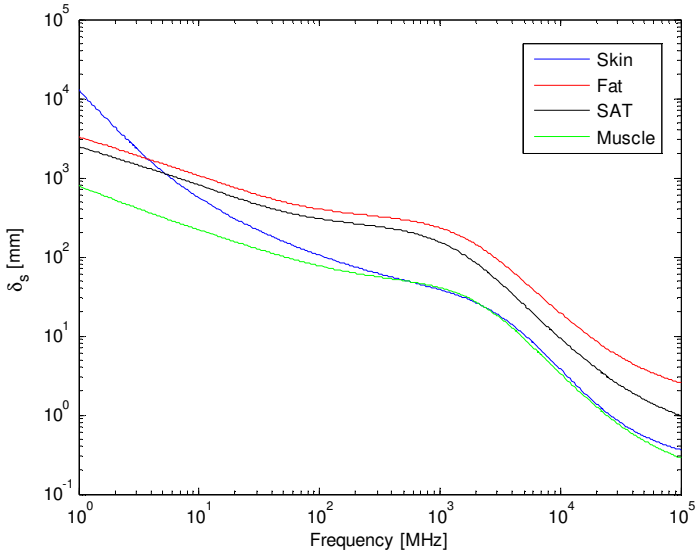

Figure 3.11: Skin depth behaviour with frequency for different human tissues using 4 Cole-Cole model

On the other hand, the phase constant also affects how the RF wave propagates through the medium by shortening the wavelength with respect to the free space value (λ_0).The phase constant can be also written as:

$$\beta = Im\{\hat{\gamma}\} = \frac{2\pi}{\lambda} \quad \textbf{3.34}$$

$$\lambda = \frac{\lambda_0}{Re\left\{\sqrt{\varepsilon_r(1 - j \cdot \tan\delta)}\right\}} \quad \textbf{3.35}$$

where λ is the wavelength in the tissue and λ_0 is the wavelength in free space.

As it has been explained in section 2.1.3, human tissue distribution is very complex. There are a different number of layers with different electrical properties. Consequently, the medium (the specific tissue) has to be properly modeled to be able to study what happens at boundaries separating the different biological materials.

The intrinsic impedance of a lossy medium can be defined as [67]:

$$\eta = \sqrt{\frac{j\omega\mu}{\sigma_e + j\omega\varepsilon'}} \quad \textbf{3.36}$$

At the boundary between two different tissues, RF energy is reflected or transmitted. For a plane wave impinging normally from a medium of intrinsic impedance η_1 on a flat medium of intrinsic impedance η_2, the reflection coefficient Γ and transmission coefficient T are given by:

$$\Gamma = \frac{\eta_2 - \eta_1}{\eta_2 + \eta_1} \quad \textbf{3.37}$$

$$T = \frac{2\eta_2}{\eta_2 + \eta_1} \quad \textbf{3.38}$$

where Γ and T are related as:

$$T = 1 + \Gamma \quad \textbf{3.39}$$

The fraction of incident power reflected by the discontinuity is Γ^2 and the transmitted fraction is $T^2 = 1 - \Gamma^2$.

3.3 Standards and protocols for communication with implantable devices

Regulation is an important aspect currently in progress, particularly when dealing with patients and emerging technologies. The European Telecommunications Standards Institute (ETSI) [68] has a Technical Committee on Electromagnetic Compatibility and Radio Matters which deals with different types of Short Range Devices and their applications. Inside the Committee, there is a wireless medical devices group (ERM/TG30). It develops a number of standards for wireless medical devices in different frequency ranges.

In this section the two most important standards for implantable devices are explained. At the same time, the Industrial Scientific and Medical (ISM) bands are described due to the potential of these frequency bands for implanted applications.

3.3.1 9-315 kHz band

The most common electromagnetic link to medical implants is based on inductive coupling and fulfills the standard ETSI EN 302 195-1 [69] defined by ETSI.

In these kind of communications, the inductive link uses a carrier frequency between 9 and 315 kHz, and transmits data at a speed of up to 512 Kbps [70]. The range of communication is limited to the “touch” range. The placement is often guided by indicators on the external coil, since the link is sensitive to the position of the external coil.

Another drawback of these kinds of systems is that the low frequency limits the available bandwidth and results in a low data rate.

3.3.2 402-405 MHz band (MICS)

ETSI has standardized the Medical Implant Communication System (MICS) in ETSI EN 301 839-1 [71]. This document lists two main fields of application for the standard. The first field is for telecommunication between a base station and an implanted device. The second field is for telecommunication between medical implants within the same body.

The frequency band allocated is from 402 MHz to 405 MHz. The maximum emission bandwidth to be occupied is 300 kHz. This maximum bandwidth is for the complete session. The maximum power limit is set to 25 μW equivalent radiated power (ERP). It is precisely this low power budget allowed by regulation what makes implant communication a challenge. The final

communication range is constraint to the considered media (the body) and its intrinsic high losses.

The main advantage is the additional flexibility compared to previously used inductive technologies, which required the external transceiver to touch the skin of the patient. The MICS standard has the potential for long range communications (meters) between an external reader and the implanted node.

There is also another standard that keeps the spectrum previously allocated for MICS but adds additional adjacent spectrum (405-406 MHz), it is known as the MedRadio standard. It is defined by the U.S. Federal Communications Commission (FCC) and European Telecommunications Standards Institute (ETSI) for wireless communication with medical implants.

It should be pointed out that the same spectrum allocation of 401-406 MHz is also in use for meteorology services (Met Aids [72]), like weather, water and climate monitoring and prediction. Consequently, MICS systems are specified to be used indoors.

3.3.3 ISM bands

The industrial, scientific and medical (ISM) radio bands are radio bands reserved internationally for the use of radio frequency (RF) energy for industrial, scientific and medical purposes.

The ISM bands in the frequency spectrum are not standardized worldwide, like shown in Figure 3.12.

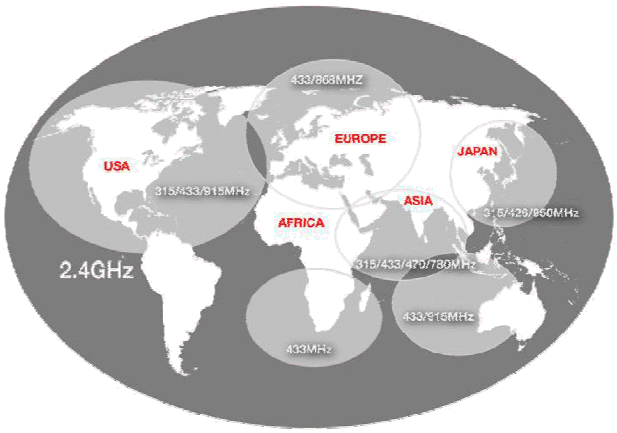

Figure 3.12: ISM Spectrum in different world regions

In this research project, some of the available ISM bands are used to check the potential and feasibility of these frequencies for the communication with implantable devices:

- f= 13.56 MHz
- f= 868 MHz
- f= 2.45 GHz
- f= 5.8 GHz

Chapter 4

Inkjet printing technology

Currently, it has been estimated that there are about 1500 worldwide research units working on various aspects of flexible electronics. Market analysis estimates the revenue of flexible electronics can reach 30 billion USD in 2017 and over 300 billion USD in 2028 [73].

Their light weight, low-cost manufacturing, ease of fabrication, and the availability of inexpensive flexible substrates (i.e.: papers, textiles, and plastics) make flexible electronics an appealing candidate for the next generation of consumer electronics [74].

The size and conformability of the antenna is one of the main constraints in the design of implantable devices. Flexible antenna designs open an innumerable number of new applications.

The new fabrication processes and new materials properties will also allow new applications that nowadays are not suitable. Conventional flexible circuits

consist of Cu tracks on polyimide substrates, they are not suitable for chronic implantation use. In the future, new technologies like inkjet printing will intend to port the current design to a different process which utilizes biocompatible materials such as Au or Pt tracks on parylene or polyurethane substrates. With this kind of materials the implantable devices will be able to be located in very sensitive part of the human body such as the eyes, like is explained in [75].

In this section a deep analysis of inkjet printing technology for the fabrication of flexible antennas is addressed. Previously, some comments about the most cumbersome traditional method for fabricating antennas (subtractive etching) is explained.

4.1 Subtractive etching

The earliest, and most cumbersome, method of antenna fabrication is subtractive etching of a metal-plated substrate (FR4 for example) also know as chemical etching. This technique emerged in the 1960s as a branch-out of the Printed Circuit Board (PCB) industry. Chemical etching has gained a wide popularity since it can produce highly complex patterns with high resolution accurately [76].

Chemical etching often accompanied by photolithography, that it is the process of fabricating metallic patterns using a photoresist and etchants to mill out a selected area corrosively.

Photoresist materials are organic polymers whose chemical characteristics change when exposed to ultraviolet light. When the exposed area becomes more soluble in the developer, the photoresist is positive, while if it becomes less soluble, the compound is considered as negative.

A major drawback of negative resists is that the exposed regions swell as the counterpart is dissolved by the developer, which compromises the resolution of the process. Swelling occurs due to the penetration of the developer solution

into the photoresist material which in turn leads to a distortion in the patterned region [76]. Hence, current practice in the photolithography based antenna and RF circuits Industry relies mainly on positive resists since they present higher resolution than negative resists.

The antenna design is printed onto a clear film as a positive image (black on clear). The film positive is placed over the copper plating, which has been coated with a photo-resist and exposed to light. The copper-clad board is then processed in photographic development solution, which removes the resist from the exposed areas. The developed board is immersed in an etching bath until the exposed areas are etched away. The fabrication process is summarized in Figure 4.1:

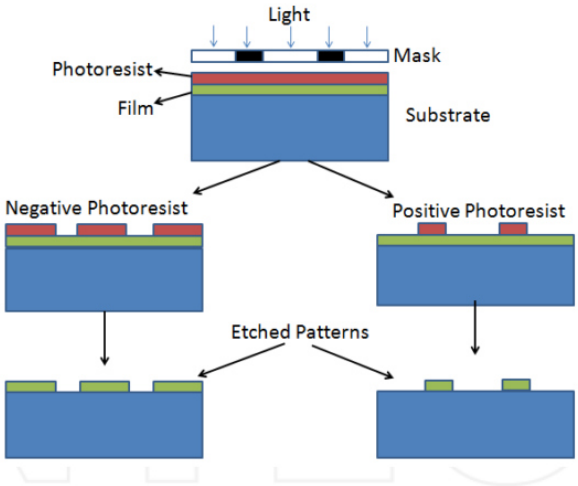

Figure 4.1: Process flow of the chemical etching (photolithography) process [77]

Subtractive etching has matured to the point where it has become a low-tech process requiring inexpensive off-the-shelf materials and equipment. High complexity pattern with high resolution can be obtained, however, for larger production runs, etching creates significant amounts of metal salt and chemical waste products, incurring increased costs due to regulatory fees and reclamation charges. Besides, it requires clean room environments.

As conclusion, it can be stated that this fabrication method is very suitable for mass fabrication of antennas, however, as the substrate is rigid and due to the characteristics of the materials that are employed, this fabrication technique presents several drawbacks for the fabrication of implantable antennas.

New techniques that allow the use of different materials and at the same time offer the possibility of fabricating the antennas into flexible substrates (like inkjet printing technology) should be considered.

4.2 Inkjet printing technology

In the last two decades inkjet printing has grown to a major topic in scientific research, especially drop-on-demand (DOD) inkjet printing systems. DOD inkjet printing has progressed from printing text and graphics, where it started originally, to a tool for (rapid) manufacturing technology.

Inkjet printers were introduced first in 1976. Inkjet printing is a direct-write technology by which the designed pattern is transferred directly to the substrate, and there is no requirement of masks contrary to the traditional etching technique which is widely used [78].

Inkjet printing is a novel method to promote electrical circuit by printing metal nano-particles onto flexible substrates. New inkjet material printers operate by depositing ink droplets of a size down to few pL, and hence, these high resolution printers can produce compact designs with tiny details accurately [79]. The fabrication process can be visualized in Figure 4.2.

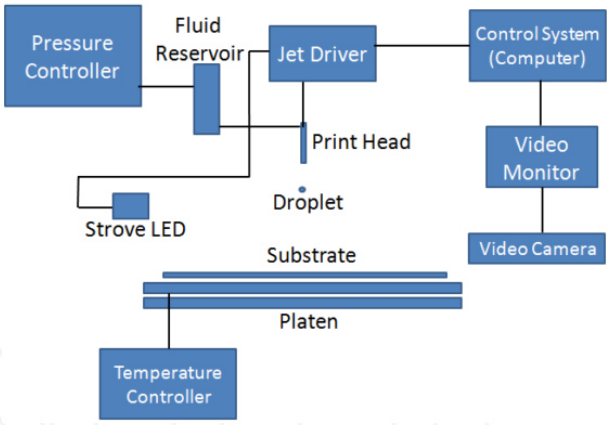

Figure 4.2: Illustration of the ink jet (drop on demand) printing process

The fabrication of thin conductive tracks by methods of inkjet printing has been recently investigated extensively [80][81].

Unlike photolithography, which is a subtractive method since it involves removing unwanted pattern from the substrate's metallic/conductive side, inkjet printing lowers the production costs of electronic devices, because material can be positioned on-demand, which reduces the amount of necessary material resulting in an economical, clean, and fast solution.

4.2.1 Different technologies

There are two main technologies currently used in inkjet devices: continuous inkjet and drop-on-demand inkjet.

Continuous inkjet printing uses pressure pumps to release ink onto substrates and is primarily used for printing on packages and commercial products, thus high volume printing.

Drop on demand print heads apply pressurized pulses to ink with either a piezo or thermo element in which drives a drop from a nozzle when needed. *Thermal inkjets* excite electrically driven cavities that release “aqueous” inks using an applied current, and are used in most commercial inkjet printers. Most printed

electronics manufacturers however, utilize the piezo pulse type. The printing mechanism of the printer that will be used in this research uses also *piezoelectric* devices.

The operation of the jetting system consists on applying a voltage at the orifice of each nozzle causing the nozzle to change in shape and size. The desired pattern is created, generating a pulse in the ink material used and creating the printing process by continuously applying voltage across theses nozzles.

This proves to be a slightly complicated process due the common inkjet printing problems, such as the drying of the ink on the print head's nozzles.

4.2.2 Inks

Inkjet printing technology utilizes conductive inks based on different nano-structural materials. Metallic nanoparticle inks typically consist of silver or gold nanoparticles with diameters ranging from just 2nm to above 50nm, encapsulated with a protective shell and dispersed in a liquid solvent [82][83]. Once printed, a continuous conducting structure can be obtained by sintering, that is, by increasing the temperature of the structure so that the separate nanoparticles melt together.

A conductive ink's characteristic properties of flow, adhesion and cohesion are crucial to resolution of fine detail. In addition to fine detail, however, it is paramount that the printed image has the lowest possible resistance to electromagnetic energy. Metal particle density determines the conductivity of the printed antenna. The higher the particle density of the metallization, the better the conductivity is. But as the particle density increases so does the ink's viscosity, resulting in a thicker ink that is difficult to apply. Jetting an ink with lower viscosity could have the opposite problems: dimensional instability, poor adherence and a higher electrical resistance.

The typical dimensions of inkjet printed features depend on the nozzle diameter, and are usually not below 100 µm [84]. The most obvious way to minimize the

feature size, that is, line width, is by reducing the nozzle diameter. However, this introduces restrictions with respect to the surface tension and viscosity of the ink that can be used and therefore, it limits the choice of inks that can be printed [85][86].

There are several ink manufactures. Taking into account the literature and the study of the state of the art about inkjet printing technology that has been carried out, three manufactures are the most used ones: Cabot [87], Advanced Nano Products (ANP) [88] and SunJet (use Cabot formulation) [89].

4.2.3 Substrates

The substrate is one of the most important elements in inkjet printing technology fabrication process. The substrate determines the final mechanical characteristics of the printed prototype. Along the different polymers, plastics and polyamides that are used to fabricate inkjet printed prototypes one of the most employed one is Kapton.

Kapton is a polyimide film developed by DuPont which can remain stable in a wide range of temperatures, from -273 to +400 °C (0 – 673 K). DuPont makes several types of Kapton films. Types HN, FN and VN are used most commonly.

All the information about the mechanical and physical properties can be found in the datasheet [90].

Other Polymer based and synthesized flexible substrates have been also used in several designs [91–94].

The research on new flexible substrate material for printed circuits is becoming more important nowadays due to the ever growing demand for flexible wireless electronics.

For an optimal RF performance, substrate characterization becomes essential especially for implanted applications where the properties of the materials.

RF characterization of high-frequency materials becomes a critical step for the qualification of the materials as host substrate for a wide range of frequency domain applications. The knowledge of the dielectric properties such as dielectric constant and loss tangent become necessary for the design of any high frequency structure.

There are several techniques used to characterize the electromagnetic properties of thin and flexible substrates. There are different methods for high-frequency dielectric characterization such as ring resonators [95][96], parallel plate resonators [97] and cavity resonators [98][99].

4.2.4 Sintering process

A sintering process is necessary to remove excess solvent and material impurities from the depositions. It also helps increasing the bond of deposition with the paper substrate.

The manufacturer indicates a range of temperature and time to sintering the silver ink and this depends on the amount of solid material in that ink [88]. Generally, higher sintering temperatures yield higher conductivity.

The sintering process is represented in Figure 4.3.

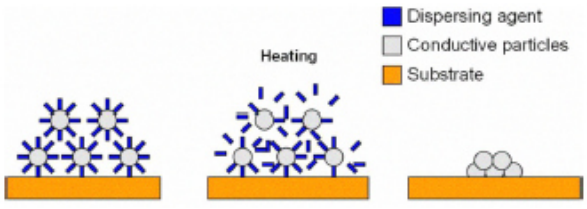

Figure 4.3: Sintering process

The sintering process is crucial in the final performance of the printed circuit. When low temperatures are used, a large gap exists between the particles, resulting in a poor conductivity. When the temperature is increased, the particles begin to expand and gaps start to diminish. Consequently, the

conductivity increases. Nevertheless, if the curing temperature is too high, the obtained results are worse.

The main bottleneck in inkjet printed features on flexible substrates is the low softening point T_g of the substrates, which limits the processing temperature. Typically, the suspensions of nanoparticles with a diameter below 50nm have a significantly reduced sintering temperature, typically between 160 and 300ºC. which is well below the melting temperature of the bulk material. Despite these low sintering temperatures conventional heating methods are still not compatible with common polymer foils such as Polyethylene Terephthalate (PET), due to its low glass-transition temperature. Ink's manufacturers are working hard to try to get inks that require lower sintering temperatures.

Sintering below 100 ºC is not complete and therefore considered as partial, since the final resistance is very different from other values of resistance for longer times. At temperatures of 150 ºC and 200 ºC the fall of resistance is abruptly reaching a constant value in about 30 minutes of testing and remained so until the end of the stipulated time. For temperatures above 230 ºC it is not possible to interpret the results since the solder pastes (which will be explained later) reaches its melting point in value thereby causing a difficulty in electrical conductivity and masking the result of the resistance of the trace.

It can be concluded that the sintering process is important because it determines at a certain extent the final performance of the printed prototype. Both, the temperature and time values are not easy to select since the substrate characteristics limit the range of possible values.

Chapter 5

Objectives

The main objective of this research work is to characterize and optimize the wireless links for implanted applications and check the feasibility of using inkjet printing technology as fabrication process for the design of implanted antennas.

For the realization of this global objective, this research work has been split into the following partial objectives:

5.1 Near field approach partial objectives

- **Characterization and optimization of implanted communications based on inductively coupled systems**. A study on stability, required compensation on primary circuit and efficiency is developed for the different resonant topologies, describing the main advantages and disadvantages of each of them.

- **Feasibility study of inkjet printing technology for the fabrication of implanted coil antennas.** A study on the effects of using this technology for implanted applications is addressed by explaining the main differences respect to traditional processes. The effect of using an inkjet printed coil antenna in the secondary side of a resonant topology is also addressed in terms of stability, needed compensation on primary circuit and efficiency.

5.2 Far field approach partial objectives

- **Characterization and limitation of cost effective sugar based tissue simulating liquids for the fabrication of homogeneous phantoms.** The description of the fabrication process and measurements techniques for the correct dielectric characterization of this kind of phantoms is developed. The frequency band where these phantoms can be used is also studied.
- **Characterization of a reliable strategy for far field implant communication based on a combination of analytical, computational and experimental approaches by:**

    - **Characterization of plane wave attenuation in homogeneous phantoms.** The set-up and procedure to measure the attenuation of a plane wave in a homogeneous phantom in an anechoic chamber is explained.

    - **Analytical and simulation study of heterogeneous layered planar phantoms for subcutaneous implanted applications.** The frequency behavior and the effect of human tissue

distribution on E-field is addressed using different phantom models.

- **Voxel phantom model simulation.** Different voxel phantom models are used to characterize the E-field behavior in Human torso. Virtual Family from IT'IS foundation and CST Voxel Family models are used.

5.3 Inkjet printing technology optimization for implanted applications

- **Description of the fabrication process for printing conductive traces into flexible substrates.** Inkjet printing fabrication process using conductive inks involves several aspects for getting reliable and repeatable results. A detailed methodology is described to achieve this goal.
- **Resolution study of inkjet printing technology using DMP2800 printer.** A study of minimum printable trace width and estimation of the obtainable trace's thicknesses is addressed.
- **Methodology definition for ink's characterization.** A methodology for the characterization of the electrical ink's conductivity is addressed.

Chapter 6

Methodology

In this chapter the methodology that has been followed to obtain the results that are analyzed and described in next chapters is explained. The chapter is divided into three different parts: near field, far field and inkjet printing.

In the first two sections, the analytical approach, simulation and measurement procedures are explained for near field and far field approaches respectively. In the third section, the used equipment and material and the fabrication process description for implementing flexible antennas using inkjet printing technology is addressed.

6.1 Near field approach

In this section the methodology that is followed for the study of different resonant topologies is explained. With this methodology some basic guidelines are provided, giving boundary frequencies that separate various topologies, thereby allowing the selection of the best topology that suits the necessary

requirements of the application. The four basic topologies are shown in Figure 6.1:

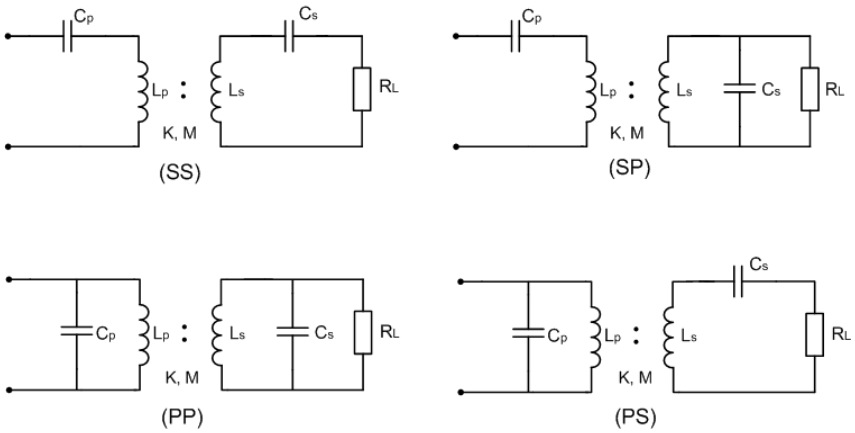

Figure 6.1: Four basic topologies

This section is divided into four different subsections. In the first one, an analytical approach is made in order to extract a circuit model of the behavior of these circuits. In the second one, this analytical model is checked using a circuit simulator (using lumped elements). Once the analytical model and the circuit model are compared, a 3D simulator is used to simulate a real antenna instead of a circuit model. In the third section, the measurement set-up and procedures for measuring the input impedance and the coupling between two coils are addressed. Finally, in the fourth one the way the efficiency analysis is done is explained.

6.1.1 Analytical approach

In this section the analytical study of the inductance calculation and circuits based on inductive coupling is addressed.

An analytical study is necessary to understand the interaction between the different architectures of primary and secondary systems and to be able to design the optimum system for a specific application.

6.1.1.1 Inductance calculation

A typical 2D multiloop antenna as a coil with a narrow separation between tracks is used mainly for two reasons:

- Achievable analytical expressions.
- Perfect candidate to test inkjet printing feasibility for the fabrication of these kinds of antennas.

Based on the Greenhouse method [100] , the inductance of a rectangular coil can be obtained by adding the self inductance of each segment, the positive and the negative mutual inductance between all pairs of segments.

In Figure 6.2 a general rectangular planar spiral inductor is shown.

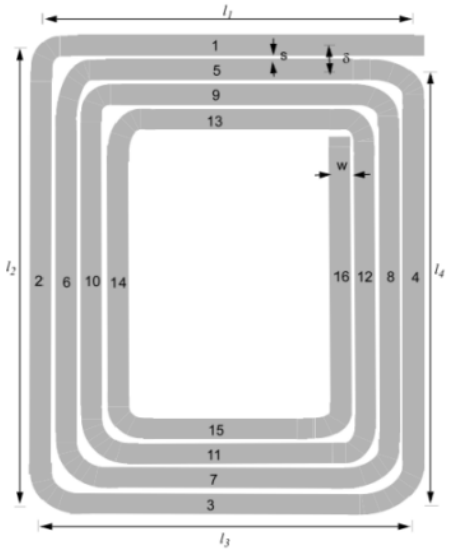

Figure 6.2: Rectangular planar spiral inductor

The total inductance of a N-turn planar spiral inductor coil can be calculated as [100]:

$$L_T = L_0 + M_+ - M_- \text{ [μH]} \quad \textbf{6.1}$$

where L_T is the total inductance, L_0 is the sum of self inductances of all straight segments, M_+ is the sum of positive mutual inductances and M_- is the sum of negative ones.

The self inductances of a rectangular cross-section conductor can be obtained using the equation 6.2 [100]:

$$L = 0{,}002l\left\{ln\left(\frac{2l}{w+t}\right) + 0.50049 + \frac{w+t}{3l}\right\} [\mu H] \quad \textbf{6.2}$$

where *w*, *t* and *l* are the segment's width, thickness and length in cm respectively.

The mutual inductance is the inductance that results from the magnetic fields produced by adjacent conductors. The mutual inductance is positive when the directions of the current along the conductors are in the same direction, and negative when the directions of currents are in opposite directions. The mutual inductance between two parallel conductors of equal length is a function of the length of the conductors and of the geometric mean distance *d* between them. It is calculated by equation 6.3 [101]:

$$M = 2lF\ [nH] \quad \textbf{6.3}$$

where F can be calculated as:

$$F = ln\left\{\left(\frac{l}{d}\right) + \left[1 + \left(\frac{l}{d}\right)^2\right]^{1/2}\right\} - \left[1 + \left(\frac{d}{l}\right)^2\right]^{1/2} + \left(\frac{d}{l}\right) \quad \textbf{6.4}$$

The geometric mean distance *d* is approximately equal to the distance between the track centres of the conductors involved. When the two segments are not equal in length, equations 6.5, 6.6 and 6.7 should be applied according to Figure 6.3.

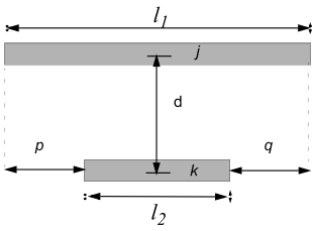

Figure 6.3: Two conductor segments for mutual inductance calculation

$$M_{k,p} = \frac{1}{2}\left\{\left(M_{k+p} + M_{k+q}\right) - \left(M_p + M_q\right)\right\} \quad \textbf{6.5}$$

where

$$M_{k+p} = 2l_{k+p}F_{k+p} \quad \textbf{6.6}$$

$$F_{k+p} = ln\left\{\left(\frac{l_{k+p}}{d_{j,k}}\right) + \left[1 + \left(\frac{l_{k+p}}{d_{j,k}}\right)^2\right]^{1/2}\right\} - \left[1 + \left(\frac{d_{j,k}}{l_{k+p}}\right)^2\right]^{1/2} + \left(\frac{d_{j,k}}{l_{k+p}}\right) \quad \textbf{6.7}$$

The value of any rectangular planar spiral inductor can be calculated accurately following the described method.

6.1.1.2 Phasor model for the coupling system

There are several approaches to solve systems based on inductive and resonant coupling. In this project, phasor model is used (Figure 6.4). In all the procedure, sinusoidal voltages and steady-state conditions are assumed.

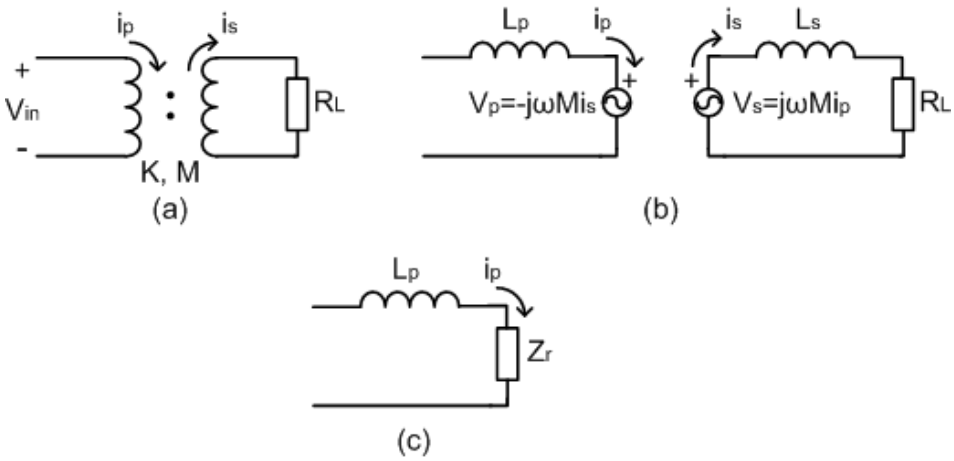

Figure 6.4: Phasor model: (a) Coupling circuit. (b) Equivalent coupling circuit. (c) Primary circuit with reflected impedance

In this research work, p and s sub indexes are employed to denote primary and secondary parameters respectively.

The phasor model is based on calculating equivalent impedance that affects the primary in the same way as the secondary circuit. This equivalent impedance is defined as reflected impedance (Z_r) (Figure 6.4c), and it is different depending on the secondary compensation.

Applying Kirchhoff's law on both sides of the circuit of Figure 6.4b, the equations 6.8 and 6.9 can be obtained:

$$V_{in} = jL_p\omega i_p - jM\omega i_s \quad \textbf{6.8}$$

$$jM\omega i_p = jL_s\omega i_s + R_L i_s \quad \textbf{6.9}$$

Substituting equation 6.9 in 6.8, the following equations are obtained:

$$i_s = \frac{jM\omega i_p}{jL_s\omega + R_L} \quad \textbf{6.10}$$

$$V_{in} = jL_p\omega i_p + \frac{M^2\omega^2}{jL_s\omega + R_L} i_p \quad \textbf{6.11}$$

The reflected impedance is defined as:

$$Z_r = \frac{M^2\omega^2}{jL_s\omega + R_L} \quad \textbf{6.12}$$

The denominator of the reflected impedance is the equivalent impedance of the secondary circuit (Z_s) seen by the secondary equivalent voltage generator $jM\omega i_p$. The expression 6.12 can be therefore written as:

$$Z_s = j\omega L_s + R_L \quad \textbf{6.13}$$

$$Z_r = \frac{M^2\omega^2}{Z_s} \quad \textbf{6.14}$$

This model is applied in the four basic topologies (Figure 6.1). Therefore depending on the secondary circuit (series or parallel) the expressions 6.15 and 6.16 are obtained:

- Series compensated secondary:

$$Z_s = j\omega L_s + \frac{1}{j\omega C_s} + R_L \quad \textbf{6.15}$$

- Parallel compensated secondary:

$$Z_s = j\omega L_s + \frac{1}{j\omega C_s + \frac{1}{R_L}} \quad \textbf{6.16}$$

Consequently, separating the real and imaginary parts, the reflected impedance can be written as:

- Series compensated secondary:

$$Re\{Z_r\} = \frac{\omega^4 {C_s}^2 M^2 R_L}{(\omega^2 C_s L_s - 1)^2 + \omega^2 {C_s}^2 R^2} \quad \textbf{6.17}$$

$$Im\{Z_r\} = \frac{-\omega^3 C_s M^2 (\omega^2 C_s L_s - 1)}{(\omega^2 C_s L_s - 1)^2 + \omega^2 {C_s}^2 {R_L}^2} \quad \textbf{6.18}$$

- Parallel compensated secondary:

$$Re\{Z_r\} = \frac{\omega^2 M^2 R}{{R_L}^2(\omega^2 C_s L_s - 1)^2 + \omega^2 {L_s}^2} \quad \textbf{6.19}$$

$$Im\{Z_r\} = \frac{-\omega^3 M^2 \left[C_s {R_L}^2(\omega^2 C_s L_s - 1) + L_s\right]}{{R_L}^2(\omega^2 C_s L_s - 1)^2 + \omega^2 {L_s}^2} \quad \textbf{6.20}$$

The total impedance, seen by the primary source (V_{in}), is denoted as Z_p and its expression depends on the topology on the primary side (Figure 6.5).

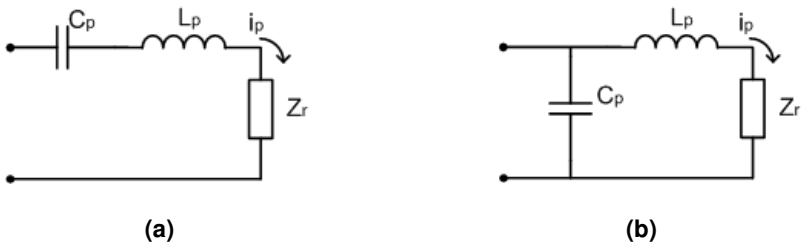

Figure 6.5: Primary circuits with reflected impedance: (a) Series compensated primary; (b) Parallel compensated primary

The expression of Z_p for series and parallel compensated primary are shown in equations 6.21 and 6.22 respectively.

- Series compensated primary:

$$Z_p = j\omega L_p + \frac{1}{j\omega C_p} + Z_r \quad \textbf{6.21}$$

- Parallel compensated primary:

$$Z_p = \frac{1}{j\omega C_p + \frac{1}{j\omega L_p + Z_r}} \quad \textbf{6.22}$$

The analysis of the behavior of each topology is carried out by studying the Z_r and Z_p expressions. For each topology, the following issues are studied.

a) Q factor

The quality factor of the primary and secondary systems plays an important role in the final system behavior. Therefore, the quality factor for the different cases will be calculated and as it will be shown in chapter 9, different conditions or requirements for the primary and secondary systems quality factor will be fixed.

b) Compensation

If it is desired that the primary and secondary circuits resonate at the same frequency, depending on the topology, a compensation is needed in the primary. In order to calculate this value the next condition is applied to each case:

$$Im\{Z_p\}\big|_{\omega=\omega_0} = 0 \qquad \textbf{6.23}$$

where ω_0 is the resonance frequency of the secondary circuit.

$$\omega_0 = \frac{1}{\sqrt{C_s L_s}} \qquad \textbf{6.24}$$

c) Bifurcation phenomena

The existence and calculation of the limit between bifurcation and bifurcation-free regions is done checking the following condition:

$$Im\{Z_p\} = 0 \qquad \textbf{6.25}$$

As it can be seen, the condition is the same one that is used to calculate the compensating capacitor of the primary. However, in this case, the existence of more solutions for this condition is studied.

Due to the complexity of the expressions, a normalization procedure to analyze the expression easier is followed, which is used in previous studies [55] [59].

- Frequency is normalized to the resonant frequency:

$$u = \frac{\omega}{\omega_0} \qquad \textbf{6.26}$$

- $Im\{Z_p\}$ is normalized to $Re\{Z_r\}|_{\omega=\omega_0}$:

$$Im\{Z_n\} = \frac{Im\{Z_p\}}{Re\{Z_r\}|_{\omega=\omega_0}} \quad \textbf{6.27}$$

With these two normalizations, some constants can be simplified and the expression can be easily rewritten in terms of the quality factors of the primary and secondary (Q_p and Q_s). Consequently the boundary condition to have a bifurcation free system can be shown in terms of the quality factors and frequency.

6.1.2 Simulation

Several programs are available to make numerical computations to calculate resonant circuits. Most of the simulators are circuit simulators, which help to study a circuit through the simulation of a lumped element model.

However, in this work a second step is also required: the simulation of the real structure to study the effect of locating the coil in different scenarios and also to have a tool more near the real system to compare the simulating results with the measurements with the real antenna.

CST STUDIO has been used for the simulations. It is a fully featured software package for electromagnetic analysis and design in the high frequency range. The program is specially suited to the fast, efficient analysis and design of components like antennas, filters… The main advantage of using CST is that the circuital model of the inductance can be easily replace by its corresponding 3D model.

6.1.2.1 Circuit simulation

CST STUDIO has an especial module DESIGN STUDIO to work with different circuit schemes with lumped elements or 3D models that can be simulated in the 3D solver and then imported to Design Studio.

The objective of the circuit simulation is firstly to check if the analytical approach described in section 6.1.1 is correct. For that purpose, two circuits are studied: the real one (Figure 6.6a), where the primary and secondary parts are defined with certain parameters and the phasor model (Figure 6.6b), where the expression obtained for the reflected impedance in the analytical approach is introduced in the simulator. In Figure 6.6 the studied model for SP topology is shown as an example.

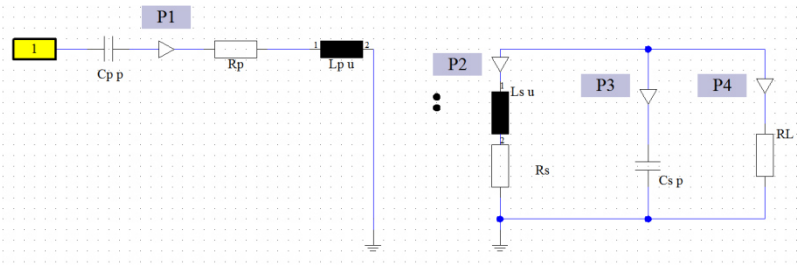

(a)

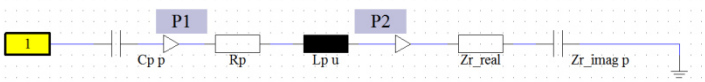

(b)

Figure 6.6: Design Studio model of SP Topology: (a) Real circuit; (b) Phasor model

Once the analytical approach and the simulation are correlated, Design Studio is employed to study any desired effect or behavior of the resonant circuits.

6.1.2.2 3D model simulation

The module CST MWS MICROWAVE studio has been used for the analysis with the 3D model.

There are two main solvers in the software: transient solver and frequency solver. Each of them is more efficient for different cases.

Transient solver:

- Electrically medium and large sized problems
- Broadband analysis
- Arbitrary time signals

Frequency solver:

- Electrically small to medium sized problems
- Narrow band / single frequency

As the problem that is analyzed is very resonant and the frequency range of interest is narrow, frequency solver has been used. The main task for the frequency domain solver module is to calculate S-parameters. Due to the fact that each frequency sample requires a new simulation run, the relationship between calculation time and frequency steps is linear unless special methods are applied to accelerate subsequent frequency domain solver runs.

An alternative method in the frequency domain is the "*Resonant: Fast S-Parameter*" solver, which calculates S-parameters and fields in the case of a tetrahedral mesh and S-parameters in the case of a hexahedral mesh. For this method, one simulation run is performed to obtain the S-parameters for the entire desired frequency range.

In the simulations, the feature "*Resonant Fast S-Parameter"* has been used with Tetrahedral mesh since it gives a good trade-off between accuracy and simulation time restrictions. The coil has been excited with discrete ports. The 3D model of the designed coil is shown in Figure 6.7.

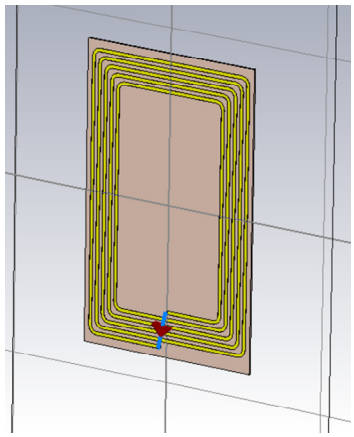

Figure 6.7: CST 3D model of the inductor

6.1.3 Measurements

The measurements have been carried out using an Agilent 87050E Network analyzer to measure the input impedance of the primary circuit. A structure made of foam material is designed to have a set up where the primary and secondary coils are fixed and parallel for different distances (Figure 6.8).

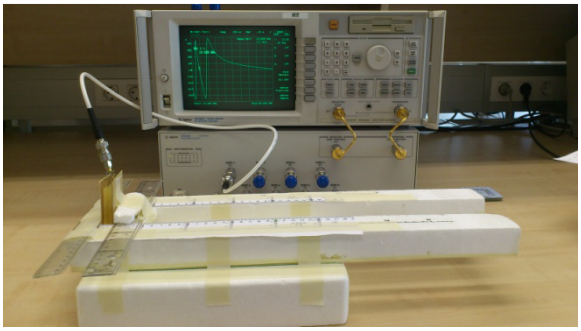

Figure 6.8: Setup for the measurements

In Figure 6.9, the used system for controlling the distances between the coils is shown.

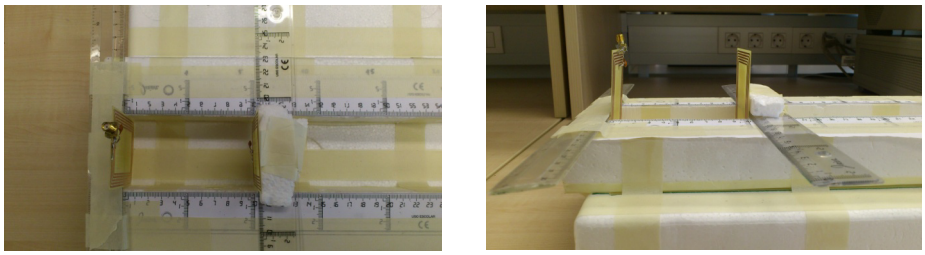

Figure 6.9: System for controlling the distances between the coils

6.2 Far field approach

In the far field approach the attention is focused on studying the behavior of the human body for communication with implantable devices at different frequencies.

In this section the methodology that is followed for the correct characterization of the human body is explained. It is virtually impossible to measure electric fields in real human bodies, therefore simulation is usually used. Consequently, it is important to be sure that the simulations are reliable. In order to check this issue, firstly a homogeneous phantom analysis has been done to compare the simulation with the corresponding measurements. In this context, the procedure for the fabrication and characterization of sugar based phantom is explained.

Once the phantom is correctly fabricated and its dielectric properties are properly measured, the characterization of plane wave attenuation in homogeneous phantoms in an anechoic chamber is done. These measurements are compared with the corresponding simulations.

Secondly, a heterogeneous planar layered block phantom model is used to study the effect of the different layers in implanted communications. Measurements with heterogeneous phantom are complicated because it is difficult to keep the materials of different compositions from mixing with each other. Therefore, as the validity has been demonstrated with homogeneous model, in this case the simulation results are compared only with the equivalent analytical approach.

Finally, once the main effects of the most relevant human tissues have been studied with the heterogeneous model, a preliminary study of different voxel models is analyzed. In this case, all the conclusions are based only on the simulations, since measurements and the analytical approach for this kind of geometry is too complex.

The section is divided into three different parts. Firstly, the analytical approach that is used for the different cases is explained. Secondly, all the concepts and tools for simulating the human body with different models are shown and finally the measurements setup for the fabrication of sugar based phantoms and the setup for measuring the power absorbed in a physical phantom in an anechoic chamber are addressed.

6.2.1 Analytical approach

Analytical methods to calculate the reflection and transmission coefficients and the waves behavior are restricted to very simple geometries, but provide valuable information to understand the basic behavior of the waves in ideal conditions.

For all cases, a plane wave with normal incidence is considered. A plane-wave travels in free space with a wave impedance equal to $377\,\Omega$ and when it meets the human body it finds a medium with lower impedance.

6.2.1.1 Two layers

The case for 2 layers can be solved directly applying the reflection and transmission coefficients at the boundary (equations 3.37 and 3.38) and then using the equations that define the wave into the medium (equation 3.30).

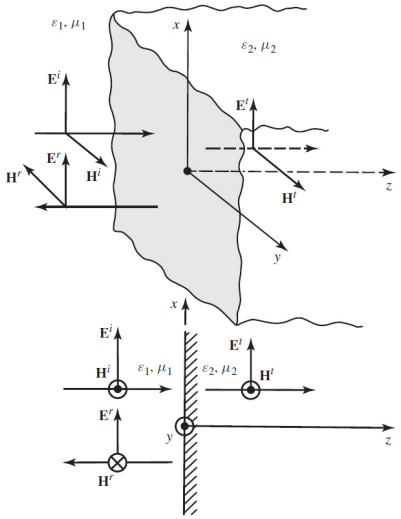

Figure 6.10: Wave reflection and transmission at normal incidence on a planar interface [67]

6.2.1.2 Three layers

The case for 3 layers is more complex but an exact solution can be obtained. In Figure 6.11 this case is shown, describing the wave's behavior.

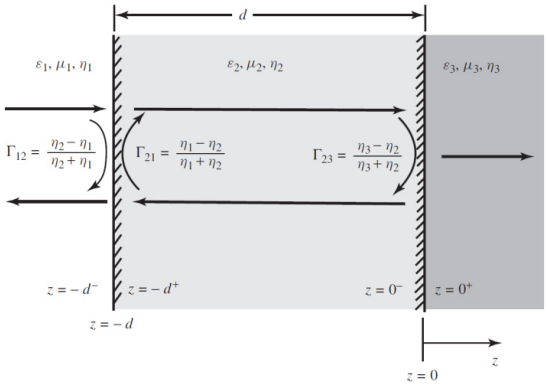

(a)

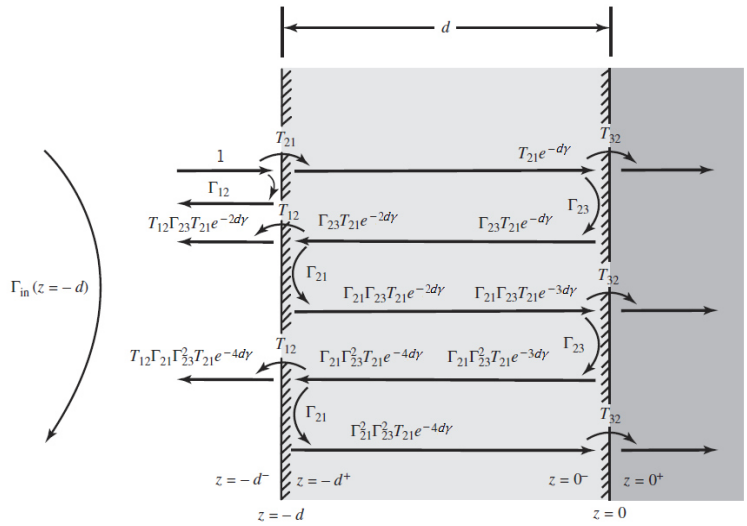

(b)

Figure 6.11: Reflection and transmission coefficients for wave propagation in 3 layers dielectric slab. (a) Referred to impedance and intrinsic reflection coefficient. (b) Ray-tracing model [67]

The total input reflection coefficient can be written as a geometric series that takes the form of:

$$\Gamma_{in}(z=-d^-)=\Gamma_{12}+\frac{T_{12}T_{21}\Gamma_{23}e^{-2d\gamma}}{1-\Gamma_{21}\Gamma_{23}e^{-2d\gamma}} \qquad \textbf{6.28}$$

where

$$\gamma=\alpha+j\beta \qquad \textbf{6.29}$$

The first term comes from the intrinsic reflection coefficient of the initial reflection (Γ_{12}) and the second term is due to the multiple bounces within the medium 2 ($T_{12}T_{21}\Gamma_{23}e^{-2d\gamma}, T_{12}T_{21}\Gamma_{21}{\Gamma_{23}}^2e^{-4d\gamma}$ ...), which can be seen as a geometric series (S) (equation 6.30) with initial value of $a=T_{12}T_{21}\Gamma_{23}e^{-2d\gamma}$ and a ratio of $r=\Gamma_{21}\Gamma_{23}e^{-2d\gamma}$.

$$S=\frac{a}{1-r}=\frac{T_{12}T_{21}\Gamma_{23}e^{-2d\gamma}}{1-\Gamma_{21}\Gamma_{23}e^{-2d\gamma}} \qquad \textbf{6.30}$$

If the magnitudes of the intrinsic reflection coefficients $|\Gamma_{12}|$ and $|\Gamma_{23}|$ are low compared to unity, equation 6.28 can be approximated by:

$$\Gamma_{in}(z = -d^{-}) = \Gamma_{12} + \Gamma_{23}e^{-2d\gamma} \qquad \textbf{6.31}$$

6.2.1.3 N-layers

With the approximation of Equation 6.31 the reflection coefficient for N layers can be easily calculated. In this case multiple reflections can occur between tissue interfaces. The transmitted field will combine with the reflected field to form standing waves in each tissue layer.

A structure made of different materials to study the reflection and transmission when there are multiple interfaces is shown in Figure 6.12.

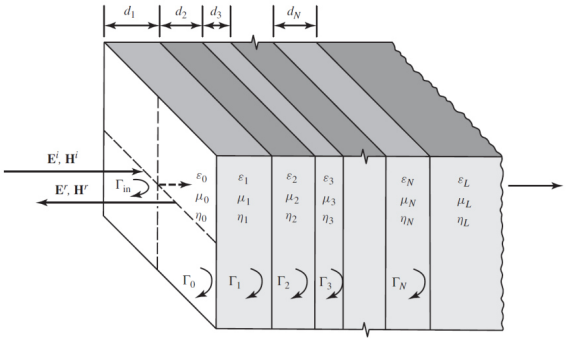

Figure 6.12: Normal wave propagation through N layers sandwiched between two media [67]

The reflections and transmissions of this system are calculated by the following expressions:

$$\Gamma_0 = \Gamma_{01} = \frac{\eta_1 - \eta_0}{\eta_1 + \eta_0} \qquad \textbf{6.32}$$

$$\Gamma_1 = \Gamma_{12} = \frac{\eta_2 - \eta_1}{\eta_2 + \eta_1} \qquad \textbf{6.33}$$

$$\vdots$$

$$\Gamma_N = \Gamma_{N-1,N} = \frac{\eta_N - \eta_{N-1}}{\eta_N + \eta_{N-1}} \quad \textbf{6.34}$$

The total reflection coefficient at the input of the system are given by:

$$\Gamma_{in} = \Gamma_0 + \Gamma_1 e^{-j2\beta_1 d_1} + \Gamma_2 e^{-j2(\beta_1 d_1 + \beta_2 d_2)} + \cdots + \Gamma_N e^{-j2(\beta_1 d_1 + \beta_2 d_2 + \cdots + \beta_N d_N)} \quad \textbf{6.35}$$

As mentioned, this expression is only accurate when at each boundary the intrinsic reflection coefficients of equation (6.32) through (6.34) are small in comparison to unity. This issue is extremely important and should be checked before using the equation 6.35.

However, as it will be demonstrated in chapter 9, the intrinsic reflection coefficients for human tissues are not small comparing with the unity; consequently, the previous approach is not accurate.

6.2.2 Simulation

As in the analytical approach, in the simulation approach the study starts with a simplified case. Firstly, the study is done with homogeneous muscle phantoms and the obtained results are compared with measurements. Secondly, a heterogeneous layered planar phantom with different number of layers is analyzed and finally, voxel models are used. In all cases, some basic procedures must be followed in order to get reliable results. In this section the most important ones are explained.

6.2.2.1 Biological material characterization

This step is extremely important for simulating in bioelectromagnetics. As it has been explained in chapter 2, human body tissues have dielectric properties that are frequency dependent. It has been also explained that there are different ways to represent these properties by mathematical models, to define the dispersion curve that permittivity and conductivity exhibit with frequency.

In CST the dielectric properties of human body tissues are based on the 4 Cole-Cole model studied by Gabriel [19–21]. When one material is used, there is a specific macro called “Define Human Materials Properties” to define the corresponding parameters (Figure 6.13).

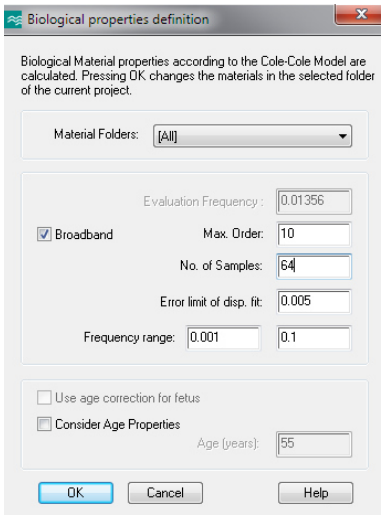

Figure 6.13: Screen shot of the macro to define the biological properties in CST MWS

As it can be seen, different options are available. A discrete evaluation frequency can be chosen. In that case the material is only correctly defined for this frequency. In most cases, however, it is interesting to fit the correct properties in a frequency range. In order to do that, the number of samples, the maximum error of dispersion and the maximum order of the model can be chosen. In practice, the best way to know if the parameters that are selected are good enough is to check the dispersion curves of the bio-material (Figure 6.14).

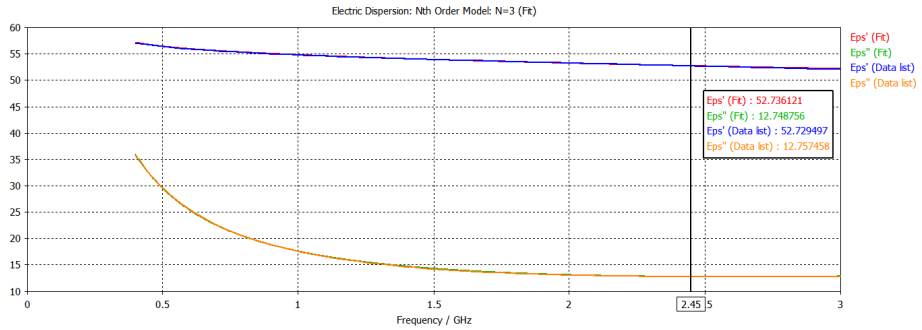

Figure 6.14: Electric dispersion for Muscle using CST MWS macro for defining human material properties

CST uses the fit data (red and green curves) in the simulation. The blue curve and yellow curve are the data list taken from Gabriel's database.

In Figure 6.14 a perfect fit can be observed between the data imported by Gabriel's measurements and the curve fitting CST internally performs to use in the computation. If the obtained curves are not accurate enough, more restricted parameters must be selected by changing the number of samples, the error limit of dispersion fit or the maximum order of the model. It should be pointed out that for larger frequency ranges, the approximation would be less accurate.

a) Voxel data material definition

As mentioned in chapter 4, there are several phantom models that can be used for determining the behavior of the electromagnetic waves inside the human body. CST has its own Voxel Family that can be easily imported.

In our case, the Virtual Family from IT'IS foundation has been mainly used. There is a problem to define the materials of the different biological tissues that are used in the Virtual Family phantoms since the names used in them differ from the ones that are used in CST models. Consequently, when the aforementioned macro is used to define the tissue properties for the desired frequency range, CST cannot manage the materials whose name do not correspond with the ones defined by CST models. For example for CST

models, the muscle is called “SkeletonMuscle” and in Virtual Family models it is called “Muscle”: the program will not have any Cole-Cole model associated with Muscle.

Besides, Virtual Family voxel models are more accurate since the resolution is higher and they have more types of human tissues. Obviously, these extra tissues do not have the corresponding Cole-Cole model neither.

The Cole-Cole models are based, as mentioned before, in Gabriel’s research. The software employs an internal table, called “Material_Map” in CST\Library\Bio Models directory, that matches the user defined materials with the ones defined by Gabriel.

As part of the current study, all the new tissues and the ones that are named differently have been included in this table to be able to simulate the Virtual Family from IT’IS foundation in CST (included in Appendix A). The material_map of CST 2014 has partially included the materials of Virtual Family.

6.2.2.2 Mesh resolution

In case of biological materials, as the wavelength inside the tissues is shorter than the one in the air, it is advisable to check the minimum needed resolution to get reliable results. A tradeoff between accuracy and computation effort must be made. The resolution in (x,y,z) directions can be changed independently and for first and preliminary simulations the activation of the “Adaptative mesh refinement” option is recommended.

There are two main mesh types in CST Microwave Studio: hexahedral and tetrahedral mesh. For broadband problems, the hexahedral mesh in combination with the transient solver is very efficient. Besides, in voxel models, tetrahedral mesh is not supported. Consequently, hexahedral mesh will be used for all simulations.

6.2.2.3 Boundary conditions

Different boundaries must be selected depending on the study that is done. The ones that are used in this research work are:

- *Electric:* Operates like a perfect electric conductor, all tangential electric fields and normal magnetic fluxes are set to zero.
- *Magnetic:* Operates like a perfect magnetic conductor, all tangential magnetic fields and normal electric fluxes are set to zero.
- *Open:* with this boundary absorbing boundary conditions are recreated.
- *Open add space:* with this boundary free space conditions are recreated.
- Periodic: connects two opposite boundaries with a definable phase shift such that the calculation domain is simulated to be periodically expanded in the corresponding direction. Thus, changing one boundary to periodic condition always changes the opposite boundary to periodic as well. This is very useful when an infinite medium in certain direction is desired. In our case, it is used when only the direction of the penetration of the signal is studied and neglecting the possible reflection from transversal directions.

6.2.2.4 Electromagnetic excitation

Two different types of excitation are used: plane wave excitation and waveguide port excitation. With plane wave excitation no S-parameter is calculated, instead the stimulation amplitude in V/m is recorded. With waveguide ports S-parameters are calculated.

In all simulations, it is desired to excite the phantom with a planar wave. When plane wave excitation is used, the boundaries must be selected as “open add space” in all directions to reflect the finite size phantom condition (Figure 6.15)

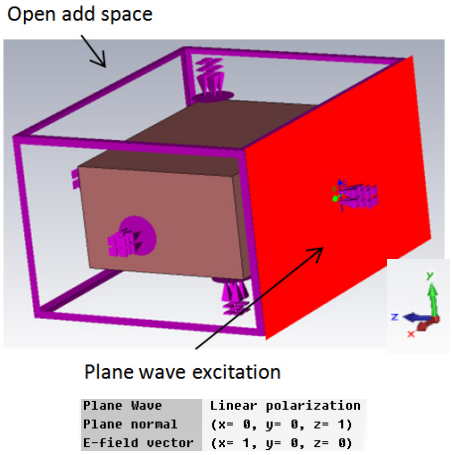

Figure 6.15: Screen shot of the simulation set-up

In Figure 6.15, a plane wave with linear polarization is defined with 1 V/m E-field in *x* direction and the corresponding H-field in *y* direction. Consequently, the plane wave travels in *z* direction.

The boundaries are defined as open add space (pink color) when the phantom is considered finite. Otherwise, when the interest is focused only in the behavior of the wave propagation in a certain direction and the other directions wants to be considered as infinite, periodic boundaries have to be defined when plane wave excitation is used (Figure 6.16a).

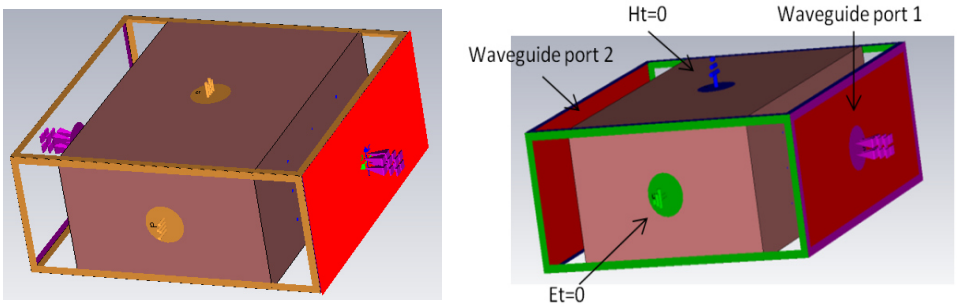

(a) **(b)**

Figure 6.16: Screen shot of the simulation set-up: (a) Plane wave excitation; (b) Waveguide port

The analogous way to simulate under the same conditions by using waveguide ports is shown in Figure 6.16b. In this case, two ports are defined and the boundaries are chosen to force a plane wave in the structure. For that, $E_t = 0$ condition in *Xmax* and *Xmin* boundaries, $H_t = 0$ conditions in *Ymax* and *Ymin* boundaries and open add space condition in *Zmax* and *Zmin* boundaries have been defined. Both cases are electromagnetically equivalent and provide different computation outcomes. As mentioned before, the advantage of using waveguide ports is that the S11 and S21 parameters can be automatically obtained for a given structure.

6.2.2.5 Simulated results monitors

As the interest is focused on the characterization of the phantom, and not in antenna's one, the electric field is monitored with ideal probes for the desired frequency range at certain positions and/or along a curve for a specific frequency. For this second case, a line in the middle of the phantom is defined and the E-field is calculated through this line (Figure 6.17).

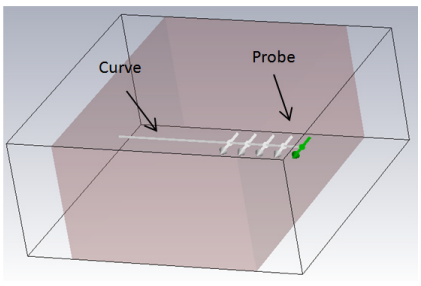

Figure 6.17: Definition of the curve and probes to evaluate the electric field

In order to compare the measurements with the simulation results, the presented data have been normalized to the value at the interface between air and phantom. In the measurements this normalization is done for the first position of the antenna and in the simulation is done for the beginning of the curve. This parameter is referenced as "S21 normalized [dB]" in subsequent sections.

6.2.3 Measurements

In this section the measurement procedures and set-ups used for the characterization of homogeneous phantom models are explained. Firstly, the procedure for the fabrication of sugar-salt based phantom will be addressed explaining the methodology for measuring the dielectric properties of liquids. Secondly, the procedure to measure the field attenuation within an homogeneous phantom is explained. For the correct characterization of this last issue, an anechoic chamber is required.

6.2.3.1 Phantom characterization

In order to fabricate liquid phantoms, it is necessary to be able to measure the dielectric properties of different liquids. There are several methods for measuring the dielectric properties of materials as it has been reported in section 2.3.1.2. Coaxial probe is used mainly for two reasons: the interest of having a broadband characterization of the proposed phantoms to see its limited frequency range of functionality, and the capability of this method to measure liquid materials. The following equipment has been used:

- Agilent E8362B PNA Network Analyzer
- 85070E high temperature dielectric probe (200 MHz - 50 GHz)

In Figure 6.18, the dielectric probe and the recommended setup is shown.

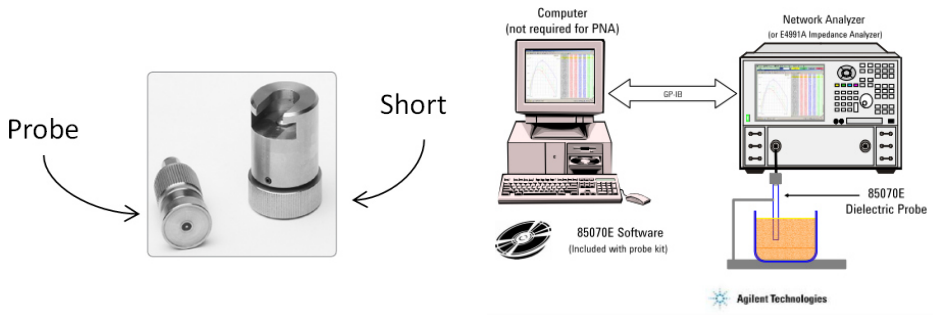

(a) **(b)**

Figure 6.18: 85070E dielectric probe and recommended set up scheme [102]

The calibration procedure is summarized in three steps:

- Firstly the probe is calibrated in open condition (air measurement). This is done in the same environment as the actual measurements, i.e. the plastic cup in which the phantom is contained. This reduces the influence of the equipment when the real measurements are done.
- Secondly the probe is shorted, using a shorting block (Figure 6.18). At this step a fixed reference point in the measurement is achieved.
- The last step consists of calibrating the probe submerged in distilled water of a specified temperature.

Once calibrated, it is important to check if the calibration is correct since the dielectric probe is extremely sensitive to any change in the set-up. Some important considerations for getting reliable measurements are:

- *Air gaps:* It is critical that no air gets trapped between the probe and the material to avoid errors in the measurements. If there are air bubbles under the probe the results will get distorted.

- *Cable stability:* The high temperature must be fixed using a stand. This is one of the most critical parts in the setup, because the probe cannot be moved after calibration.

- *Sample thickness:* The sample must also be thick enough to seem "infinite" to the probe. In equations 6.36 and 6.37, a rule to calculate the approximate thickness of the sample for getting reliable results are shown [102]:

$$thickness\ [mm] > \frac{20}{\sqrt{|\varepsilon_r^*|}} \qquad \textbf{6.36}$$

$$diameter\ [mm] > 20 \qquad \textbf{6.37}$$

Preferably, the probe should be completely submerged into the material, but that is not always possible for example when working with a solid or semi-solid material

Taking into account all these issues the set up shown in Figure 6.19 is used for getting reliable measurement results.

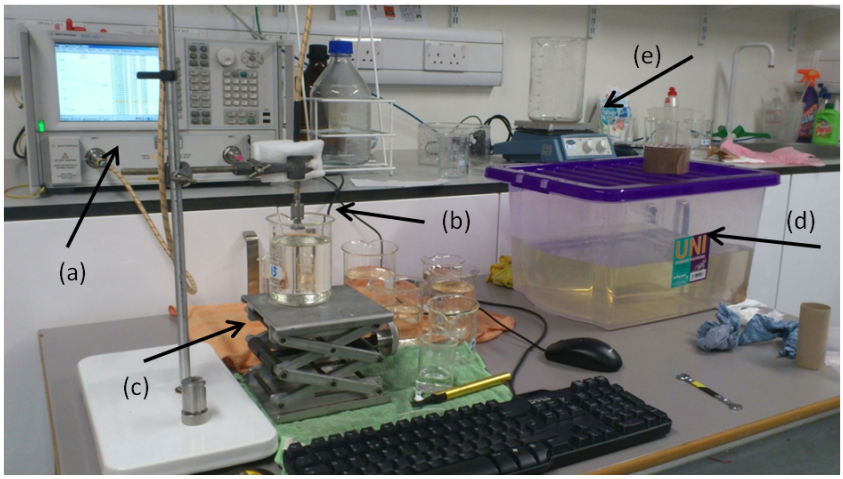

Figure 6.19: Set up for measuring the dielectric properties of liquid phantoms. (a) PNA. (b) Dielectric probe. (c) Platform to move the sample. (d) Tank to store the phantom. (e) Heater and mixer to fabricate the phantom

6.2.3.2 Characterization of plane wave attenuation

In this section, the equipment and the procedures that have been followed for the characterization of plane wave attenuation in homogeneous liquid phantoms are explained.

The methodology consists of moving a probe antenna into the phantom, to characterize the plane wave attenuation for different distances measuring the S21 parameter at each position. In all the measurements, the S11 parameter is checked to ensure that the antenna is matched and the obtained results are consequently reliable.

The interest is focused on the phantom characterization and not in the antenna's characterization. Consequently, the obtained results must be independent from the used antenna, since relative measurements are taken. The normalization is done, with respect to the first position inside the phantom so the different frequencies cases would be comparable.

The frequencies that are analyzed are f=402 MHz, f=868 MHz, f=2.45 GHz and 5.8 GHz.

This section is divided into three different subsections: antennas, phantom and anechoic chamber set-up.

a) Antennas

The use of two implanted broadband antennas is considered in this study to cover the desired frequency range (Figure 6.20).

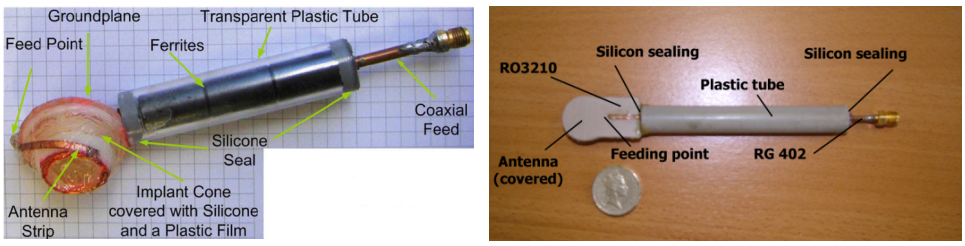

(a) **(b)**

Figure 6.20: Antennas used for the measurements: (a) Antenna 1, (b) Antenna 2

These antennas are selected for this measurements since both of them have been used and characterized for similar conditions as it is explained in [103][104]. The antenna 1, is designed to work at 402 MHz (MICS) and ISM 2.45 GHz and the antenna 2 is designed to work at ISM 868 MHz. Both antennas have good adaptation at 5.8 GHz. Therefore, they cover the frequencies that are used in the current research work. It is out of the scope of this research to study and explain the behavior of this antennas and the design process. As they will be used for measuring the received power when the antenna is placed inside the phantom and moved at different distances from the

air-phantom interface (relative measurements), the only parameter that should be checked to be sure that the measurements are reliable is the matching (S11 parameter). The assumption that is made is that the gain of the antenna is independent from the position of the antenna in the phantom. The normalization process is made with respect to the S21 parameter at the first position (the closest to the air-phantom interface).

The obtained measurements are compared with the simulation results evaluating the E-field along the curve (as explained in section 6.2.2.5). The measurements of both polarizations are taken to ensure that the reflections on the phantom walls do not affect the results. For a certain frequency, the difference between horizontal and vertical polarization should be independent of the distance where the antenna is located from the air-phantom interface.

b) Phantom

The cross section of the torso is modeled by a polystyrene tank of 355 mm x 255 x160 mm filled with the corresponding muscle tissue mimicking liquid. The height of the phantom is chosen to ensure that the probe antennas gain in the horizontal plane when placed at 9 mm from the interface is not affected by this dimension. However, the limited dimensions of the phantom will make an impact particularly at the lower frequencies by the reflections on the interfaces and this should be carefully considered as it will be shown in section 9.1.2. The used dimension is based on the study that is developed in [103].

With this study, the minimum phantom height that will dramatically influence the radiation properties in the horizontal plane of the considered implanted antennas can be set. Simulations have been performed to investigate this minimum height z that the phantom should have in order to represent its impact on the gain pattern for the vertical polarization (theta-component) in the horizontal plane with antenna 1 (Figure 6.21)

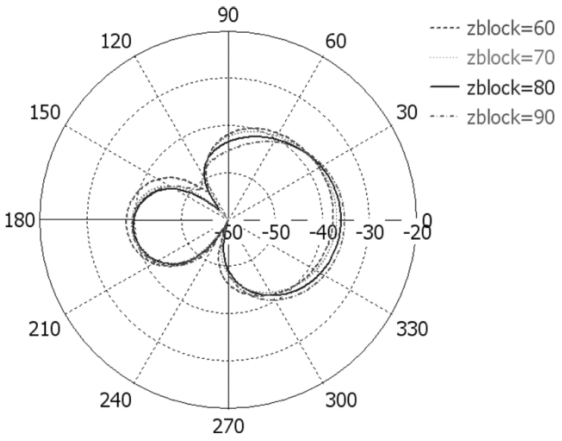

Figure 6.21: Simulated antenna gain (dBi) in relation to phantom height z (zblock=z/2 mm) for 402 MHz (vertical polarization, horizontal plane)

In Figure 6.21, the change of the gain in relation to the phantom height z is shown for antenna 1. A value of z=160 mm is estimated to be sufficient to account for body effects as the simulated gain patterns reasonably converge at 403 MHz. For higher frequencies, the phantom will be electrically larger and, therefore, representative, as well. In this manner, the antenna is placed at z=80 mm.

c) Set-up in the anechoic chamber

An anechoic chamber is a room designed to completely absorb reflections of electromagnetic waves. For far field approach, this environment is necessary to avoid unwanted reflections. All the measurements have been realized in the anechoic chamber of the School of Electronic Engineering & Computer Science, Queen Mary University of London. Two different chambers have been used: semi-anechoic and anechoic one.

As a preliminary approach, the measurements are carried out in the semi-anechoic chamber, and once the methodology and the obtained results are consistent, the full anechoic chamber is used to ensure better accuracy and reliability of the obtained results.

a) Set up in the semi-anechoic chamber

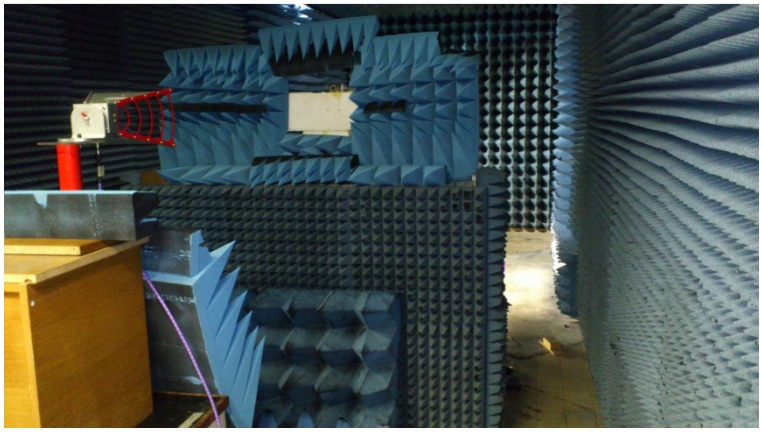

Figure 6.22: Semi-anechoic chamber of Queen Mary University of London

The distance between the transmitting horn antenna and the AUT is of 1.75 meters which is enough to assume far-field conditions at 2.45 GHz.

b) Set up in the full anechoic chamber

The transmitting horn antenna that has been used for the measurements is the model 3164-03 Dual Polarized Horn from ETS Lindgren [105] (Figure 6.23).

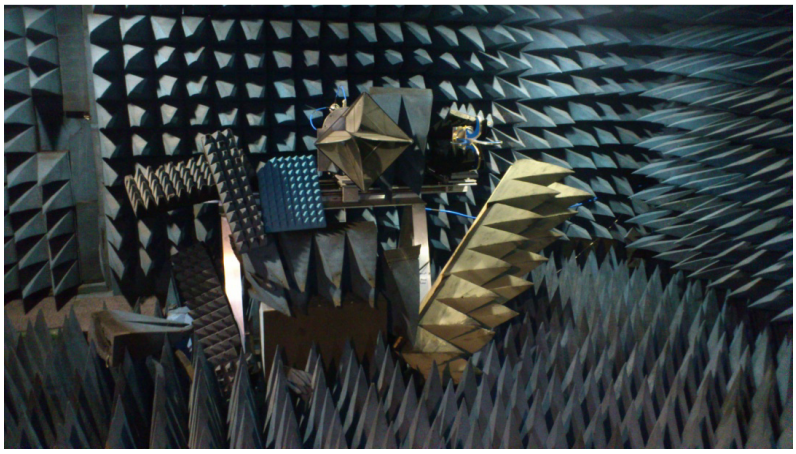

Figure 6.23: Transmitting horn antenna

With this horn antenna it is possible to transmit with horizontal and vertical polarization without the need of moving the antenna physically.

The distance between the transmitting horn antenna and the AUT is fixed to 3.32 meters according to the plane shown in Figure 6.24.

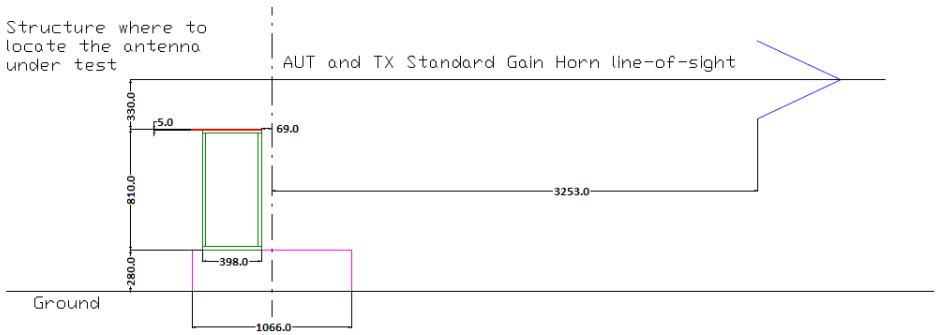

Figure 6.24: Plane of the anechoic chamber set-up

The phantom and the AUT are located in such a way that the receiving antenna is at the same height of the horn antenna (to have the same horizontal line of sight).

The placement of the phantom in the anechoic chamber is shown in Figure 6.25.

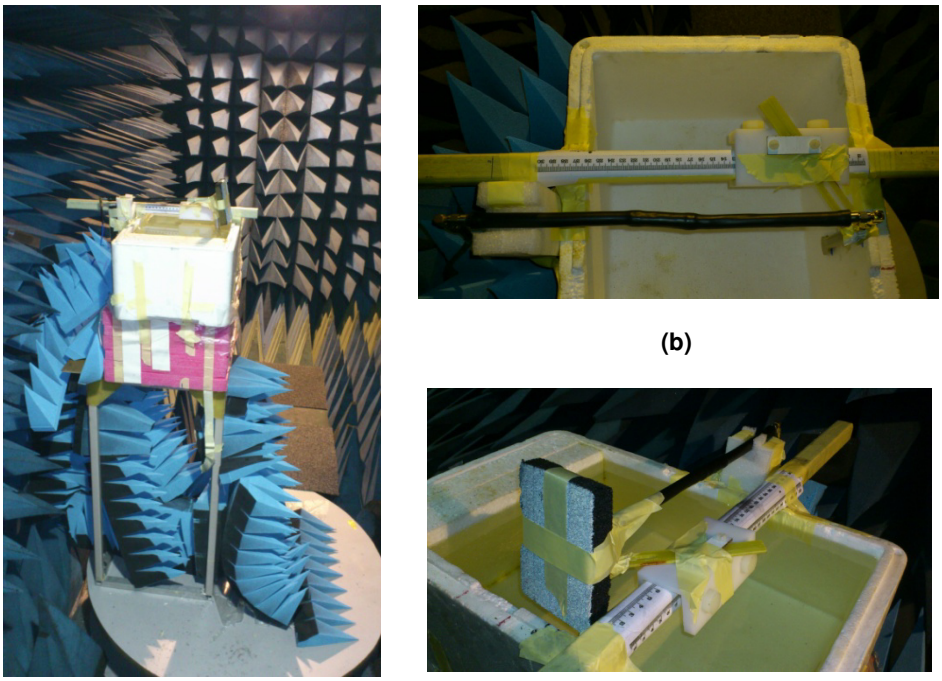

(a) **(b)** **(c)**

Figure 6.25: Antenna under test location: (a) Phantom general location overview. (b), (c) Designed system to move the antenna into the phantom.

As it can be seen, to ensure that no reflections are produced near the phantom, the supporting table has been surrounded with absorbing materials (Figure 6.25a). The most critical part is the cable. It is very important that the horn antenna sees the cable as a point, in that way the disturbance in the measurement results is lower. In Figure 6.25b it can be seen that the cable is in parallel with the structure designed to move the antenna. To ensure the cable position, a foam structure is designed in the backside of the phantom. Besides, this cable is covered by ferrite material to minimize the possible effect in the measurement [103].

The structure implemented to move the antenna is made of non-metallic material, consequently, its effect in the measurements is negligible and the same for all positions. An absorber is also put in front of the antenna and cable

that is outside the liquid phantom, so the aforementioned effect of the cable is further attenuated (Figure 6.25c).

With this setup the procedure followed is to measure the S-parameters for both polarizations for each position, moving the AUT inside the liquid phantom every 2mm.

6.3 Inkjet printing implementation

In this section, the equipment, materials and procedures followed for implementing flexible conductive circuits are explained. This section is divided into three subsections. In the first one, the printer and the materials used are described. In the second one, the procedure followed for the correct fabrication of conductive traces into flexible substrates is explained.

6.3.1 Used equipment and materials

There are three main components for the fabrication process in inkjet printing technology: the printer, the substrate and the ink.

6.3.1.1 Dimatix material printer (DMP)

The printer that has been used in this project is the Dimatix Materials Printer (DMP2831). It is a laboratory and limited production tool that enables to evaluate the use of inkjet technology for new manufacturing and analytical processes (Figure 6.26).



Figure 6.26: Dimatix Material Printer 2800

Printing processes and setups are completely controlled from the user's computer, and do not require a clean-room environment which reduces the levels of environmental contamination.

It is designed to be convenient and easy to use to carry out “proof of concept” and development work using inkjet technology.

The cartridge of the printer is the most critical component in the fabrication process.

DMP 2800 uses piezoelectric print head which consist of a piezoelectric transducer, nozzles, manifolds, fluid pumping chambers, and fluid inlet passages. When a voltage is applied to the lead zirconate titanate (PZT) piezoelectric transducer, the transducer deforms and creates mechanical vibrations. These vibrations create acoustic waves, which in turn force fluid out of the chamber through the nozzle. Piezoelectric inkjet printing is a thermally constant process that can be carried out in a variety of temperatures.

The main features of the cartridges that are used in DMP printer are the following ones:

- Type: Piezo-driven jetting device with integrated reservoir and heater.
- Usable Ink Capacity: Up to 1.5 ml.
- Number of Nozzles: 16 nozzles, 254 µm spacing, single row.
- Drop Volume: 1 (DMC-11601) and 10 (DMC-11610) pL nominal.
- Built-in heaters: up to 70°C.

In this work, only the DMC-11610 cartridge is used (Figure 6.27).

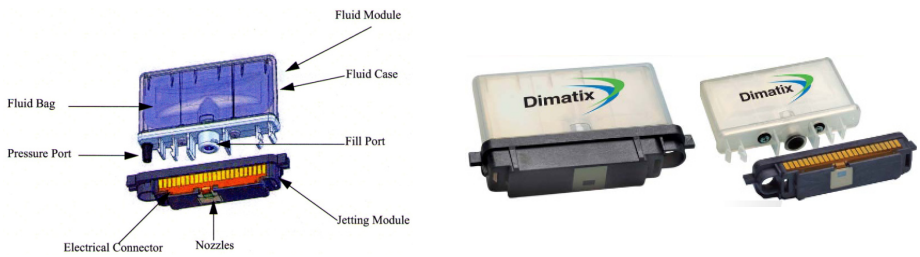

Figure 6.27: Cartridge

In general terms it can be said that the 10 pL cartridge should be used in patterns or parts of the patterns where there are not very small tracks or other structures, letting the 1 pL cartridge for these smaller parts.

The key difference is that the new 1 pL cartridge has a nominal nozzle size of 9 µm whereas the 10 pL cartridge has a nominal opening of 21 µm. Consequently filtering of the fluid and use of ultrasonic to break up aggregates is more important in 1pL cartridges. Further explanations on the most important differences can be found in [106] where different graphs show the difference in performance of both cartridges and some recommendations are given.

6.3.1.2 Substrate

Kapton Type HN polyimide is used in this project. It is a tough, aromatic polyimide film, exhibiting an excellent balance between physical, chemical, and electrical properties with a low loss factor ($\tan\delta=0.002$) over a wide temperature and frequency range. It is available in different gauges. In this project 127 µm is used.

Plastic substrate is employed only for measuring the thickness of the printed layers, since it has been observed that because of the weight of the deposited ink, Kapton is bent.

One of the main problems of using flexible substrates and inkjet printing technology is that typical soldering methods are not suitable. Therefore, other assembly methods such as conductive pastes or conductive adhesive tapes must be used.

6.3.1.3 Ink

The ink that is used in this project is SunTronic Jettable Silver U5714 from Sunjet. SunTronic Jettable Silver is a solvent based silver nano-particle inkjet ink, suitable for printing conductive lines and features in printed electronics and related applications. More information and the most important parameters of the ink can be found in [89].

6.3.2 Fabrication process description

In the fabrication process using inkjet printing technology there are several aspects that are very important for the final correct performance such as ink characteristics (viscosity, surface tension, particle size…), the surface topology of the substrate, surface tension of the particle and of the substrate ,the platen temperature, the print head parameters, time and temperature of the ink sintering, among others [107].

In this section the procedure and the parameters that have been chosen are described.

a) Filling and installing the cartridge

It is very important to shake the bottle of ink for 1-2 minutes to ensure that the particles are well dissolved in the vehicle. The use of ultrasonic to break the bigger particles that could be melted together is recommendable. Filtering of the ink also prevents from clogging of the nozzles.

When filling the cartridge minimising air bubbles is critical for reliable jetting. Tapping the cartridge while filling helps bubbles to move out of the bag.

It is checked that letting the cartridge set for one hour with the nozzles facing down is recommendable to improve the performance of the cartridge.

b) Select cartridge settings

There are several parameters that can be modified and that affect the performance of the jetting process. The most important ones are the ones that affect the waveform that is applied to each nozzle. Each nozzle can be excited with a different voltage level to get the desired jetting performance (Figure 6.28a).

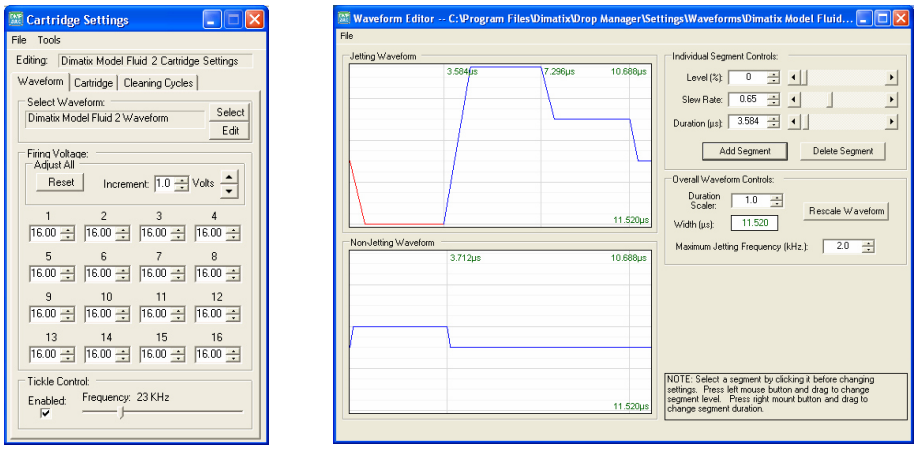

(a) (b)

Figure 6.28: Applied voltage and waveform each nozzle: (a) Voltage value and (b) waveform.

With this menu the voltage of each nozzle can be individually adjusted. The necessary voltage value to get the desired performance depends on the cartridge. In Figure 6.28b, the waveform that has been applied to each nozzle is shown. Each segment has three properties: duration, level and slew rate. Changing these parameters affects the jetting performance. There is a full chapter in the Dimatix User's Manual [108], that explains the effect of each segment of the waveform in the jetting performance. A deeper study on this issue is out of the scope of this research work.

Apart from the voltage and waveform that is applied to each nozzle, the cartridge temperature, the meniscus vacuum and the cartridge print height also determine the final jetting performance. These three parameters also depend on the cartridge. The cartridge temperature is the one that affects more the jetting process, rising the temperature the jetting performance improves significantly. The temperature can be selected from 28ºC to 45ºC, usually 40ºC is a good value. The meniscus vacuum can be selected from 0 to 5,0 inches H_2O, a value of 4,0 has been used and the height of the print head has been fixed to 1 mm.

c) Checking cartridge performance

Once the main important cartridge settings are selected, the performance has to be checked to decide which nozzles are used for printing. This process is iterative, because when the performance is checked it is necessary, in most cases, to change some of the aforementioned parameters.

The jetting performance is checked with the Drop Watcher camera. Drop Watcher allows direct viewing of the jetting nozzles, the faceplate surrounding the nozzles and the actual jetting of the fluid (Figure 6.29).

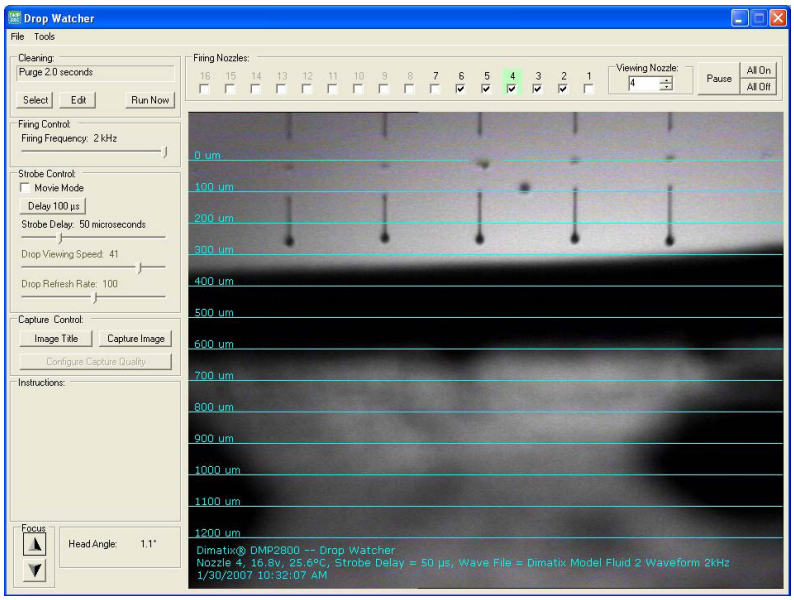

Figure 6.29: Drop Watcher

Drop watcher is used to adjust the cartridge setting to obtain the drop formation that is desired. The main parameter that can be easily control is the drop velocity.

In Figure 6.29, the performance of the selected five nozzles can be seen. Usually, it is difficult to print with more than 5 nozzles. The selected nozzles must be consecutive ones.

d) Cartridge performance maintenance

The DMP contains hardware and software to perform one or more maintenance activities which are designed to initialize and maintain optimal jetting performance and are crucial in the fabrication process.

The cleaning station contains an absorbent pad to draw fluid off the nozzle plate when it is brought close to it. It does not actually touch the nozzle surface but it rather touches the face plate of the cartridge around the nozzle plate.

The cleaning station uses air pressure to press the outside of the fluid bag, which forces fluid out through the nozzles. This is mainly used to initially prime the cartridge, but also as a method for reviving problematic nozzles. The DMP includes a pump for this function, which is also used for meniscus control.

There are three different clean options:

- **Spit:** It refers to firing the nozzles for the designated time and frequency.
- **Purge:** It refers to pushing fluid out through the jetting device with pressure (system is preset to 5 psi). This process is usually used to get air out of the jetting device.
- **Blot:** It refers to the cartridge simply coming down and making contact with the cleaning pad for the designated time. As the nozzle plate is recessed into the cartridge it does not touch the cleaning pad. The cleaning pad gets close enough to absorb fluid residue on the nozzle plate.

It is important to make sure that the cleaning pad is not saturated or clogged to ensure good removal of the fluid from the nozzles after purging or spitting.

The cleaning cycles are extremely important in the fabrication process; it has been observed that a making a Spit-Purge-Blot-Spit process (Figure 6.30) and then a Purge of two seconds before printing improves the jetting performance significantly.

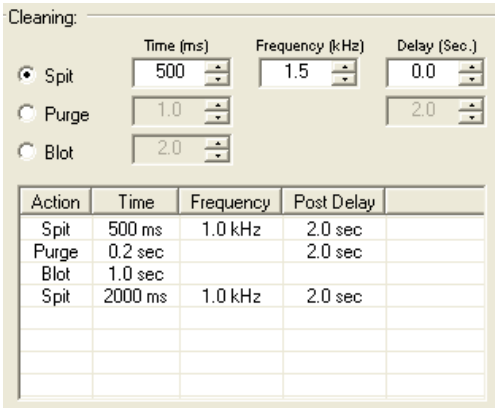

Figure 6.30: Spit-Purge-Blot-Spit cleaning cycle

A purge of two seconds is also advisable every 5 minutes during the printing process.

e) Selection of the pattern

Bitmap or gerber files can be imported to the DMP2800 software. As CST MWS allows to export gerber files of the desired structures, gerber files are imported. The resolution has to be selected before starting with the printing process. In this work a drop spacing of 25µm is selected which corresponds to a cartridge angle of 5,6º. In Figure 6.31, the functionality of the drop spacing and cartridge angle is illustrated.

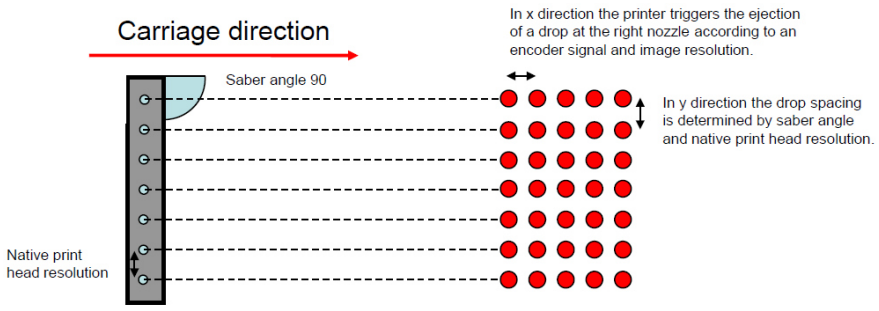

(a)

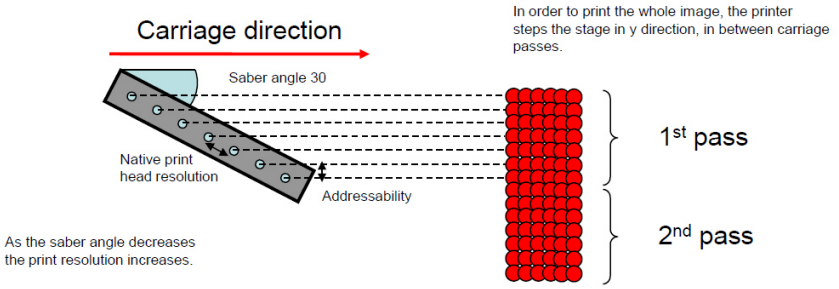

(b)

Figure 6.31: Resolution with DMP2800 printer: (a) cartridge angle of 90º and (b) cartridge angle of 30º [108]

The printer has a cartridge alignment scale system for selecting the correct cartridge angle. In Figure 6.32 an example for an angle of 11,4º is shown:

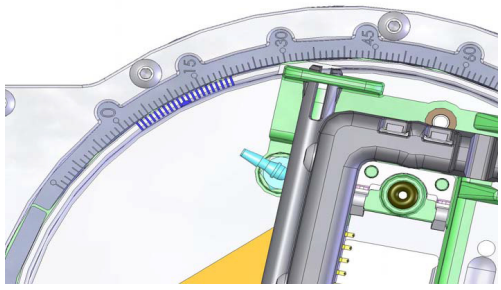

Figure 6.32: Cartridge alignment scale system [108]

There are two sets of scales: the outer scale is to fix the angle with increments of one degree and the inner scales to adjust the head's angle to 0,1 degree increments.

In [108] a detailed information about the necessary angle for different resolutions and the process to fix the angle correctly are deeply explained.

f) Substrate conditions and placement

The selected substrate must be placed in the plate. The plate has a vacuum system to fix the substrate to the platen, however, it has been observed that for

substrates thicker than 100µm it is necessary to fix the substrate using adhesive tape to ensure that it is fixed.

The plate's temperature can be modified from 28ºC to 60ºC. It is advisable to increase the temperature when more than two layers are printed to avoid scattering of the traces. In this work, the temperature has been fixed to 60ºC.

g) Printing process and checking the printed pattern

Once the substrate has been located at the desired position, the reference point in which the printing pattern is located must defined using the Fiducial Camera (Figure 6.33).

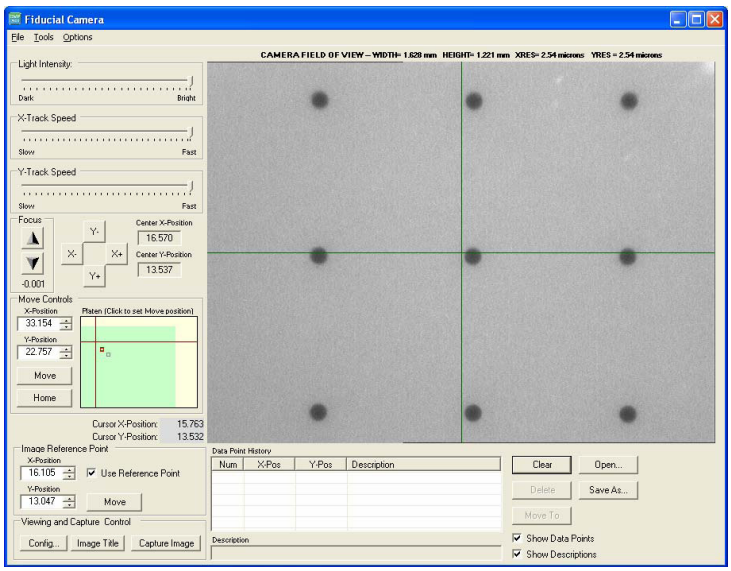

Figure 6.33: Fiducial Camera

Figure 6.33 is a sample screen shot of the main Fiducial Camera window. From this window and using the camera the following features can be done:

- Allows substrate alignment using reference marks
- Allows positioning a print origin or reference point to match substrate placement

- Provides measurement of features and locations
- Provides inspection and image capture of printed pattern or drops

In most cases, more than one layer is printed but it is advisible to ensure the quality of the printed pattern for intermediate layers by checking if there are undesired printed traces using this camera.

h) Sintering process

Once the prototypes have been printed a sintering process is necessary to improve the conductivity of the ink. The sintering time and temperature depend on the substrate that is used. For Kapton, 30 minutes at 200ºC has been considered as an appropriate sintering process.

Chapter 7

Inkjet Printing Technology Analysis

In this chapter a first approach to the main advantages and constraints that this fabrication technique offers for the fabrication of flexible conductive structures is made. The chapter is divided into two sections: in the first one, a resolution study is made to check the minimum printable width and estimate the typical track's thickness that can be obtained; in the second one, ink's characterization is realized.

7.1 Resolution study

7.1.1 Minimum printable width

The pattern that has been used for checking the minimum width that can be printed vertically and horizontally is shown in Figure 7.1:

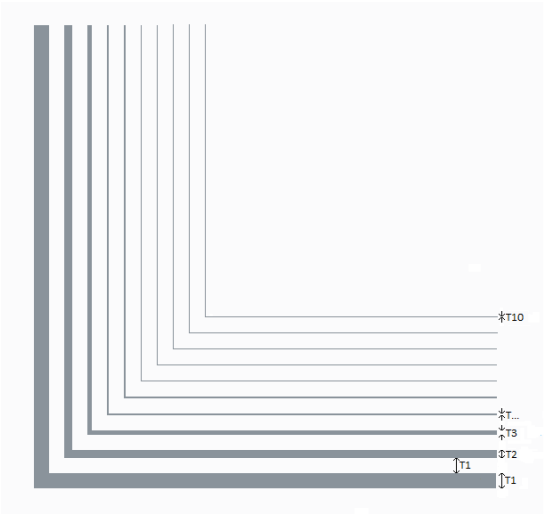

Figure 7.1: Designed pattern for resolution study

where the thickness of each line is shown in Table 7.1:

Table 7.1: Dimension of the printed pattern for resolution study

Trace Number	*T1*	*T2*	*T3*	*T4*	*T5*	*T6*	*T7*	*T8*	*T9*	*T10*
Dimension [μm]	*1000*	*500*	*250*	*100*	*75*	*50*	*40*	*30*	*20*	*10*

There are several parameters in the fabrication process that can affect the obtainable resolution. In this project the study is focused on the sintering time and number of printed layers. The measurements are obtained with the fiducial camera that has been previously explained. The printed prototype is shown in Figure 7.2:

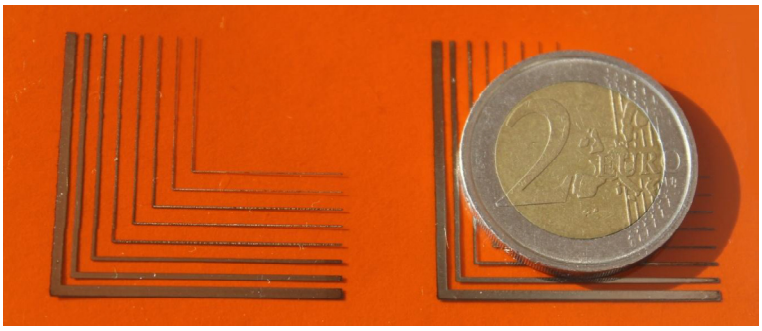

Figure 7.2: Printed pattern for resolution study

Two different studies are performed. In one hand, the effect of the sintering time is studied for 1 layer prototypes at 200ºC sintering temperature. The results taken with the fiducial camera and are summarized in Table 7.2.

Table 7.2: Obtained line's width for different sintering times at 200ºC and 1 layer prototypes

TIME (min)		*30*	*40*	*50*	*60*
WIDTH OF LINES (µm)	*1000*	*1040*	*1030*	*1005*	*1002*
	500	*516*	*512*	*504*	*501*
	250	*265*	*262*	*260*	*264*
	100	*116*	*112*	*110*	*112*
	75	*98*	*96*	*94*	*97*
	50	*94*	*93*	*91*	*89*
	40	*57*	*51*	*52*	*53*
	30	*56*	*49*	*50*	*51*
	20	--	--	--	--
	10	--	--	--	--

The second column corresponds with the theoretical width of the lines. As it can be seen, the two narrower lines, which correspond with 10 and 20 µm have not been printed. This can be due to the small size of these lines in comparison with the nozzle size of this 10 pL cartridge (DMC-11610), which is of 21 µm. It should be mentioned that these dimensions could be obtained changing some printing parameters, filtering the ink or using the 1pL cartridge (DMC-11601).

However, a deeper analysis on this aspect is out of the scope of the presented work. For the designs that are manufactured in this research the obtained resolution is good enough.

The other conclusion that can be obtained from this table is that the line widths are closer to the theoretical values by simply increasing the sintering time.

the images of the 500 and 75 µm tracks taken by the fiducial camera of the printer are shown in Figure 7.3.

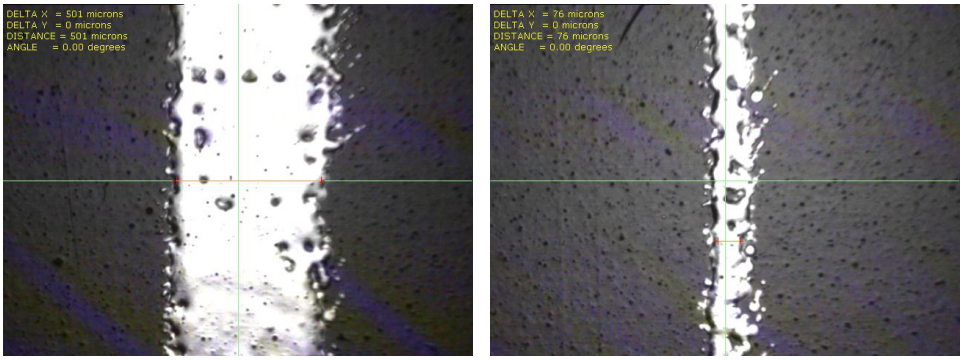

(a) (b)

Figure 7.3: Images of the tracks taken by the fiducial camera. (a) 500 µm line. (b) 75 µm line

As it can be observed, due to the printing process drop by drop, there are several "holes" in the track. These "holes" may have little impact on wide tracks, but when it comes to narrower tracks they may cut the trace. However, it should be pointed out that this two images correspond with one layer prototypes without sintering process, when more layers are printed on or the prototypes have its corresponding sintering process, these non-uniformities tend to diminish as it is shown in Figure 7.4.

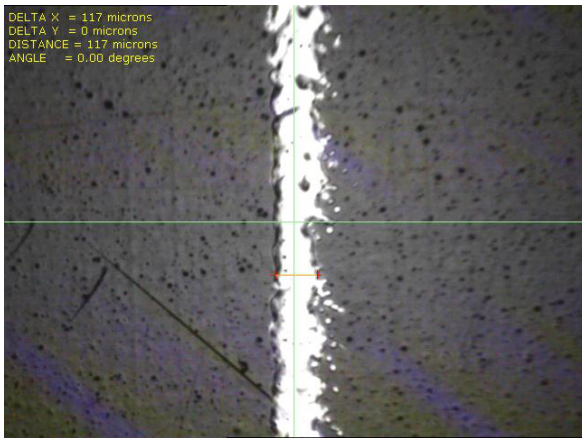

Figure 7.4: Images of the 75 µm line taken by the fiducial camera after 30min@200ºC sintering process

In this figure, the same 75 µm line is shown once is sintered. It can be clearly seen that the non-uniformities are less important in comparison with the non-sintered case.

On the other hand, the effect of the number of layers in the resolution is studied and the obtained results for different number of layers are summarized in Table 7.3.

Table 7.3: Obtained line's width for different number of layers prototypes with 30min@200ºC sintering process

NUMBER OF LAYERS		*1*	*2*	*3*	*4*
WIDTH OF LINES (µm)	*1000*	*1008*	*1016*	*1023*	*1029*
	500	*496*	*509*	*511*	*516*
	250	*271*	*276*	*282*	*296*
	100	*119*	*127*	*131*	*139*
	75	*83*	*89*	*94*	*103*
	50	*79*	*81*	*87*	*93*
	40	*65*	*72*	*79*	*85*
	30	*51*	*57*	*65*	*72*
	20	-	-	-	-
	10	-	-	-	-

It can be concluded that when the number of layers is increased the ink tends to expand more since there is more volume of ink and consequently the obtained pattern width is wider than the original one. This issue can be solved by changing some printing parameters, such as plate temperature or in some cases when the line width is extremely thin, re-scaling the pattern considering the broadening of printed traces could be a good approach.

7.1.2 Thickness estimation

As inkjet printing technology enables deposition of a different number of layers, an accurate adjustment of the printed conductive tracks thickness is possible. This capacity offers a great degree of freedom for different applications such as NFC systems, by controlling to Q factor of the designed coils [54].

The KLA-Tencor P-16+ Profiler is used to measure the thickness of the tracks. This profiler is a highly sensitive surface profiler that measures step height, roughness and waviness on sample surfaces [109].

It is important to select a proper substrate that it is not bend because of the weight of the deposited ink. For this reason, a plastic card is used for measuring the thickness.

In order to avoid possible deformation of the substrates, low temperature and short time is used in the sintering process. The sintering process is 30 min at 80ºC of temperature. This sintering process is enough to dry the ink. It is important to point out that this temperature is not enough to get good values of conductivity since more temperature is needed to achieve this goal. However, for the thickness measurements this fact is not important. It is assumed that the change of the thickness with more temperature is negligible and therefore is better to use lower temperatures to be sure that the substrate is not curved.

In Figure 7.5, it can be observed the different thickness and the profile that has been obtained for different number of layers using the plastic card and a sintering process of 30 min at 80ºC of temperature.

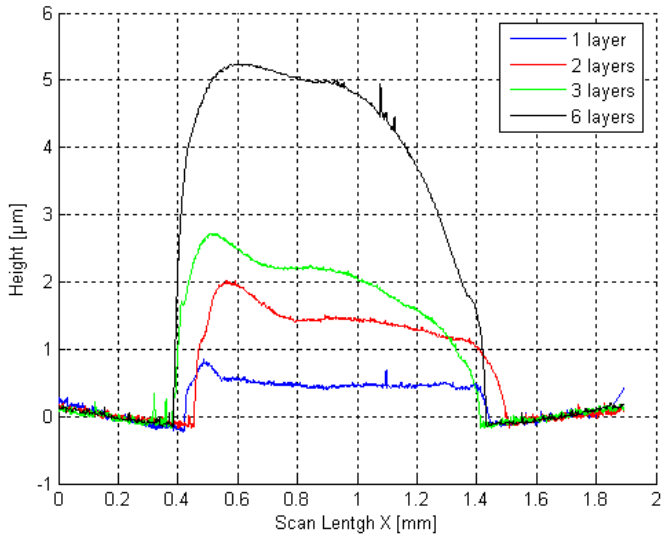

Figure 7.5: Obtained profiles for different number of layers under same sintering conditions

As expected, the thickness of the ink track increases with the number of layers. It can be seen that this increment is quite constant. Each of the layers gives a thickness less than 1µm. This value fits well with the values found in the bibliography [86]. A summary of the obtained thickness as a function of the number of layers is shown in Table 7.4.

Table 7.4: Obtained thickness for different number of layers

Number of layers	*Mean Thickness*	*Maximum Thickness*
1	*0,5*	*0,8*
2	*1,5*	*2*
3	*2*	*2,7*
6	*4,5*	*5,3*

7.2 Ink's characterization

The characterization of the ink is crucial to anticipate the final performance of the printed prototype. The most important property of the ink is its conductivity, which depending on the application affects strongly the final behavior.

In order to estimate the conductivity of the ink, taking into account equation 7.1, the electrical resistance and the thickness are the parameters that have to be measured.

$$R = \frac{1}{\sigma} \cdot \frac{L}{t \cdot w} \qquad \textbf{7.1}$$

where R is the electrical resistance, σ ink's conductivity, L is the longitude of the prototype (of the track), t is the thickness (that depends on the number of printed layers) and w is track`s width.

The electrical resistance is measured using the software package Keithley Model 2000DMM. This software allows measuring of the resistance every certain time and therefore is an optimum tool to study the change of the electrical resistance with time.

Different prototypes with different number of layers have been used to estimate the conductivity and to study the thickness of each layer. The conductivity is independent of the number of layers but different pairs of electrical resistances and thicknesses have been use to check the repeatability of the fabrication process.

As it has been mentioned before, the connections are a critical point in inkjet printing technology and consequently even more important for measuring the electrical resistance. In order to connect the necessary cables, the following test bench is made with FR4 (Figure 7.6).

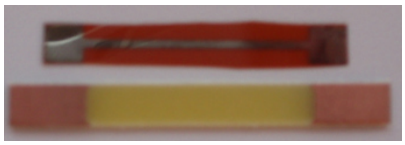

Figure 7.6: Designed plate and printed structure for measuring the electrical resistance

The copper layer in the corner is used to connect the printed structure to the FR4. This connection is done using the conductive paste [110] that has been explained previously.

The printed structure`s dimensions are summarized in Table 7.5:

Table 7.5: Printed prototype's dimensions

Track length	*40 mm*
Track width	*1 mm*
Pads	*5x5 mm^2*

The designed plated is 5mm longer in both sides to have the necessary gap to connect the cables. The set-up of the measurement system is shown in Figure 7.7.

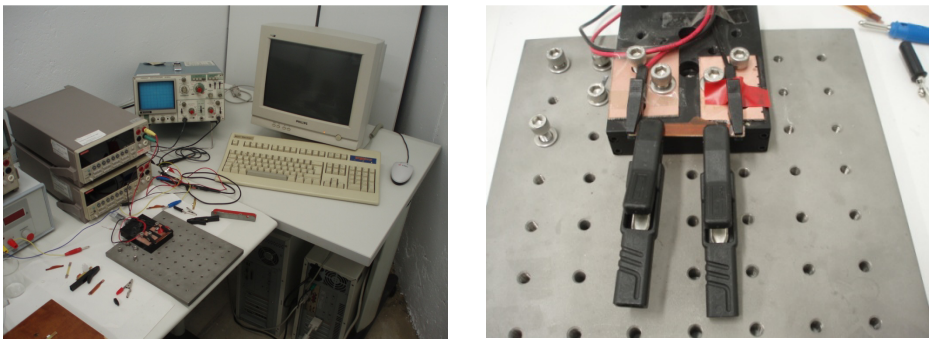

(a) **(b)**

Figure 7.7: Set-up: (a) General overview and (b) Connection system

7.2.1 Electrical resistance estimation

In all cases Kapton is used as substrate and the sintering process is 30min@200ºC. This sintering process is used since the conductivity value that is given by the ink's manufacturer is obtained with the same process. Therefore, making the prototypes under the same conditions should give similar results.

In order to ensure that the measurements are reliable, the measuring process has been taken for a certain time. If only punctual electrical resistance is measured, the obtained results vary too much because the connections (using the conductive paste) are not very stable. Therefore, it is recommendable to take measurements during certain time. By this way, it can be checked if the results are stable or not. The results that will be analysed are taken every 150 seconds during two hours.

In Figure 7.8, the obtained electrical resistances are presented depending on the number of layers. These results are the average of different measurements; it means that the value that is given for the resistance with two layers, for example, is the average of different measured prototypes of two layers.

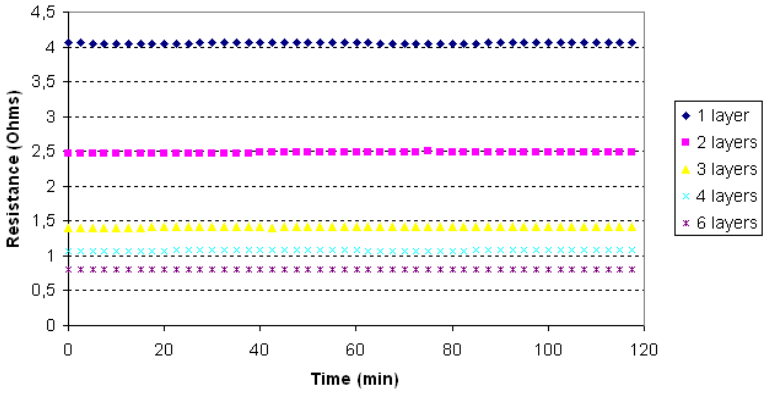

Figure 7.8: Electrical Resistance vs. time for different number of layers

As it can be seen in Figure 7.8, the electrical resistance decreases with the number of printed layers. This result is the expected one since looking at the electrical resistance formula, it can be concluded that the difference between

the different prototypes is only in the number of layers, and in principle, this parameter only affects the amount of ink that has been used, and therefore it only affects the section (thickness) of the ink´s track.

Looking at the previous figure, it can be seen that the study has been done for 1, 2, 3, 4 and 6 layers. In Table 7.6, the average value for the different number of layers is shown.

Table 7.6: Electrical Resistance depending on the number of layers

Number of layers	*Electrical Resistance (Ohms)*
1	*4,06*
2	*2,48*
3	*1,41*
4	*1,08*
6	*0,80*

In Table 7.7 the decrease of the electrical resistance in percentage from one layer to different number of layers is shown.

Table 7.7: Decrement of the electrical resistance in percentage with respect to one layer

From 1 layer to Y layers	*Electrical Resistance Decrease (%)*
1 to 2	*38,87*
1 to 3	*65,27*
1 to 4	*73,40*
1 to 6	*80,30*

7.2.2 Ink conductivity estimation

Once the different electrical resistance values for different number of printed layers and the thickness for each of the layers have been measured, an estimation of the ink's conductivity can be made using the resistance equation 7.1.

As mentioned in previous chapters, although conductivity is independent of the number of printed layers, the conductivity study is done in samples with different

number of layers, which correspond to different electrical resistance and thickness pairs for comparison purposes.

The obtained data is shown in Table 7.8.

Table 7.8: Obtained conductivity values with 30min@200ºC sintering process

Material: Silver	*Conductivity*$(\Omega m)^{-1}$	*Conductivity with respect to pure silver (%)*
Pure	$63.01 \cdot 10^6$	*100*
One layer	$8 \cdot 10^6$	*12.6*
Two layers	$9 \cdot 10^6$	*14.3*
Three layers	$7.9 \cdot 10^6$	*12.5*
Six layers	$8.5 \cdot 10^6$	*13.5*

The obtained results by this method are in accordance with the ones found in bibliography [107], [111]. As an indicative value, a 10% or 15% of the conductivity of the pure silver can be considered. In this work a conductivity of $8 \cdot 10^6(\Omega\mathrm{m})^{-1}$ is considered as representative of ink performance.

Chapter 8

Near field implanted wireless links optimization

In this section the studies related with near field systems are described following the methodology that has been explained in section 6.1 to reach the objectives described in Chapter 5.

First of all, the designed coil is characterized by comparing the analytical, simulation and measurements results for two different implementations: etched copper and inkjet printed.

Once the prototypes that are used are characterized the topology analysis is made in terms of needed compensation on primary circuit, bifurcation phenomena and efficiency.

The effect of using an inkjet printed prototype as secondary coil is also addressed explaining its main advantages and disadvantages.

Finally, a case study of using the antenna (coil) not only as a part of the communication system, but also, for sensor purposes by adding a capacitor is explained.

8.1 Coil implementation and characterization

A 5 turn rectangular (80mm x 50mm) planar spiral inductor with a track's width and separation between tracks of 1 mm is used as inductor. These dimensions verify the ISO 7810 standard [112]. This standard defines the physical characteristics of identification cards (Table 8.1).

Table 8.1: Nominal dimensions of ID-1 card type

Width (mm)	*Height (mm)*	*Thickness (mm)*
85.6	*53.98*	*0.76*

The analytically obtained inductance for the presented antenna is independent from the fabrication process. Following the process explained in chapter 7, the obtained value is 2.8 µH.

In Figure 8.1, two prototypes are shown, one manufactured by subtractive etching and the other one by inkjet printing technology.

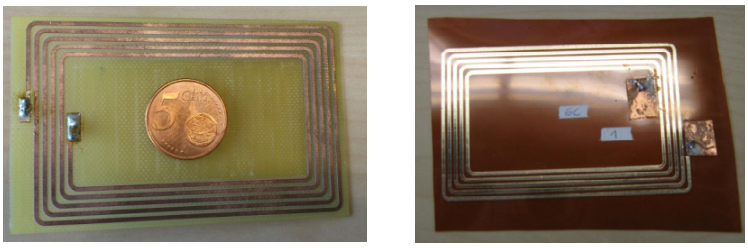

(a) **(b)**

Figure 8.1: Fabricated prototypes. (a) Subtractive etching method. (b) Inkjet printing technology

Four different prototypes have been fabricated to study the difference between them and are presented in Table 8.2.

Table 8.2: Fabricated prototypes

Name	*Technique*	*Substrate*	*Antenna*
Prototype 1	*Subtractive etching*	*FR4 (0.8 mm)*	*Copper (18 µm)*
Prototype 2	*Inkjet*	*Kapton (127 µm)*	*Silver ink (5 µm - 4 layers)*
Prototype 3	*Inkjet*	*Kapton (127 µm)*	*Silver ink (5 µm - 6 layers)*
Prototype 4	*Inkjet*	*Kapton (127 µm)*	*Silver ink (8 µm - 10 layers)*

The first prototype is made with subtractive etching and the rest of them are made with inkjet printing technology with different number of layers. In Table 8.3, the obtained results are shown.

Table 8.3: Obtained results: Analytical (A), Simulation (S) and Measurement (M)

Name	*Parameter*	*A*	*S*	*M*
Prototype 1	*R [Ω]*	*1.5*	*1.6*	*1.6*
	L [µH]	*2,80*	*2,78*	*2,96*
	Q	*159*	*148*	*157*
Prototype 2	*R [Ω]*	*46,58*	*51,13*	*50,25*
	L [µH]	*2,82*	*2,79*	*2,9*
	Q	*5,16*	*4,64*	*4,91*
Prototype 3	*R [Ω]*	*31*	*35,12*	*32,35*
	L [µH]	*2,82*	*2,79*	*2,94*
	Q	*7,75*	*6,77*	*7,76*
Prototype 4	*R [Ω]*	*22.5*	*22*	*23,5*
	L [µH]	*2.9*	*2.86*	*2,9*
	Q	*10.98*	*11*	*10,5*

With copper-etched antennas, quality factors higher than 120 can be manufactured. The obtained value are in concordance with previous studies [113].

It can be observed that the obtained inductance value is the same for both technologies, but there is a considerable change in terms of input resistance

and therefore, in the quality factor. This is due to the differences in the conductivity and thickness of the conductive track (antenna).

On one hand, the conductivity of the copper is fixed. However, the ink's conductivity depends on the sintering process as it has been explained in the previous chapter. The sintering process that has been used for these prototypes is of 30min@200ºC; the obtained conductivity values for the prototypes are shown in Table 8.4.

Table 8.4: Conductivity and skin depth calculation for the used materials

Material	Conductivity [S/m]$(\Omega m)^{-1}$	Skin depth at 13.56MHz [µm]
Pure silver	$63.01 \cdot 10^6$	17.2
Silver ink	$8 \cdot 10^6$	48.3
Copper	$59.6 \cdot 10^6$	17.7

It can be seen that, as the conductivity is lower, the input resistance of the inkjet printed prototypes is higher. In constrast to subtractive etching technique, inkjet printing technology allows accurate adjustment of the electrical properties of the antenna, and therefore offers the opportunity to fulfill different requirements keeping the same geometry. The obtained internal resistance can be modified with the sintering process as it has been shown in previous chapters.

On the other hand, the thickness of the different prototypes are different and this parameter affects directly to the input resistance. Inkjet printing technology allows varying the thickness of the printed layers with approximately 1µm resolution. As the obtained thickness is below the skin depth, a change on the track thickness directly affects both the input impedance and the quality factor. For thicknesses far deeper than skin depth, input resistance and Q factor are no longer adjustable by this degree of freedom (Figure 8.2).

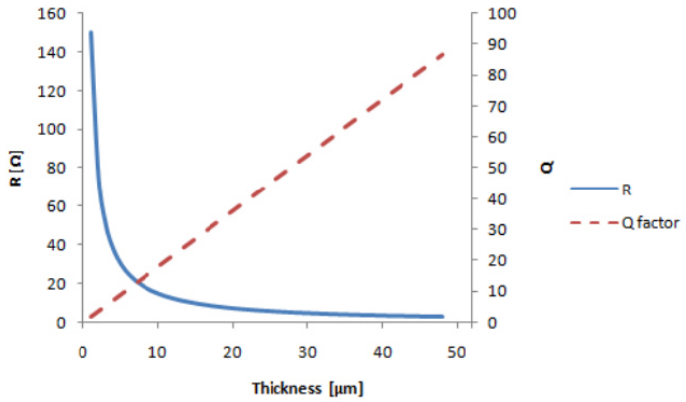

Figure 8.2: Calculation of R and Q for different thickness

A Q value up to 90 can be theoretically achieved by this technology as long as the thickness is kept below the skin depth of the silver ink at 13,56MHz, which is 47µm (Table 8.4). Nevertheless, in practice, it is not feasible to fabricate printed coil antennas with such a high thicknesses due to the ink spilling over the track when too many layers are mounted on it.

Typical coil antenna manufactured by inkjet printing technology exhibits small Q factors of around 4-10 [111][114], keeping the same inductance value. The fabricated printed prototypes are made with 4-6-10 layers whose thicknesses are 3.5-4.8-8 µm respectively[1]. This last prototype (10 layers) is a reasonable tradeoff between delivered performance in terms of Q values and complexity of the manufacturing process due to the number of layers.

The Q factor required for the antenna is directly related to the read range to be achieved by the technology. For example, in a typical RFID system for a distance of 38cm, Q factors close to 40 are required [115]. Depending on the application, the required Q is different. For example, NFC allows for shorter distances than other standards and consequently restrictions on tag Q factors are relaxed to get the same voltage to energize the RFID tag integrated circuit. Thus, the obtained Q values for inket printed coil is good enough and inkjet

[1] Considering 0.8µm of thickness per layer (data obtained from analysis in section 7.1.2)

printing technology is therefore a promising technique for the fabrication of NFC coil antennas. Moreover, due to both its low cost manufacturing process and substrate flexibility, it is a perfect candidate for the implementation of environmentally friendly NFC terminals into flexible substrates or implanted applications. However, the lower quality factor and high input impedance affect other parameters, such as bifurcation free region, needed compensation on primary to achieve same resonance frequency as in secondary... Consequently, as mentioned in the beginning of this chapter, the effect of inkjet printed prototypes in the design of near field systems is analyzed in section 8.4

8.2 Topology analysis

In this section, an analysis of the different topologies is made in terms of bifurcation phenomena and needed compensation on primary circuit (to resonate at same frequency as secondary circuit) to examine the advantages and disadvantages of each of them.

First, the effect of the secondary resonant circuit on primary circuit is analyzed.

In section 6.1.1.2, the methodology that has been used for the analysis of the topologies has been explained.

Most of the systems use Series-Parallel topology, therefore it has been decided to show the full methodology (analytical calculation, circuital simulation, 3D simulation and measurements) for this case. For the rest of cases only the final results and conclusions are shown.

8.2.1 Effects of secondary resonant circuit on primary

In this section the effect of secondary resonant circuit on primary is studied.

8.2.1.1 Non resonance – Series

The non resonance – series circuit that is analyzed and its corresponding phasor model is shown in Figure 8.3.

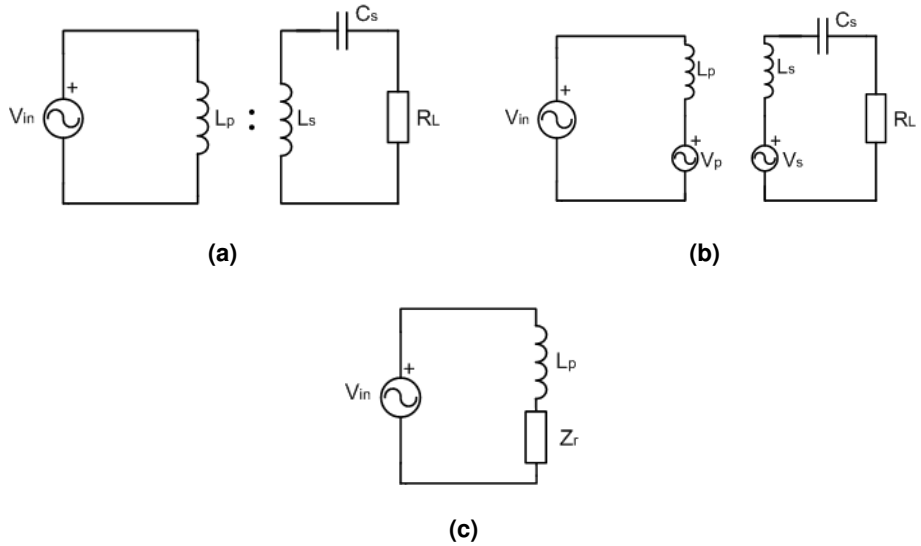

Figure 8.3: (a) Non resonance-Series circuit; (b) Equivalent coupling circuit; (c) Primary circuit with reflected impedance

Following the same procedure that has been described in section 6.1.1, the equivalent impedance of the secondary circuit (Z_s) seen by the induced voltage (V_s) and the reflected impedance (Z_r) can be deduced as:

$$Z_s = j\omega L_s + \frac{1}{j\omega C_s} + R_L \qquad \textbf{8.1}$$

$$Z_r = \frac{M^2\omega^2}{Z_s} = \frac{M^2\omega^2}{j\omega L_s + \frac{1}{j\omega C_s} + R_L} \qquad \textbf{8.2}$$

Applying the resonance condition of the secondary circuit $\omega = \omega_0 = 1/\sqrt{L_s C_s}$ and separating the real and imaginary part of Z_r equations 8.3 and 8.4 are obtained:

$$Re\{Z_r\}|_{\omega=\omega_0} = \frac{M^2}{L_s C_s R_L} = \frac{M^2 {\omega_0}^2}{R_L} \qquad \textbf{8.3}$$

$$Im\{Z_r\}|_{\omega=\omega_0} = 0 \qquad \textbf{8.4}$$

As it can be observed in equation 8.3 and 8.4, the reflected impedance is purely resistive at the resonant frequency and the real part of Z_r is neither maximum nor minimum. The real part of the reflected impedance increases with the frequency converging to the asymptotic value of equation 8.5 .

$$\lim_{\omega \to \infty} Re\{Z_r\} = \frac{R_L M^2}{{L_s}^2} \qquad \textbf{8.5}$$

8.2.1.2 Non resonance – Parallel

The non resonance – parallel circuit that is analyzed and its corresponding phasor model is shown in Figure 8.4

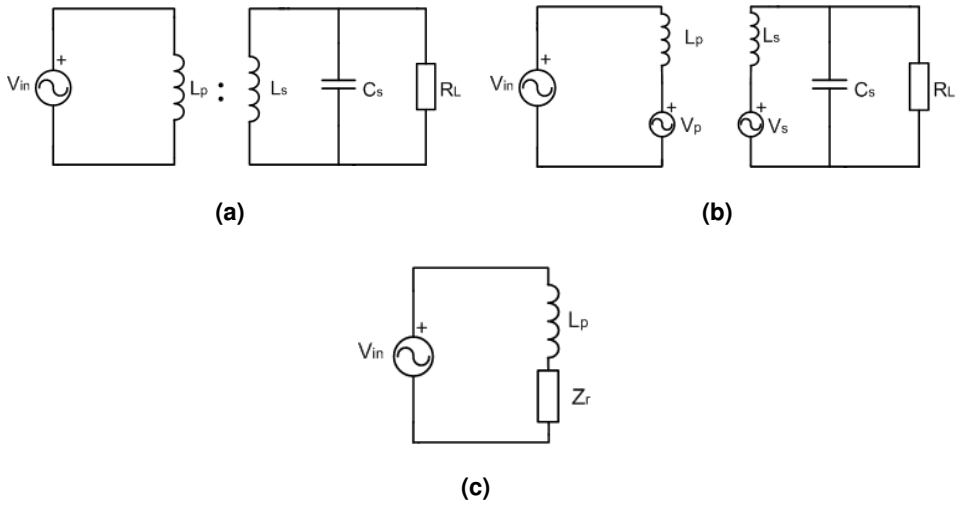

Figure 8.4: (a) Non resonance- Parallel topology; (b) Equivalent coupling circuit; (c) Primary circuit with reflected impedance

Following the same procedure of the previous case, Z_s and Z_r can be deduced as:

$$Z_s = j\omega L_s + \frac{1}{j\omega C_s + \frac{1}{R_L}} \qquad \textbf{8.6}$$

$$Z_r = \frac{M^2\omega^2}{Z_s} = \frac{M^2\omega^2}{j\omega L_s + \dfrac{1}{j\omega C_s + \dfrac{1}{R_L}}} \quad \textbf{8.7}$$

Applying the resonance condition and separating the real and imaginary part of Z_r , the equations 8.8 and 8.9 are obtained:

$$Re\{Z_r\}|_{\omega=\omega_0} = \frac{M^2}{L_s C_s R_L} = \frac{R_L M^2}{{L_s}^2} \quad \textbf{8.8}$$

$$Im\{Z_r\}|_{\omega=\omega_0} = -\frac{\omega_0 M^2}{L_s} \quad \textbf{8.9}$$

Contrary to the series case, the reflected impedance at the resonance frequency is complex and consequently the primary must be compensated. Calculating the derivative with respect to the frequency, it is checked that the real part of Z_r is a maximum.

Moreover, the imaginary part is frequency dependent, so this compensation must be different for each coupling. The imaginary part of reflected impedance does not converge (equation 8.10).

$$\lim_{\omega\to\infty} Im\{Z_r\} = -\infty \quad \textbf{8.10}$$

Several conclusions can be obtained about the way secondary resonance affects the primary behavior based on the analysis made in sections 8.2.1.1 and 8.2.1.2. The main differences of the two compensations can be analyzed by looking at the corresponding reflected impedance.

In series compensation, the obtained Z_r is purely real and its value is not a maximum or minimum, whereas in parallel compensation, $Re\{Z_r\}$ is maximum and at resonance Z_r is complex. Thus, a compensation is recommended in the primary to compensate the generated reactive power. This is one of the most important differences between series and parallel compensated secondary circuits.

With this analysis it is interesting to find if there is any boundary frequency where one of the compensations gives a higher reflected impedance value at the desired resonant frequency. As it will be mentioned when the efficiency analysis is studied in section 8.3, the behavior of Z_r plays a crucial role in the efficiency of the total system.

With series compensation, the resistance is at its maximum depending on the working frequency. However, in the parallel case, the system is always working at its maximum resistance. The boundary frequency can be obtained by comparing equations 8.3 and 8.8:

$$f_c = \frac{\omega_c}{2\pi} = \frac{R_L}{2\pi L_s} \qquad \textbf{8.11}$$

- For $f_0 < f_c$, maximum value of $Re\{Z_r\}$ is achieved with parallel compensation.

- For $f_0 > f_c$, maximum value of $Re\{Z_r\}$ is achieved with series compensation.

In Figure 8.5, 8.6 and 8.7 an illustrative example for different cases is shown. The system resonant circuit is fixed to 13,56MHz and the real part of Z_r is shown for both compensations. In Table 8.5, the main parameters of the circuit under study are summarized:

Table 8.5: Parameters of the circuit under study

Parameter	*Value*
C_s	*49.2 pF*
L_s	*2.8 µH*
L_p	*2.8 µH*
k	*0.1*
f_0	*13.56 MHz*

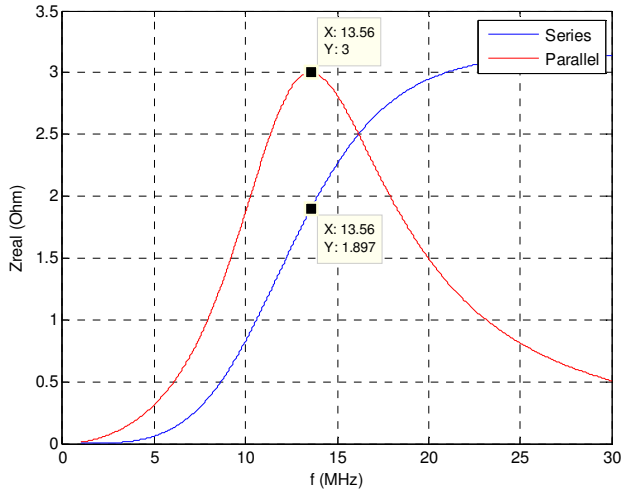

Figure 8.5: Frequency vs. $Re\{Z_r\}$ for a system with $f_c = 17.05MHz$. ($R_L = 300\Omega$)

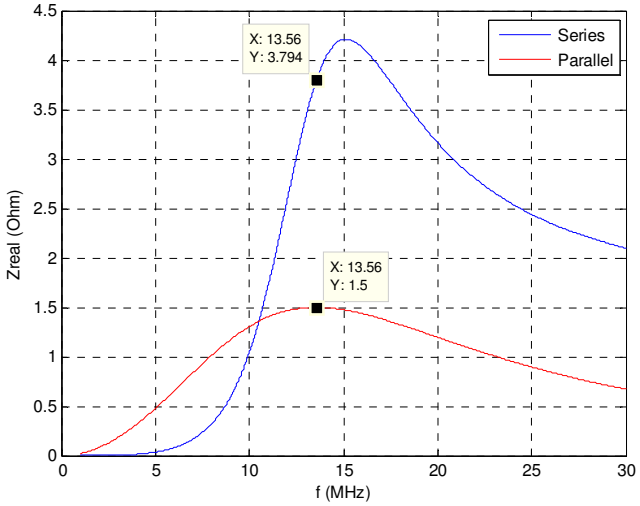

Figure 8.6: Frequency vs. $Re\{Z_r\}$ for a system with $f_c = 8,52MHz$. ($R_L = 150\Omega$)

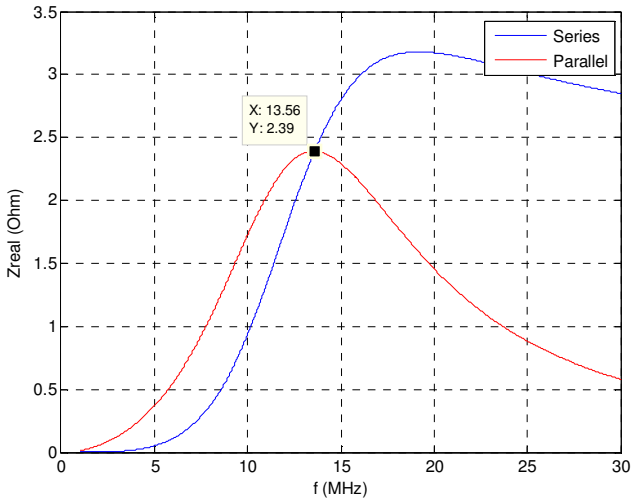

Figure 8.7: Frequency vs. $Re\{Z_r\}$ for a system with $f_c = 13,56MHz$. ($R_L = 240\Omega$)

In Figure 8.5, f_0 is under the boundary frequency (f_c). Therefore, the maximum value of $Re\{Z_r\}$ is achieved by parallel compensation. In the contrary, in Figure 8.6, f_0 is above f_c, consequently the maximum value is achieved in series compensation case. Finally when the resonant frequency and boundary frequency are equal, the same $Re\{Z_r\}$ is obtained for both compensations (Figure 8.7).

8.2.2 SP topology (Methodology validation)

The circuit that is analyzed is shown in Figure 8.8.

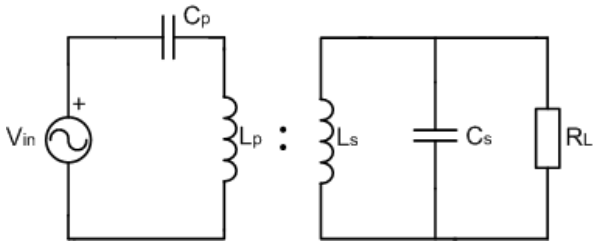

Figure 8.8: Series-Parallel topology

8.2.2.1 Analytical approach

Applying the phasor model, the obtained equivalent circuit model for the primary is shown in Figure 8.9:

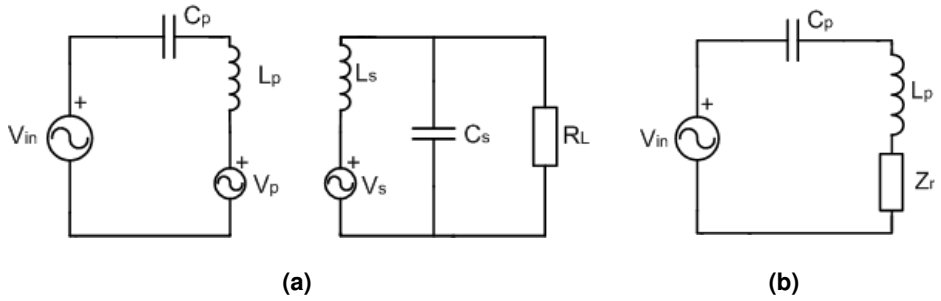

Figure 8.9: Equivalent circuit of SP topology: (a) Equivalent coupling circuit. (b) Primary circuit with reflected impedance

Following the same procedure that has been described in section 6.1.1, the equivalent impedance of the secondary circuit (Z_s) seen by the induced voltage (V_s), the reflected impedance (Z_r) and the equivalent impedance of the primary circuit (Z_p) seen by input source V_{in}can be deduced.

$$Z_s = j\omega L_s + \frac{1}{j\omega C_s + \frac{1}{R_L}} \quad \textbf{8.12}$$

$$Z_r = \frac{M^2\omega^2}{Z_s} = \frac{M^2\omega^2}{j\omega L_s + \frac{1}{j\omega C_s + \frac{1}{R_L}}} \quad \textbf{8.13}$$

$$Z_p = \frac{M^2\omega^2}{j\omega L_s + \frac{1}{j\omega C_s + \frac{1}{R_L}}} + j\omega L_p + \frac{1}{j\omega C_p} \quad \textbf{8.14}$$

By separating the real and imaginary parts of Z_p equation 8.15 is obtained.

$$Z_p = \frac{\omega^2 M^2 R_L}{{R_L}^2(\omega^2 C_s L_s - 1)^2 + \omega^2 L_s^2} + j\left(\omega L_p - \frac{1}{\omega C_p} - \frac{\omega^3 M^2 (C_s^2 {R_L}^2 \omega^2 L_s - C_s {R_L}^2 + L_s)}{{R_L}^2(\omega^2 C_s L_s - 1)^2 + \omega^2 L_s^2}\right) \quad \textbf{8.15}$$

At resonance frequency Z_r and Z_p are:

$$Re\{Z_r\}|_{\omega=\omega_0} = \frac{M^2 R_L}{{L_s}^2} \quad \textbf{8.16}$$

$$Im\{Z_r\}|_{\omega=\omega_0} = -\frac{M^2 C_s}{(L_s C_s)^{3/2}} \quad \textbf{8.17}$$

$$Re\{Z_p\}\big|_{\omega=\omega_0} = \frac{M^2 R_L}{{L_s}^2} \quad \textbf{8.18}$$

$$Im\{Z_p\}\big|_{\omega=\omega_0} = -\frac{\sqrt{L_s C_s}}{C_p} + \frac{L_p}{\sqrt{L_s C_s}} - \frac{M^2 C_s}{(L_s C_s)^{3/2}} \quad \textbf{8.19}$$

a) Needed compensation in primary circuit

The capacitance necessary for the compensation is calculated as:

$$Im\{Z_p\}\big|_{\omega=\omega_0} = -\frac{\sqrt{L_s C_s}}{C_p} + \frac{L_p}{\sqrt{L_s C_s}} - \frac{M^2 C_s}{(L_s C_s)^{3/2}} = 0 \quad \textbf{8.20}$$

In order to cancel the imaginary part, the following C_P is needed.

$$C_p = \frac{C_s {L_s}^2}{L_p L_s - M^2} = \frac{1}{{\omega_0}^2 \left(L_p - \frac{M^2}{L_s}\right)} \quad \textbf{8.21}$$

According to equation 8.21, the compensating capacitor is independent from R_L and depends on both inductances, the resonant frequency and the mutual inductance, and consequently on the coupling coefficient.

b) Quality factor

The quality factors of the primary and secondary are calculated following the same procedure described in section 6.1.1.2. For the calculation of the primary circuit quality factor (Q_p), in this case, the load has to be replaced by the reflected impedance, the corresponding circuit scheme is shown in Figure 8.9b.

The average loss of the circuit can be expressed as:

$$P_{loss} = \frac{1}{2}|I|^2 Re\{Z_r\} \quad \textbf{8.22}$$

The average magnetic energy stored in the inductor is:

$$W_m = \frac{1}{4}|I|^2 L_p \quad \textbf{8.23}$$

The average electric energy stored in the capacitor C_p is:

$$W_e = \frac{1}{4}|I|^2 \frac{1}{\omega^2 C_p} \quad \textbf{8.24}$$

The resonance occurs when $W_e = W_m$, thus the quality factor can be written as follows:

$$Q_p = \omega_0 \frac{W_m + W_e}{P_{loss}} = \frac{2W_m}{P_{loss}} = \frac{\omega_0 L_p {L_s}^2}{M^2 R_L} \quad \textbf{8.25}$$

The calculation procedure of the secondary circuit quality factor (Q_s) is identical to the previous one and it is identical to the one described in section 6.1.1.2 (equation 8.26).

$$Q_s = \frac{R_L}{\omega_0 L_s} \quad \textbf{8.26}$$

c) Bifurcation phenomena

For a bifurcation free transfer, the condition of $Im\{Z_p\} = 0$ must be satisfied only for $\omega = \omega_0$. Applying the methodology explained in section 6.1.1.2, the condition for bifurcation free system can be obtained.

Applying the normalization process that has been explained in section 6.1.1.2 the following solutions are obtained.

1. Frequency is normalized to ω_0:

$$u = \frac{\omega}{\omega_0} \tag{8.27}$$

2. Imaginary part of Z_p is normalized to the real part of the reflected impedance at resonance and it is denoted as Z_n:

$$\begin{aligned} Im\{Z_n\} &= \frac{Im\{Z_p\}}{Re\{Z_r\}|_{\omega=\omega_0}} = \\ &= -\frac{1}{\omega C_p\left(Re\{Z_r\}|_{\omega=\omega_0}\right)} + \frac{\omega L_p}{Re\{Z_r\}|_{\omega=\omega_0}} + \frac{Im\{Z_r\}}{Re\{Z_r\}|_{\omega=\omega_0}} \\ &= -\frac{L_s^2}{\omega C_p M^2 R} + \frac{\omega L_p L_s^2}{M^2 R} \\ &- \frac{\omega^3 M^2 (C_s^2 R^2 \omega^2 L_s - C_s R^2 + L_s)}{R^2(\omega^2 C_s L_s - 1)^2 + \omega^2 L_s^2} \cdot \frac{L_s^2}{M^2 R} = \\ &= -\frac{Q_p - \frac{1}{Q_s}}{u} + uQ_p - \frac{u^3\left[Q_s(u^2-1) + \frac{1}{Q_s}\right]}{(u^2-1)^2 Q_s^2 + u^2} \end{aligned} \tag{8.28}$$

Note that, C_p also contains the necessary value to compensate the imaginary part of the reflected impedance (equation 8.21).

The denominator has five different solutions:

$$u_1 = 0 \tag{8.29}$$

$$u_2 = \frac{1}{2} \cdot \frac{\sqrt{2} \cdot \sqrt{2Q_s^2 - 1 + \sqrt{-4Q_s^2 + 1}}}{Q_s} \tag{8.30}$$

$$u_3 = -\frac{1}{2} \cdot \frac{\sqrt{2} \cdot \sqrt{2Q_s^2 - 1 + \sqrt{-4Q_s^2 + 1}}}{Q_s} \tag{8.31}$$

$$u_4 = \frac{1}{2} \cdot \frac{\sqrt{4Q_s^2 - 2 + 2\sqrt{-4Q_s^2 + 1}}}{Q_s} \tag{8.32}$$

$$u_5 = -\frac{1}{2} \cdot \frac{\sqrt{4Q_s^2 - 2 + 2.\sqrt{-4Q_s^2 + 1}}}{Q_s} \quad \textbf{8.33}$$

All the roots except the first one are imaginary numbers for $Q_s > 0$, and $u = 0$ belongs to the $\omega = 0$ condition as $u = \frac{\omega}{\omega_0}$ which happens with DC current. In the case of power transfer via inductive coupling, the denominator of the equation 8.28 is not nullified by any values of u.

Consequently, only numerator can nullify the equation 8.28 and $u = 1$ must be the only real root. For this, the equation 8.34 must be satisfied:

$$Q_p > Q_s + \frac{1}{Q_s} \quad \textbf{8.34}$$

8.2.2.2 Circuital simulation

The objective of this section is to check if the analytical approach and the phasor model work as expected. For this purpose as explained in section 6.1.2, CST Design Studio module is used. In Figure 8.10, the SP circuit scheme and the corresponding phasor model that are simulated are shown.

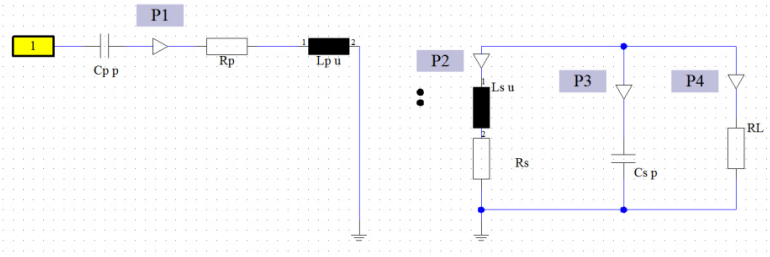

(a)

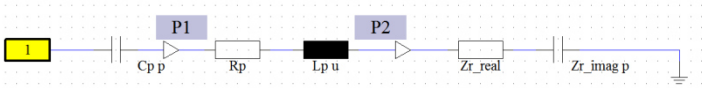

(b)

Figure 8.10: Design Studio (CST) model for series-parallel topology: (a) Real model; (b) Phasor model

In Table 8.6, the corresponding values for both models are summarized:

Table 8.6: Parameters used in the simulation

Name	*Description*	*Value*
R_p	*Internal resistance of* L_p	*0 Ω*
C_p	*Capacitance in primary*	*49.2 pF*
L_p	*Inductance in primary*	*2.8 µH*
R_L	*Load*	*1000*
C_s	*Capacitance in secondary*	*49.2 pF*
L_s	*Inductance in secondary*	*2.8 µH*
R_s	*Internal resistance of* L_s	*0 Ω*
$Re\{Z_r\}$	*Real part of reflected impedance*	*9.99 Ω*
$Im\{Z_r\}$	*Imaginary part of the reflected impedance*	*4920pF*
k	*Coupling coefficient*	*0.1*

The real model and phasor model are only checked at the resonant frequency. The value inserted on the mathematical model is the one obtained from the analytical approach.

Both system's input source is a 50 Ω power source. Observing the S_{11} scattering parameter, the validity of the model must be confirmed (Figure 8.11).

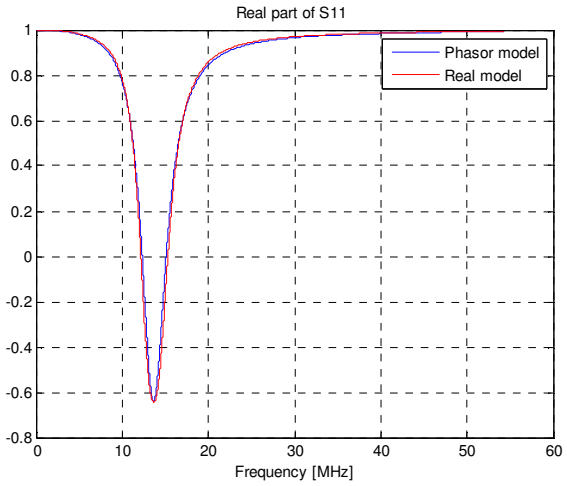

(a)

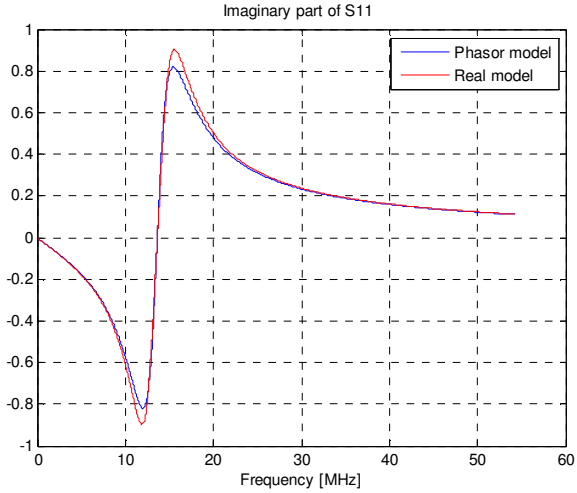

(b)

Figure 8.11: S_{11} parameter: (a) Real part; (b) Imaginary part

As shown in Figure 8.11, for the resonant frequency (13.56 MHz) a complete match of both circuits is achieved.

Once the phasor model has been checked, the analytical expression for the needed compensation at primary circuit (equation 8.21) is checked with Design Studio. The compensation capacitance for the circuit under study can be calculated using the equation 8.21, the obtained C_p is 49,7pF. In Figure 8.12, the obtained simulation with and without compensation using the circuit of Figure 8.10a is shown.

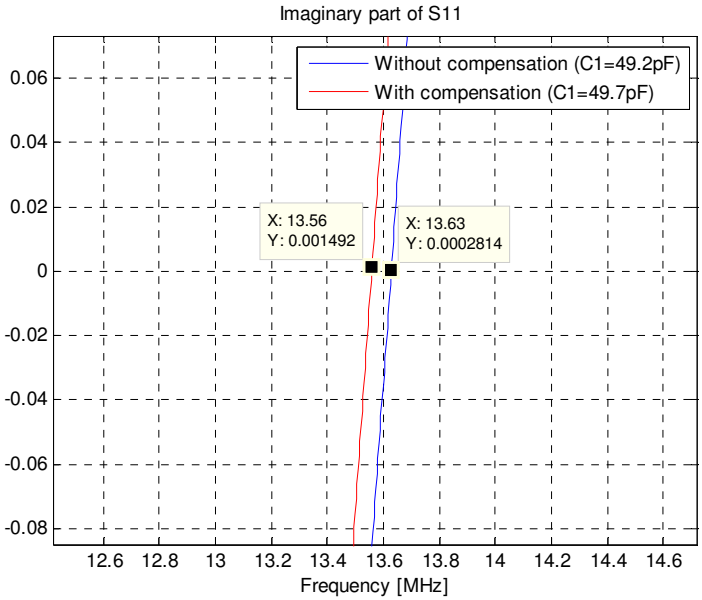

Figure 8.12: Comparison of the imaginary part of S11 with compensated and non compensated primary

As shown in Figure 8.12, there is a shift of the resonant frequency when the system is not compensated. In this case, as the coupling coefficient is 0.1, the change in the resonant frequency and the necessary compensating capacitor is very similar to the original one. However, this compensating capacitor depends on the coupling coefficient, in Figure 8.13 same case is shown for k=0,2, in that case C_p is 51,25pF.

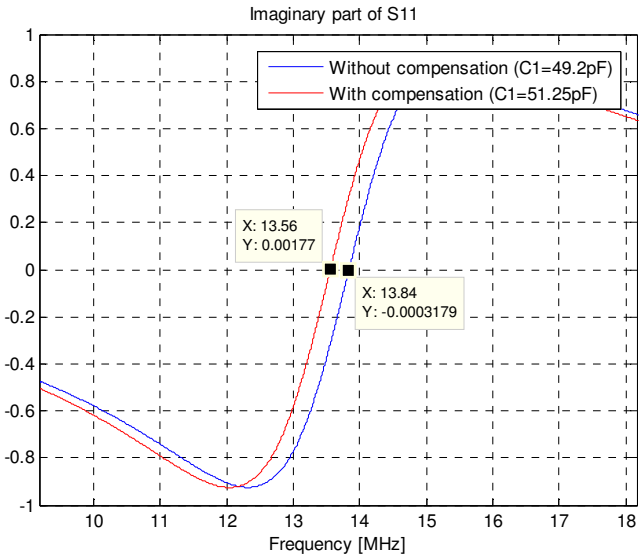

Figure 8.13: Comparison of the imaginary part of S11 with compensated and non compensated primary (k=0,2)

8.2.2.3 3D simulation

As explained in section 6.1.2.2, CST MICROWAVE STUDIO has been used with the frequency solver and tetrahedral mesh with Resonant Fast S-parameter method.

The results of the different implemented coils (Table 8.2) have been presented in section 8.1. This is the starting point of the 3D simulation, to check if the obtained input impedance, and consequently the input resistance and inductance value are in concordance with the one that has been calculated analytically.

In Table 8.3 the comparison between the analytical, simulated and measured coils has been shown. However, some guidelines related to the coils characterization in CST MWS are summarized:

- An adaptive mesh refinement is must be done to obtain reliable results.

- Silver ink must be defined as *normal material* and not as *lossy metal* material. Conductors such as, copper, gold… are usually modeled by using *loss metal* material type. This material type simulates the penetration of electromagnetic fields inside a very good but not perfect electrically conductor by the use of an internal one-dimensional surface impedance model. This offers the possibility to take the so-called skin effect into account without refining the mesh for these materials. However, this model has some limitations; it is not valid when the thickness of the considered geometry is below the skin depth, which is the case when inkjet printing technology is used, consequently silver ink must be considered as a *normal material*.
- The properties of the materials defined in the simulation are summarized in Table 8.7:

Table 8.7: Main parameters of the material used in CST 3D simulation

Name	*Type*	*Main parameters*
Copper (annealed)	*Lossy metal*	$\sigma = 5.8 \cdot 10^7 S/m$
Silver ink	*Normal (user defined)*	$\sigma = 8 \cdot 10^6 S/m$
FR-4 (lossy)	*Normal*	$\varepsilon_r = 4.3$ $tg\partial = 0.025\ (constant\ fit)$
Polyimide lossy	*Normal*	$\varepsilon_r = 3.5$ $tg\partial = 0.0027\ (constant\ fit)$

Once the coil is characterized, the 3D model of the antenna is substituted in the corresponding circuital model of Design Studio (Figure 8.14).

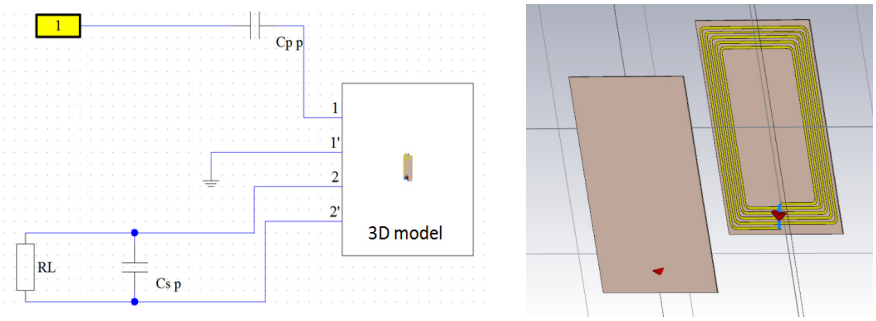

(a) (b)

Figure 8.14: (a) Representation of the SP topology scheme combining Design Studio and 3D model from CST MWS. (b) 3D model from CST MWS

This model is compared with the measurements that are presented in section 8.2.2.4 .

8.2.2.4 Measurements

In this section the measurements obtained with the procedure and set up explained in section 6.1.3 are compared with the results obtained with the simulator.

All the prototypes presented in Table 8.2, have been characterized with analytical formulas, simulation and measurements as shown in Table 8.3.

In this section, using the set up of Figure 6.8 the Prototype 1 (described in Table 8.2) made of FR-4 and copper is used for measuring two coils in SP topology configuration to compare with the results obtained by simulation.

This comparison can be done with inkjet prototypes, but due to the difficulty of soldering the connections when inkjet printed prototypes are used, it has been decided to use the Prototype 1 to validate the simulations with the measurements. However, as the 3D models of the antennas are characterized, the validity of the methodology can be extended for the other prototypes.

In Table 8.8, the value of the circuit elements that are studied are summarized.

Table 8.8: Real circuit components values used in SP topology

Name	*Value*
R_L	*1000Ω*
C_p	*47 pF*
C_s	*47 pF*

It can be seen that the main difference with respect to the previous circuit is that for lumped elements values a capacitor of 47 pF is used instead of 49,2 pF because the capacitor 47 pF is available in the market allowing the use of single capacitor instead of adding two or more capacitors in parallel.

The measurements are taken from 5mm to 50mm every 5mm. For bigger distances, the coupling is really small, therefore, the antennas are completely decoupled. For practical reasons, the results for only certain distances are shown Figure 8.15:

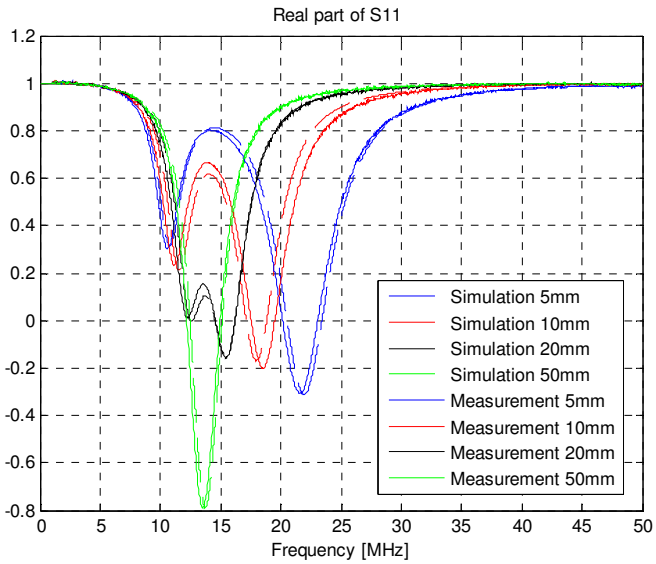

(a)

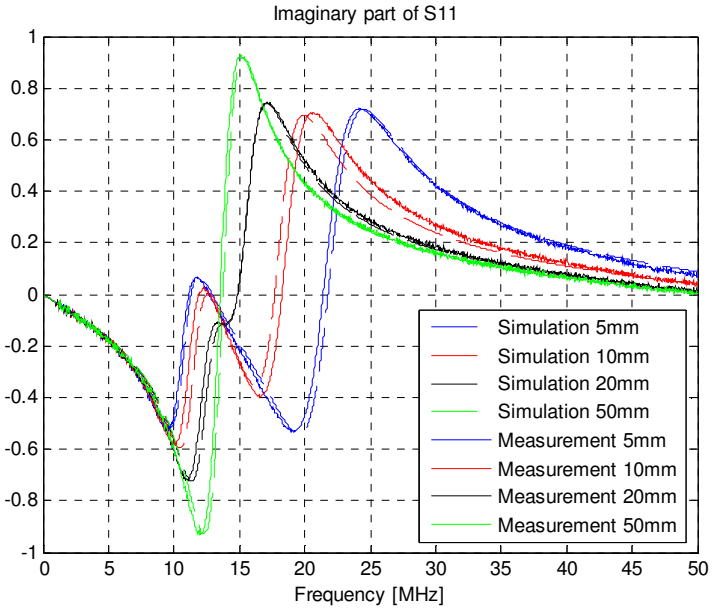

(b)

Figure 8.15: Comparison of the simulated and measured of S11 for different distances: (a) Real Part of S11; (b) Imaginary part of S11

As shown in Figure 8.15, the measurements and simulations are very similar. For 5 and 10 mm there is bifurcation phenomena, and for bigger distance the system is in stable zone (bifurcation-free zone).

The methodology that has been explained in section 6.1 has been applied to SP topology to check the correlation between the analytical approach, simulation and measurements.

Therefore, it can be stated that the explained methodology is a verified, reliable and exact method for studying systems based in inductive coupling and resonant systems.

For the rest of the topologies only the final results are shown, the full development is analogous to this case.

8.2.3 Final results of all topologies

8.2.3.1 Compensation

The required primary compensation capacitance (C_p) for the four topologies is shown in the following equations:

- SS topology:

$$C_p = \frac{1}{{\omega_0}^2 L_p} \tag{8.35}$$

- SP topology:

$$C_p = \frac{1}{{\omega_0}^2 \left(L_p - \frac{M^2}{L_s}\right)} \tag{8.36}$$

- PS topology:

$$C_p = \frac{{C_s}^2 {L_s}^2 L_p {R_L}^2}{M^4 + C_s {L_p}^2 L_s {R_L}^2} \tag{8.37}$$

- PP topology:

$$C_p = \frac{\left(L_s L_p - M^2\right) {L_s}^3 C_s}{M^4 C_s {R_L}^2 + {L_p}^2 {L_s}^3 + M^4 L_s - 2 L_p {L_s}^2 M^2} \tag{8.38}$$

On one hand, in all cases, except SS topology, the compensation required at primary depends on the coupling coefficient, consequently a different capacitance is required when any parameter that affects the coupling coefficient is changed, such as, angle between coils, distance, change of the medium…

This property makes SS topology an excellent candidate for applications in which the coupling coefficient is not fix, such as implanted applications. As mentioned before, in implanted applications due to the change of media, the difficulty of having a constant distance or exactly the same angle between the implanted and the external coil, the coupling coefficient of the system is variable. Consequently, the SS topology has a clearly advance in this aspect.

On the other hand, when the primary side is in series (SS and SP topologies), C_p is independent from the load.

8.2.3.2 Quality factor

The expressions obtained for the quality factor are different depending on the secondary compensations.

When secondary compensation is in series $\mathrm{Q_p}$ and $\mathrm{Q_s}$ are expressed as:

$$Q_p = \frac{L_p R_L}{\omega_0 M^2} \quad \textbf{8.39}$$

$$Q_s = \frac{\omega_0 L_s}{R_L} \quad \textbf{8.40}$$

When secondary compensation is in parallel $\mathrm{Q_p}$ and $\mathrm{Q_s}$ are expressed as:

$$Q_p = \frac{\omega_0 L_p {L_s}^2}{M^2 R_L} \quad \textbf{8.41}$$

$$Q_s = \frac{R_L}{\omega_0 L_s} \quad \textbf{8.42}$$

As it can be observed in equations 8.39 and 8.41 both primary quality factors are proportional to $1/M^2$ and as it is discussed in section 8.2.3.3, this plays an important role in the stability of the system.

The effect of the load resistance in $\mathrm{Q_p}$ and $\mathrm{Q_s}$ is different depending on the compensations that is used. The obtained results are in concordance with the values founded in [55].

8.2.3.3 Bifurcation phenomena

In this section the stability analysis of the system is carried out. In the next equations the four basic topologies are summarized.

- SS topology:

$$Q_p > \frac{4{Q_s}^3}{4{Q_s}^2 - 1} \quad \textbf{8.43}$$

- SP/PP topology:

$$Q_p > Q_s + \frac{1}{Q_s} \quad \textbf{8.44}$$

- PS topology:

$$Q_p > Q_s \quad \textbf{8.45}$$

The obtained results are in concordance with [55]. The full procedure to obtain these conditions for SS, PS and PP topologies is addressed in Appendix B (the procedure of SP topology can be found in section 8.2.2.1).

Same condition is obtained for SP and PP topologies. All the conditions are slightly different but if $Q_s \gg 1$, for all topologies the condition that can be considered is the following one:

$$Q_p > Q_s \quad \textbf{8.46}$$

In all cases, stability problems can occur by increasing the coupling coefficient since in all topologies Q_p is proportional to $1/M^2$ and consequently when the coupling coefficient increases, Q_p decreases and the stability zone decreases.

At this point it should be pointed out that Q_p and Q_s are referred to the quality factor of the primary and secondary circuit and not to the quality factor of the primary and secondary coil.

In Figure 8.16, a comparison between the different topologies is made to show the advantages and disadvantages with respect to bifurcation phenomena.

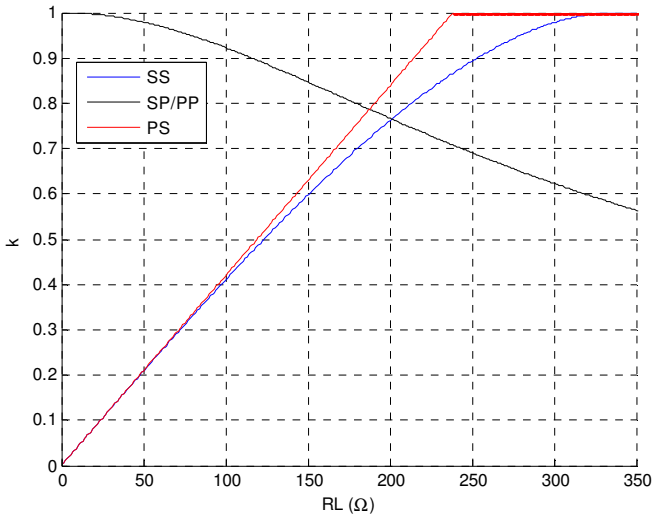

Figure 8.16: Behaviour of the limit coupling factor for bifurcation free system with R_L

According to Figure 8.16, parallel compensated secondary topologies offer a great advantage to have stable systems with small loads. On the contrary, series compensated secondary circuits are very stable for higher loads.

8.3 Efficiency analysis

One of the crucial parameters that quantifies an inductive power link is its power transfer efficiency [65]. The difference and the concepts of Maximum Power Transfer and Maximum Power Transfer Efficiency have been explained in section 0.

In this case the study is focused on systems not purely resistive, so the impedance with imaginary part must be taken into account. Furthermore, it is also stated in [116] that, the source of the main loss in a inductively coupled circuit may be the internal resistance of the coupled coils, thus the internal resistance of the coils must be also taken into account.

The primary compensation does not affect to the final efficiency of the system, consequently it can be stated that non-resonance series, SS and PS topologies have the same efficiency and non-resonance parallel, SP and PP topologies have also the same one [65] [117]. In this section the analysis is made using SS and SP topologies.

8.3.1 Efficiency in SS topology

The circuit that is studied is shown in Figure 8.17.

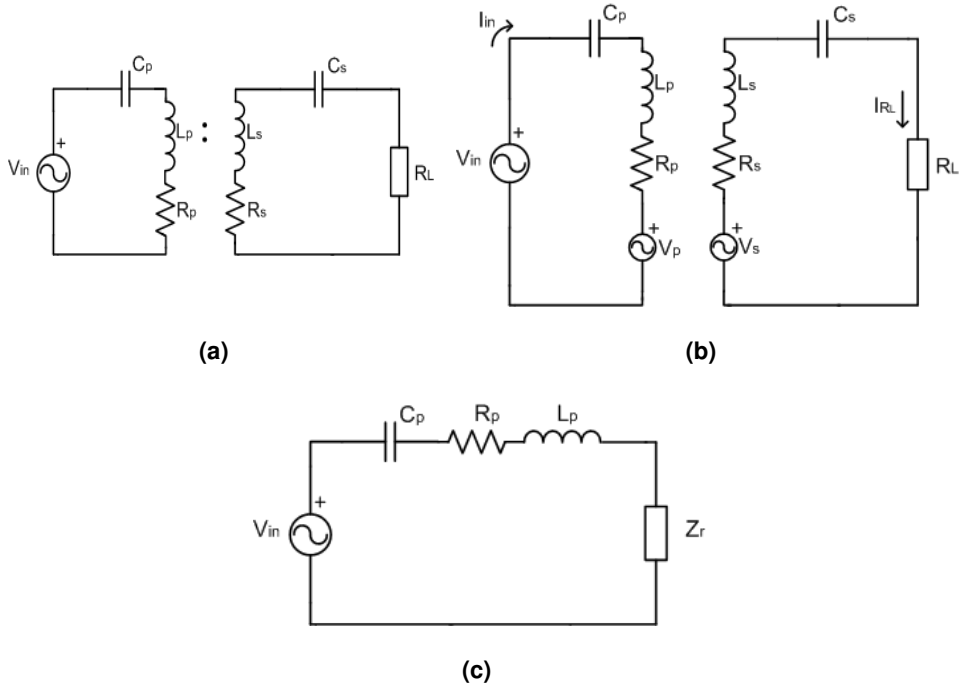

Figure 8.17: (a) SS topology circuit scheme. (b) Equivalent coupling circuit. (c) Primary circuit with reflected impedance

The efficiency calculation is made in two steps. First, the efficiency of primary circuit (η_p) is calculated as the ratio of active power delivered to the reflected impedance (Z_r) and active power delivered from the source (equation 8.47).

$$\eta_p = \frac{Re\{V_{Z_r} I_{Z_r}^*\}}{Re\{V_{in} I_{in}^*\}} \quad \textbf{8.47}$$

where

$$V_{Z_r} = \frac{Z_r}{j\omega L_p + \frac{1}{j\omega C_p} + R_p + Z_r} V_{in} \quad \textbf{8.48}$$

$$I_{Z_r} = I_{in} = \frac{V_{in}}{j\omega L_p + \frac{1}{j\omega C_p} + R_p + Z_r} \quad \textbf{8.49}$$

Secondly, the efficiency from the induced voltage ($V_s = j\omega M i_p$) to the load in the secondary circuit is calculated:

$$\eta_s = \frac{Re\{V_{R_L} I_{R_L}^*\}}{Re\{V_s I_{V_s}^*\}} \quad \textbf{8.50}$$

where

$$V_{R_L} = \frac{V_s}{R_s + j\omega L_s + \frac{1}{j\omega C_s} + R_L} R_L \quad \textbf{8.51}$$

$$I_{R_L} = I_{V_s} = \frac{V_s}{R_s + j\omega L_s + \frac{1}{j\omega C_s} + R_L} \quad \textbf{8.52}$$

Finally, the total efficiency of the system is obtained by the product between equations 8.47 and 8.50.

$$\eta = \eta_p \eta_s \quad \textbf{8.53}$$

By combining equations 8.48, 8.49, 8.51 and 8.52 into equation 8.53 the total efficiency for SS topology can be expressed as:

$$\eta^{SS} = \left(1 + \frac{R_s}{R_L} + \frac{R_p}{k^2 L_p R_L}\left(L_s + \frac{1}{\omega^2}\left(\frac{(R_L + R_s)^2}{L_s} - \frac{2}{C_s}\right) + \frac{1}{\omega^4 L_s {C_s}^2}\right)\right)^{-1} \quad \textbf{8.54}$$

8.3.2 Efficiency in SP topology

The circuit that is analyzed is shown in Figure 8.18.

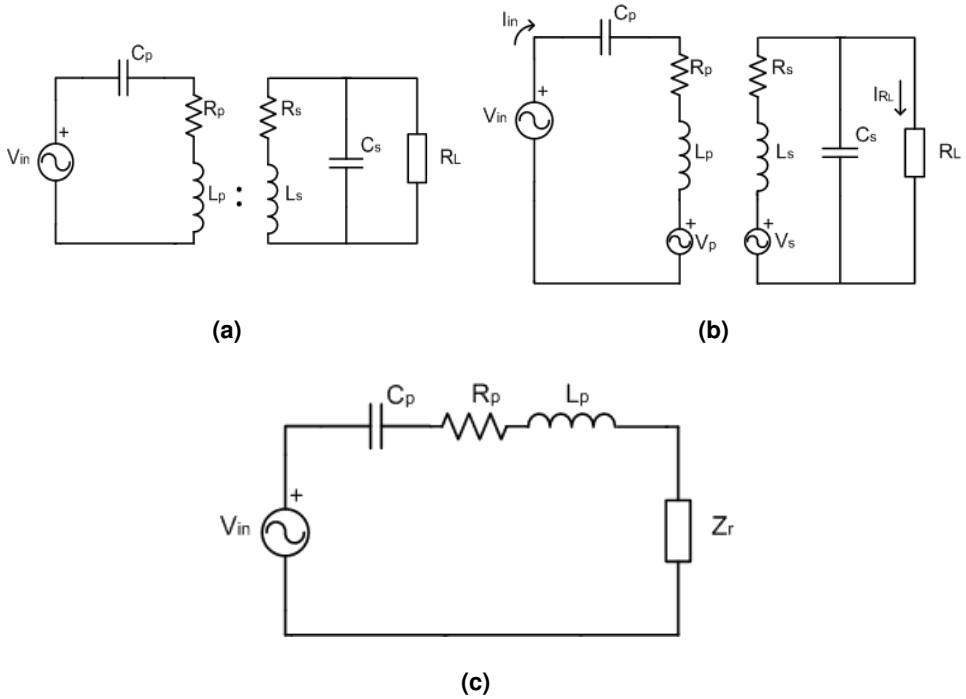

Figure 8.18: (a) SP topology circuit scheme ((b) Equivalent coupling circuit. (c) Primary circuit with reflected impedance

The same expression 8.50 is obtained for η_p with parallel compensation.

The expressions to calculate η_s are different to the series case. The voltage in the load is calculated as:

$$V_{R_L} = \frac{Z_s V_s}{Z_s + jL_s\omega + R_s} \qquad \textbf{8.55}$$

where Z_s is the resulting impedance of C_s in parallel with R_L and V_s represents the induced voltage from the primary to the secondary.

In contrast with series compensated secondary case, the current across the load and induced source (V_s), is not the same:

$$I_{R_L} = \frac{V_{R_L}}{R_L} \quad \textbf{8.56}$$

$$I_{V_s} = \frac{V_s}{R_s + jL_p\omega + Z_{eq}} \quad \textbf{8.57}$$

According to equations 8.47, 8.50 and 8.53, the total efficiency for SP topology (η^{SP}) is expressed as:

$$\eta^{SP} = \left(1 + \frac{R_s}{R_L} + \omega^2 R_L {R_s C_s}^2 + \frac{R_p}{k^2 L_p L_s R_L}\left(\left(\frac{(1-\omega^2 L_s C_s)R_L + R_s}{\omega}\right)^2 + (L_s + R_L C_s R_s)^2\right)\right)^{-1} \quad \textbf{8.58}$$

Based on the analysis in section 8.3.1 and 8.3.2, an analysis of efficiency is made by comparing the series and parallel compensated cases. As it can be observed in equations 8.54 and 8.58, both efficiency expressions depend on several parameters, consequently different studies are made to study the effect of each parameter in the overall efficiency.

Both efficiencies improve when the coupling coefficient is higher as it can be seen in Figure 8.19.

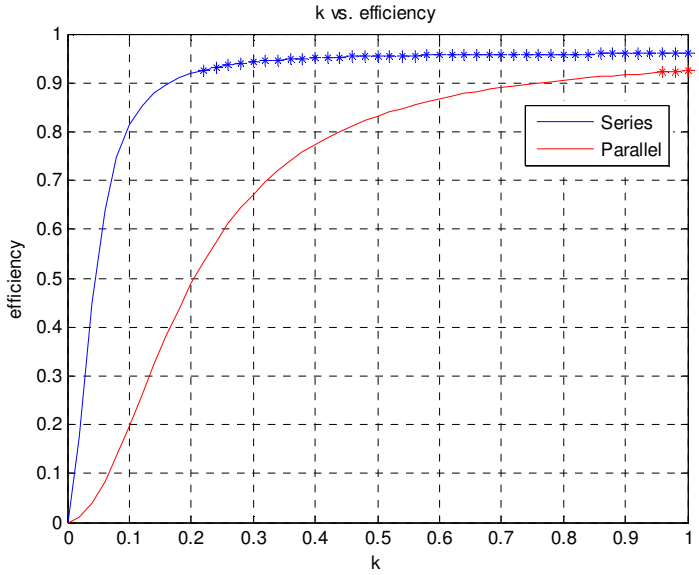

Figure 8.19: Effect of the coupling factor in the efficiency for both compensations. (-) stable (*) unstable

It can be observed that for both compensations, the efficiency improves with higher coupling coefficients. The slope of the curve depends on the internal resistances of the coils and load impedance. Attention must be paid to avoid the bifurcation region, this issue in some cases is an important restriction. In this case, for example, if the proposed system is supposed to be working with $k > 0.21$, the series compensation cannot be used. It should be pointed out that the stability criterion that has been used for series compensation is based on SS topology and parallel compensation on SP topology. Nevertheless, as mentioned in section 8.2.3.3, very similar condition is achieved with SS/PS and the same for SP/PP.

In order to have a criterion to choose one compensation instead of the other for a certain designed system, a boundary frequency can be calculated to choose the best one. On one hand, when parallel compensation is used, the efficiency has a local maximum with respect to frequency, and it is always at the resonant frequency of the system. For higher frequencies the efficiency is lower. On the

other hand, in SS topology, the efficiency is not maximum value at the resonant frequency.

The reasoning followed in section 8.2.1 can be applied to obtain to boundary frequency in which series or parallel compensation is better since the efficiency is maximized when the reflected impedance is also maximized. Consequently, following the same criterion, the equation 8.59 has been deduced:

$$f_c = \frac{R_L}{2\pi L_s}\left(\sqrt{1-\frac{k^2 L_p L_s}{L_s R_p}}\right) \qquad \textbf{8.59}$$

The obtained boundary is similar to the expression obtained in section 8.2.1, in this case a new factor that depends on the internal resistances is obtained.

In Figure 8.20, 8.21 and 8.22, the behavior of a system in which the load impedance has been changed to have different f_c is shown. The circuits that are used for these calculations are the one of Figure 8.17a and 8.18a for series and parallel case respectively and its parameters are shown in Table 8.9.

Table 8.9: Parameters of the circuit under study

Parameter	*Value*
C_s	*49.2 pF*
L_s	*2.8 µH*
R_s	*2Ω*
C_p	*49.2 pF*
L_p	*2.8 µH*
R_p	*2Ω*
k	*0.05*
f_0	*13.56 MHz*

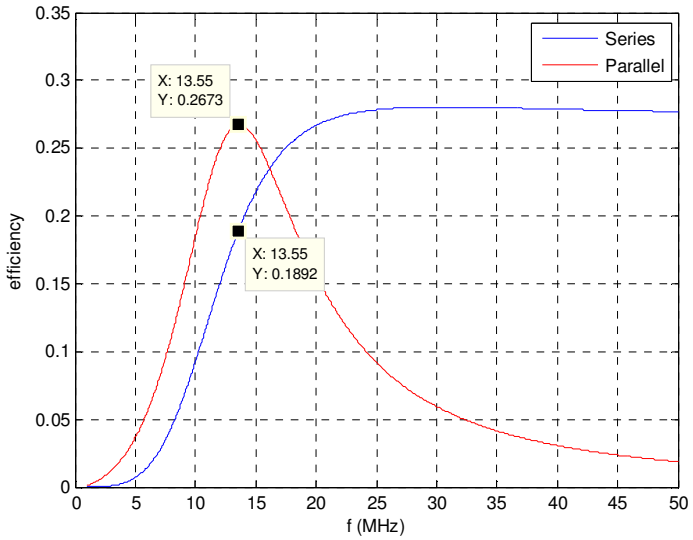

Figure 8.20: Frequency vs. efficiency for a system with $f_c = 17.07MHz$. ($R_L = 300\Omega$)

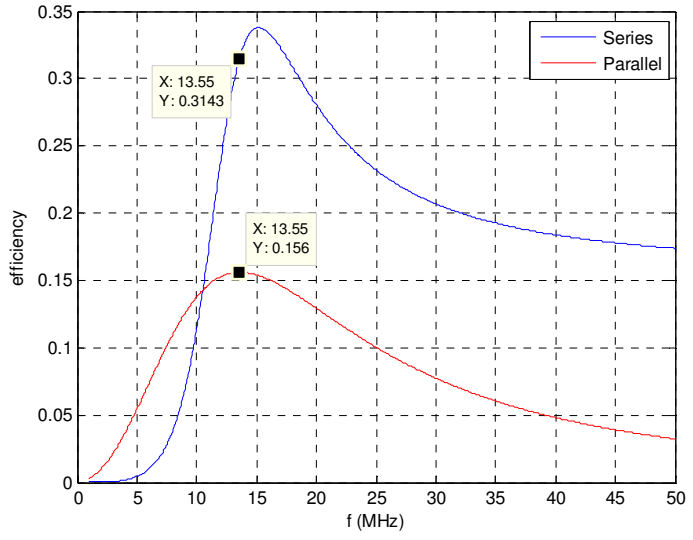

Figure 8.21: Frequency vs. Efficiency for a system with $f_c = 8,53MHz$. ($R_L = 150\Omega$)

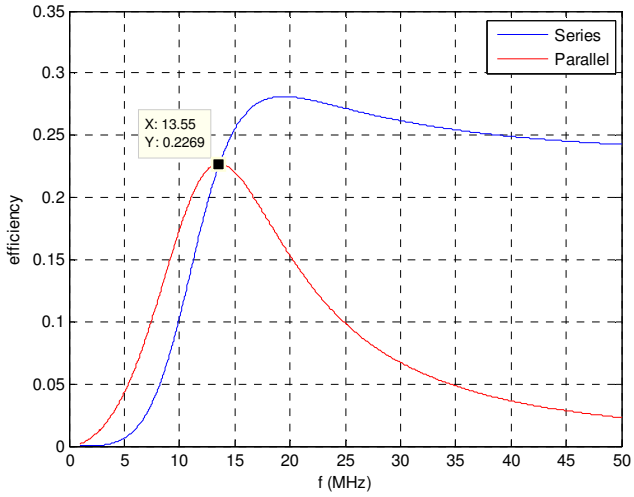

Figure 8.22: Frequency vs. $Re\{Z_r\}$ for a system with $f_c = 13,56MHz$. ($R_L = 240\Omega$)

With these three figures, the obtained expression for the boundary frequency has been checked. The efficiency in parallel compensated secondary systems is always maximum at the resonant frequency. This maximum efficiency is also the maximum obtainable efficiency if $f_0 < f_c$. Otherwise, the maximum efficiency is achieved in series compensation secondary case.

The efficiency also depends on the load impedance. In Figure 8.23, the behavior of the efficiency with respect to the load is clearly demonstrated for a system with the same parameters (Table 8.9).

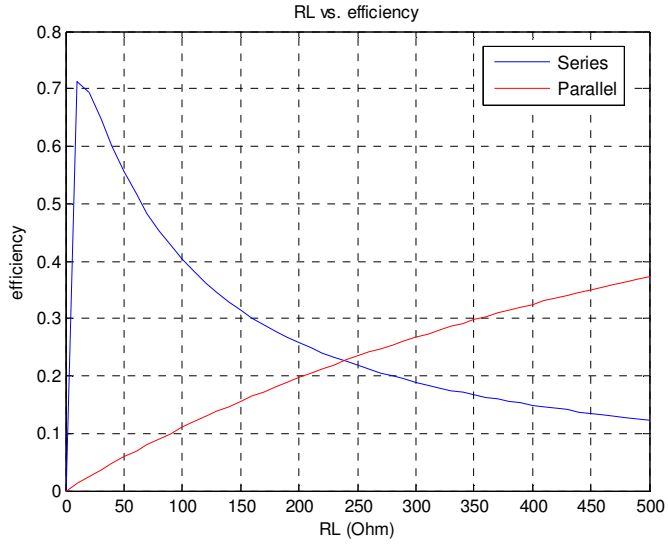

Figure 8.23: Efficiency behaviour with load resistance

As it can be observed in Figure 8.23, series compensation is more efficient for lower loads and higher efficiency is obtained for higher loads when parallel compensation is used.

Finally, as general conclusion it can be said that given a pair of inductors, the most efficient topology can be chosen by calculating the aforementioned boundary frequency (equation 8.59) and checking if the system is in the stable zone, which once the circuit parameters are fixed, it depends on the coupling coefficient of the application.

The series compensation is more efficient for higher frequencies and smaller loads, whereas, when lower frequencies and larger loads are required, parallel compensation secondary systems are preferred.

The main use of low frequency of operation in implants has favoured the SP topology. However, with the recent advancements in the study of biomedical implants, stating that it is safer and more efficient to transfer power at the sub-GHz to the GHz range [63], [118], [119], the SS topology will be an interesting approach. Besides the SS topology has also the advantage of having the

compensation capacitance independent from the coupling coefficient, which for implanted applications is a very interesting feature.

8.4 Inkjet Printing implementation and analysis

In previous sections an analysis in terms of efficiency, needed compensation on primary circuit and stability criteria for the four topologies has been shown. The main difference between etched copper antennas and inkjet printed ones is that the internal resistance in no longer negligible. Consequently, this internal resistance must be taken into account in the analysis of efficiency, compensation, and stability. In this study, the influence of implementing an inkjet printed coil in the secondary side is studied. However, all the expressions are calculated taking both coil's internal resistances.

The reflected impedance (Z_r) expressions taking into account the internal resistances can be expressed as:

- Series compensated secondary (Figure 8.17):

$$Z_r{}^{SS/PS} = \frac{\omega^4 k^2 L_p L_s {C_s}^2 (R_s + R_L)}{\omega^2 {C_s}^2 (R_s + R_L)^2 + (1 - \omega^2 L_s C_s)^2} + j \frac{(1 - \omega^2 L_s C_s)\omega^3 k^2 L_p L_s C_s}{\omega^2 {C_s}^2 (R_s + R_L)^2 + (1 - \omega^2 L_s C_s)^2} \quad \textbf{8.60}$$

- Parallel compensated secondary (Figure 8.18):

$$Z_r{}^{SP/PP} = \frac{\omega^2 k^2 L_p L_s \left(R_L + R_s + \omega^2 {R_L}^2 {C_s}^2 R_s\right)}{[R_s + R_L(1 - \omega^2 L_s C_s)]^2 + [\omega L_s + \omega R_L C_s R_s]^2} + j \frac{\omega^3 k^2 L_p L_s \left[C_s {R_L}^2 (1 - \omega^2 L_s C_s) - L_s\right]}{[R_s + R_L(1 - \omega^2 L_s C_s)]^2 + [\omega L_s + \omega R_L C_s R_s]^2} \quad \textbf{8.61}$$

In the next sections the needed compensation at primary side, quality factor, bifurcation phenomena and efficiency analysis is addressed. The parameters used for all the different cases are summarized in Table 8.10.

Table 8.10: Parameters of the circuit

Parameter	*Value*
C_s	*49.2 pF*
L_s	*2.8 µH*
L_p	*2.8 µH*
R_p	*2Ω*
f_0	*13.56 MHz*

8.4.1 Compensation

The needed compensating capacitor on primary side (to resonate at same frequency as secondary circuit) for each topology is obtained applying the same procedure defined in section 6.1.1.2 and they can be express as:

- SS topology:

$$C_p = \frac{1}{{\omega_0}^2 L_p} \quad \textbf{8.62}$$

- SP topology:

$$C_p = \frac{L_s C_s (C_s R_s R_L + L_s)^2 + (L_s C_s R_s)^2}{L_p (C_s R_s R_L + L_s)^2 + C_s L_s L_p {R_s}^2 - L_s M^2} \quad \textbf{8.63}$$

- PS topology:

$$C_p = \frac{L_p (R + R_s)^2}{{R_p}^2 (R + R_s)^2 + {\omega_0}^2 {L_p}^2 (R + R_s)^2 + 2{\omega_0}^2 M^2 R_p (R + R_s) + (\omega_0 M)^4} \quad \textbf{8.64}$$

- PP topology:

$$C_p = \frac{\left(\left(C_s^2 L_p R^2 R_s^2 + 2 C_s L_p L_s R R_s + C_s L_p L_s R_s^2 + L_p L_s^2 - L_s M^2 \right) C_s L_s^2 \right)}{(A + B + C)} \quad \textbf{8.65}$$

where

$$A = C_s^3 L_s^2 R^2 R_p^2 R_s^2 + C_s^2 L_p^2 L_s R^2 R_s^2 + 2 C_s^2 L_s^3 R R_p^2 R_s + C_s^2 L_s^3 R_p^2 R_s^2 \quad \textbf{8.66}$$

$$B = 2 C_s L_s^2 M^2 R_p R_s + C_s M^4 R^2 + L_p^2 L_s^3 - 2 L_p L_s^2 M^2 + L_s M^4 + C_s L_s^4 R_p^2 \quad \textbf{8.67}$$

$$C = 2C_s L_s^2 M^2 R R_p + 2C_s^2 L_s M^2 R^2 R_p R_s + 2C_s L_p^2 L_s^2 R R_s + C_s L_p^2 L_s^2 R_s^2 \qquad \textbf{8.68}$$

Several conclusions can be obtained from the previous equations. As it can be observed in equation 8.62, SS topology is the only one in which the compensation capacitance is independent from the internal resistance of the used coils. This is an advantage of this topology for implementing inkjet printed antennas, since the C_p is the same that is needed when other traditional fabrication techniques are used, such as subtractive etching.

The rest of topologies are affected by the internal resistances; consequently, if inkjet printed prototypes are used, it is important to check its influence.

In Figure 8.24, the effect of the internal resistance of the secondary coil (R_s) on C_p is shown for SP, PS and PP topologies under different load and coupling factors conditions.

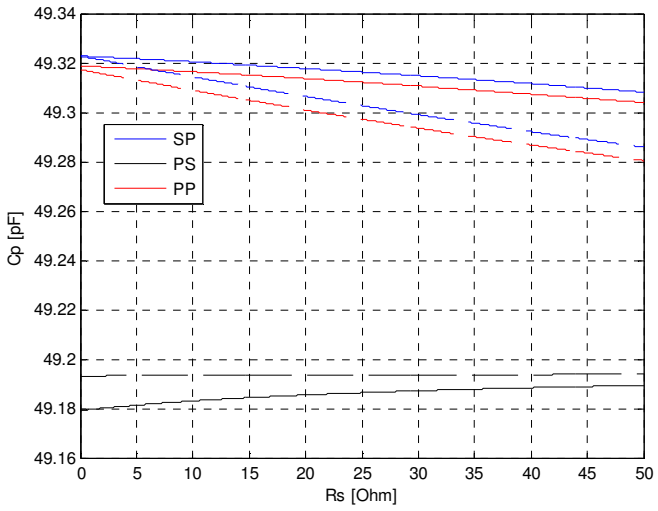

(a)

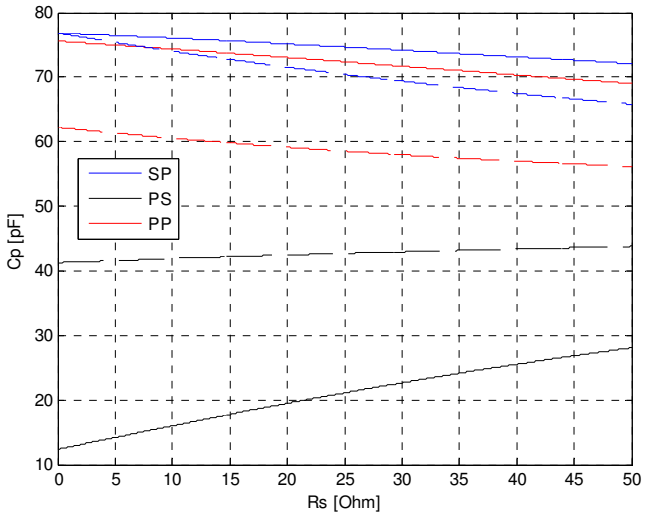

(b)

Figure 8.24: Effect of R_s in the primary compensation capacitance:(a) k=0,05. (b) k=0,6. Continuous line represents $R_L = 50\Omega$ and dotted line $R_L = 200\Omega$

It can be observed that when the coupling coefficient is very small (k=0.05), the change of the capacitance is negligible. Therefore, for implanted applications it is not necessary to recalculate the compensating capacitance. However, in applications in which the coupling coefficient is high (k=0.6), it can be observed that the change of the capacitance is more important. This change depends also on the topology and on the load resistance. For example, in PS topology, for $\mathrm{R_L} = 50\Omega$, the effect of R_s in C_p is much more important than for the case of $\mathrm{R_L} = 200\Omega$.

As conclusion, if the coupling coefficient is increased, the difference between the corrected compensation capacitance taking into account the internal resistances is higher and the effect of the load impedance is different depending on the selected topology.

8.4.2 Quality factor

The procedure is analogous to the one that has been explained in section 8.2.2.1.

- When secondary compensation is in series Q_p and Q_s are expressed as:

$$Q_p = \frac{\omega L_p}{R_p + Re\{Zr^{SS}\}|_{\omega=\omega_0}} \quad \textbf{8.69}$$

$$Q_s = \frac{L_s \omega_0}{R_L + R_s} \quad \textbf{8.70}$$

- When secondary compensation is in parallel $\mathrm{Q_p}$ and $\mathrm{Q_s}$ are expressed as:

$$Q_p = \frac{\omega L_p}{R_p + Re\{Zr^{SP}\}|_{\omega=\omega_0}} \quad \textbf{8.71}$$

$$Q_s = \frac{R_L L_s \omega_0}{{R_s}^2 + (L_s \omega_0)^2 + R_s R_L} \quad \textbf{8.72}$$

The effect of R_s in the secondary quality factor (Q_s) is studied for different loads in Figure 8.25.

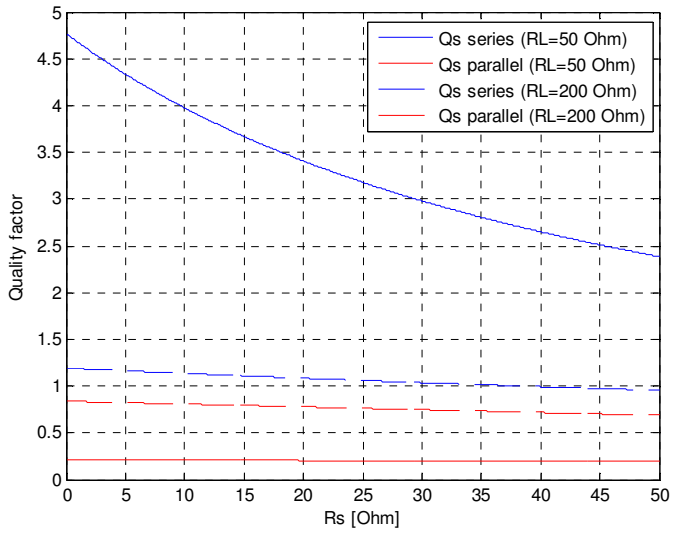

Figure 8.25: Effect of R_s in the secondary quality factor for different loads

As shown in Figure 8.25, the calculated quality factor taking into account the internal resistance differs more from the simplified case for series compensations. Besides, it can be appreciated that the load impedance (R_L) plays also an important role in the behavior; the internal resistance variation has more influence in the change of the overall quality factor for lower load values since it is adding in series with the internal one, and consequently the weight of internal resistance is higher for smaller loads. In parallel case, the effect of the internal resistance is not very significant for any value of R_L.

The effect of the coupling coefficient in the primary is studied in two cases: loosely coupled systems (k=0,05) and normal coupling (k=0,6) (Figure 8.26).

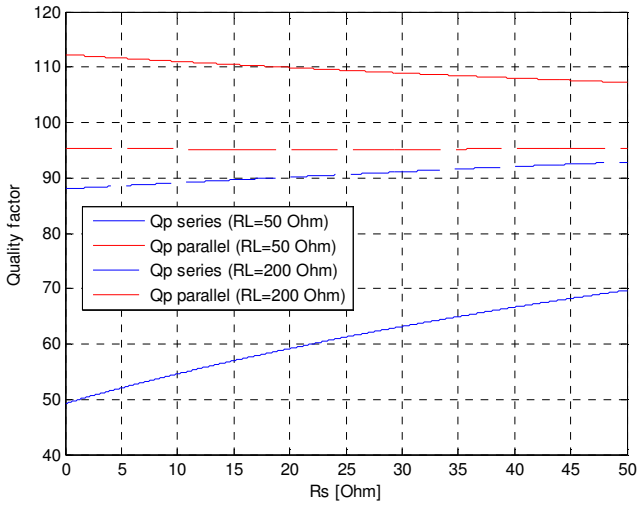

(a)

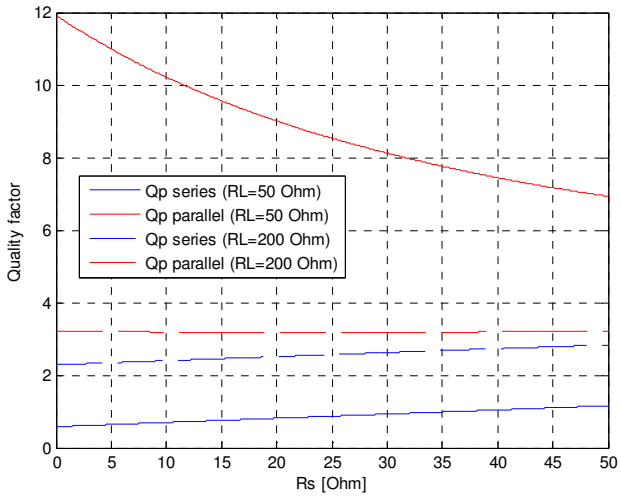

(b)

Figure 8.26: Effect of R_s in the primary quality factor for different loads (a) k=0,05. (b) k=0,6

As shown in Figure 8.26, the coupling factor has a strong effect in the quality factor. In series secondary compensation, the change of the quality factor is considerable for small coupling factor. Nevertheless, when a bigger coupling factor is used, the change is negligible. Opposite behavior is observed in parallel case, since for small coupling coefficient the quality factor is almost the same for any value of R_s and there is a considerable change for bigger coupling coefficients.

As mentioned for the secondary quality factor (Q_s), the load impedance (R_L) affects also the obtained quality factor. The same behavior respect to the R_L is observed for Q_p.

8.4.3 Bifurcation phenomena

As described in section 8.4.2, the quality factors that are obtained for primary and secondary circuits depend on R_s. The bifurcation-free conditions depend on Q_p and Q_s according to equations 8.43, 8.44 and 8.45. Subsequently, substituting the expression of Q_p and Q_s in section 8.4.2 in the equations 8.43, 8.44 and 8.45, the effect of R_s in the bifurcation-free conditions can be studied.

In Figure 8.27, the effect of R_s on the coupling factor that limits the bifurcation-free area is shown for different load impedances.

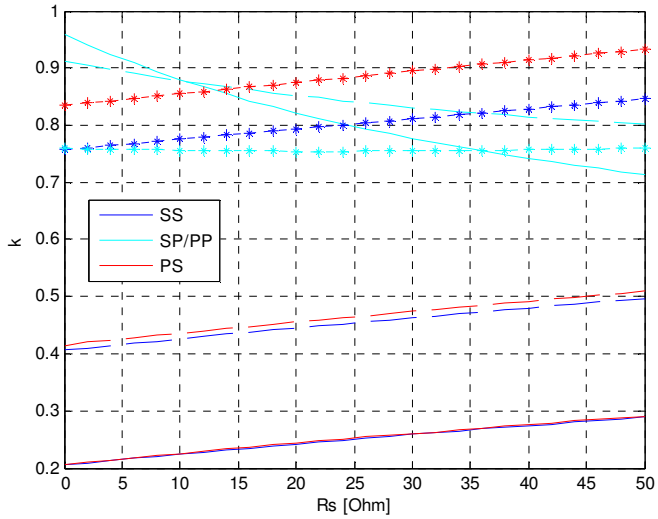

Figure 8.27: Effect of R_s in the boundary coupling coefficient for bifurcation free system for all topologies with different load impedances. $R_L = 50\Omega$ (-), $R_L = 100\Omega$ (--), $R_L = 200\Omega$ (*-)

The coupling coefficient values that are shown in Figure 8.27, they are the ones that are obtained in the limit between bifurcation and bifurcation-free area. In other words, for higher coupling coefficient values, bifurcation phenomena occur.

On one hand, it can be observed that the behavior of SS and PS topologies is the same with respect to the change of R_s. When the R_L is increased, the difference between them is bigger but the behavior with respect to the change of R_s keeps equal. For these two topologies, there is no problem with respect to bifurcation phenomena, since when R_s is increased the coupling coefficient which produces bifurcation is higher, so the system is less restricted to be in the bifurcation-free area. In other words, if for a certain application with etched copper antennas with SS or PS topology, there is no bifurcation, if the secondary coil is manufactured with inkjet printing technology, at the same conditions, the system is also stable.

Furthermore, as the coupling coefficient increases when the distance between the coils decreases, smaller distances can be used without bifurcation phenomena with inkjet printed prototypes.

On the other hand, different behavior is observed in SP/PP topologies, in which the increase of R_s reduces the needed coupling coefficient to be in the bifurcation zone. The effect of R_s is reduced when the load impedance is increased, as it can be appreciated in Figure 8.27. Then, care must be taken in this case, since for certain conditions (certain coupling factor or certain distance), using etched copper coils, if the system is in the bifurcation-free area, when inkjet printed prototype is replaced in the secondary coil, the system can move to the bifurcation area.

It should be noticed at this point, that if the primary coil is inkjet printed, the behavior of the system is different, but as it is mentioned at the beginning of section 8.4, in this work, the effect of manufacturing the secondary coil with inkjet printing is only studied.

8.4.4 Efficiency analysis

As it is mentioned in section 8.3, the internal resistances play an important role in the final efficiency of the system. In this section, the effect of the internal resistance of the secondary (R_s) is addressed.

In Figure 8.28, the effect of R_s in the efficiency for different load impedances is shown.

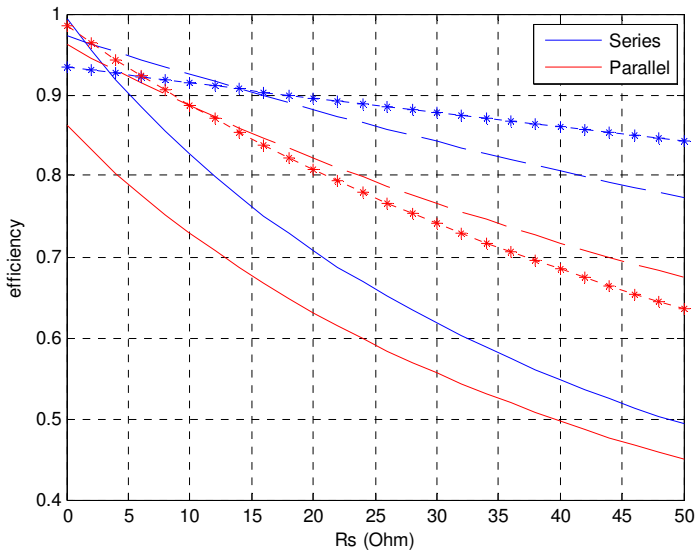

Figure 8.28: Effect of R_s in the efficiency for different load impedances (-) 50Ω. (--) 100Ω, (*)200 Ω

As shown in Figure 8.28, the efficiency decreases for both compensations when the internal resistance of the secondary is increased. The decrease of efficiency is more important for smaller load values in both compensations. This can be because when the load is smaller an increase of the internal resistance is more significant in the overall losses of the system. Nonetheless, when the load is higher, the internal resistance weight in the overall loss is not so important and consequently, its effect in the efficiency is lower.

It must be also reminded, that the use of inkjet printing technology in the secondary coil affects also the boundary frequency which defines which topology is better in terms of efficiency (equation 8.59). In Figure 8.29, the change of the boundary frequency (f_c) with respect to R_s for different coupling factors and load impedances is shown.

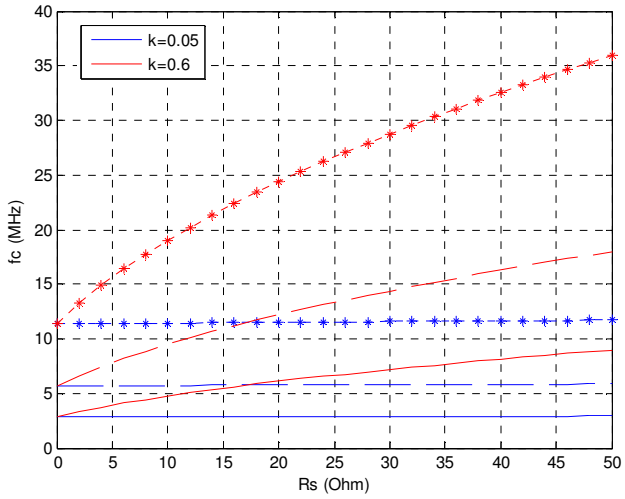

Figure 8.29: Effect of R_s in f_c for different coupling and load impendances (-) 50Ω. (--) 100Ω, (*)200 Ω

As shown in Figure 8.29, the boundary frequency remains constant for any load for low coupling factors, but considerable change is appreciated when the coupling coefficient is higher, being the change more important as R_L is increased.

8.5 Case study: Sensor-antenna approach

In this conception the feasibility of using the antenna as a LC sensor is studied. The technical idea is to simplify the implanted structure at the maximum level so that the most of the electronics and the power source are placed outside the body. In this conception, the implant consists of an antenna (coil) and a capacitor in parallel that acts as a sensor with no electronics involved. It would change its properties depending on physiological parameters variations. As the LC sensor is a passive resonant element, if its resonant frequency is dependent

on the parameter variation is aimed at (pressure, temperature, flow, pH etc.), the shift can detected by the reader.

In this section a first approach to this concept is shown. The structure of the system is very simple. The secondary circuit is just the inductance and a capacitor connected, since in this case there is not a load. Consequently, the secondary can be seen as a series compensation with $R_L = 0$ or parallel compensation with $R_L = \infty$.

Two different implementations can be done in the primary, using series or parallel topology. In implanted application the coupling factor is not constant, consequently it would be interesting to have a system in which the change of the resonant frequency only depends on C_s. In Figure 8.30, the change of the resonance frequency at primary circuit with the coupling coefficient is shown for series and parallel compensation on primary. $(C_p = C_s = 49.2pF, L_p = L_s = 2.8\mu H, R_p = R_s = 2\Omega)$

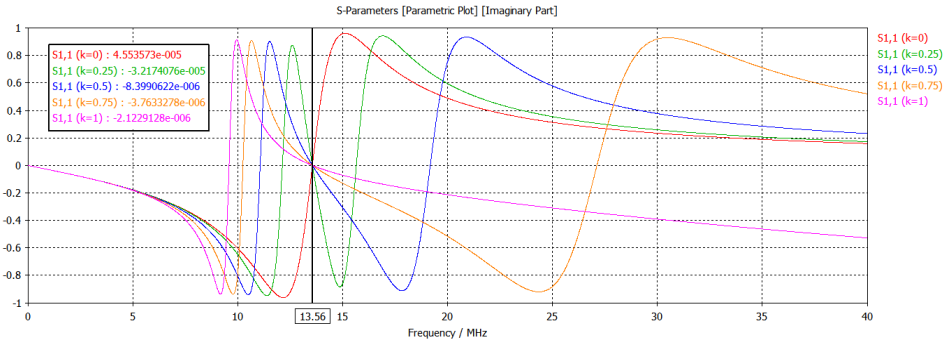

(a)

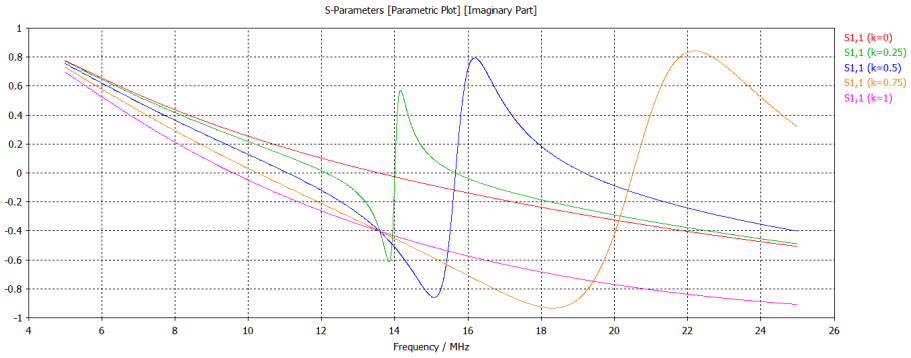

(b)

Figure 8.30: Behaviour of the imaginary part of S11 with coupling coefficient. (a) Series primary compensation. (b) Parallel primary compensation

As it can be seen, in series compensation case (Figure 8.30a), one of the nulls of the imaginary part of S11 is located at the resonant frequency of the system ($f_0 = 13.56\,MHz$) for every *k*. In contrast, when parallel compensation is used, there is not a null always at the resonant frequency. This is due to the fact that in series compensation the compensating capacitor is independent from the coupling factor, contrary to the parallel case, in which is dependent on the coupling coefficient.

For sensor antenna approach it is desired to be able to detect a shift of C_s, in other words, a shift in the secondary's resonance frequency, by observing the primary. Consequently, the series compensation case is used since in that case, the shift is only due to the change of C_s and the shift of the coupling coefficient does not disturb the measurement. If parallel compensation is implemented, a different compensating capacitor should be choose depending on the coupling coefficient, making the primary side more complicated.

Taking into account the available market pressure transducers, it has been estimated that a variable range of 5 pF is a reasonable resolution to test the feasibility of this approach [120].

In Figure 8.31, C_s is varied 5 pF and the shift of the resonant frequency on primary side is observed.

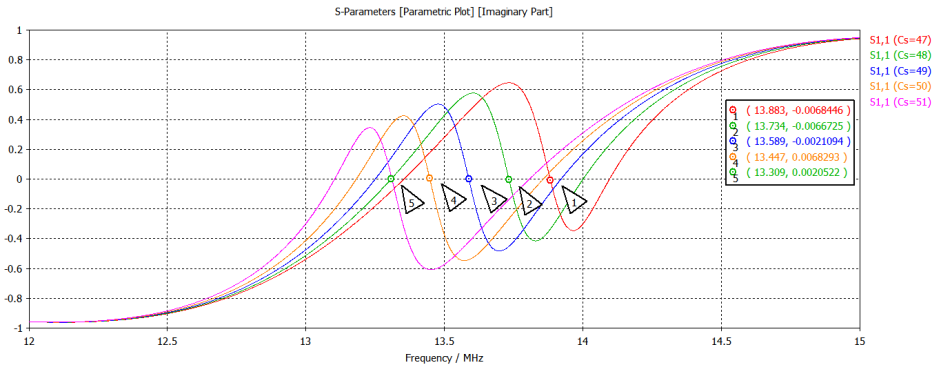

Figure 8.31: Shift of the S11 imaginary part with C_s (k=0,05)

It can be seen that the obtained resolution is approximately 140 KHz per 1 pF variation.

In Figure 8.32, the same case is included but in this case for a coupling factor of 0,6 to ensure that the coupling coefficient does not affect the obtained resolution.

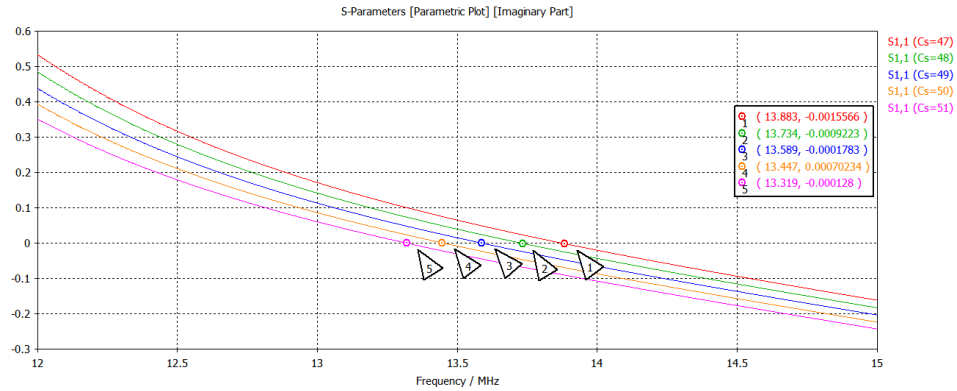

Figure 8.32: Shift of the S11 imaginary part with C_s (k = 0.6)

As expected, the obtained resolution is independent from the coupling coefficient. Further research must be addressed to check the influence of the human body. In this preliminary study, the effect of human body has been considered by using a very low coupling coefficient (k=0,05). Nevertheless, the human body can introduce other effects that has not been considered in this study. Simulation and measurements including the human body must be done.

Chapter 9

Far field implanted wireless links optimization

In this chapter the results obtained using the methodology that has been explained in section 6.2 are presented. The chapter is divided into three different parts. Firstly, the characterization of plane wave attenuation in homogeneous phantoms is studied to compare with the corresponding simulation results and validate the simulation procedure. At the same time, an analysis of sugar based phantoms is addressed.

Secondly, by combining analytical and computational approaches, a heterogeneous layered planar phantom is used to study the effect and the frequency behavior of the E-field in human body for communications with

implants. Finally, the obtained results using voxel phantom models are presented.

9.1 Homogeneous phantom characterization

First of all the analysis of sugar based phantoms is shown describing its advantages and limitations. The recipes for muscle tissue at 402 MHz, 868 MHz, 2.45 GHz and 5.8 GHz frequencies are obtained.

The characterization of plane wave attenuation for the proposed phantoms is studied and compare with the simulations.

9.1.1 Sugar based phantom analysis

Following the procedure that has been explained in section 6.2.3.1, a study of the influence of the sugar concentration in water's dielectric constant and conductivity has been carried out. As it has been mentioned in chapter 4, sugar based phantoms are used for frequencies usually in the range from 400 MHz to 1 GHz. In this section, a sugar based phantom is used for creating phantoms for higher frequencies to check the limitation of this kind of phantoms.

In Figures 9.1, 9.2 and 9.3, the obtained values for different sugar concentrations are shown.

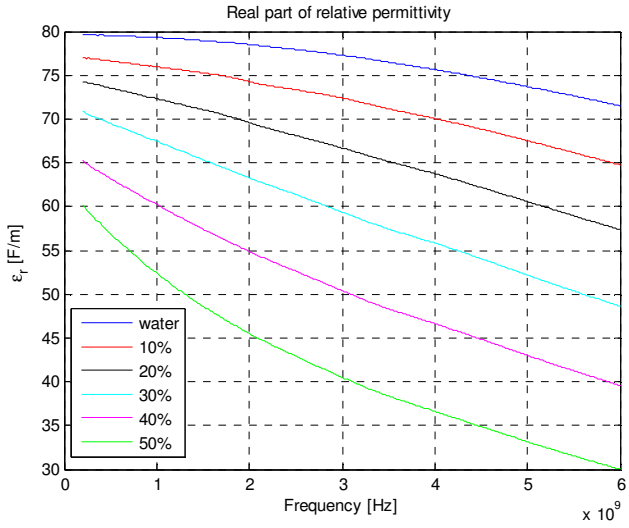

Figure 9.1: Measured real part of permittivity for different sugar concentration liquids

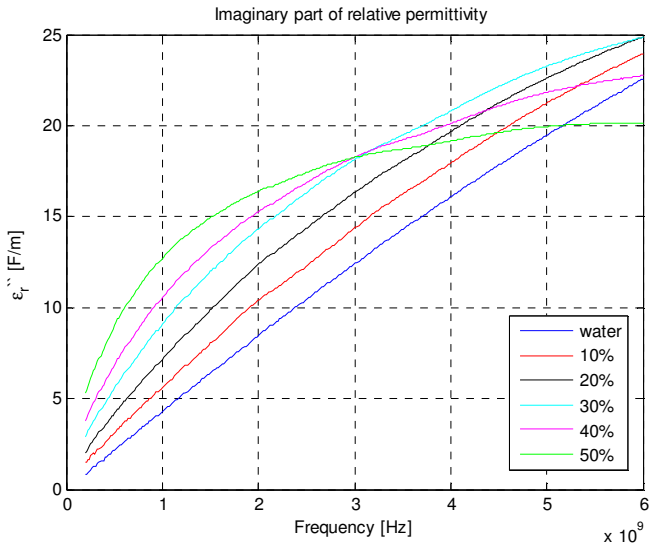

Figure 9.2: Measured imaginary part of permittivity for different sugar concentration liquids

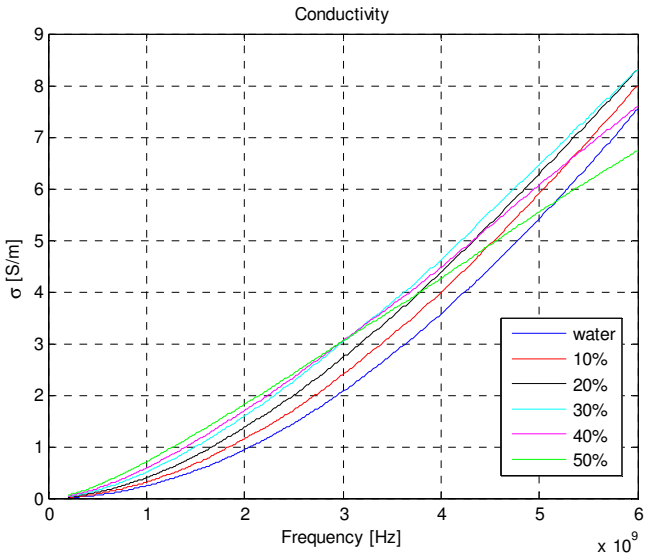

Figure 9.3: Measured conductivity for different sugar concentration liquids

As expected, when the sugar concentration is increased, the real part of the permittivity is decreased (Figure 9.1). Regarding the conductivity, as it can be observed the effect of the sugar is not so important (Figure 9.3). The conductivity increases with frequency.

From the obtained results, three different recipes are fabricated for the desired frequencies of interest. The target values and the obtained ones are shown Table 9.1.

Table 9.1: Fabricated phantom recipes for the frequencies of interest

Tissue information		*Phantom materials (%)*			*Phantom properties*		*Gabriel properties*	
tissue	*Frequency (GHz)*	*sugar*	*water*	*salt*	*ε*	*σ*	*ε*	*σ*
muscle	*0,402*	*51*	*49*	*0*	*57*	*0,4*	*57,11*	*0,797*
muscle	*0,868*	*51*	*49*	*0*	*54*	*0,75*	*55,10*	*0,932*
muscle	*2,45*	*41*	*59*	*0*	*52,5*	*2,5*	*52,72*	*1,738*
muscle	*5,8*	*29*	*71*	*0*	*48,8*	*7,5*	*48,48*	*4,961*

The same recipe has been used for 402 and 868 MHz since the obtained values are still close to the desired ones.

Several aspects can be extracted from the previous table. It can be seen that the permittivity can be easily adjusted by changing the sugar concentration. However, focusing on the conductivity, on one hand, it can be seen that for 402 MHz and 868 MHz the measured conductivity is below but very similar to the target one. The obtained conductivity can be increased a little by adding a small amount of salt. On the other hand, for 2.45 GHz and 5.8 GHz the obtained conductivity is clearly above the target value and it this case, it is not possible to decrease the conductivity with the proposed materials. This effect is studied when the characterization of plane wave attenuation is made in section 9.1.2 and the frequency bandwidth of these kinds of phantoms is discussed.

9.1.2 Characterization of plane wave attenuation in homogeneous phantoms

In this section the results obtained in the anechoic chamber are shown and the correlation with simulations is addressed to test if the fabrication process of the phantom is correct and also to check the feasibility of the simulator for studying this kind of problems. The section is divided into different subsections: firstly, a set-up verification is made by comparing the measurements in the semi-anechoic and anechoic chamber for the f=2.45 GHz case; secondly, the obtained measurements with both antennas and both polarizations is presented and discussed and finally, a comparison between the measurements and simulations is made. The antennas that are used has been described in section 6.2.3.

9.1.2.1 Set-up verification

The preliminary measurements are carried out in the semi-anechoic chamber at 2.45 GHz and this results are compared with the same scenario in the anechoic chamber (Figure 9.4).

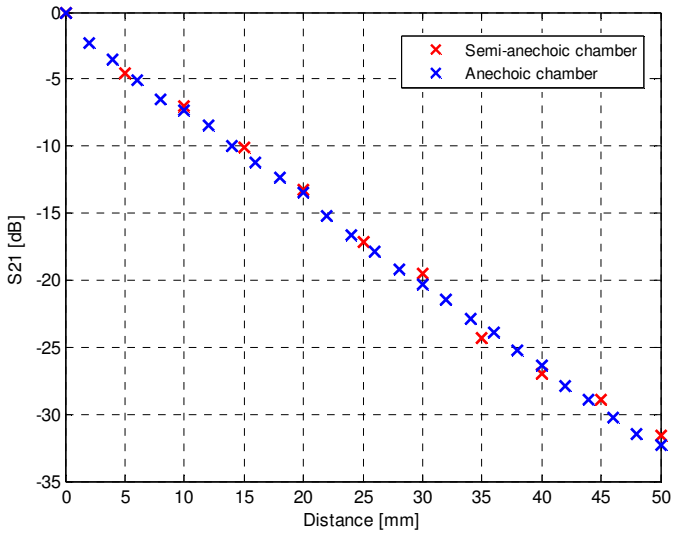

Figure 9.4: Measurements with antenna 1 horizontal polarization

As it can be observed, the results are normalized with respect to the first value to compare the results of both chambers. The correlation is very high, consequently it can be assumed that both set-ups are correct. Only the results for the antenna 1 with horizontal polarization have been shown for simplicity of the figure. Very similar results are also obtained with antenna 2.

9.1.2.2 Measurements in anechoic chamber

In Figure 9.5, the obtained results in the anechoic chamber are shown for the four frequencies of interest and both antennas:

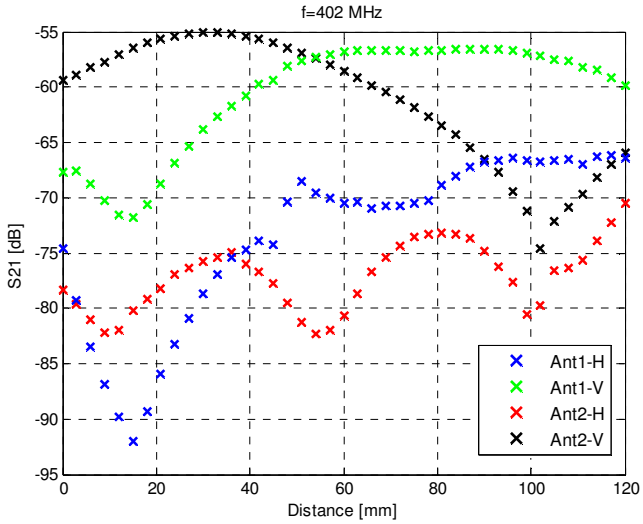
f=402 MHz
S21 [dB]
Distance [mm]
Ant1-H
Ant1-V
Ant2-H
Ant2-V

(a)

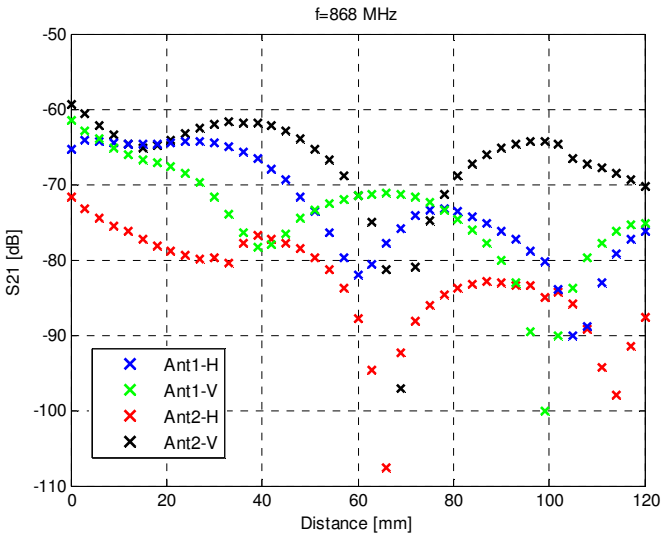
f=868 MHz
S21 [dB]
Distance [mm]
Ant1-H
Ant1-V
Ant2-H
Ant2-V

(b)

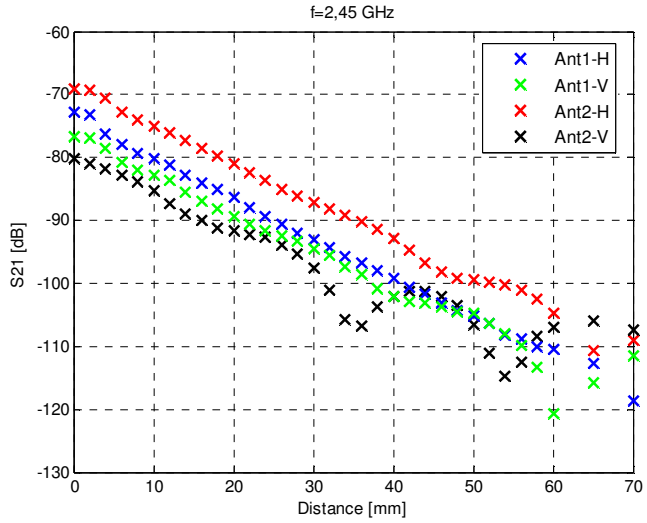

(c)

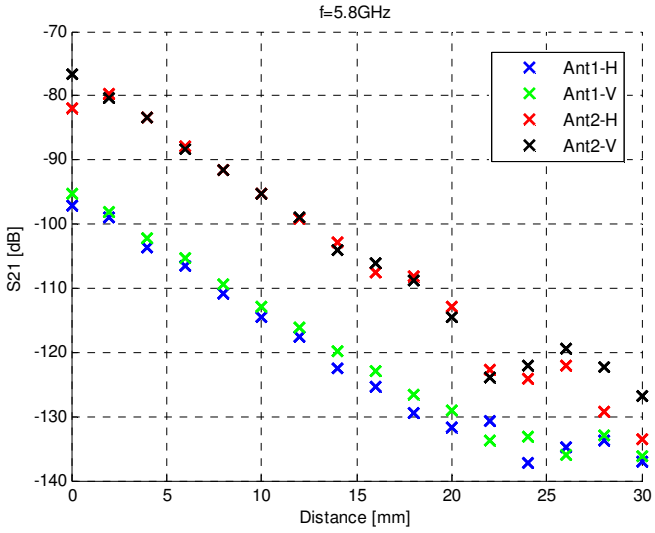

(d)

Figure 9.5: S21 dB vs. frequency: (a) f=402 MHz, (b) f=868 MHz, (c) f=2.45 GHz and (d) f=5.8 GHz. Antenna 1 (Ant1), Antenna 2 (Ant2), horizontal polarization (H) and vertical polarization (V).

Several conclusions can be obtained from these measurements.

On one hand, it can be seen that the performances of the antennas at 2.45 GHz and 5.8 GHz follow the same trend for all cases. In each case, the difference between the antennas is due to the gain at these frequencies. Differences between polarizations within the same antenna are also observed, as expected. As it has been explained before, the interest is focused on the behavior of the phantom and not in the characterization of the antenna. As it can be seen, the decay of the power received by the antenna because of the change of the position is independent from the antenna that is used, since in all cases the slope of the decay is the same. The four plots overlap for each frequency (2.4 GHz, 5.8 GHz) once the values are normalized by their respective maximum. This demonstrates that the probe antenna and its polarization do not have an impact on the expected results for these high frequencies.

It can be also appreciated that for distances larger than 50 mm at 2.45 GHz and 20 mm at 5.8 GHz, the measured S21 parameter is so low that the noise masks the results. The effect that is clearly seen for smaller distances in the phantom is no longer appreciated because the noise disturbs the obtained measurements.

Taking into account the obtained results, at 2.45 GHz and 5.8 GHz any antenna can be taken to compare the results with the simulation.

On the other hand, at 402 MHz and 868 MHz the behavior is totally different not only by a vertical offset but in many cases for the locations of the dips (Figure 9.5a and 9.5b) since reflection effects are produced in the phantom free space interfaces in all directions in contrast to both previous cases (2.45 GHz and 5.8 GHz). There are two main reasons to explain the obtained results.

Firstly, the anechoic chamber is prepared to work efficiently for frequencies above 1GHz. For lower frequencies and due to the characteristics of the chamber, the obtained results may be influenced by undesired reflections in the walls.

Secondly, as the frequency is lower, the dimensions of the phantom affects more since the wavelength is higher.

Different tests changing some parts of the set up have been carried out to check these aforementioned effects. A metallic sheet has been located at the bottom part of the phantom, the width and thickness of the phantom have been also modified. In all cases, the results change significantly, in contrast to 2.45 and 5.8 GHz cases where these changes in the phantom, do not affect the obtained results.

In contrast to the case of f=2.45 GHz and f=5.8 GHz, at f=402 MHz and f=868 MHz the decision on which of the measurements of Figure 9.5 are reliable is based on taking into account the S11 parameter of the antenna. The fact that the behavior of the two polarizations of each antenna are similar with a certain shift is also considered.

In Figure 9.6, the S11 parameter is shown for each antenna's position and both frequencies.

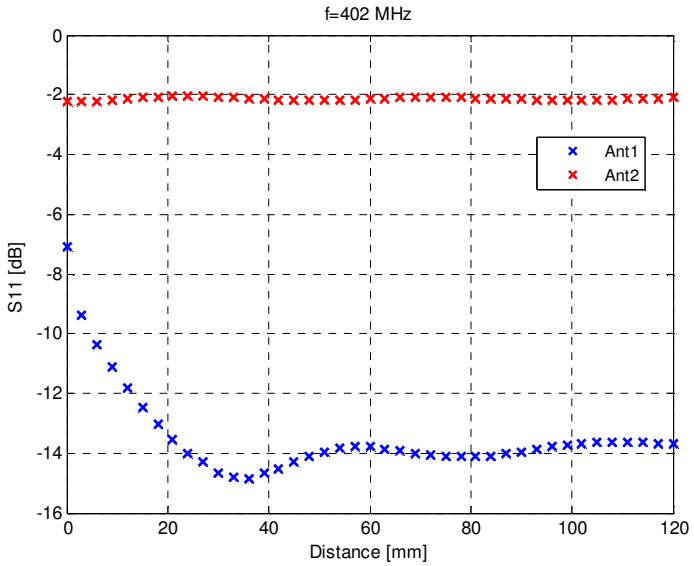

(a)

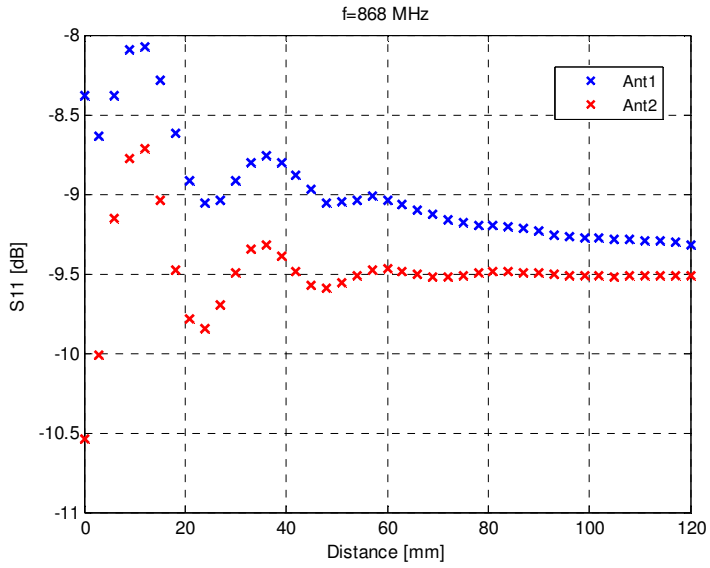

(b)

Figure 9.6: S11 parameter for both antennas. (a) f=402 MHz; (b) f=868 MHz

From Figure 9.6a, the antenna 2 can be discarded for f=402 MHz because the S11 is very low. In the case of f=868 MHz, the S11 parameter is similar for both antennas (Figure 9.6b), but taking into account the obtained measurements (Figure 9.5b), antenna 2 is used since the behavior of S21 parameter for both polarizations is similar with a certain shift in amplitude.

In other words, the offset in amplitude with the same dips locations in frequency between the two polarizations in the same antenna is a sign that the impact of reflections coming from the interfaces phantom-free space is repeatable for this antenna. Therefore, a comparison with a finite-size phantom in simulation is done only for these measured cases.

Once the antenna that is used for each frequency is selected, these measurements are compared with simulations.

9.1.2.3 Simulation vs. Measurements

For the simulation a muscle block is defined with open add space boundary conditions in all directions (Figure 9.7).

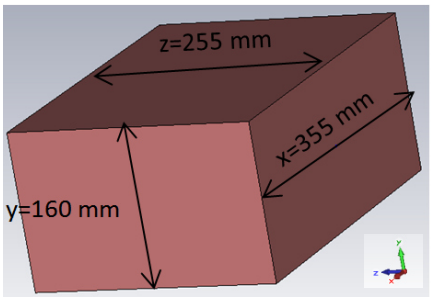

Figure 9.7: Simulated homogeneous phantom model

In Figure 9.8, the comparison between simulations and measurements is shown for the four frequencies of interest. In all cases, the measurement results of the antenna that has been selected in the previous section and the simulation using the dielectric properties of the fabricated phantom and the theoretical muscle properties are shown.

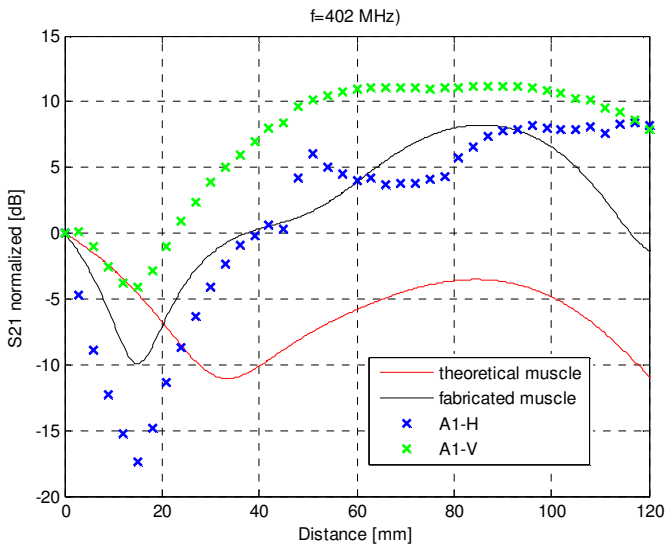

(a)

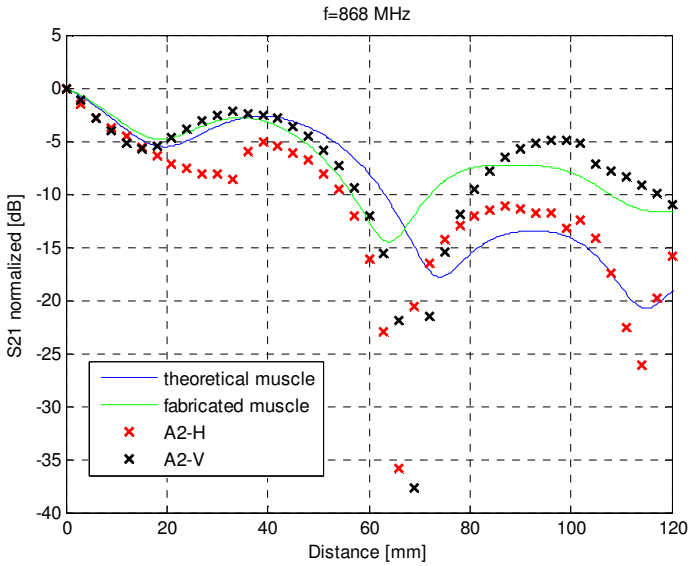
f=868 MHz
S21 normalized [dB]
Distance [mm]
theoretical muscle
fabricated muscle
A2-H
A2-V

(b)

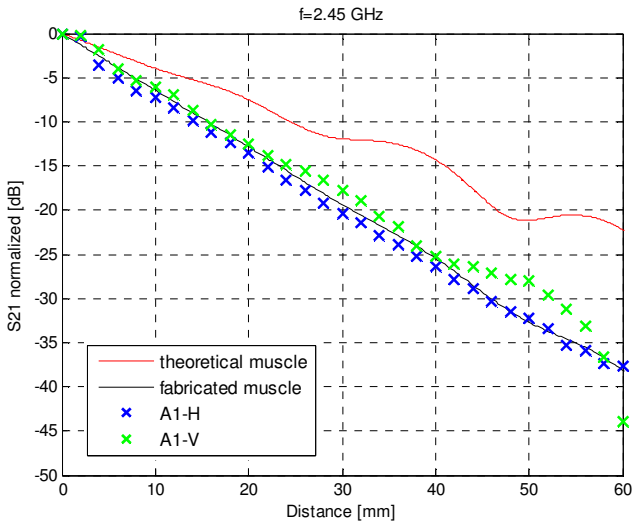
f=2.45 GHz
S21 normalized [dB]
Distance [mm]
theoretical muscle
fabricated muscle
A1-H
A1-V

(c)

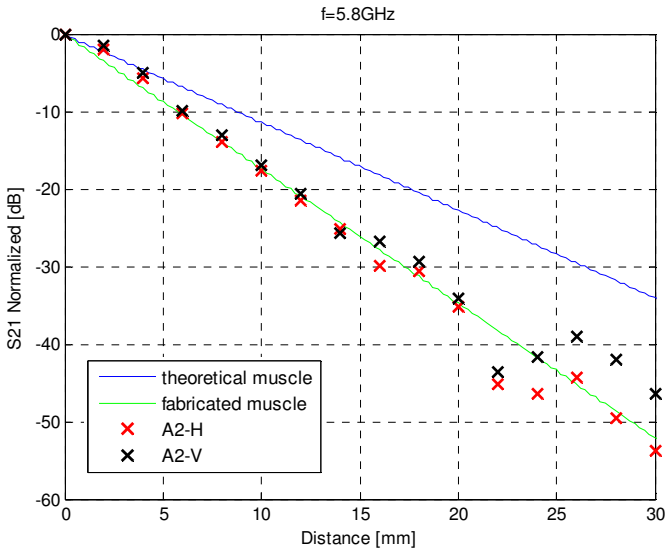

(d)

Figure 9.8: Simulation vs. Measurements (a) f=402 MHz, (b) f=868 MHz, (c) f=2.45 GHz and (d) f=5.8 GHz.

Different important conclusions can be obtained from the previous comparison: the limitation of the sugar based phantom can be extracted and the importance of the phantom size and its dependence with the frequency can be also deduced.

a) Limitation of sugar based phantoms

On one hand, taking into account the comparison at both higher frequencies (2.45 GHz and 5.8 GHz), the correlation between the measurements and simulation is very high when the values that are used in the simulation are the properties of the fabricated phantom. This result certifies that the fabrication and the characterization of sugar based phantoms have been carried out successfully and that the simulation tool is working properly with the aforementioned assumptions.

On the other hand, the results differ if the measurements are compared with the simulation using the Cole-Cole model that CST uses for the characterization of

muscle. This difference can be explained by comparing the conductivity of the fabricated muscle and the theoretical muscle (Table 9.1). In that table, it can be observed that the difference in conductivity is considerable and therefore the decay of power is different. In Figure 9.9, this effect is shown by plotting the normalized S21 parameter at f=5.8 GHz for the theoretical muscle, for the fabricated muscle and for two materials with the same permittivity of the muscle but intermediate conductivity between the fabricated and the theoretical one.

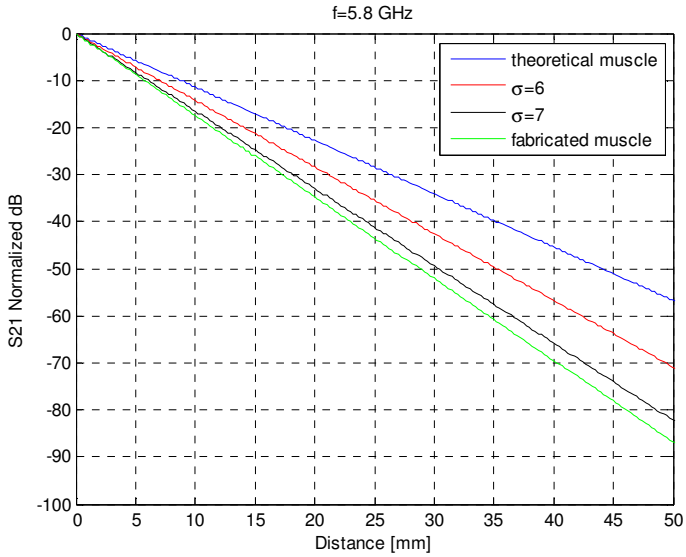

Figure 9.9: Effect of the conductivity at 5.8 GHz

It can be concluded that the suitability of sugar based phantoms for the characterization of implanted links is limited by the conductivity of the water. It should be pointed out that, for subcutaneous implanted applications, the error is not so considerable as the implant insertion depth does not go further than a few millimeters.

At 402 MHz and 868 MHz (Figure 9.8a, Figure 9.8b respectively), the conductivity also affects, but in those cases, as the conductivity of the proposed phantom is below the target, a certain amount of salt could be added to get to the desired conductivity value.

The validity of using sugar based phantoms is therefore limited by the conductivity when the obtained conductivity of the proposed recipe is above the target value. In Figure 9.10, the conductivity of muscle, skin, water and typical needed sugar based liquids with different concentrations is shown.

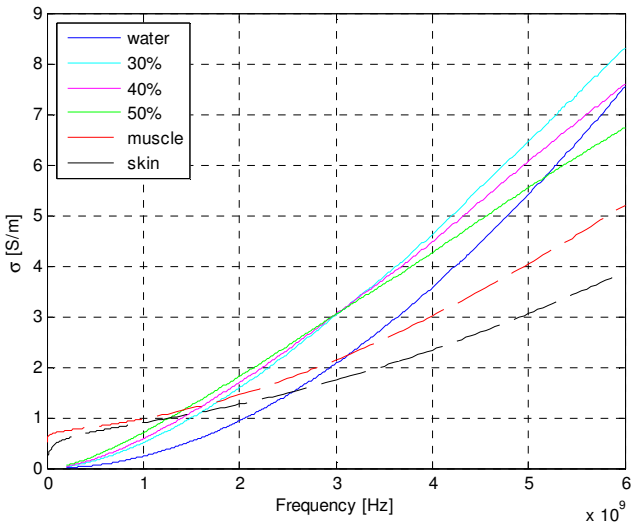

Figure 9.10: Conductivity behaviour with frequency for different materials

From this figure the limitations of sugar based phantoms for the fabrication of skin and muscle phantom can be extracted. The concentrations of 30%, 40% and 50% have been chosen since with these ranges of concentrations the target permittivity values for skin and muscle can be obtained. Once the needed concentration of sugar is calculated for a specific frequency, if the obtained conductivity is below the target, some salt could be added to increase the conductivity. Care should be taken since the salt has some effect on the permittivity of water. On the other hand, if the obtained conductivity is above the target one, there is no way to decrease the conductivity using salt-sugar combinations. From Figure 9.10 it can be concluded that this limit is at f=1.5 GHz.

For higher frequencies, if the phantom is fabricated for subcutaneous applications, maybe the error introduced by the difference of conductivity can be affordable. However, if the phantom is used for modeling a communication with implants that are deeply located, other kind of materials should be considered. Some of these materials were presented in section 2.3.1 and Table 2.3.

b) Phantom dimension effects (boundary conditions study)

The correlation between the simulation and the measurements when the fabricated muscle dielectric properties are used for 2.45 GHz and 5.8 GHz is very accurate. This correlation is not so good for the lower frequencies.

At f=402 MHz it can be appreciated for example, that the minimum is at the same position at around 16 mm (Figure 9.8a) and that at f=868 MHz, the correlation is very good for the vertical polarization until 60 mm (Figure 9.8b). As it has been mentioned, in one side, the effect of the chamber can be important since possible unwanted reflections that disturb the measurements can be produced due to low frequencies (below 1 GHz). In this context, as the frequency is lower, the dimensions of the phantom also affect since reflections can be produced in the walls due to the larger wavelengths at those frequencies.

In order to check this issue, periodic boundaries have been defined in the *x* and *y* directions to replicate infinite boundary conditions perpendicular to the propagation direction and, therefore, see the influence of this boundaries in the measurements at f= 402 MHz and f=868 MHz.

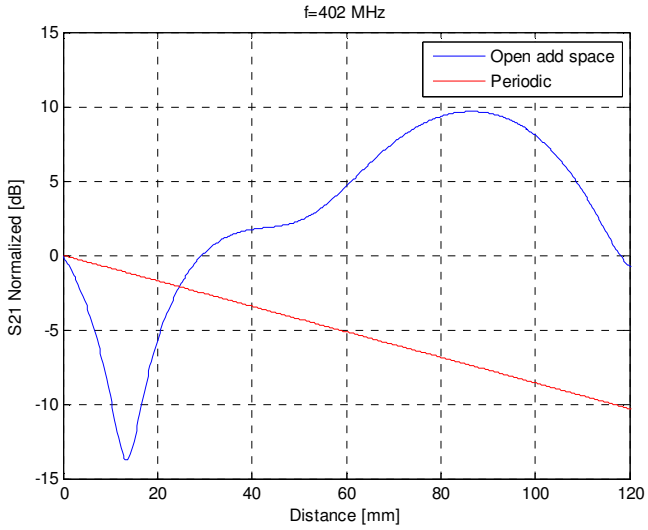

(a)

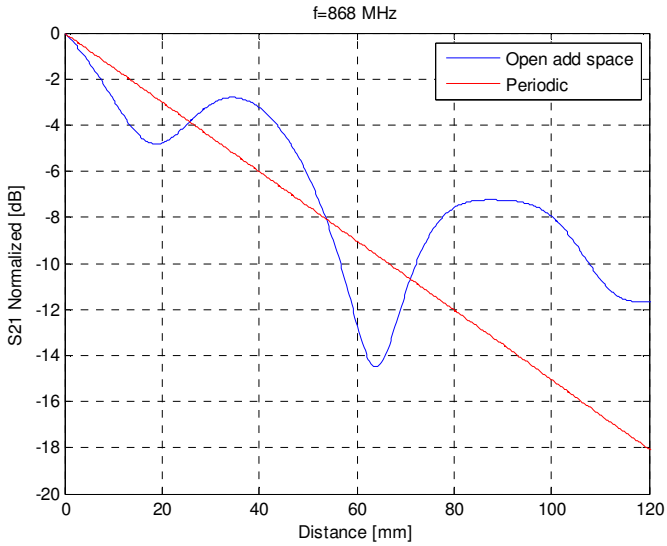

(b)

Figure 9.11: Effect of boundary conditions in x and y directions: (a) f=402 MHz and (b) f= 868 MHz

When periodic boundaries are defined in the *x* and *y* directions, the obtained results are totally different and the behavior is similar to the one obtained for f=2.45 GHz and f=5.8 GHz with other slope decay. This demonstrates that the results for f=402 MHz and f=868 MHz are affected by the reflections produced in the walls of the phantom. This effect is negligible at the higher frequencies, since when periodic boundaries are defined the same results are obtained (Figure 9.12)

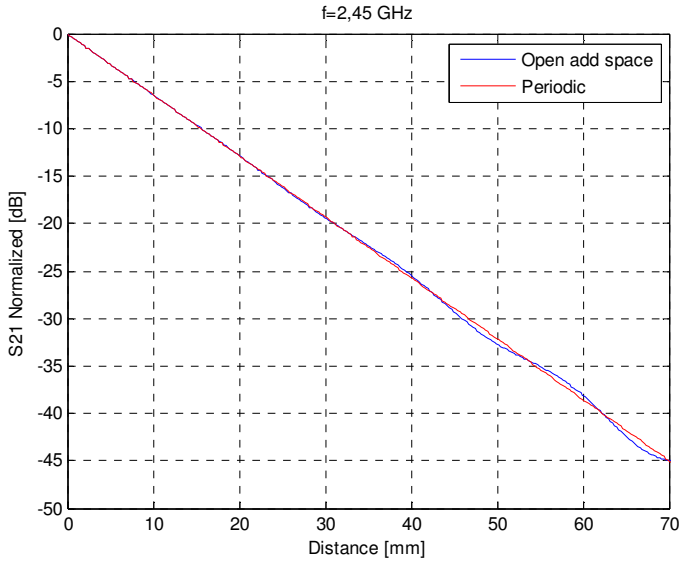

Figure 9.12: Effect of boundary conditions in x and y directions at f=2.45 GHz

As summary, it can be stated that the characterization of plane wave attenuation in homogeneous phantoms has been made by comparing measurements obtained in the anechoic chamber with simulations.

In homogeneous phantoms the attenuation of the waves is higher when frequency is increased. This effect can be clearly observed at the 5.8 GHz and 2.45 GHz cases. At f=5.8 GHz the attenuation is 1dB per mm and at f=2.45 GHz it is 0,5dB per mm. The lower frequencies are affected by reflections.

Once the simulations with homogeneous phantoms have been validated with measurements, the analysis of more complex phantom models can be done.

9.2 Heterogeneous layered planar phantom analysis

In this section, an analysis of different heterogeneous layered planar phantoms is made in order to study the effect of human tissues in the communication with implantable devices. The interest is focused on studying the influence of the thickness of the human tissue layers and its effect on the electric field distribution inside the human body.

The study is focused on the human torso and, consequently, the thicknesses of the biological tissues that are considered in this study are based on the typical values that have been reported in humans (Table 2.1).

In order to have a reliable phantom model that is representative of the real human tissue distribution, a four layer model phantom is required. As it has been mentioned in section 6.2.1, the analytical approach is difficult to calculate for the cases in which the number of layers exceeds three. An approximation can be applied for the calculation of N-layer structures (Equation 6.35), but it is not suitable for biological tissues since the partial reflections between the layers are not small enough comparing to the unity.

Therefore, the simulation procedure has been tested with the analytical approach for two and three layers, in order to ensure that the parameters defined in the simulation are reliable. Once this issue is checked, the simulation is used to study the effect on a four layered planar phantom.

9.2.1 Checking simulation methodology

9.2.1.1 Air-Skin (2 layers)

In this case the analytical approach that is used is based on the case of two infinite layers with planar interface (Figure 6.10). In Figure 9.13 the frequency behavior of the reflection coefficient for air and skin is shown. The dielectric properties of the skin tissue are based on Gabriel's database [19–21] and the reflection coefficient is calculated using equation 3.37.

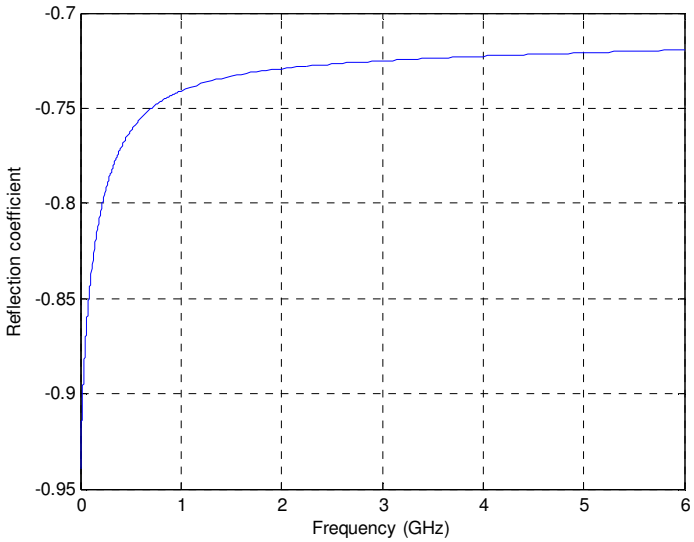

Figure 9.13: Frequency behaviour of the reflection coefficient

In order to be able to compare the analytical approach with the simulation, the fact that the skin seems to be infinite for the simulator is needed. For that, waveguide ports have been used as excitation and the boundaries have been defined as explained in section 6.2.2.4. The thickness of the skin has been selected sweeping it until reaching, by simulation, a very low S_{21} parameter ($S_{21} < -50dB$). Under this condition the S11 parameter can be defined as:

$$S_{11} = 10log|\Gamma|^2 \qquad \textbf{9.1}$$

Applying equation 9.1 to the results shown in Figure 9.13, the simulator obtained S_{11} parameter is compared with the analytical approach result in Figure 9.14.

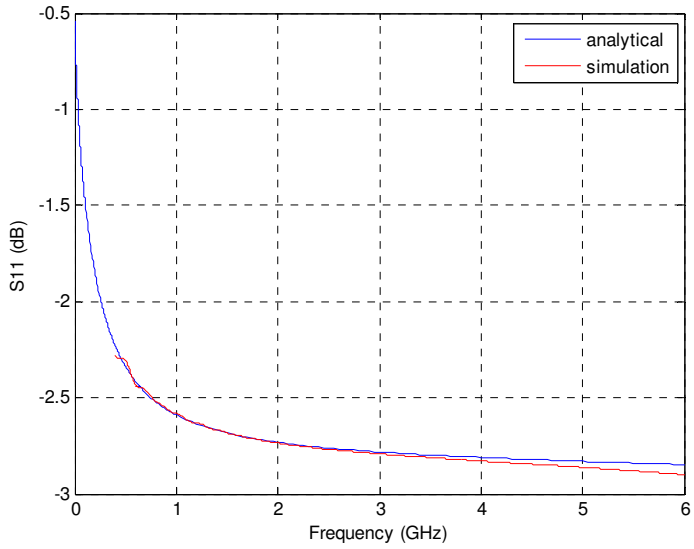

Figure 9.14: Comparison between analytical and simulation approach

It can be observed that the correlation between the simulated model and the analytical approach is very high.

9.2.1.2 Air-Skin-Fat (3 layers)

Following the same procedure as in the previous case, in this section a three layered block phantom is studied. Considering the scheme shown in Figure 6.11 and applying Equation 6.28, the calculated reflection coefficient is plotted in Figure 9.15 for a model with a 2 mm thick skin layer.

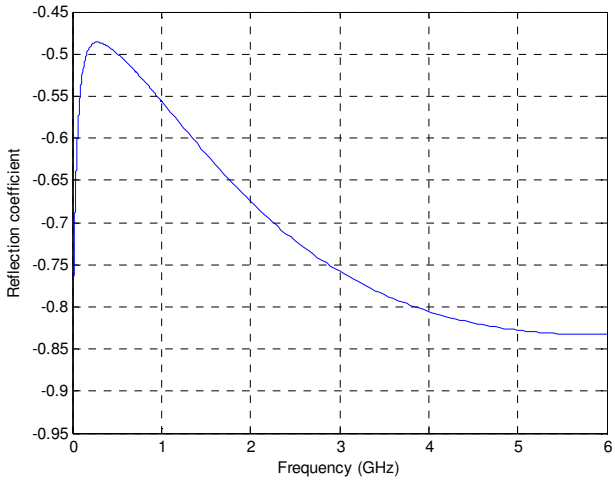

Figure 9.15: Frequency behaviour of the reflection coefficient

Following the same procedure as in the previous section (section 9.2.1.1), but in this case for the fat layer, the comparison between the analytical approach and the simulation is shown in Figure 9.16.

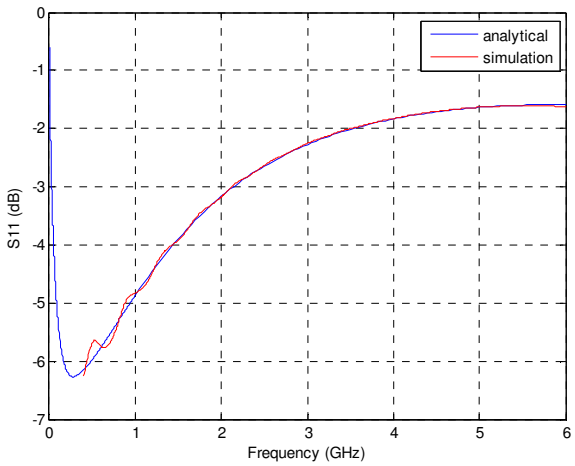

Figure 9.16: Comparison between analytical and simulation approach

As shown in Figure 9.16, very similar results are obtained with both approaches. Once the simulation procedure has been checked, the four layered planar phantom model is analyzed.

9.2.1 Heterogeneous four layered planar phantom analysis

In Figure 9.17 the simulated structure is shown.

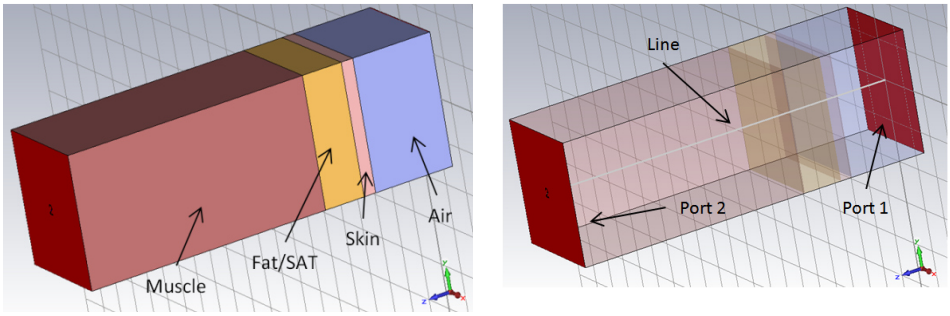

(a) (b)

Figure 9.17: Simulation set up: (a) General overview and (b) Definition of two ports and central line to evaluate the fields.

As mentioned in the beginning of this section, the analysis is based on the typical human tissue distribution for the human torso. According to Table 2.1, the following cases have been studied (Table 9.2).

Table 9.2: Physical dimensions of the proposed phantom

Tissue	*Thickness reported in* [14]	*Sweep*
Skin	*0,8-2,6 mm*	*1-3 mm (1 mm step)*
Fat/SAT	*1,4 – 23,2 mm*	*2-24 (2 mm step)*
Muscle	*0 – 30 mm*	-

Several studies can be made with the proposed model. It has been decided to check the effect of skin and fat/SAT variations for subcutaneous implantable devices. To achieve this goal, a probe has been defined in the interface between fat/SAT and muscle. In the same way, the effect of using fat or SAT will be addressed.

9.2.1.1 Difference between fat and SAT

As explained in section 2.1.3, fat and SAT have similar dielectric properties. SAT can be considered as a mixture of fat with blood. Consequently, the permittivity and conductivity are higher comparing with fat (Figure 9.18).

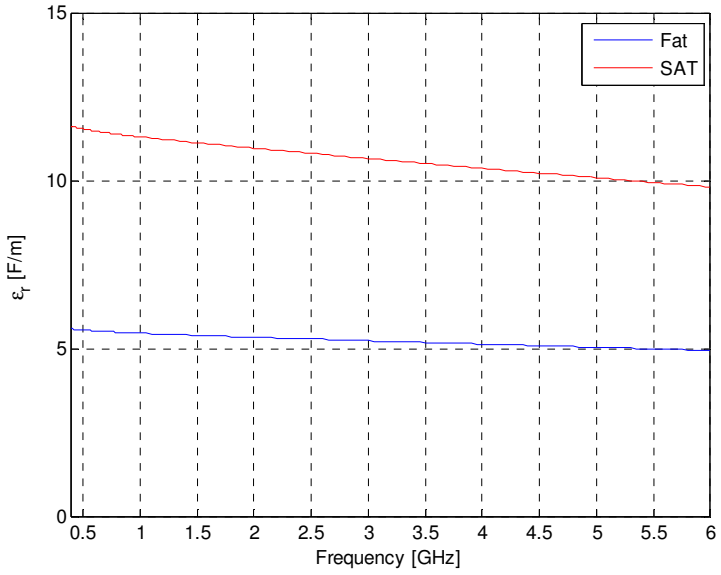

(a)

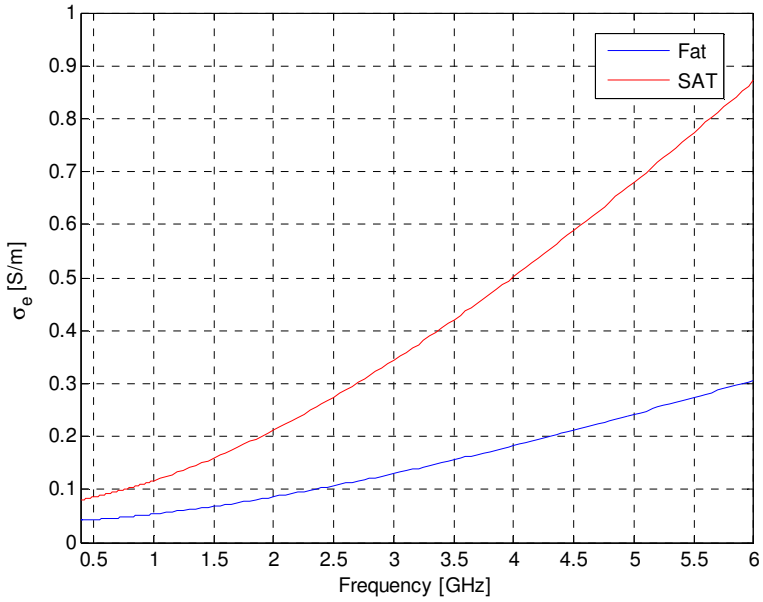

(b)

Figure 9.18: Dielectric properties of fat and SAT tissues: (a) Dielectric constant; (b) Conductivity

In this section, the effect of using fat or SAT is studied because, for example, the Virtual Family from IT'IS foundation uses SAT and that the CST Voxel Family uses fat. Therefore, it has been considered that it is important to analyze the effect of these tissues in the E-field behaviour for subcutaneous implantable devices.

In Figure 9.19, the E-field at the interface between fat/SAT and muscle is shown for a model with a 2 mm thick skin layer and different fat/SAT thicknesses (2 mm, 10 mm and 18 mm).

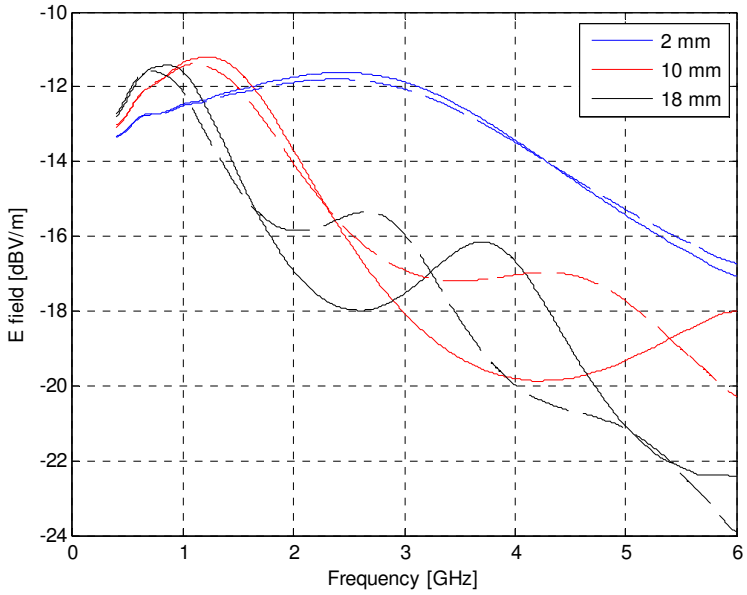

Figure 9.19: E-field frequency behaviour for subcutaneous implants for different fat (solid line) and SAT (dotted line) thicknesses

From Figure 9.19, it can be observed that changing the material from fat to SAT affects the E-field magnitude and its tendency along the frequency. This change is different depending on the thickness of the layer. This is due to the difference in permittivity and conductivity of both tissues.

It can also be observed, that for the lower frequencies (around 400 MHz), the difference between using fat or SAT is not very relevant for the typical thicknesses of this layer, which has been contemplated in the plot.

From this comparison, it can be stated that it is important to characterize properly the dielectric properties of the tissues for subcutaneous implantable devices at frequencies above 1 GHz. The difference that is observed in using fat or SAT is relevant at those frequencies and care should be taken in which model is used.

9.2.1.2 Fat/SAT thickness effect

In this section, the effect of fat/SAT thickness is studied for subcutaneous implanted applications. In Figure 9.20, the obtained E-field in the interface between fat/SAT and muscle is shown for different fat/SAT thicknesses. A 2 mm thick skin layer is used in all the cases.

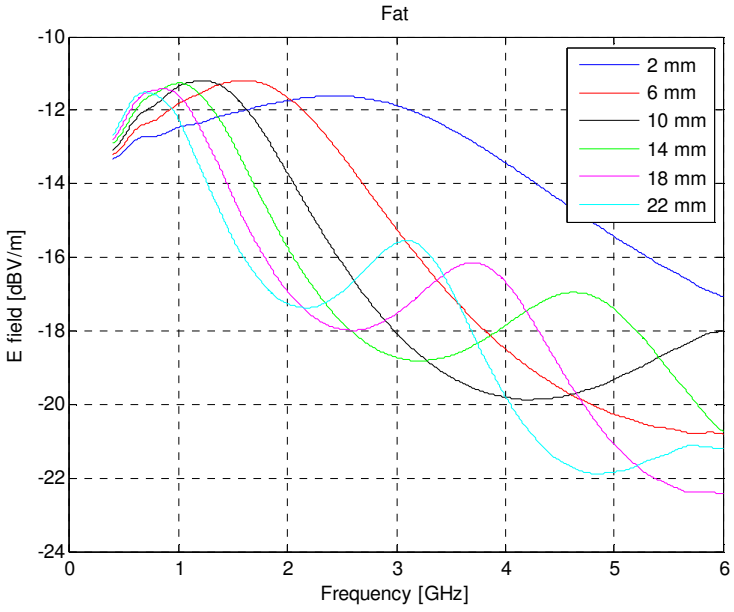

(a)

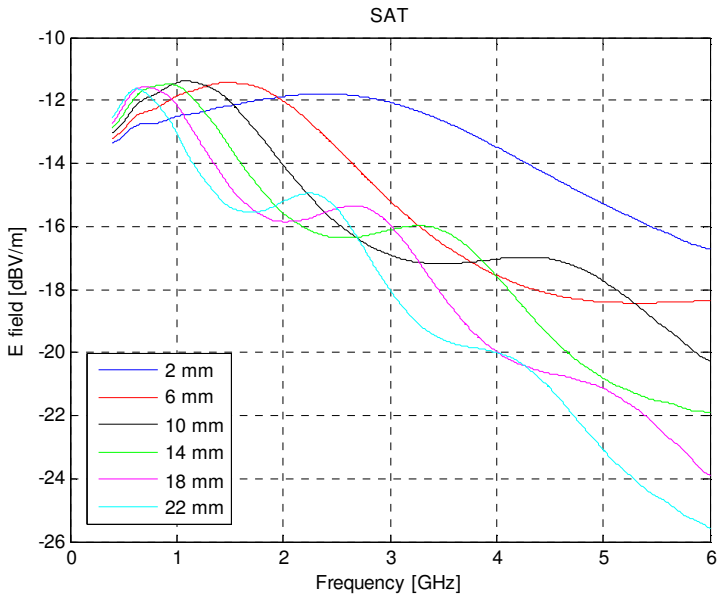

(b)

Figure 9.20: E-field frequency behaviour at the interface between fat/SAT and muscle layer: (a) fat and (b) SAT

In the previous figure, it can be observed that several phenomena related to the thickness of fat/SAT layers take place.

When the fat/SAT layer is increased, the oscillation of the E-field amplitude is more acute, since more relative E-field maximums can be observed. This effect could be explained as a result of the generation of constructive and destructive interferences between the incident and reflected waves in the boundary between fat/SAT and muscle. This effect becomes important in the observed frequency range when fat/SAT thicknesses are comparable to a multiple of the wavelength (λ).Tissue sequences like these lead to standing-wave effects in the low-permittivity layer (fat/SAT) in between two high permittivity layers.

Another effect that can be observed is that the peaks of the E-field shift to the left when increasing the thickness of the fat/SAT layers.

There are certain frequency ranges for each thickness in which increasing the frequency does not decrease the E-field magnitude. This is very interesting since it shows that going down in frequency is not always a synonymous of having more E-field magnitude.

The main advantage of the low frequencies is that the E-field magnitude is quite independent from the thickness of fat/SAT. This happens because, at lower frequencies, the thicknesses are not comparable to the wavelength as shown in Table 9.3 and, consequently, no standing waves are created in the fat/SAT layer.

Table 9.3: Wavelength for different tissues and frequencies

Freq (GHz)	*λ (mm)*				
	Air	*Skin*	*Fat*	*SAT*	*Muscle*
0.402	*749.5*	*104.5*	*313.1*	*217.3*	*95*
0.868	*344.6*	*52.3*	*146.7*	*101.8*	*45.7*
2.45	*122.4*	*19.7*	*53.1*	*37*	*16.7*
5.8	*51.7*	*8.6*	*23.1*	*16.3*	*7.3*

This issue is crucial for a long-term implantable devices since as human tissue distribution changes with time, the use of lower frequencies have clear advantages.

9.2.1.3 Skin thickness effect

In this section the effect of changing the skin thickness on the E-field behavior at fat/SAT-muscle interface (subcutaneous implant) is addressed. In Figure 9.21, different cases are shown to understand its effect for different SAT thicknesses (the same effect has been observed when fat is used). The skin thickness is studied for 1, 2 and 3 mm.

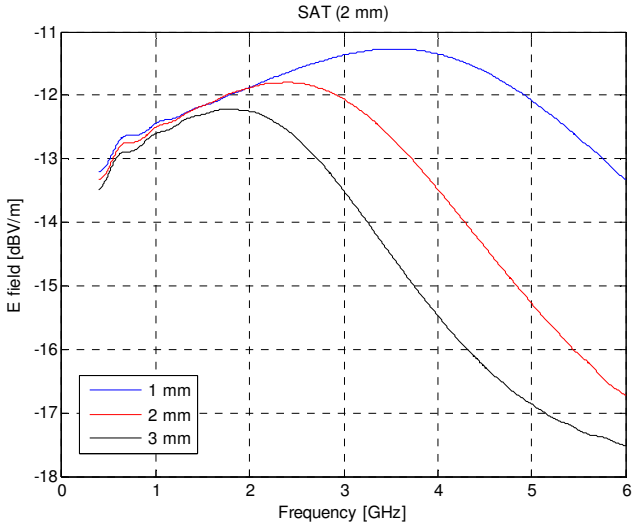
SAT (2 mm)
E field [dBV/m]
Frequency [GHz]
1 mm
2 mm
3 mm

(a)

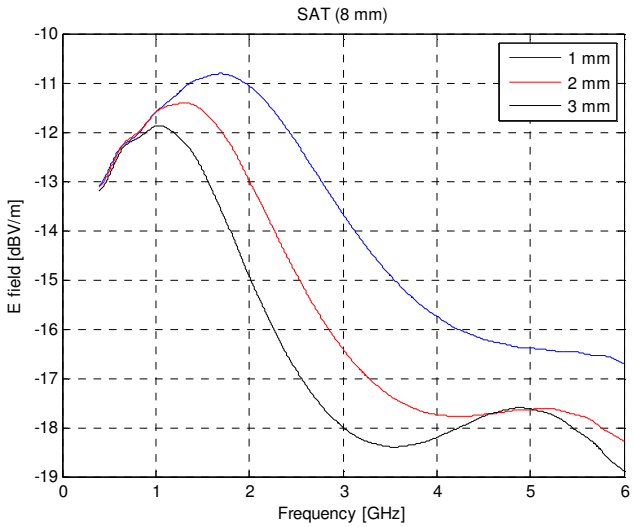
SAT (8 mm)
E field [dBV/m]
Frequency [GHz]
1 mm
2 mm
3 mm

(b)

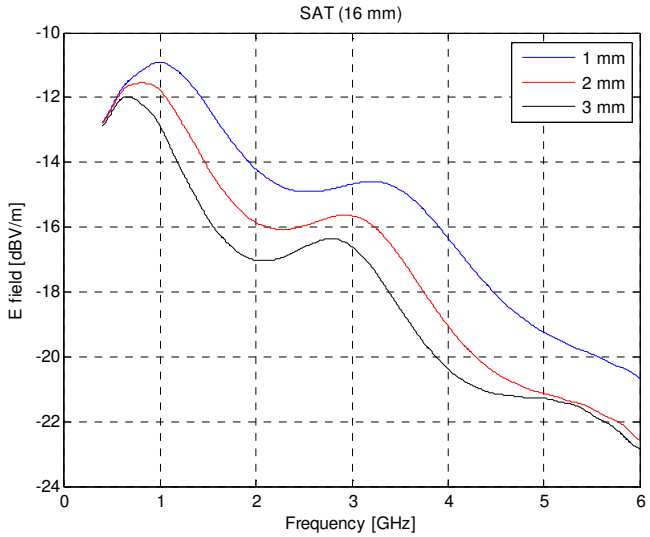

(c)

Figure 9.21: Skin's thickness effect in E-field's frequency behaviour for different SAT thicknesses: (a) 2 mm, (b) 8 mm and 16 mm

It can be observed that the main effect of the skin's thickness is that the E-field (in magnitude) goes down and that the peaks of the electric field shift to the left in the frequency domain while increasing the thickness. Skin layer is a high water content tissue and, consequently, its conductivity is high. This explains that when the skin thickness is increased the main effect is that the E-field magnitude decreases because the incoming wave has to travel more distance in this layer with a high attenuation constant. Depending on the SAT thickness and working frequency, the change is considerable.

As a general conclusion, it can be stated that the electric field distribution in first human body tissues is very variable with the properties and dimensions of skin and fat/SAT layers. It can also be stated that the main advantage of using low frequencies is that the E-field is stable for skin and fat/SAT variations. The maximum obtainable E-field, however, is not for the lower frequency case, but

its value and frequency are very dependent on the phantom's characteristics. When the thickness of fat/SAT layers are comparable to the wavelength (λ), standing wave effects appear in fat/SAT layers. As a result, the E-field distribution presents relative maximum levels at certain frequencies for subcutaneous implanted devices. Depending on the location and the desired working frequency for an implant, these issues must be considered.

This model is a simplification of a real human body phantom. In the next section, an analysis with more realistic geometries is addressed using Voxel models.

9.3 Voxel phantom analysis

In this section the results obtained with voxel models are presented. First of all, the results obtained with the Virtual Family from IT'IS foundation are shown. For all the models the same procedure as the one described in section 0 is applied.

The tissue distribution of the phantom depends on two main factors: the resolution of the phantom and the resolution of the mesh. After some preliminary simulations to check the accuracy and simulation time for human's torso, it has been decided that a phantom's resolution of $1\mathrm{mm}^3$ and a mesh grid with the same resolution strike a balance between accurate results and a reasonable simulation time.

As it has been presented in section 2.3.2.2, there are four different models in the Virtual Family. Firstly, Duke is analyzed (Figure 9.22)

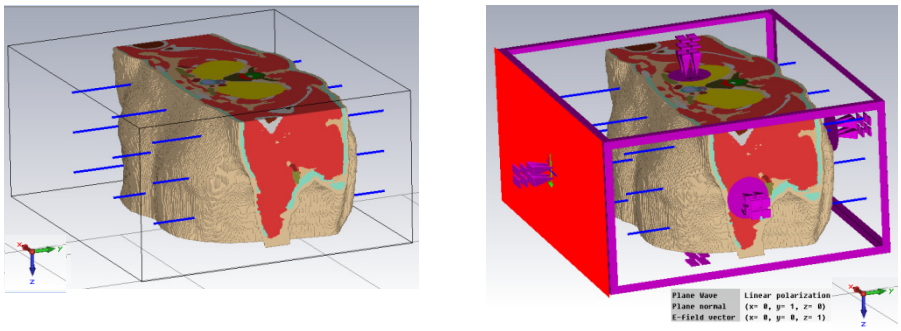

(a) **(b)**

Figure 9.22: Duke's torso simulation set-up

As the human tissue distribution in this kind of models is not planar and as it is difficult to estimate the exact transitions between the different tissue layers, the E-field behavior along the central line has been monitored. In Figure 9.23, the E-field magnitude is plotted in dBV/m along the central curve for the four frequencies of interest. The distance of 0 mm represents the interface between air and phantom model.

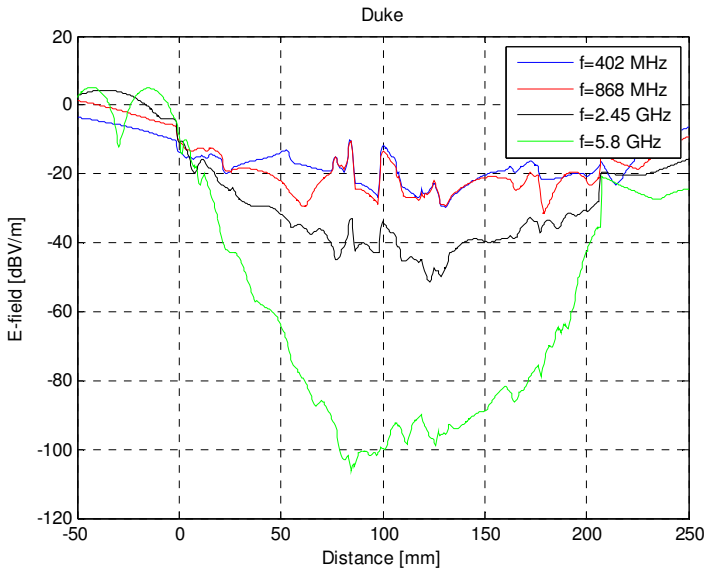

Figure 9.23: E-field behaviour along the central line

It can be observed that the E-field has more attenuation when the frequency is increased. For f=402 MHz and f=868 MHz the difference is not very considerable. It can be concluded that, for deeply implanted systems such as devices implanted in the stomach, with lower frequecies, the obtainable E-field magnitude is much higher than when higher frequencies such as f=2.45 GHz or f=5.8 GHz are used. This happens because the losses produced in the different tissues increase with the working frequency.

However, for subcutaneous implanted systems, as the propagating wave does not cross that many tissues, the E-field magnitude in small distances from the air-body interface, is not always higher for the lower frequencies. In Figure 9.24, a zoom of Figure 9.23 is done to see this effect.

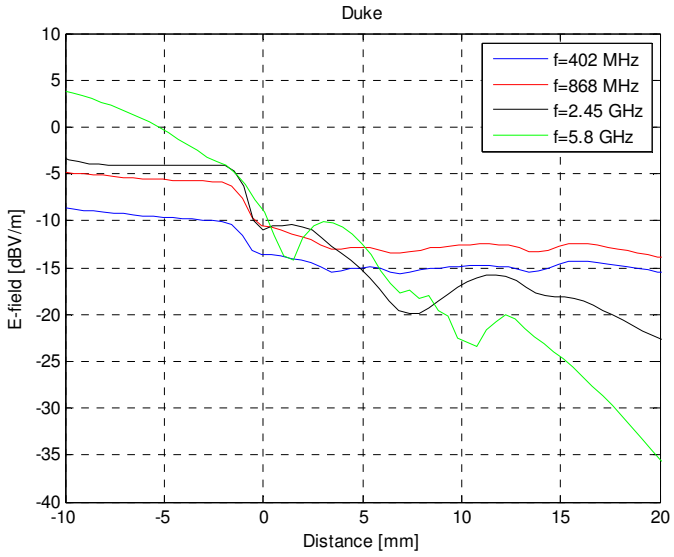

Figure 9.24: E-field behaviour along the central line in air-phantom interface zoom in

For distances of some milimeters from the air body interface, the E-field magnitude can be higher for higher frequencies. For example, for a distance of 3 mm from the air-body interface, the E-field magnitude is higher at 5.8 GHz.

It shoud be pointed out that, as it has been observed with the heterogenous layered planar phantom, at higher frequencies changes in the tissue properties (thickness, dielectric constant or conductivity) have more influence on the E-field.

It is difficult to compare the obtained results with the ones computed in the previous heterogeneous planar layered phantom models, since the geometry in the voxel case is very complex and multiple reflections are produced between layers. For instance, in the heterogeneous model, the E-field distribution is not affected by the transversal boundaries (with respect to the propagation direction), which are defined as infinite.

In order to compare both approaches, it is necessary to estimate the exact thicknesses of skin, fat/SAT and muscle layers of the voxel. In Figure 9.25, the tissue distribution of Duke's torso is shown with a mesh cell size of $1\ \mathrm{mm}^3$.

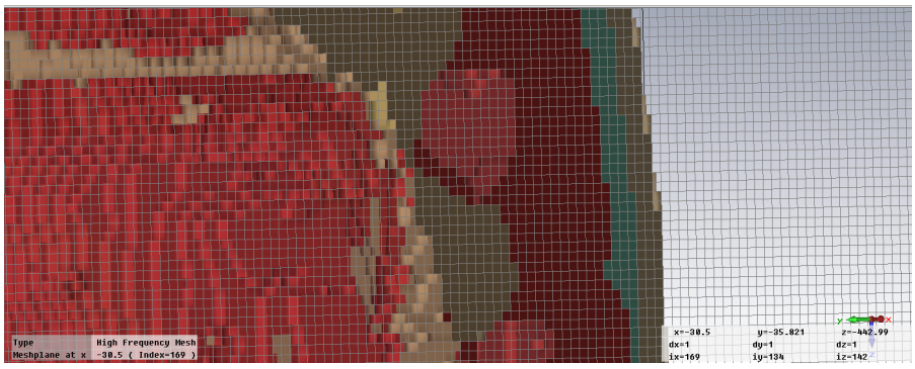

Figure 9.25: Tissue distribution of Duke's Torso

It is estimated that a skin layer of 3 mm and SAT layer of 3 mm is representative to compare Duke's results with the corresponding four layered planar phantom model (Figure 9.26).

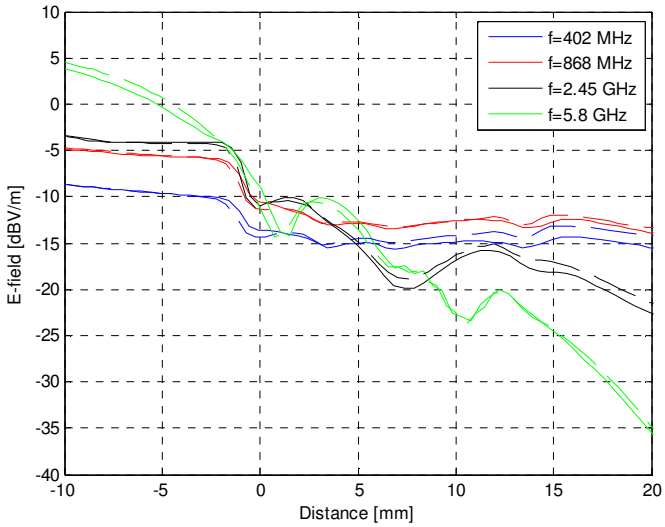

Figure 9.26: Comparison between Duke voxel model (solid lines) and its equivalent four layered planar phantom model (dotted lines)

The behaviour is very similar for both models. The latter demonstrates that the four layered planar phantom model is a useful tool to make estimations for the impact of different tissues and for preliminary simulations focused on the design of subcutaneous implantable devices.

For voxel simulations, the required computer features are important since the models are very complex and the number of mesh cells increase significantly when compared to planar layered phantoms. In Table 9.4, the main features of the computer that is used for these simulations are shown.

Table 9.4: Computer's features

Software	*Windows 7 Professional 2009*
Processor	*Inter(R) Xeon(R) CPU X5272 @ 3,40 GHz*
RAM	*48GB*
System type	*64 bits Operative System*

The use of layered planar phantom models reduces the computation time and the required computer resources significantly (Table 9.5)

Table 9.5: Simulation properties for the phantom models

Phantom model	*Layered planar model*	*Voxel model*
Number of mesh cells	*217000*	*25108456*
Simulation time	*7 min*	*3 h 50 min*

Three million meshcells are estimated to take 1 GB of RAM memory to compute. Then according to Table 9.5, 8,4 GB are necessary to simulate the voxel model whereas only less than 100 MB are required for the layered phantom.

It should be pointed out that, depending on the application and the working frequency, a smaller part of the torso can be used. Thus, the number of mesh cells would decrease as well as the simulation time.

Once the Duke model has been analyzed, the obtained results for the rest of the Virtual Family voxels are presented. In Figure 9.27, Figure 9.28 and Figure 9.29 the obtained E-field behaviour in the central line for Ella, Billie and Thelonious are shown, respectively, as representatives of the female mature population and female and male youngsters (Table 2.5).

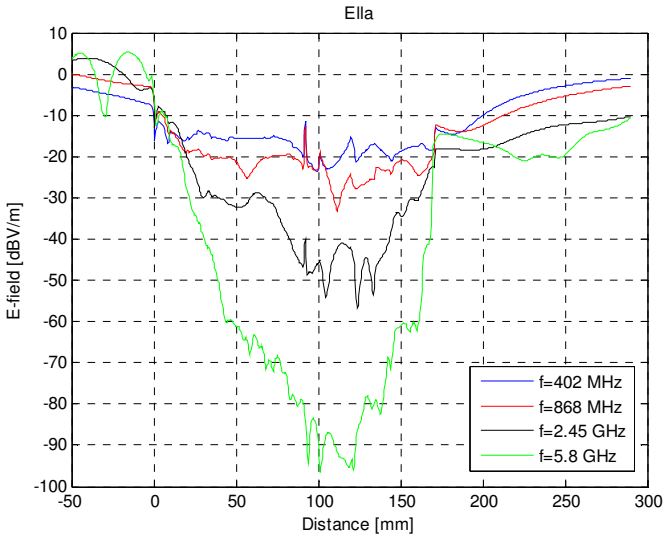

(a)

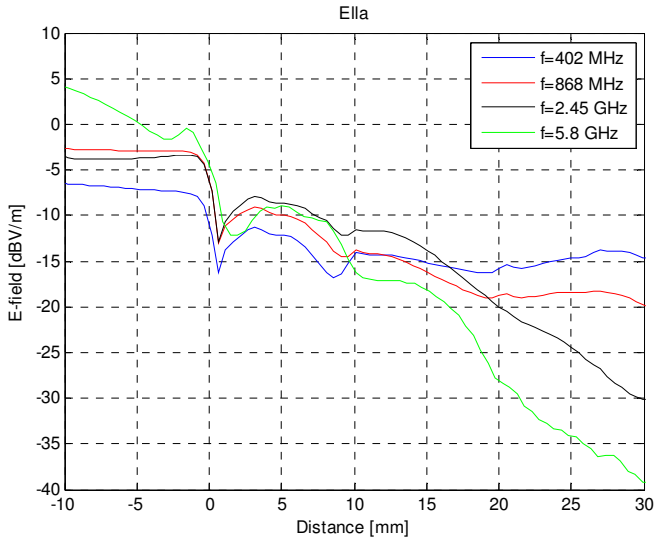

(b)

Figure 9.27: E-field behaviour along central line for Ella model: (a) full range and (b) air-phantom interface zoom in

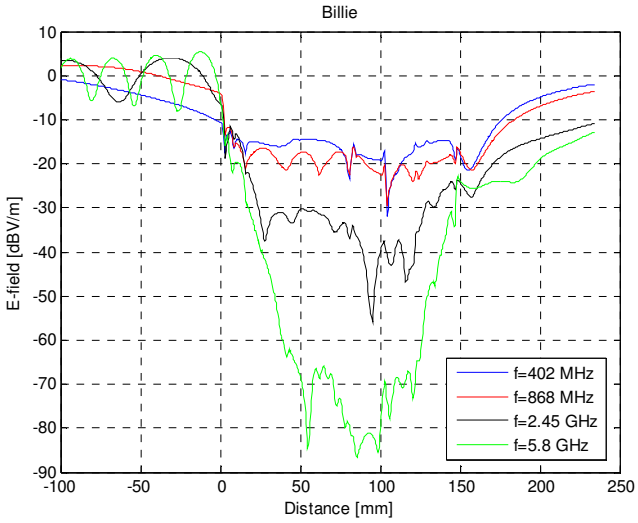

(a)

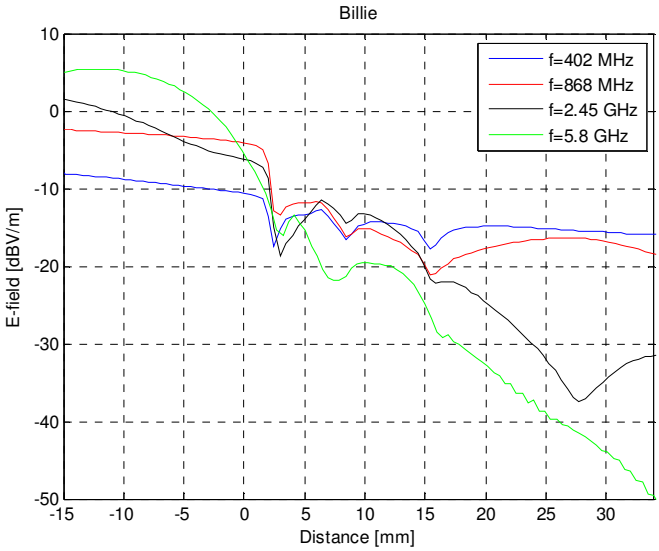

(b)

Figure 9.28: E-field behaviour along central line for Billie model: (a) full range and (b) air-phantom interface zoom in

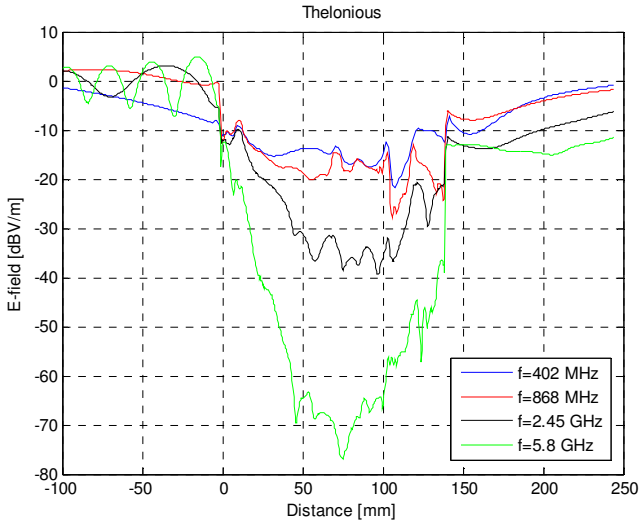

(a)

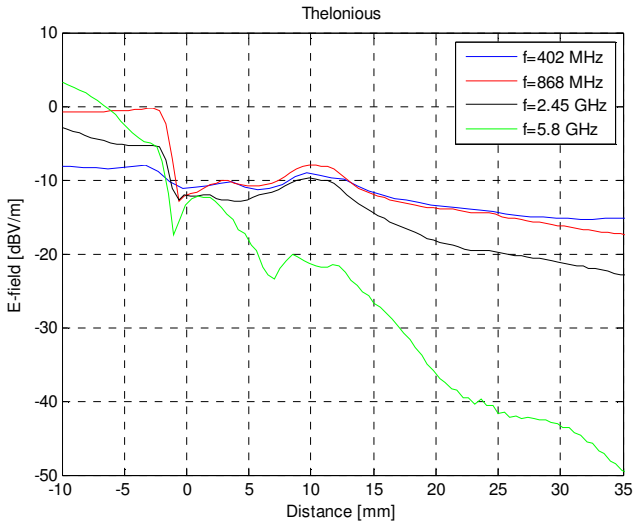

(b)

Figure 9.29: E-field behaviour along central line for Thelonious model: (a) full range and (b) air-phantom interface zoom in

Same conclusions obtained with Duke's model can be extracted from these models.

In the first place, in Figure 9.23, 9.27a, 9.28a and 9.29a, it can be observed that in all cases, for deeply implanted devices, due to the attenuation of the E-field, the use low frequencies is recommendable since a higher E-field magnitude can be obtained.

However, for subcutaneous implantable applications, higher frequencies can be used. It can be appreciated in Figure 9.24, 9.27b, 9.28b and 9.29b, that the E-field distribution for higher frequencies near the interface between air-phantom is very dependent on the tissue distribution and the tissue properties.

As expected, the E-field distribution, especially near the air-phantom interface, is different for each voxel because the properties of the tissues change. For instance, in Duke's model (Figure 9.24) at 3 mm from the air-phantom interface, the E-field magnitude at 5.8 GHz is 5dB higher than at 402 MHz. However, for the same distance this effect is not appreciable in the rest of models.

It is not possible to establish an optimum frequency for the design of subcutaneous implantable devices. It can be stated that for long term applications, the use of lower frequencies make the device more robust to changes in the body composition.

It can be concluded that voxel models are an interesting tool for the design of implantable devices. Taking into account the obtained results, it can be stated that depending on the location and restrictions of the designed implant, the implant must be tested using different phantom models. This is essential for commercial applications, as the implant must work under different conditions (each person has a different tissue distribution).

As a final remark, the CST voxel family has been also simulated under the same conditions. The main difference that should be pointed out, is that in the CST voxel family, SAT tissue is not considered. The obtained results are summarized in Appendix C. Consequently, as it has been demonstrated in

section 9.2.1, the obtained results are different. This reinforces the previously exposed idea that states that, to be sure that an implantable device is suitable for the general population, the design must be tested under different phantom models to check whether the design is robust to the different human body characteristics.

As a matter of fact, in some cases and, depending on the application, the implanted system must be designed individually for each person, or in other words, if the implant is standardized, once the system is implanted, some adjustments will be necessary to adapt the implant to the specific characteristics of the person. As a consequence, the system may require more retuning processes if the implant is for the long-term since the tissue distribution changes with time.

Chapter 10

Conclusions and areas for further research

In this research work, a characterization and optimization of wireless links for implanted applications and the feasibility study of using inkjet printing technology for the fabrication of flexible coil-antennas have been addressed.

The analysis and results of this research work are divided into three parts: inkjet printing technology analysis, implanted links in the near field and the far field systems.

10.1 Inkjet printing technology

- **The feasibility study of using inkjet printing technology for the fabrication of implanted antennas has been performed.**

The procedure to fabricate reliable and repeatable conductive tracks into flexible substrates has been explained by describing the main steps in the

fabrication process that affect the final performance of the printed tracks using the Dimatix Material Printer DMP2800. Printing parameters like plate temperature, input nozzle signals, carriage height etc have been carefully tuned to provide repeatable and accurate results.

- **A resolution study in terms of minimum obtainable track width and an estimation of thickness of each printed layer has been addressed.**

With the used equipment and the selected procedure, the minimum printable track width is 50 μm and the thickness of each layer is 0,8 μm.

- **The conductivity of a representative conductive silver ink, Sunjet U5714, has been characterized by following a rigorous procedure.**

The obtained value with the employed sintering process (200ºC for 30 min) is $8 \cdot 10^6 (\Omega \mathrm{m})^{-1}$, which is 13% of the pure silver conductivity.

10.2 Near field systems

- **The impact of canonical configurations of LC tanks in the primary and secondary of a near field system´s figures-of-merit has been analyzed. They include maximum power transfer efficiency, bifurcation phenomena and needed compensations, which have been carefully described from a theoretical point of view and corroborated by simulations and measurements.**

The main characteristics of each topology are summarized in Table 10.1.

Table 10.1: Main characteristics of each topology

Topology	$Re\{Z_r\}\|_{\omega=\omega_0}$	$Im,\{Z_r\}\|_{\omega=\omega_0}$	*Compensation capacitor on primary circuit (C_p)*	*Bifurcation-free condition*
SS	$f(M,\omega)$	*0*	*Independent of secondary circuit*	$Q_p > \frac{4{Q_s}^3}{4{Q_s}^2-1}$
SP	*Maximum*	*f(M,ω)*	$f(M,L_s)$	$Q_p > Q_s + \frac{1}{Q_s}$
PS	$f(M,\omega)$	*0*	$f(M,R_L)$	$Q_p > Q_s$
PP	*Maximum*	*f(M,ω)*	$f(M,L_s,R_L)$	$Q_p > Q_s + \frac{1}{Q_s}$

Efficiency analysis

According to Table 10.1, when series compensation is used in secondary circuit, the obtained Z_r is purely real and its value is not a maximum or minimum, whereas in parallel compensation, $Re\{Z_r\}$ is maximum and at resonance Z_r is complex. The real and imaginary parts of the reflected impedance are related to efficiency.

In SP topology, the efficiency has a local maximum with respect to frequency, and it is always at the resonant frequency of the system. For higher frequencies the efficiency is lower. On the contrary, in SS topology, the efficiency does not have a maximum value at the resonant frequency. A boundary frequency has been deduced to decide which topology is more efficient depending on the parameters of the design.

The use of low frequency of operation in implanted applications has favored the use of SP topology since it offers higher efficiencies for low frequencies. However, the use of higher frequencies will make SS topology an interesting approach for implanted communications.

Compensation capacitance on primary circuit (C_p)

In SS topology the needed compensation capacitance on primary side (to resonate at same frequency as secondary circuit) is independent from the coupling coefficient (Table 10.1). This property makes SS topology an excellent candidate for applications in which the coupling coefficient is not fixed, such as implanted applications. In these applications, due to the change of media, the difficulty of having a constant distance or exactly the same angle between the implanted and the external coil, the coupling coefficient of the system is variable. Consequently, the SS topology has a clear advance in this respect.

Bifurcation free condition

The bifurcation free condition must be verified for each topology when maximum power transfer efficiency is desired.

PS and PP topologies are not usually employed since they do not offer any special advantage for implanted systems with respect to SS and SP topologies.

- **The potential of using inkjet printing technology to fabricate implanted coil-antennas has been also investigated. A general methodology for the design, simulation, fabrication and measurement process has been explained.**

It has been demonstrated that the resistance can be controlled by the capability of this technology of varying the track thickness. Q values ranging from 4 to 10 can be obtained while keeping the same inductance value. These Q values are small compared to the typical values obtained with subtractive etching, which can be higher than 120. However, depending on the application the obtained Q values with inkjet printing technology are good enough. In some cases, such as NFC applications where the desired read range is smaller for security reasons,

it is even better since it allows the removal of typical damping resistance in current NFC inductors [54].

- **The effect of using an inkjet printed prototype as secondary coil has been studied in terms of needed compensation on primary circuit, bifurcation-free condition and efficiency. In all cases, the effect of the internal resistance of the secondary coil on these parameters has been considered.**

When SS topology is used, the **compensation capacitance C_p** is independent from the internal resistance of the used coils. However, in the rest of topologies C_p is affected by the internal resistances. Consequently, if inkjet printed prototypes are used, it is important to check its influence, since depending on the circuit parameters the change is considerable. For implanted applications (k=0.05) the change of C_p with the internal resistance is not important. Therefore, it can be concluded that in terms of needed compensation, the use of inkjet printed prototype as secondary coil does not change the behavior of the system.

The efficiency when inkjet printing prototype is used as secondary coil is lower since more losses are introduced in the system due to the higher value of the internal resistance. A balance between flexibility and efficiency should be carefully struck.

The bifurcation-free conditions are also affected by the internal resistance of the secondary coil (R_s). For SS and PS topologies, the increase of R_s is not a problem, since the coupling coefficient which produces bifurcation in the system increases. Nonetheless, opposite behavior is produced when SP and PP topologies are used. Consequently given a pair of coils separated a certain distance (in other words, certain coupling factor), if the secondary coil is substituted by an inkjet printed one, and SS or PS topologies are used, the system will continue to be stable and the coils can be brought closer. On the

contrary, if SP or PP topologies are used, depending on the circuit elements, the system could be in the bifurcation region, being necessary to move away the coils a certain distance. Therefore SS and PS are the recommended topologies for implanted inkjet based applications for systems that work very close to the bifurcation-free condition.

- **The feasibility study of using the antenna coil not only as a part of the communication system, but also, for sensor purposes by adding a capacitor has been described (sensor-antenna approach).**

It has been concluded that with series compensation at primary side, a change of the secondary capacitor can be measured at primary circuit independently from the coupling coefficient of the system. A resolution of 140 kHz per 1 pF capacitance variation has been estimated.

10.3 Far field systems

A simulation strategy for implant communications has been explained based on a combination of analytical, computational and experimental approaches. Different phantom models have been used and characterized by describing their advantages and disadvantages.

- **Homogenous phantoms have been analyzed.**

The characterization of cost effective sugar based tissue simulating liquid phantom has been done, explaining the fabrication and measurement techniques for the correct dielectric characterization of these kinds of phantoms.

The frequency band where these phantoms can be used has been analyzed. It has been concluded that the conductivity of the water solution is the parameter

that limits the frequency band. For frequencies higher than 1,5 GHz, the conductivity of typical recipes based on sugar for skin or muscle tissues is higher than the target conductivity and there is no chance to decrease the conductivity. Consequently, for frequencies higher than this limit, the obtained recipes have more conductivity than the desired one. This error can be assumed for subcutaneous implanted devices, but it cannot be assumed when devices that are deeply implanted are analyzed.

- **The procedure for measuring the attenuation of a plane wave in a human torso modelled by a homogenous muscle phantom for different frequencies in an anechoic chamber has been described.**

With the proposed methodology and set up the expected results have been obtained for f= 2.45 GHz and f= 5.8 GHz. Nevertheless, undesired reflections that disturb the results have been obtained and discussed for f=402 MHz and f=868 MHz case.

With this procedure and the obtained results, the simulation tool that is used for more complex phantoms has been validated.

- **A heterogeneous layered planar phantom has been analyzed using simulation and analytical approach.**

Two and three layers phantoms have been used to compare the simulation results with the analytical results obtaining very high correlations.

The effect of the skin and fat/SAT layers on the E-field behaviour has been studied with a four layered planar heterogeneous phantom to model the human torso. It has been concluded that for subcutaneous implanted applications, the E-field behaviour is very dependent on the tissue distribution and that it is difficult to establish an optimum frequency for subcutaneous implanted devices. Different skin and fat/SAT thicknesses have been tested to get to this

conclusion. However, for deeper implanted devices, the use of low frequencies is very recommendable since the E-field attenuation is much higher when the frequency is increased.

- **Voxel models have been used to study the E-field behaviour in human torso.**

Virtual Family from IT'IS foundation and CST Voxel Family models have been simulated under same conditions. The simulations have been put in relation to analytical models and measurements to get to a comprehensive approach for the proper characterization of the voxel models. An optimization of the mesh, electromagnetic excitation, boundaries, voxel resolution, computational time and size of the phantom has been explained.

The simulation of the Virtual Family from IT'IS foundation with CST has been very challenging and no previous documentation has been found related with it. To ensure that the obtained results are reliable, Duke voxel model from IT'IS foundation has been compared with its corresponding four layered planar heterogeneous phantom obtaining very similar values.

This demonstrates that the Virtual Family has been simulated successfully with CST and at the same time it demonstrates the suitability of the four layered planar phantom model for the design process of subcutaneous implanted applications. With this simplified model, the necessary computational requirements decrease significantly.

Virtual Family from IT'IS foundation uses SAT material as the tissue beneath the skin, contrary to CST Voxel family that uses fat. Therefore, mainly for subcutaneous applications, both families are not comparable. This conclusion is based also in the analysis of the four layered planar heterogeneous model where it has been shown that the E-field behaviour changes when these tow tissues are compared.

In some cases, like in Duke's torso, the E-field magnitude in the interface of fat/SAT and muscle is higher at higher frequencies. This demonstrates that decreasing the frequency is not always the best option to have more E-field in subcutaneous implanted devices, contrary to the result obtained with the homogeneous model.

10.4 Areas for further research

During this work, several topics have been found that deserve further research.

- **Effect of human body in system based on near field approach**

In this research work a coupling coefficient of k=0,05 has been used for representing the implanted conditions in systems based on inductive coupling. However, it should be pointed out that the insertion of the secondary coil in the human body may also introduce other effects. It is necessary to study this effect using CST MWS and to insert the antenna in human body models. The effect of the body could be represented as capacitances or resistances in series or in parallel with the proposed systems. Besides, when the antenna is inserted in biological media, it is necessary to encapsulate it. An exploration of the effect of the encapsulation on the performance of antenna should be also addressed.

In this context, a deeper study on the proposed **sensor-antenna approach** is needed including the aforementioned effects of human body.

- **Design of coil antennas for implantable devices**

In this research work, the coil-antenna that has been used is not optimum for implantable devices due to its size. This antenna, that fulfils the ISO 7810 standard [112], has been used to make a proof of concept. It will be very

interesting to find smaller and conformal coil antennas that could be adapted to different shapes inside the human body. New fabrication techniques like inkjet printing technology are promising to achieve totally biocompatible and flexible antennas that will allow countless number of new applications.

- **Voxel simulation model deeper study**

As it has been described in this project there are different modesl with different tissues properties and distributions that affect the behaviour of the E-fields inside the human body. Deeper analysis is needed to compare CST Voxel Family and Virtual Family from IT'IS foundation models and check its reliability by comparing the results with real implanted systems.

- **Human tissue distribution effect on implanted communications**

In this research work a first approach to characterize an implanted system using different phantom models have been addressed. However, further research using real antennas would be very interesting rather than using probes in the simulations, since depending on the antenna's properties, the behaviour of the E-field observed in this work could be changed.

- **Deeper optimization in the fabrication process of inkjet printing technology**

In this research work the procedure for fabricating repeatable and reliable conductive tracks into flexible substrates has been developed. However, deeper analysis would be very interesting to improve the performance.

Using of the DMC-11601 1pL Cartridge

The use of this cartridge will allow much more resolution and this issue could be key to be able to design very small implantable antennas. Considering that the

size of the nozzle of the cartridge that has been used in this project is 21 μm, and that DMC-11601 1pL Cartridge has 9 μm, the minimum obtainable track width could be decreased from 50 μm to around 20 μm.

Sintering process optimization

The sintering process is a crucial process that determines the final behavior of the printed prototypes. It would be interesting to study the optimum temperature-time process to decrease the resistance of the tracks.

There also other post deposition treatment techniques such as using microwave radiation [121] that could be interesting. Ceramics and other dielectric materials can be heated by microwaves due to dielectric losses that are caused by dipole polarization. Under ambient conditions, however, metals behave as reflectors for microwave radiation, because of their small skin depth. Nevertheless, when instead of bulk material, the material consists of particles, it absorbs microwave radiation to a greater extent. This technique is quite new and the main reasons for successful heating of metallic particles through microwave radiation are not yet fully understood. The main bottleneck in inkjet printed features on flexible substrates is the low softening point T_g of the substrates, which limits the processing temperature. With this new method, new substrates could be used with inkjet printing technology.

- **New substrates and inks for inkjet printing technology**

Inkjet printing technology will allow the fabrication of completely bio compatible antennas that will open an increasing number of new applications. Some preliminary studies about the use of PDMS (PolyDisemthylSiloxane) substrate have been made (Figure 10.1).

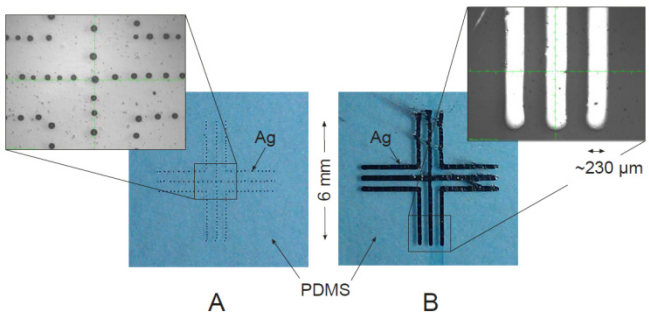

Figure 10.1: Printed prototypes in PDMS substrate: (a) With no treatment and (b) with oxygen plasma treatment (30s, 100 W)

As it can be observed due to the hydrophobic characteristic of PDMS, a surface treatment is necessary to get continuous tracks (Figure 10.1b), otherwise, the ink drops are deposited does not form a continuous structure (Figure 10.1a).

PDMS is biocompatible and consequently in the near future when inks based on Au or Pt are developed, inkjet printing technology will be a very promising fabrication technique for the fabrication of flexible and totally biocompatible materials.

References

[1] Technology Review by MIT, “Annual list on 10 emerging technologies 2010.” .

[2] J. Bakker, *Dosimetry of exposure to electromagnetic fields in daily life and medical applications*. Erasmus Universiteit Rotterdam: , 2012.

[3] A. Christ, M. G. Douglas, S. Member, J. M. Roman, E. B. Cooper, A. P. Sample, B. H. Waters, J. R. Smith, and N. Kuster, “Evaluation of Wireless Resonant Power Transfer Systems With Human Electromagnetic Exposure Limits,” vol. 55, no. 2, pp. 265–274, 2013.

[4] Jonna Wilén, “Radiofrequency fields – exposure, dose and health,” *UMEÅ UNIVERSITY MEDICAL DISSERTATIONS*, 2002.

[5] *Exposure to high frequency electromagnetic fields, biological effects and health consequences (100 kHz-300 GHz)*. .

[6] C. J. Schilling, “Effects of exposure to very high frequency radiofrequency radiation on six antenna engineers in two separate incidents,” *Occupational Medicine, Oxford Journals*, vol. 50, no. 1, pp. 49–56, 2000.

[7] Y. H. Peter S. Hall, *Antennas and Propagation for Body-Centric Wireless Communications*. Artech House: , 2006.

[8] C. Koch, W. Mokwa, M. Goertz, and P. Walter, “First results of a study on a completely implanted retinal prosthesis in blind humans,” *2008 IEEE Sensors*, pp. 1237–1240, Oct. 2008.

[9] Y.-X. Guo, D. Zhu, and R. Jegadeesan, “Inductive wireless power transmission for implantable devices,” *2011 International Workshop on Antenna Technology (iWAT)*, pp. 445–448, Mar. 2011.

[10] C. H. D. Cynthia Furse, Douglas A. Christensen, *Basic Introduction to Bioelectromagnetics*, 2nd ed. .

[11] F. S.Barnes and B. Greenebaum, *Bioengineering and Biophysical Aspects of Electromagnetic Fields*. CRC Press: , 2007.

[12] J. C. Lin, *Electromagnetic Fields in Biological Systems*. CRC Press, Taylor & Francis Group: .

[13] “Agilent Basics of Measuring the Dielectric Properties of Materials (5989-2589EN),” Application note. Agilent Technologies, 2006.

[14] A. Christ, A. Klingenböck, T. Samaras, C. Goiceanu, and N. Kuster, “The Dependence of Electromagnetic Far-Field Absorption on Body Tissue Composition in the Frequency Range From 300 MHz to 6 GHz,” vol. 54, no. 5, pp. 2188–2195, 2006.

[15] V. Spitzer, M. J. Ackerman, a L. Scherzinger, and D. Whitlock, “The visible human male: a technical report.,” *Journal of the American Medical Informatics Association*, vol. 3, no. 2, pp. 118–30, 2006.

[16] J. Wang, O. Fujiwara, and S. Watanabe, “Approximation of Aging Effect on Dielectric Tissue Properties for SAR Assessment of Mobile Telephones,” *IEEE Transactions on Electromagnetic Compatibility*, vol. 48, no. 2, pp. 408–413, May 2006.

[17] A. Arriola, “Design and Analysis of Planar and Low-Profile Antennas for Body Area Networks at 2.45 GHz,” Tecnun - University of Navarra, 2011.

[18] A. Arriola, *Design and Analysis of Planar and Low-Profile Antennas for Body Area Networks at 2.45GHz*. 2011.

[19] S. Gabriel, R. W. Lau, and C. Gabriel, “The dielectric properties of biological tissues: III. Parametric models for the dielectric spectrum of tissues.,” *Physics in medicine and biology*, vol. 41, no. 11, pp. 2271–93, Nov. 1996.

[20] C. Gabriel, S. Gabriel, and E. Corthout, “The dielectric properties of biological tissues: I. Literature survey,” *Physics in medicine and biology*, vol. 41, no. 11, pp. 2231–2249, Nov. 1996.

[21] S. Gabriel, R. W. Lau, and C. Gabriel, “The dielectric properties of biological tissues: II. Measurements in the frequency range 10 Hz to 20 GHz.,” *Physics in medicine and biology*, vol. 41, no. 11, pp. 2251–69, Nov. 1996.

[22] IEEE Standards Coordinating Committee 34, “IEEE Recommended Practice for Determining the Peak Spatial-Average Specific Absorption Rate (SAR) in the Human Head from Wireless Communications Devices: Measurement Techniques,” 2003.

[23] K. Fukunaga, S. Watanabe, and Y. Yamanaka, “Dielectric Properties of Tissue-Equivalent Liquids and Their Effects on Specific Absorption Rate,” *IEEE Transactions on Electromagnetic Compatibility*, vol. 46, no. 1, pp. 126–129, Feb. 2004.

[24] H. Ikehira, T. Sunaga, T. Obata, S. Furukawa, M. Tamura, E. Yoshitome, and S. Tanada, “Development of a dielectric equivalent gel for better impedance matching for human skin,” *Proceedings of the International Society for Magnetic Resonance in Medicine*, p. 1, 2003.

[25] “MCL Technology.” [Online]. Available: http://www.mcluk.org.

[26] “Schmid & Partner Engineering AG.” [Online]. Available: http://www.speag.com.

[27] W. Yu, X. Yang, Y. Liu, M. Raj, and A. Muto, *Advanced FDTD Methods: Parallelization, Acceleration, and Engineering Applications*. 2011.

[28] M. Clemens and T. Weiland, “Dicrete Electromagnetism with the Finite Integration Technique,” *Progress In Electromagnetics Research,*, pp. 65–87, 2001.

[29] “The Foundation for Research on Information Technologies in Society (IT’IS foundation).” [Online]. Available: http://www.itis.ethz.ch.

[30] B. Models and B. Examples, “Bio-Medical RF Simulations with CST Microwave Studio ®.”

[31] R. W. Y. Habash, *Bioeffects and Therapeutic Applications of Electromagnetic Energy*. CRC Press, Taylor & Francis Group, LLC: , 2008.

[32] H. H. Pennes, “Analysis of tissue and arterial blood temperatures in the resting human forearm,” *Applied Physiology*, vol. 1, p. 93, 1948.

[33] R. Spiegel, “A Review of Numerical Models for Predicting the Energy Deposition and Resultant Thermal Response of Humans Exposed to Electromagnetic,” vol. MTT-32, no. 8, 1984.

[34] M. H. and I. M. F. (1986) Durney C.H., *Radiofrequency radiation dosimetry handbook*. Salt Lake City, UT: The University of Utah., 1986.

[35] Y. Alfadhl, “Numerical evaluations on the interaction of electromagnetic fields with animals and tissues,” *. Queen Mary University of London*, 2005.

[36] IEEE, *Standard for Safety Levels with Respect to Human Exposure to Radio Frequency Electromagnetic Fields , 3 kHz to 300 GHz*. IEEE Standard C.95.1-1991: , 1999.

[37] IEEE, *Standard for Safety Levels with Respect to Human Exposure to Radio Frequency Electromagnetic Fields , 3 kHz to 300 GHz*. IEEE Standard C.95.1-1991: , 1992.

[38] IEEE, *Recommended practice for determining the peak spatial-average specific absorption rate (SAR) in the human head from wireless communications devices*. IEEE Standard 1528-2003: , 2003.

[39] IEEE, *Standard for Safety Levels with Respect to Human Exposure to Radio Frequency Electromagnetic Fields , 3 kHz to 300 GHz*. IEEE Standard C.95.1-2005: , 2006.

[40] NRPB, *ICNIRP guidelines for limiting exposure to time-varying electric, magnetic, and electromagnetic fields (up to 300 GHz). Advice on aspects of implementation. in the UK. Doc NRPB, 10(2)*. Chilton, Didcot, Oxon, UK: , 1999.

[41] NRPB, *Board statement on restrictions on human exposure to static and time-varying electromagnetic fields. Doc NRPB, 4(5)*. Chilton, Didcot, Oxon, UK: , 1993.

[42] NRPB, *Review of the scientific evidence for limiting exposure to electromagnetic fields (80-300 GHz). Doc NRPB, 15(2)*. Chilton, Didcot, Oxon, UK: , 2004.

[43] ICNIRP, “Guidelines for limiting exposure to time-varying electric, magnetic and electromagnetic fields (up to 300 GHz),” *Health Phys*, pp. 494–522, 1998.

[44] ICNIRP, “Responses to question and comments on ICNIRP,” *Health Phys*, pp. 438–439, 1998.

[45] ICNIRP, “General approach to protection against non-ionizing radiation,” *Health Phys*, pp. 540–548, 2002.

[46] TCO’99, *Certification, display (CRT), TCO Report No. 1*. Stockholm, Sweden: , 1999.

[47] Health Canada, “Safety Code 6. Limits of human exposure to radiofrequency electromagnetic fields in the frequency range from 3 kHz to 300 GHz.,” *Environmental Health Directorate, Health Protection Branch*, 1999.

[48] ARPANSA, “Maximum exposure levels to radiofrequency fields - 3 kHz-300 GHz. Radiation Protection Series No. 3.,” *Australian Radiation Protection and Nuclear Safety Agency*, 2002.

[49] C. Chour, “Basic problems of diversely reported biological effects of radio frequency fields.,” *Radiats Biol Radioecol*, pp. 512–518, 2003.

[50] A. Bujanda, “SA assessment methods report,” *Queen Mary University of London*, 2013.

[51] R. Jegadeesan and Y. X. Guo, “A study on the inductive power links for implantable biomedical devices,” pp. 4–7, 2010.

[52] “Wireless Power Consortium.” [Online]. Available: http://www.wirelesspowerconsortium.com.

[53] D. M. Pozar, *Microwave engineering*, 3rd ed. John Wiley & Sons, Inc: , 2005.

[54] I. Ortego, N. Sanchez, J. Garcia, F. Casado, D. Valderas, and J. I. Sancho, “Inkjet Printed Planar Coil Antenna Analysis for NFC

Technology Applications," *International Journal of Antennas and Propagation*, vol. 2012, pp. 1–6, 2012.

[55] C. Wang, G. A. Covic, S. Member, and O. H. Stielau, "Power Transfer Capability and Bifurcation Phenomena of Loosely Coupled Inductive Power Transfer Systems," vol. 51, no. 1, pp. 148–157, 2004.

[56] J. T. Boys, G. a. Covic, and a. W. Green, "Stability and control of inductively coupled power transfer systems," *IEE Proceedings - Electric Power Applications*, vol. 147, no. 1, p. 37, 2000.

[57] R. Laouamer, M. Brunello, J. P. Ferrieux, O. Normand, and N. Buchheit, "A multi-resonant converter for non-contact charging with electromagnetic coupling," *Proceedings of the IECON'97 23rd International Conference on Industrial Electronics, Control, and Instrumentation (Cat. No.97CH36066)*, vol. 2, pp. 792–797, 1997.

[58] G. A. C. O.H. Stielau, "Design of loosely coupled inductive power transfer systems," *PowerCon 2000 International Conference on Power System Technology*, vol. 00, pp. 85–90, 2000.

[59] C. Wang, G. A. Covic, and O. H. Scelau, "General Stability Criterions for Zero Phase Angle Controlled Loosely Coupled Inductive Power Transfer Systems," vol. 00, no. C, pp. 1049–1054.

[60] K. M. Silay, C. Dehollain, and M. Declercq, "Improvement of Power Efficiency of Inductive Links for Implantable Devices," *Research in Microelectronics and Electronics, 2008. PRIME 2008. Ph.D.*, pp. 229–232, 2008.

[61] W. M. Ng, C. K. Lee, and S. Y. (Ron) Hui, "Optimal operation of contactless transformers with resonance in secondary circuits," *2008 Twenty-Third Annual IEEE Applied Power Electronics Conference and Exposition*, vol. 2, pp. 645–650, Feb. 2008.

[62] M. Zargham, S. Member, P. G. Gulak, and S. Member, "Maximum Achievable Efficiency in Near-Field Coupled Power-Transfer Systems," vol. 6, no. 3, pp. 228–245, 2012.

[63] S. Kim, J. S. Ho, L. Y. Chen, and A. S. Y. Poon, "Wireless power transfer to a cardiac implant," *Applied Physics Letters*, vol. 101, no. 7, p. 073701, 2012.

[64] B.-J. Jang, “HF-BAND WIRELESS POWER TRANSFER SYSTEM: CONCEPT, ISSUES, AND DESIGN,” vol. 124, no. January, pp. 211–231, 2012.

[65] R. Jegadeesan, S. Member, Y. Guo, and S. Member, “Topology Selection and Efficiency Improvement of Inductive Power Links,” vol. 60, no. 10, pp. 4846–4854, 2012.

[66] A. Vander Vorst, A. Rosen, and Y. Kotsuka, *RF / Microwave Interaction with Biological Tissues*. NJ: John Wiley & Sons: , 2006.

[67] C. A. Balanis, *Advanced Engineering Electromagnetics*, 2nd ed. John Willey & Sons, Inc: , 2012.

[68] “European Telecommunication Standards Institute.” [Online]. Available: http://www.etsi.org.

[69] ETSI EN 302 195-1, “Electromagnetic compatibility and Radio spectrum Matters (ERM); Radio equipment in the frequency range 9 kHz to 315 kHz for Ultra Low Power Active Medical Implants (ULP-AMI) and accessories,” *European Standard (Telecommunications series)*.

[70] J. Webster, “Design of Cardiac Peacemakers,” *New York: IEEE Press*, 1995.

[71] ETSI EN 301 839-1, “Electromagnetic compatibility and Radio spectrum Matters (ERM); Short Range Devices (SRD); Ultra Low Power Active Medical Implants (ULP-AMI) and Peripherals (ULP-AMI-P) operating in the frequency range 402 MHz to 405 MHz,” *European Standard (Telecommunications series)*.

[72] ETSI EN 302-054-2, “Electromagnetic compatibility and Radio spectrum Matters (ERM); Meteorological Aids (Met Aids); Radiosondes to be used in the 400,15 MHz to 406 MHz frequency range with power levels ranging up to 200 mW; Part 2: Harmonized EN covering essential requiremen,” 2003.

[73] Jupiter Hu (Industrial Technology Research Institute (ITRI)), “Overview of Flexible Electronics from ITRI ’ s Viewpoint,” *Symposium A Quarterly Journal In Modern Foreign Literatures*, pp. 6650–6650, 2010.

[74] R. O. F. The, “Scanning the Issue Special Issue on Flexible Electronics Technology , Part 1 : Systems,” vol. 93, no. 7, pp. 1235–1238, 2005.

[75] D. C. Ng, G. Felic, and E. Skafidas, “Closed-loop Inductive Link for Wireless Powering of a High Density Electrode Array Retinal Prosthesis,” no. Table I, pp. 92–97, 2009.

[76] L. S. Raymond, L. N. Nelson, D. J. Hamilton, and W. J. Kerwin, “Fabrication of Passive Components for High-Temperature Instrumentation,” vol. C, no. 4, 1979.

[77] H. R. Khaleel, H. M. Al-rizzo, and A. I. Abbosh, “Design, Fabrication, and Testing of Flexible Antennas.”

[78] A. Rida, R. Vyas, L. Yang, C. Kruesi, and M. M. Tentzeris, “Low Cost Inkjet-printing Paper-Based Modules for RFID Sensing and Wireless Applications,” *Electronic Design*, no. October, pp. 1715–1718, 2008.

[79] V. Lakafosis, A. Rida, R. Vyas, L. Yang, S. Nikolaou, and M. M. Tentzeris, “Progress Towards the First Wireless Sensor Networks Consisting of Inkjet-Printed , Sensor Tags,” vol. 98, no. 9, pp. 1601–1609, 2010.

[80] M. L. Allen, K. Jaakkola, K. Nummila, and H. Seppa, “Applicability of Metallic Nanoparticle Inks in RFID Applications,” *IEEE Transactions on Components and Packaging Technologies*, vol. 32, no. 2, pp. 325–332, Jun. 2009.

[81] S. H. Yoon, J. H. Lee, P. C. Lee, and J. Do Nam, “Sintering and Consolidation of Silver Nanoparticles Printed on Polyimide Substrate Films,” *Macromolecular Research*, vol. 17, no. 8, pp. 568–574, 2009.

[82] J. B. Szczech, C. M. Megaridis, D. R. Gamota, S. Member, and J. Zhang, “Fine-Line Conductor Manufacturing Using Drop-On-Demand PZT Printing Technology,” *Packaging (Boston, Mass.)*, vol. 25, no. 1, pp. 26–33, 2002.

[83] D. Kim and J. Moon, “Highly Conductive Ink Jet Printed Films of Nanosilver Particles for Printable Electronics,” *Electrochemical and Solid-State Letters*, vol. 8, no. 11, p. J30, 2005.

[84] Z. Yin, Y. Huang, N. Bu, X. Wang, and Y. Xiong, “Inkjet printing for flexible electronics: Materials, processes and equipments,” *Chinese Science Bulletin*, vol. 55, no. 30, pp. 3383–3407, Nov. 2010.

[85] S. B. Fuller, E. J. Wilhelm, and J. M. Jacobson, “Ink-jet printed nanoparticle microelectromechanical systems,” *Journal of Microelectromechanical Systems*, vol. 11, no. 1, pp. 54–60, 2002.

[86] T. H. J. van Osch, J. Perelaer, a. W. M. de Laat, and U. S. Schubert, “Inkjet Printing of Narrow Conductive Tracks on Untreated Polymeric Substrates,” *Advanced Materials*, vol. 20, no. 2, pp. 343–345, Jan. 2008.

[87] “Cabot.” [Online]. Available: http://www.cabot-corp.com/Inkjet-Colorants/Inkjet-Printing.

[88] “Advanced Nano Products.” [Online]. Available: www.anapro.com.

[89] Sunchemical, “SunJet.” [Online]. Available: http://www.sunchemical.com/products/inkjet_ink_technology.

[90] Dupont, “Kapton Datasheet.” [Online]. Available: http://www.dupont.com/content/dam/assets/products-and-services/membranes-films/assets/DEC-Kapton-HN-datasheet.pdf.

[91] G. Dejean, R. Bairavasubramanian, D. Thompson, G. E. Ponchak, M. M. Tentzeris, and J. Papapolymerou, “Liquid Crystal Polymer (LCP): A New Organic Material for the Development of Multilayer,” vol. 4, pp. 22–26, 2005.

[92] S. H. Choi, H. J. Lee, and K. B. Lee, “Flexible antenna based on composite right/left-handed transmission line,” *Electronics Letters*, vol. 46, no. 17, p. 1181, 2010.

[93] M. L. Scarpello, D. Kurup, H. Rogier, S. Member, D. Vande Ginste, F. Axisa, J. Vanfleteren, W. Joseph, and L. Martens, “Design of an Implantable Slot Dipole Conformal Flexible Antenna for Biomedical Applications,” vol. 59, no. 10, pp. 3556–3564, 2011.

[94] A. A. G. and D. E. Anagnostou, “Dual Band-Reject UWB AntennaWith Sharp Rejection of Narrow and Closely-Spaced Bands,” *IEEE Transactions on Antennas and Propagation*, vol. 60, no. 4, pp. 2071–2076, 2012.

[95] N. K. I. Wolff, “Microstrip Ring Resonator and Dispersion Measurement on Microstrip Lines,” *Electronics Letters*, vol. 7, pp. 779–781, 1971.

[96] P. A. Bernard and J. M. Gautray, “Measurement of Dielectric Constant Using a Microstrip Ring Resonator,” *IEEE Transactions on Microwave Theory and Techniques*, vol. 39, no. 3, pp. 592–595, 1991.

[97] J. Yoon, J. Kwon, and H. Lee, “The Microwave Measurement of the Dielectric Properties by the Parallel Plate Resonator and Ceramic Cavity Method,” *Proceedings of 5th International Conference on Properties and Applications of Dielectric Materials*, vol. 2, pp. 964–968, 1997.

[98] U. Arz, J. Leinhos, and M. D. Janezic, “Broadband Dielectric Material Characterization : A Comparison of On-Wafer and Split-Cylinder Resonator Measurements,” *Proceedings of the 38th European Microwave Conference*, no. October, pp. 913–916, 2008.

[99] J. Baker, R. G. Geyer, J. H. Grosvenor, M. D. Janezic, C. A. Jones, B. Riddle, and C. M. Weil, “Dielectric Characterization of Low-loss Materials: A Comparison of Techniques,” *IEEE Transactions on Dielectrics and Electrical Insulation*, vol. 5, no. 4, pp. 571–577, 1998.

[100] H. M. Greenhouse, “Design of Planar Rectangular Microelectronic Inductors,” vol. II, 1974.

[101] C. R. Paul, “Inductance - Loop and Partial,” John Wiley & Sons, Inc.

[102] Agilent Technologies, “Agilent 85070E Dielectric Probe Kit 200 MHz to 50 GHz - Technical Overview.” .

[103] C. Schmidt, F. Casado, A. Arriola, I. Ortego, P. D. Bradley, and D. Valderas, “Broadband UHF Implanted 3-D Conformal Antenna Design and Characterization for In-Off Body Wireless Links,” *IEEE Transactions on Antennas and Propagation*, vol. 62, no. 3, pp. 1433–1444, Mar. 2014.

[104] C. Schmidt, D. Valderas, J. García, I. Ortego, and X. Chen, “Passive UHF RFID Near Field Link Budget for Implanted Sensors,” *European Conference on Antennas and Propagation (EUCAP)*, pp. 3479–3483, 2011.

[105] ETS LINDGREN, “Dual Polarized Horns - Model 3164,” *An ESCO Technologies Company*, 2005.

[106] “Dimatix. All About Inkjet Printheads.” [Online]. Available: http://www.dimatix.com/files/SGIA06-Present.pdf.

[107] R. E. S. Mancosu, R. D. Quintero, J, A. Q. Azevedo, “Sintering, in Different Temperatures, of traces of Silver Printed in Flexible Surfaces,” *11th. Int. Conf, on Thermal, Mechanical and Multiphysics Simulation and Experiments in Micro-Electronics and Micro-Systems*, 2010.

[108] Fujifilm, “Dimatix Material Printer DMP 2800 series User’s Manual,” 2010.

[109] “KLA-Tencor, P-16+ Profiler User’s Manual.” [Online]. Available: http://www.lot-oriel.com/files/downloads/tencor/eu/P16_Profiler_eu.pdf.

[110] Henkel, “Multicore MP218.” [Online]. Available: http://www.henkel.com.ar/ags/content_data/MP218_Manual_105.pdf.

[111] A. Rida, R. Vyas, and M. M. Tentzeris, “Conductive Inkjet-Printed Antennas on Flexible Low-Cost Paper-Based Substrates for RFID and WSN Applications,” *IEEE Antennas and Propagation Magazine*, vol. 51, no. 3, pp. 13–23, Jun. 2009.

[112] Identification cards - Physical Characteristics, *International Standard ISO 7810*. .

[113] M. Gebhart and R. Szoncso, “Optimizing Design of Smaller Antennas for Proximity Transponders,” *2010 Second International Workshop on Near Field Communication*, pp. 77–82, 2010.

[114] E. Ramon and E. Diaz, “Inkjet Printed Antennas for NFC systems,” pp. 1220–1223, 2010.

[115] A. L. Scholtz and R. Weigel, “Antenna design for future multi-standard and multi-frequency RFID systems,” 2009.

[116] Y. X. Guo and R. Jegadeesan, “Analysis of inductive power link for efficient wireless power transfer,” *2012 4th International High Speed Intelligent Communication Forum*, pp. 1–2, May 2012.

[117] H. Ali, T. J. Ahmad, and S. a Khan, “Mathematical modeling of an inductive link for optimizing efficiency,” *2009 IEEE Symposium on Industrial Electronics & Applications*, no. Isiea, pp. 831–835, Oct. 2009.

[118] A. S. Y. Poon, S. O. Driscoll, and T. H. Meng, “Optimal Frequency for Wireless Power Transmission into Dispersive Tissue,” *Area*, no. 1, pp. 1–12.

[119] A. S. Y. Poon, S. O'Driscoll, and T. H. Meng, "Optimal operating frequency in wireless power transmission for implantable devices.," *Conference proceedings : ... Annual International Conference of the IEEE Engineering in Medicine and Biology Society. IEEE Engineering in Medicine and Biology Society. Conference*, vol. 2007, pp. 5674–9, Jan. 2007.

[120] P. C. H. Chan, a. Teng, and M. M. F. Yuen, "A pressure sensor using flip-chip on low-cost flexible substrate," *2001 Proceedings. 51st Electronic Components and Technology Conference (Cat. No.01CH37220)*, pp. 750–754.

[121] M. K. Jolke Perelaer, C. E. Hendriks, and U. S. Schubert, *Microwave Flash Sintering of Inkjet-Printed Silver Tracks on Polymer Substrates*. Willey-VCH: .

I. Appendix A: Material mapping

The Table A.1 shows the material mapping between the materials defined in the Virtual Family from IT'IS foundation with the ones defined by Gabriel [19–21].

Table A.1: Material mapping

Tissue	ϵ_r, σ ***(corresponding tissue in Gabriel et. al)***
Adrenal Gland	*Gland*
Air Internal	*Air Internal*
Aorta	*Aorta*
Artery	*Artery*
Bladder	*Bladder*
Blood	*Blood*
Cortical Bone	*Cortical Bone*
Cancellous Bone	*Cancellous Bone*
Bone Marrow Not Infiltr.	*Bone Marrow Not Infiltr.*
Grey Matter	*Grey Matter*
White Matter	*White Matter*
Breast	*BreastFat*
Bronchi	*Blood Vessel*
Bronchi Lumen	*Air*
Cartilage	*Cartilage*
Cerebellum	*Cerebellum*
Cerebro Spinal Fluid	*Cerebro Spinal Fluid*
Cervix	*Cervix*
Commissura Anterior	*White Matter*
Commissura Posterior	*White Matter*
Connective Tissue	*Tendon*
Cornea	*Cornea*
Diaphragm	*Muscle*
Dura	*Dura*
Ear Cartilage	*Cartilage*
Epididymis	*Gland*
Esophagus	*Esophagus*
Esophagus Lumen	*Air*
Eye Lens	*Lens Nucleus*
Eye Sclera	*Eye Sclera*
Eye Vitreous Humor	*Eye Vitreous Humor*

Tissue	ϵ_r, σ ***(corresponding tissue in Gabriel et. al)***
Fat Average Infiltr.	*Fat Average Infiltr.*
Fat Not Infiltr.	*Fat Not Infiltr.*
Gall Bladder	*Gall Bladder*
Heart Lumen	*Blood*
Heart Muscle	*Heart*
Hippocampus	*Grey Matter*
Hypophysis	*Gland*
Hypothalamus	*Gland*
Intervertebral Disc	*Cartilage*
Kidney Cortex	*Kidney*
Kidney Medulla	*Kidney*
Large Intestine	*Colon*
Large Intestine Lumen	*Muscle*
Larynx	*Cartilage*
Lens Cortex	*Lens Cortex*
Lens Nucleus	*Lens Nucleus*
Liver	*Liver*
Lung (Inflated)	*Lung (Inflated)*
Lung (Deflated)	*Lung (Deflated)*
Mandible	*Cortical Bone*
Red Marrow	*Bone Marrow Infiltr.*
Medulla Oblongata	*White Matter*
Meniscus	*Cartilage*
Midbrain	*White Matter*
Mucosa	*Skin (Wet)*
Muscle	*Muscle*
Nerve	*Nerve*
Ovary	*Ovary*
Pancreas	*Gland*
Patella	*Cortical Bone*
Penis	*Blood*
Pharynx	*Air*
Pineal Body	*Gland*
Pons	*White Matter*
Prostate	*Prostate*
SAT	*Fat Average Infiltr.*
Skin	*Skin (Dry)*
Skull	*Cortical Bone*
Small Intestine	*Small Intestine*
Small Intestine Lumen	*Muscle*
Spinal Cord	*Nerve*
Spleen	*Spleen*
Stomach	*Stomach*
Stomach Lumen	*Muscle*
Theeth	*Cortical Bone*
Tendon Ligament	*Tendon*
Testis	*Testis*
Thalamus	*Grey Matter*

Tissue	ϵ_r, σ ***(corresponding tissue in Gabriel et. al)***
Thymus	*Thymus*
Thyroid Gland	*Gland*
Tongue	*Tongue*
Trachea	*Trachea*
Trachea Lumen	*Air*
Ureter Urethra	*Blood Vessel*
Uterus	*Uterus*
Vagina	*Colon*
Vein	*Blood*
Vertebrae	*Cortical Bone*

II. Appendix B: Topology analysis results

In this appendix the calculation to obtain bifurcation free conditions for SS, PS and PP topologies is addressed.

a) <u>SS topology</u>

For a bifurcation free transfer, the condition of $Im\{Z_p\} = 0$ (equation B.1) must be satisfied only for $\omega = \omega_0$.

$$Im\{Z_p\} = -\frac{1}{\omega C_p} + \omega L_p - \frac{\omega^3 C_s M^2 (\omega^2 C_s L_s - 1)}{(\omega^2 C_s L_s - 1)^2 + \omega^2 C_s^2 R^2} = 0 \qquad \textbf{B.1}$$

Applying the normalization process that has been explained in section 6.1.1.2 the following solutions are obtained:

1. Frequency is normalized to ω_0:

$$u = \frac{\omega}{\omega_0} \qquad \textbf{B.2}$$

2. Imaginary part of Z_p is normalized to the real part of the reflected impedance at resonance and it is denoted as Z_n:

$$Im\{Z_n\} = \frac{Im\{Z_p\}}{Re\{Z_r\}|_{\omega=\omega_0}} \qquad \textbf{B.3}$$

where $Re\{Z_r\}|_{\omega=\omega_0}$ for series compensated secondary circuit is:

$$Re\{Z_r\}|_{\omega=\omega_0} = \frac{\omega_0^2 M^2}{R_L} \tag{B.4}$$

Substituting equations B.1 and B.4 into B.3, $Im(Z_n)$ can be expressed as:

$$\begin{aligned}(Z_n) &= -\frac{1}{\omega C_p (Re\{Z_r\}|_{\omega=\omega_0})} + \frac{\omega L_p}{(Re\{Z_r\}|_{\omega=\omega_0}} + \frac{Im\{Z_r\}}{(Re\{Z_r\}|_{\omega=\omega_0}} \\ &= -\frac{R_L}{\omega C_p \omega_0^2 M^2} + \frac{\omega L_p R_L}{\omega_0^2 M^2} \\ &- \frac{\omega^3 C_s M^2 (\omega^2 C_s L_s - 1) R_L}{\omega_0^2 M^2 [(\omega^2 C_s L_s - 1)^2 + \omega^2 C_s^2 R_L^2]} \\ &= -\frac{Q_p}{u} + uQ_p - \frac{u^3 (u^2 - 1) Q_s}{(u^2 - 1)^2 Q_s^2 + u^2} \\ &= \frac{(u^2 - 1)\left[\left(Q_p Q_s^2 - Q_s\right)u^4 + \left(Q_p - 2Q_p Q_s^2\right)u^2 + Q_p Q_s^2\right]}{u(u^2 - 1)^2 Q_s^2 + u^3}\end{aligned} \tag{B.5}$$

The denominator of the equation B.5 has five roots:

$$u_1 = 0 \tag{B.6}$$

$$u_2 = \frac{1}{2} \cdot \frac{\sqrt{2} \cdot \sqrt{2Q_s^2 - 1 + \sqrt{-4Q_s^2 + 1}}}{Q_s} \tag{B.7}$$

$$u_3 = -\frac{1}{2} \cdot \frac{\sqrt{2} \cdot \sqrt{2Q_s^2 - 1 + \sqrt{-4Q_s^2 + 1}}}{Q_s} \tag{B.8}$$

$$u_4 = \frac{1}{2} \cdot \frac{\sqrt{2} \cdot \sqrt{4Q_s^2 - 2 - 2\left(\sqrt{-4Q_s^2 + 1}\right)}}{Q_s} \tag{B.9}$$

$$u_5 = -\frac{1}{2} \cdot \frac{\sqrt{2} \cdot \sqrt{4Q_s^2 - 2 - 2\left(\sqrt{-4Q_s^2 + 1}\right)}}{Q_s} \tag{B.10}$$

All the roots except the first one are imaginary numbers for $Q_s > 0$, and $u = 0$ belongs to the $\omega = 0$ condition as $u = \frac{\omega}{\omega_0}$ which happens with DC current. In the case of power transfer via inductive coupling, the denominator of the equation B.5 is not nullified by any values of u.

Consequently, only numerator can nullify the equation B.5 and $u = 1$ must be the only real root. For this, the equation must be satisfied:

$$Q_p > \frac{4Q_s^3}{4Q_s^2 - 1} \quad \textbf{B.11}$$

b) <u>PS topology</u>

For a bifurcation free transfer, the condition of $Im\{Z_p\} = 0$ (equation B.12) must be satisfied only for $\omega = \omega_0$.

$$Im\{Z_p\} = -\frac{\omega N(\omega) - \omega L_p}{D(\omega) + 1} \quad \textbf{B.12}$$

where

$$N(\omega^6) = C_p L_p^2 L_s^2 C_s^2 - 2C_p L_p L_s C_s^2 M^2 + C_p M^4 C_s^2 \quad \textbf{B.13}$$

$$N(\omega^4) = -L_p L_s^2 C_s^2 + M^2 C_s^2 L_s + C_p L_p^2 R_L^2 C_s^2 - 2C_p L_p^2 L_s C_s + 2C_p L_p M^2 C_s \quad \textbf{B.14}$$

$$N(\omega^2) = -L_p R_L^2 C_s^2 + 2L_p L_s C_s - M^2 C_s + C_p L_p^2 \quad \textbf{B.15}$$

$$D(\omega^8) = C_p^2 C_s^2 M^4 - 2C_p^2 C_s^2 L_p L_s M^2 + C_p^2 C_s^2 L_p^2 L_s^2 \quad \textbf{B.16}$$

$$D(\omega^6) = 2C_p C_s^2 L_s M^2 - 2C_p C_s^2 L_p L_s^2 + 2C_p^2 C_s L_p M^4 - 2C_p^2 C_s L_p^2 L_s + C_p^2 C_s^2 L_p^2 R_L^2 \quad \textbf{B.17}$$

$$D(\omega^4) = L_s^2 C_s^2 + 4C_p C_s L_p L_s + C_p^2 L_p^2 - 2C_p C_s^2 L_p R_L^2 \quad \textbf{B.18}$$

$$D(\omega^2) = -2L_sC_s - 2C_pL_p + R_L^2C_s^2 \quad \textbf{B.19}$$

Following the same procedure as for the SS topology case the bifurcation free condition can be obtained. However, for a parallel compensated primary, it is easier to manipulate the admittance Y_n rather than the impedance, therefore $Im(Y_n)$ can be expressed as:

$$Im(Y_n) = \omega C_p\left(Re\{Z_r\}|_{\omega=\omega_0}\right) - \frac{\frac{\omega L_p}{Re\{Z_r\}|_{\omega=\omega_0}} + \frac{Im\{Z_r\}}{Re\{Z_r\}|_{\omega=\omega_0}}}{\left(\frac{Re\{Zr\}}{Re\{Z_r\}|_{\omega=\omega_0}}\right)^2 + \left(\frac{\omega L_p}{Re\{Z_r\}|_{\omega=\omega_0}} + \frac{ImZr}{Re\{Z_r\}|_{\omega=\omega_0}}\right)^2} \quad \textbf{B.20}$$

$$= \frac{uQ_p}{1+Q_p^2} - \frac{uQ_p + \frac{-u^3(u^2-1)Q_s}{(u^2-1)^2Q_s^2+u^2}}{\left(\frac{u^4}{(u^2-1)^2Q_s^2+u^2}\right)^2 + \left(uQ_p + \frac{-u^3(u^2-1)Q_s}{(u^2-1)^2Q_s^2+u^2}\right)^2}$$

It should also be reminded that in order to do the conversion, C_p must be replaced by equation 8.37. The solution of equation B.20 requires a biquartic polynomial to be greater than zero. The approach serie-serie nor serie-parallel cannot be applied in this situation as those polynomials do not have coefficients in u^6. In this situation it is rather applied a practical value of Q_p, Q_s and compared the results with the literature [55].

In Figure B.1, the imaginary part of the normalized admittance $(Im\{Y_n\})$ is plotted for $Q_p = 20$ and for different Q_s to obtain the bifurcation free condition.

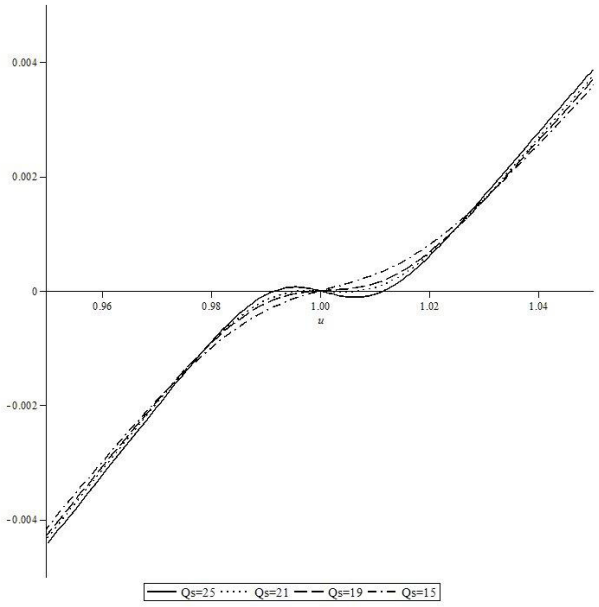

Figure B.1: Change in $Im\{Y_n\}$ for different $Q_s$values

From Figure B.1, the bifurcation free condition can be express as:

$$Q_p > Q_s \tag{B.21}$$

c) <u>PP topology</u>

For a bifurcation free transfer, the condition of $Im\{Z_p\} = 0$ (equation B.22) must be satisfied only for $\omega = \omega_0$.

$$Im\{Z_p\} = -\frac{\omega(N(\omega) - L_p R_L^2)}{D(\omega + R_L^2)} \tag{B.22}$$

where

$$N(\omega^6) = -2C_p C_s^2 L_p L_s M^2 R_L^2 + C_p C_s^2 M^4 R_L^2 + C_p C_s^2 L_p^2 L_s^2 R_L^2 \tag{B.23}$$

$$N(\omega^4) = -L_p L_s^2 C_s^2 R_L^2 + M^2 L_s C_s^2 R_L^2 + 2C_p C_s L_p M^2 R_L^2 L_s R_L^2 - 2C_p C_s L_p^2 + C_p M^4 + C_p L_p^2 L_s^2 - 2C_p L_p L_s M^2 \tag{B.24}$$

$$N(\omega^2) = 2L_p L_s C_s R_L^2 - M^2 C_s R_L^2 - L_p L_s^2 + M^2 L_s + C_p L_p^2 R_L^2 \tag{B.25}$$

$$D(\omega^8) = C_p^2 C_s^2 M^4 R_L^2 - 2C_p^2 C_s^2 L_p L_s M^2 R_L^2 + C_p^2 C_s^2 L_p^2 L_s^2 R_L^2 \quad \textbf{B.26}$$

$$D(\omega^6) = C_p^2 M^4 - 2C_p^2 L_p L^s M^2 + C_p^2 L_p^2 L_s^2 + 2C_p C_s^2 L_s M^2 R_L^2 - 2C_p C_s^2 L_p L_s^2 R_L^2 + 2C_p^2 C_s L_p M^2 R_L^2 - 2C_p^2 C_s L_p^2 L_s R_L^2 \quad \textbf{B.27}$$

$$D(\omega^4) = 2C_p L_s M^2 - 2C_p L_p L_s^2 + L_s^2 C_s^2 R_L^2 + 4C_p C_s L_s R_L^2 + C_p^2 L_p^2 R_L^2 \quad \textbf{B.28}$$

$$D(\omega^2) = L_s^2 - 2L_s C_s R_L^2 - 2C_p L_p R_L^2 \quad \textbf{B.29}$$

For a bifurcation free transfer, the condition $Im\{Z_p\} = 0$ should be achieved only for the ω= ω0 case. As the primary circuit is parallel compensated as in parallel-series topology, the normalization process is applied to the admittance, Y_p rather than the impedance, Z_p.

$$Im(Y_n) = \frac{u\left(Q_p - \frac{1}{Q_s}\right)}{1 + \left(Q_p - \frac{1}{Q_s}\right)^2} - \frac{(uQ_p) + \frac{-u^3\left(Q_s(u^2-1) + \frac{1}{Q_s}\right)}{Q_s(u^2-1)^2 + u^2}}{\left(\frac{u^2}{{Q_s}^2(u^2-1)^2 + u^2}\right)^2 + \left(uQ_p - \frac{u^3\left(Q_s(u^2-1) + \frac{1}{Q_s}\right)}{{Q_s}^2(u^2-1)^2 + u^2}\right)^2} \quad \textbf{B.1}$$

The compensation needed for the primary capacitor is found from equation B.22. The solution for B.30 require a biquartic polynomial to be greater than zero. A similar approach used in parallel-serie topology is used in this case: A practical value of Q_p and Q_s is applied and compared to the literature [55]. A primary quality factor of 3 is fixed and secondary is ranging from 2 to 3 with additional emphasis on Q_s = 2,6 and Q_s = 2,7 while the effect on imaginary part on the admittance $Im(Y_n)$ is verified. From Figure B.2, the condition of bifurcation free power transfer is found.

$$Q_p > Q_s + \frac{1}{Q_s} \quad \textbf{B.31}$$

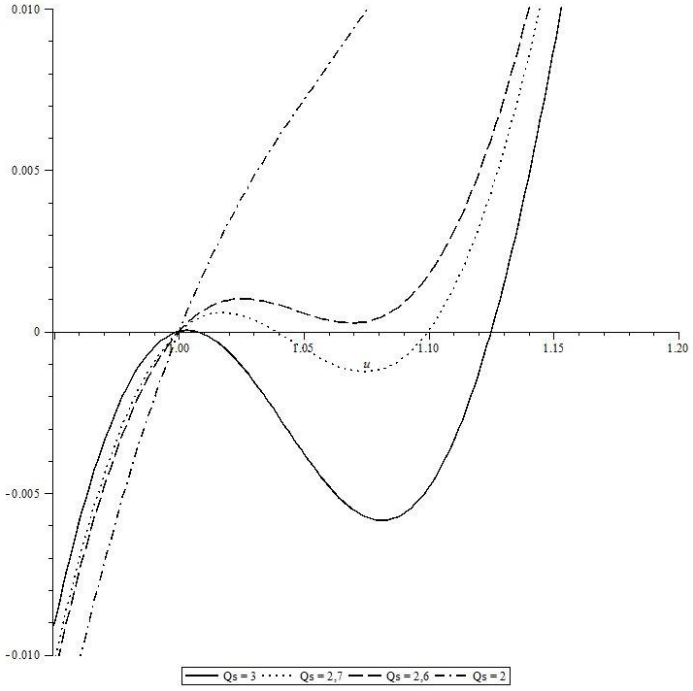

Figure B.2: Change in $Im\{Y_n\}$ for different $Q_s$values

III. Appendix C: CST Voxel Family

In this appendix the E-field behavior along a central line that crosses the torso of the different CST Voxel Family are shown. The procedure is the same that has been applied for Virtual Family from IT'IS foundation and that is explained in sections 0 and 9.3.

The voxel models that have been simulated are summarized in Table 2.6, where its main characteristics are described. As in section 9.3. the E-field behavior along the central line has been represented in the full range and also a zoon in has been made near the air-phantom interface.

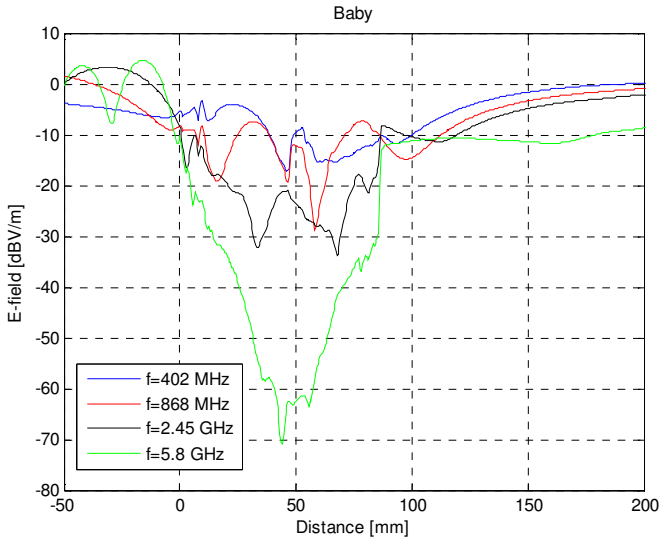

(a)

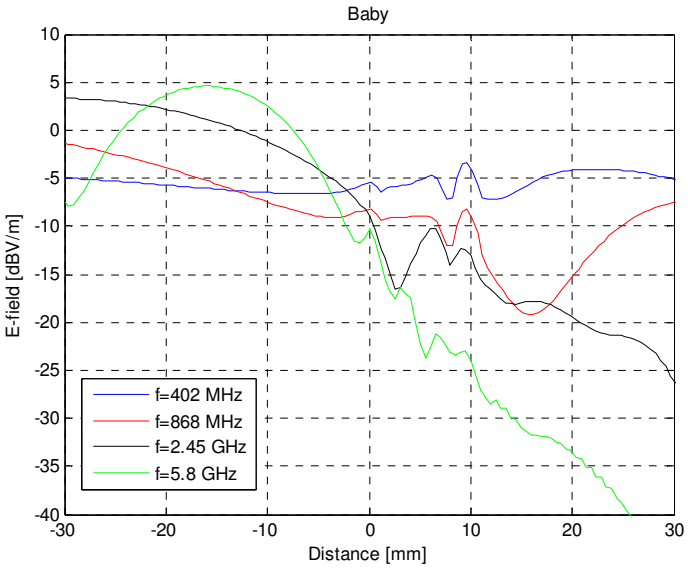

(b)

Figure C.1: E-field behaviour along central line for Baby voxel model: (a) full range and (b) air-phantom interface zoom in

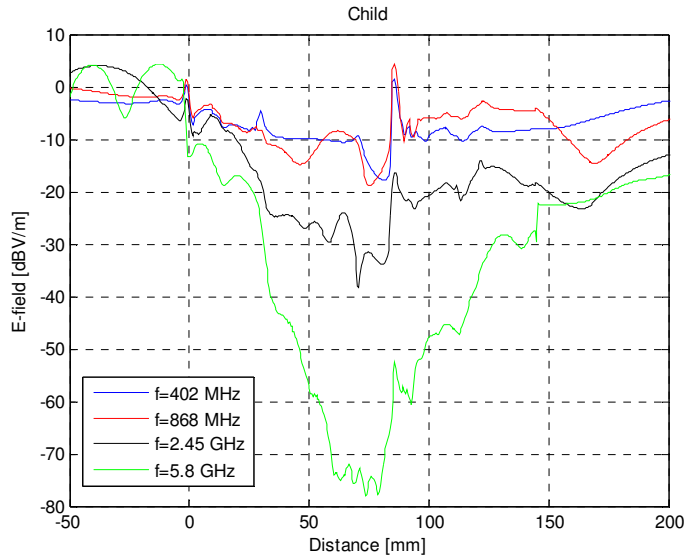

(a)

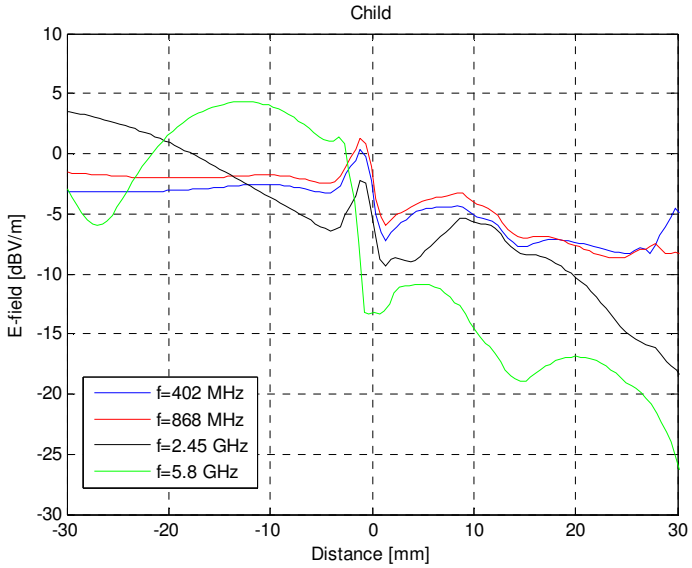

(b)

Figure C.2: E-field behaviour along central line for Child voxel model: (a) full range and (b) air-phantom interface zoom in

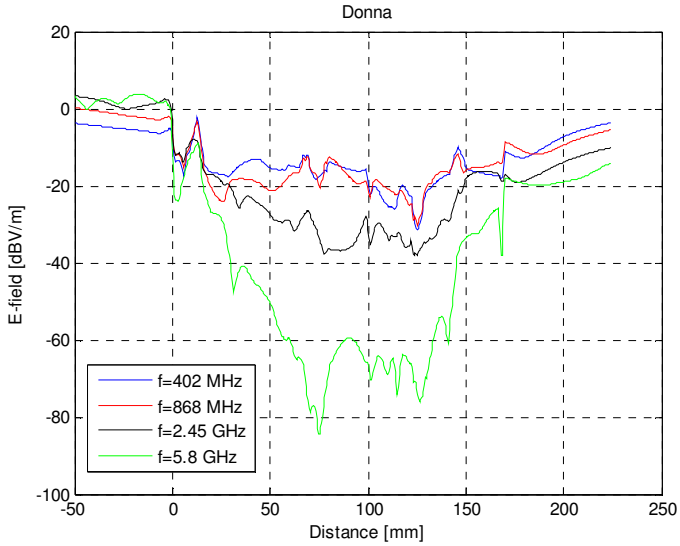

(a)

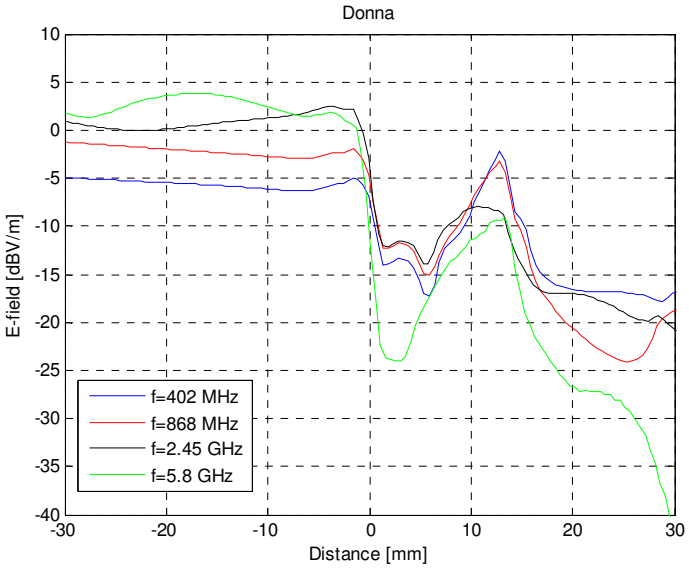

(b)

Figure C.3: E-field behaviour along central line for Donna voxel model: (a) full range and (b) air-phantom interface zoom in

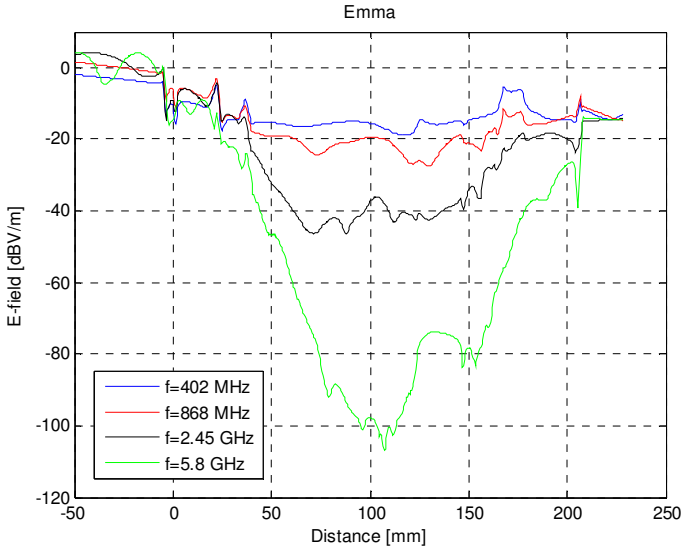

(a)

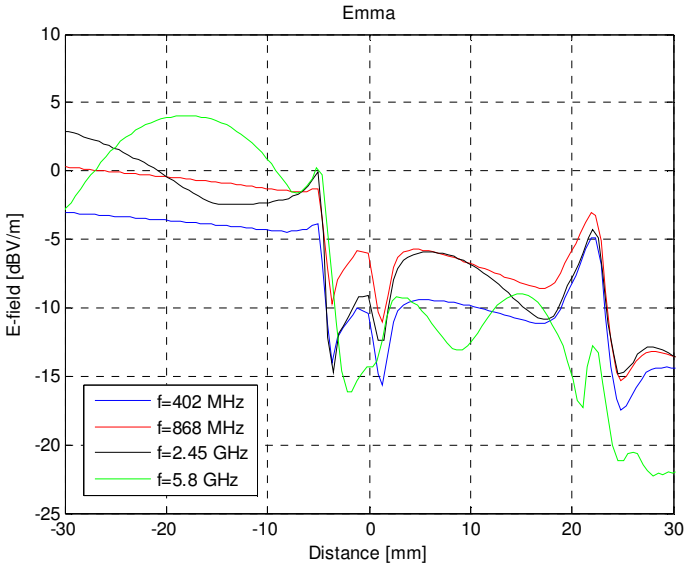

(b)

Figure CIII.4: E-field behaviour along central line for Emma voxel model: (a) full range and (b) air-phantom interface zoom in

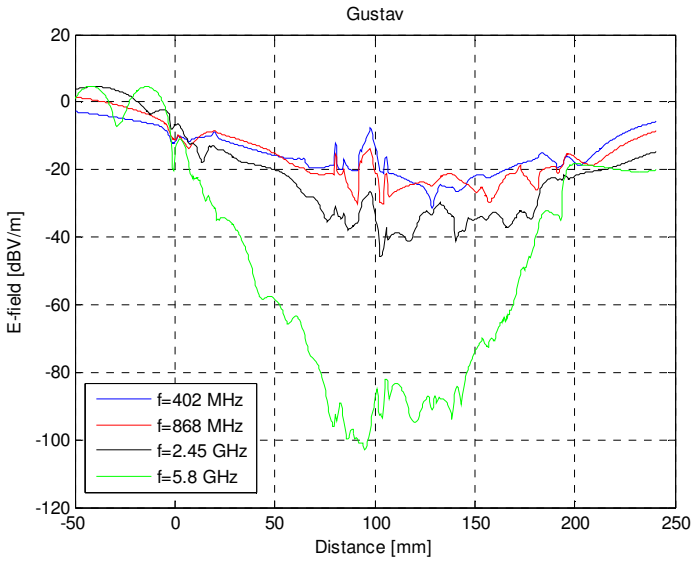

(a)

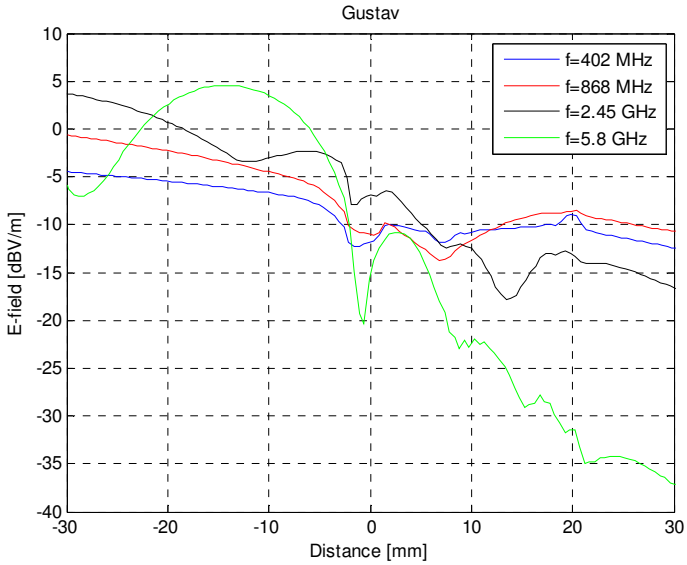

(b)

Figure C.5: E-field behaviour along central line for Gustav voxel model: (a) full range and (b) air-phantom interface zoom in

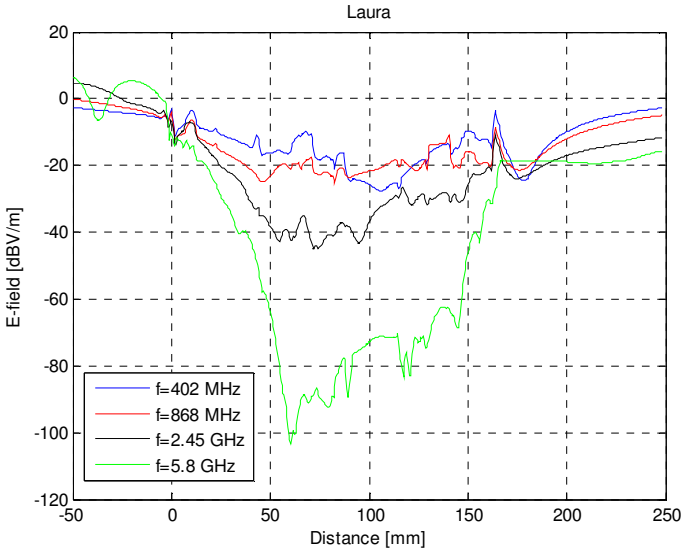

(a)

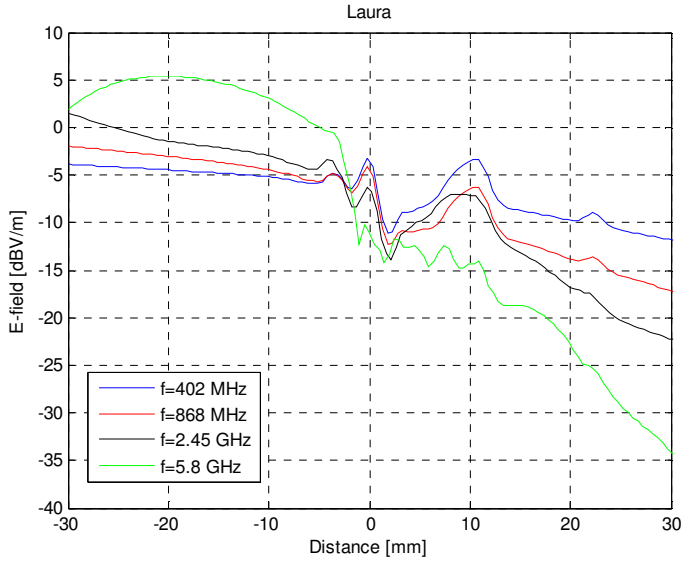

(b)

Figure C.6: E-field behaviour along central line for Laura voxel model: (a) full range and (b) air-phantom interface zoom in

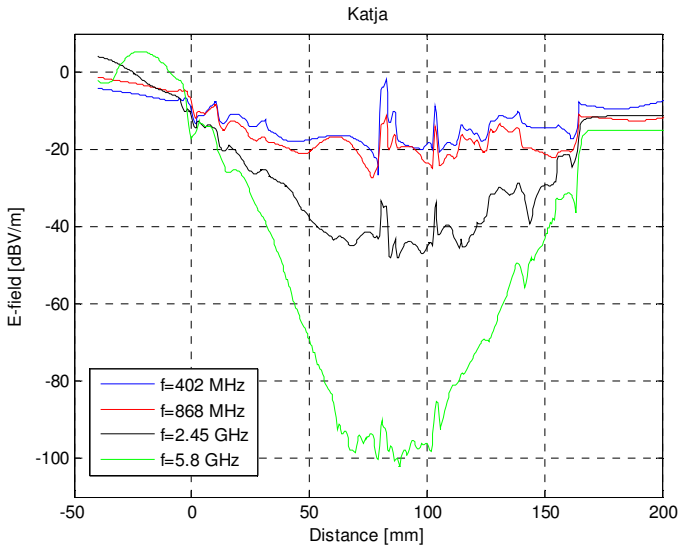

(a)

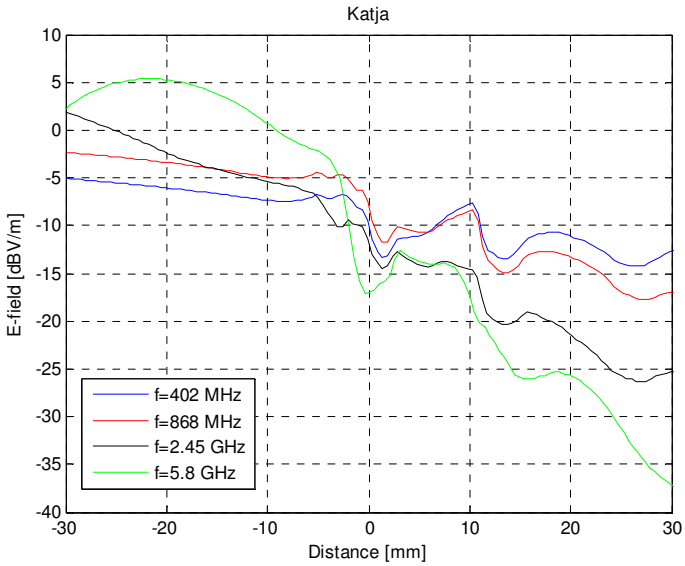

(b)

Figure C.7: E-field behaviour along central line for Katja voxel model: (a) full range and (b) air-phantom interface zoom in

IV. Appendix D: Publications

The publications that came out during the PhD. period are summarized below. Those most related with the presented research are included in the following pages.

Journals:

- I. Ortego, N. Sanchez, J. Garcia, F. Casado, D. Valderas, and J. I. Sancho, “Inkjet Printed Planar Coil Antenna Analysis for NFC Technology Applications,” *International Journal of Antennas and Propagation*, vol. 2012, pp. 1–6, 2012.
- C. Schmidt, F. Casado, A. Arriola, I. Ortego, P. D. Bradley, and D. Valderas, “Broadband UHF Implanted 3-D Conformal Antenna Design and Characterization for In-Off Body Wireless Links,” *IEEE Transactions on Antennas and Propagation*, vol. 62, no. 3, pp. 1433–1444, Mar. 2014.
- F. Casado, A. Arriola, E. Arruti, I. Ortego and J. I. Sancho, “PIN Diodes and their Impact on Reconfigurable Compact Microstrip Antennas with High Frequeny-Ratio,” *Microwave and Optical Technology Letters,* vol. 56, pp. 2676-2681, 2014.

Conferences:

- I. Ortego and D. Valderas, “Potentials and Comparison between Subtractive Etching and Inkjet Printing Technology for the Fabrication of NFC Coil Antennas,” *Proceedings of the XVIII Conference on the Design of Circuits and Integrated Systems*, pp. 182–185, 2013.
- C. Schmidt, D. Valderas, J. García, I. Ortego, and X. Chen, “Passive UHF RFID Near Field Link Budget for Implanted Sensors,” *European Conference on Antennas and Propagation (EUCAP)*, pp. 3479–3483, 2011
- I. Ortego, N. Sanchez, J. Garcia, F. Casado, D. Valderas, and J. I. Sancho, “Inkjet Printed Flexible Antenna Analysis for Near Field Communication Systems,” *50th Anniversary Conference - Engineering: Science and Technology*, p. 5, 2012.
- Jon del Portillo, Iñigo Adin, Jaizki Mendizabal, Daniel Valderas, Iñaki Ortego, Gonzalo Solas, “Enhancing the rolling stock standards towards a harmonized electromagnetic environment”, Transport Research Arena 2014, 14-17 April 2014, Paris La Defense (France)
- F. Casado, A. Arriola, J. Parron, E. Arruti, I. Ortego and J. I. Sancho, “Reconfigurable Matching Network for 2.45 GHz Printed IFA on Metallic Environments,” Loughborough Antennas and Propagation Conference (LAPC), 2012
- F. Casado, A. Arriola, E. Arruti, J. Parron, I. Ortego and J. I. Sancho, “2.45 GHz Printed IFA on Metallic Environments: Clearance Distance and Retuning Considerations,” *6th European Conference on Antennas and Propagation (EUCAP)*, 2012

I. Ortego, N. Sanchez, J. Garcia, F. Casado, D. Valderas, J. I. Sancho

Inkjet Printed Planar Coil Antenna Analysis for NFC Technology Applications

International Journal of Antennas and Propagation

Hindawi Publishing Corporation
International Journal of Antennas and Propagation
Volume 2012, Article ID 486565, 6 pages
doi:10.1155/2012/486565

Research Article

Inkjet Printed Planar Coil Antenna Analysis for NFC Technology Applications

I. Ortego,[1] N. Sanchez,[1] J. Garcia,[1] F. Casado,[2] D. Valderas,[1] and J. I. Sancho[1]

[1] *Electronics and Communications Department, CEIT and Tecnun University of Navarra, Manuel de Lardizábal 15, 20018 San Sebastián, Spain*
[2] *Communications Area, IKERLAN-IK4, P J.M. Arizmendiarrieta, 20500 Arrasate-Mondragon, Spain*

Correspondence should be addressed to I. Ortego, iortego@ceit.es

Received 15 December 2011; Accepted 9 January 2012

Academic Editor: Ana Collado

Copyright © 2012 I. Ortego et al. This is an open access article distributed under the Creative Commons Attribution License, which permits unrestricted use, distribution, and reproduction in any medium, provided the original work is properly cited.

The aim of this paper is to examine the potential of inkjet printing technology for the fabrication of Near Field Communication (NFC) coil antennas. As inkjet printing technology enables deposition of a different number of layers, an accurate adjustment of the printed conductive tracks thickness is possible. As a consequence, input resistance and Q factor can be finely tuned as long as skin depth is not surpassed while keeping the same inductance levels. This allows the removal of the typical damping resistance present in current NFC inductors. A general methodology including design, simulation, fabrication, and measurement is presented for rectangular, planar-spiral inductors working at 13.56 MHz. Analytical formulas, computed numerical models, and measured results for antenna input impedance are compared. Reflection coefficient is designated as a figure of merit to analyze the correlation among them, which is found to be below −10 dB. The obtained results demonstrate the suitability of this technology in the fabrication of low cost, environmentally friendly NFC coils on flexible substrates.

1. Introduction

Near Field Communication (NFC) is a recent wireless technology working on HF band that enables the exchange of data in a short range. It is an ideal solution where reliable exchange of data is paramount to quality user operations such as mobile payments. It is estimated that this system will be used in more than 1.2 billion smartphones by 2015 [1]. Therefore, it is necessary to reduce the cost of the manufacturing process keeping at the same time an environmentally friendly approach to pave the way for this promising technology.

In this context, there are a number of approaches to implement an NFC antenna layout onto a selected substrate. The earliest and most cumbersome method of antenna fabrication has been subtractive etching on a metal-plated laminate (e.g., FR4). Subtractive etching has matured to the point where it has become a low-tech process requiring inexpensive off-the-shelf materials and equipment. However, for larger production runs, etching creates significant amounts of metal salt and chemical waste products, incurring increased costs due to regulatory fees.

Contrary to the traditional etching technique, inkjet printing technology is a direct-write technology by which the designed pattern is transferred directly to the substrate [2]. This technology has become a major topic in scientific research, especially drop-on-demand (DOD) inkjet printing systems [3]. With these systems, the production costs of electronic devices are dramatically reduced, as material can be deposited on demand.

It has been estimated that there are about 1500 worldwide research units working on various aspects of flexible electronics [4]. The fabrication of thin conductive tracks by methods of inkjet printing has been recently investigated extensively [5, 6].

Up to date, inks made of silver conductive nanoparticles have been used to produce printed electronic circuits on flexible surfaces. Metallic nanoparticle inks typically consist of silver or gold nanoparticles with diameters ranging from just 2 nm to over 50 nm, encapsulated by a protective shell

and dispersed in a liquid solvent [7, 8]. Once printed, a continuous conducting structure can be obtained by sintering, that is, by increasing the temperature of the structure so that the separate nanoparticles melt together.

In the fabrication process, several parameters are involved, such as, size of ink nanoparticles, substrate, surface tension of the particle and of the substrate, time and temperature of the ink sintering, among others [9], which provide a wide range of degree of freedom for circuit designs, and particularly for antennas, on flexible substrates. Future terminals, such as smartphones, are envisaged to be completely flexible in the near future [10–12]. The antenna has a considerable size in the system; therefore, its flexibility is crucial if a flexible terminal is desired.

The usage of inkjet technology for NFC implementation on flexible terminals stills finds another motivation for the antennas involved. The Q factor required for the antenna is directly related to the read range to be achieved by the technology. For example, in a typical RFID system, for a distance of 38 cm, Q factors close to 40 are required [13, 14]. As NFC allows for shorter distances motivated for a whole sort of reasons, as, for example, security and privacy of users, restrictions on tag Q factors are relaxed to get the same voltage to energize the RFID tag integrated circuit.

As long as a decreasing of Q factor can be tolerated by performing antennas with tracks thinner than their skin depth, the input resistance can be increased to make up a possible removal of the damping resistance. With copper-etched antennas, Q-factors of more than 100 could be realized [13, 15]. In this technology, the conductive track thickness is fixed and longer than the skin depth of the copper (18 μm at 13.56 MHz). However, inkjet printing technology allows to vary the thickness of the printed layers with approximately 1 μm resolution all the way from 0 μm to the skin depth. Thus, typical coil antenna manufactured by inkjet printing technology exhibits small Q factors of around 4–10 [5].

Therefore, an exploration of the potentials and limitations of inkjet printing technology for NFC flexible terminals should be addressed in this context since it provides a low cost, environmentally friendly manufacturing process on flexible materials with no damping resistance involved.

This paper provides a rigorous approach, involving analytical and computational models, for rectangular planar spiral coils at 13,56 MHz with subsequent experimental verification on flexible substrates. It is divided into four parts. The second section deals with the methodology, where a general method for the design, fabrication, simulation, and measurement of inkjet printed loop antennas for NFC systems on a flexible substrate is explained. The third part includes the implementation and obtained results. Lastly, the fourth part states the conclusions.

2. Methodology

2.1. Analytical Approach. In this section, all the necessary equations to analytically calculate the total inductance, Q factor, and resistance of a rectangular planar spiral inductor (Figure 1) will be shown.

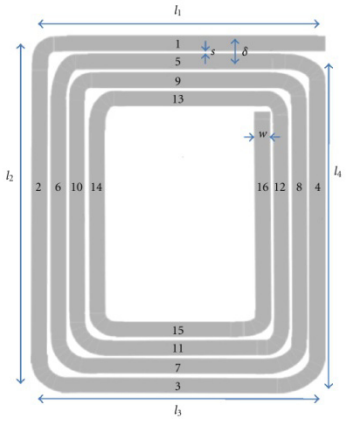

Figure 1: Rectangular planar spiral inductor.

2.1.1. Inductance Calculation. The total inductance of an N-turn planar spiral inductor coil (Figure 1) can be calculated as follows:

$$L_T = L_0 + M_+ - M_- \ [\mu\text{m}], \tag{1}$$

where L_T is the total inductance, L_0 is the sum of self inductances of all straight segments, M_+ is the sum of positive mutual inductances, and M_- is the sum of negative ones.

The self inductances of a rectangular cross-section conductor can be obtained using the following equation [14]:

$$L = 0,002l\left\{\ln\left(\frac{2l}{w+t}\right) + 0.50049 + \frac{w+t}{3l}\right\} \ [\mu\text{m}], \tag{2}$$

where w, t, and l are the segment's width, thickness, and length in cm, respectively.

The mutual inductance is the inductance that results from the magnetic fields produced by adjacent conductors. The mutual inductance is positive when the directions of the current along the conductors are in the same direction, and negative when the directions of currents are in opposite directions. The mutual inductance between two parallel conductors of equal length is a function of the length of the conductors and of the geometric mean distance d between them. It is calculated by [16]

$$M = 2lF[nH], \tag{3}$$

where F can be calculated as

$$F = \ln\left\{\left(\frac{l}{d}\right) + \left[1 + \left(\frac{l}{d}\right)^2\right]^{1/2}\right\} - \left[1 + \left(\frac{d}{l}\right)^2\right]^{1/2} + \left(\frac{d}{l}\right). \tag{4}$$

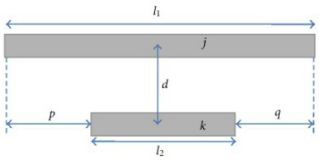

FIGURE 2: Two conductor segments for mutual inductance calculation.

The geometric mean distance d is approximately equal to the distance between the track centres of the conductors involved. When the two segments are not equal in length, (5) should be applied according to Figure 2:

$$M_{k,p} = \frac{1}{2}\left\{\left(M_{k+p} + M_{k+q}\right) - \left(M_p + M_q\right)\right\}, \quad (5)$$

where

$$M_{k+p} = 2l_{k+p}F_{k+p},$$
$$F_{k+p} = \ln\left\{\left(\frac{l_{k+p}}{d_{j,k}}\right) + \left[1 + \left(\frac{l_{k+p}}{d_{j,k}}\right)^2\right]^{1/2}\right\} - \left[1 + \left(\frac{d_{j,k}}{l_{k+p}}\right)^2\right]^{1/2} + \left(\frac{d_{j,k}}{l_{k+p}}\right). \quad (6)$$

2.1.2. Resistance and Quality Factor Calculation. The thickness of the conductive track deposited by inkjet printing technology can be adjusted by the number of layers micron by micron. Provided that skin effect at 13,56 MHz is approximately 47 μm for the silver conductive ink, the input resistance varies inversely with the thickness t according to the following expression:

$$R = \frac{1}{\sigma} \cdot \frac{L}{S} = \frac{1}{\sigma} \cdot \frac{L}{t \cdot w}, \quad (7)$$

where R is the electrical resistance, σ is the ink's conductivity, L is the longitude, S is the track cross section, t is the thickness, and w is the width of the track.

The spiral inductor Q factor is then calculated as:

$$Q = \frac{L\omega}{R}. \quad (8)$$

2.2. Numerical Computation. Frequency domain solver implemented by CST MICROWAVE STUDIO simulation software has been selected to make the numerical computation of the design. Adaptative hexahedral mesh is used and local mesh refinement strategy is adopted within the coil conductive track.

2.3. Implementation. The material used as substrate is Dupont Kapton polyimide film 127 μm thick. It can remain stable in a wide range of temperatures, from −269 to +400°C.



FIGURE 3: Cartridge and Printer Dimatix 2831 [17].

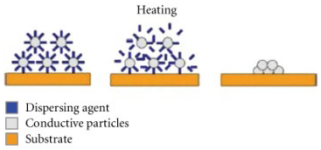

FIGURE 4: Sintering process [9].

SunTronic Jettable Silver U5714 ink by Sunjet has been used as conductive ink. It is a solvent-based silver nanoparticle inkjet ink and 20% of its weight is due to silver particles.

The printer that has been used is the Dimatix Materials Printer DMP-2831 (Figure 3). The platen temperature can be varied from 28°C to 60°C. In the fabricated prototypes, 60°C is chosen as it prevents the ink from spreading out.

DMC-11610 cartridge which has 16 nozzles, 254 μm spaced with a nominal opening of 21 μm, and a 10 pL drop volume capacity has been employed. Only two nozzles with 16-17 v applied voltage, 40°C of temperature and a meniscus vacuum of 4,5 inches H_2O have been used at a height of 0,5 mm with a drop spacing of 20 μm.

Once the prototypes have been printed, a sintering process is required to improve the conductivity of the ink. The manufacturer recommends a range of temperature and time to sinter the silver ink and this depends on the amount of solid material present in the ink. In general, the lower the sintering time or temperature, the higher the electric resistance since a larger gap between the nanoparticles occurs. This process (Figure 4) determines the final performance of the ink. A sintering process of 30 min@200°C has been selected for all the prototypes.

2.4. Measurements

2.4.1. Thickness of Printed Traces. Once the methodology to print is defined, some traces are printed into a substrate to study the corresponding thickness depending on the number of layers.

A KLA-Tencor P-16+ Profiler has been used to measure the overall thickness of the printed traces and estimate the one of each layer by average. In Figure 5, the obtained profile of the printed traces is shown for different number of layers.

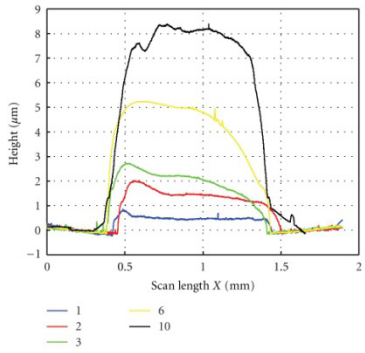

FIGURE 5: Obtained profiles for different number of printed layers.

TABLE 1: Obtained conductivity values with 30 min@200°C sintering process.

Material: silver	Conductivity $(\Omega m)^{-1}$	Conductivity with respect to pure silver (%)
Pure	$63.01 \cdot 10^6$	100
One layer	$8 \cdot 10^6$	12.6
Two layers	$9 \cdot 10^6$	14.3
Three layers	$7.9 \cdot 10^6$	12.5
Six layers	$8.5 \cdot 10^6$	13.5

A thickness of 0.8 μm for each layer can be assumed when considering the obtained profiles and the measured thickness.

2.4.2. Characterization of the Conductivity of the Ink. Once the thickness of the printed layers is found, conductivity is characterized.

Although conductivity is independent of the number of printed layers, the conductivity study has been done in samples with different number of layers, which correspond to different electrical resistance and thickness pairs for comparison purposes. The electrical resistance of the structure has been measured using a Keithley 6517B Electrometer/High Resistance Meter.

The conductivity can be calculated using (7). Table 1 shows averaged results collected from various samples.

The obtained results by this method are in accordance with the ones found in bibliography [9, 18]. As an indicative value, a 10% or 20% of the conductivity of the pure silver can be considered. In this work, a conductivity of $8 \cdot 10^6$ $(\Omega m)^{-1}$ has been considered as representative of ink performance.

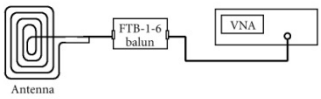

FIGURE 6: Measurement set up.

2.4.3. Input Impedance and Q Factor. Once the antenna has been printed, its impedance can be measured by a standard VNA according to the setup shown in Figure 6 and the corresponding Q factor can be calculated. A FTB-1-6 balun by Mini-Circuits is employed between the feeding cable and the fabricated prototype. The flexibility of the substrate and the ink do not allow the use of typical soldering methods. Therefore, pad connections are implemented by conductive adhesive tape.

2.5. Methodology Validation. The reflection coefficient will be used as figure of merit to estimate the correlation between the results obtained by analytical formulas, computed numerical models, and measurements.

The amplitude of the reflection coefficient between two different complex impedances can be calculated as [19]

$$|\Gamma| = 20 \log\left(\left|\frac{Z_1 - Z_2^*}{Z_1 + Z_2}\right|\right), \quad (9)$$

where Z_1 and Z_2 are the complex impedances. The methodology is based on this equation by substituting Z_1 and Z_2 for pairs chosen among analytically calculated, simulated, and measured results referred to the same coil layout. The only consideration to apply this equation is that for the correct calculation one of the impedances must be conjugated (e.g., $Z_2 = Z_{ant2}^*$). In that way, if $|\Gamma| \leq -10$ dB, a good correlation is achieved.

3. Implementation and Results

An analytical study of the effect of the thickness for a 5 turn rectangular (80 mm × 50 mm) planar spiral inductor with $w = s = 1$ mm has been realized. These dimensions have been selected to fulfil the ISO7810 standard [20]. This standard defines the physical characteristics of identification cards (Table 2).

The analytically obtained inductance for the presented antenna is 2.82 μH according to expressions (1)–(7), and it remains unchanged with thickness t. However, this parameter has a strong impact on the input impedance (as the damping resistance is changed) and therefore on the coil quality factor. The obtained results are shown in Figure 7 where expressions (7) and (8) are used.

A Q value up to 90 can be theoretically achieved by this technology as long as the thickness is kept below the skin depth (47 microns). For thicknesses deeper than skin depth, input resistance and Q factor is no longer adjustable by this degree of freedom.

Table 2: Nominal dimensions of ID-1 card type.

Width (mm)	Height (mm)	Thickness (mm)
85.6	53.98	0.76

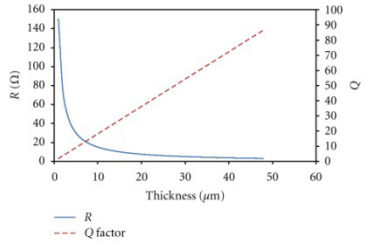

Figure 7: Calculation of R and Q for different thickness.

Table 3: Obtained results of the two prototypes: analytical (A), simulation (S), and measured (M).

		A	S	M
4 layers	R [Ω]	46,58	51,13	50,25
	L [μH]	2,82	2,79	2,9
	Q	5,16	4,64	4,91
6 layers	R [Ω]	31	35,118	32,35
	L [μH]	2,82	2,79	2,947
	Q	7,75	6,77	7,76

In practice, it is not feasible to fabricate coil antennas with such a high thicknesses due to the ink spilling over the track when too many layers are mounted on it. Two different prototypes have been implemented; one with 4 layers and another one with 6 layers (Figure 8) to validate the proposed methodology. The obtained results are shown in Table 3.

The correlation between the three outcomes (analytical, simulated, and measured) is studied as explained in the methodology validation section. The obtained values are summarized in Table 4.

All the correlations are below −10 dB; therefore, it can be concluded that the obtained results are reliable. In order to explore inkjet printing technology limits once the procedure is validated, a prototype with 10 layers has been fabricated. This represents a reasonable trade off between delivered performance in terms of Q values and complexity of the manufacturing process due to the number of layers. A measured inductance value of 2.9 μH, a resistance of 23.5 Ω and a Q factor of 10.5 are obtained in perfect accordance with the aforementioned results.

4. Conclusions

The potential of using inkjet printing technology to fabricate NFC antennas has been investigated. A general methodology for the design, simulation, fabrication, and measurement process has been explained.

Table 4: Results validation.

	Comparison		$\lvert\Gamma\rvert$ [dB]
4 layers	A	S	−25.16
	A	M	−21.94
	S	M	−20.35
6 layers	A	S	−22.78
	A	M	−15.39
	S	M	−14.08

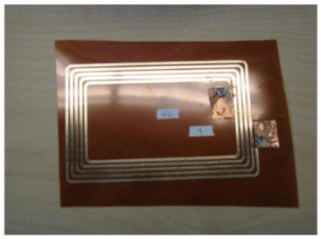

Figure 8: Printed prototype (6 layers).

The ink conductivity is shown to be around $8 \cdot 10^6\ (\Omega m)^{-1}$ and the approximate thickness of each deposited layer 0.8 μm. The resistance can be controlled by the capability of this technology of varying the track thickness, which prevents from extra damping resistor implementations. With the aforementioned resolution, Q values ranging from 4 to 10 can be obtained while keeping the same inductance value.

Inkjet printing technology is therefore a promising technique for the fabrication of NFC coil antennas. Moreover, due to its low cost manufacturing process and substrate flexibility, it is a perfect candidate for the implementation of environmentally friendly NFC terminals into flexible substrates.

Acknowledgment

Iñaki Ortego's scholarship has been granted by the Department of Education of the Basque Government. Joseba García's contract is partially supported by the Spanish Ministry of Education within the framework of the Torres Quevedo Program, and cofinanced by the European Social Fund. The authors would like to thank the collaboration agreement between Tecnun and CST that has made possible the achievements of this piece of research.

References

[1] "Wireless Design Online," http://www.wirelessdesignonline.com/article.mvc/NFC-Chip-Shipments-To-Surpass-12-Billio-

n-By-000?sectionCode=News&templateCode=SponsorHeader&user=1742815&source=nl:32237.

[2] A. Rida, R. Vyas, L. Yang, C. Kruesi, and M. M. Tentzeris, "Low cost inkjet-printing paper-based modules for RFID sensing and wireless applications," in *Proceedings of the 38th European Microwave Conference (EuMC '08)*, pp. 1715–1718, Amsterdam, The Netherlands, October 2008.

[3] T. H. J. van Osch, J. Perelaer, A. W. M. de Laat, and U. S. Schubert, "Inkjet printing of narrow conductive tracks on untreated polymeric substrates," *Advanced Materials*, vol. 20, no. 2, pp. 343–345, 2008.

[4] J. Hu, "Overview of flexible electronics from ITRI's viewpoint," in *Proceedings of the 28th IEEE VLSI Test Symposium (VTS '10)*, p. 84, Santa Cruz, Calif, USA, April 2010.

[5] M. L. Allen, K. Jaakkola, K. Nummila, and H. Seppa, "Applicability of metallic nanoparticle inks in RFID applications," *IEEE Transactions on Components and Packaging Technologies*, vol. 32, no. 2, pp. 325–332, 2009.

[6] S. H. Yoon, J. H. Lee, P. C. Lee et al., "Sintering and consolidation of silver nanoparticles printed on polyimide substrate films," *Macromolecular Research*, vol. 17, no. 8, pp. 568–574, 2009.

[7] J. B. Szczech, C. M. Megaridis, D. R. Gamota, and J. Zhang, "Fine-line conductor manufacturing using drop-on-demand PZT printing technology," *IEEE Transactions on Electronics Packaging Manufacturing*, vol. 25, no. 1, pp. 26–33, 2002.

[8] D. Kim and J. Moon, "Highly conductive ink jet printed films of nanosilver particles for printable electronics," *Electrochemical and Solid-State Letters*, vol. 8, no. 11, pp. J30–J33, 2005.

[9] R. D. Mancosu, J. A. Q. Quintero, and R. E. S. Azevedo, "Sintering, in different temperatures, of traces of silver printed in flexible surfaces," in *Proceedings of the 11th International Conference on Thermal, Mechanical and Multi-Physics Simulation, and Experiments in Microelectronics and Microsystems (EuroSimE '10)*, pp. 1–5, Bordeaux, France, April 2010.

[10] "Samsung And Nokia Are Moving Towards With Flexible Screens Smartphone," http://www.mobiussite.com/samsung-nokia-moving-flexible/1830.html.

[11] "Samsung flexible display phones & tablets in 2012," http://www.slashgear.com/samsung-flexible-display-phones-tablets-in-2012-28191673/.

[12] Y. Min, "Mobile Terminal Using Flexible Display And Method Of Controlling The Mobile Terminal," U.S. Patent US 2010/0117975 A1, 2010.

[13] A. L. Scholtz and R. Weigel, "Antenna design for future multistandard and multi-frequency RFID systems," 2009.

[14] Youbok Lee, "Antenna circuit design for RFID applications," *Microchip*, pp. 1–50, 2003.

[15] M. Gebhart and R. Szoncso, "Optimizing design of smaller antennas for proximity transponders," in *Proceedings of the 2nd International Workshop on Near Field Communication (NFC '10)*, pp. 77–82, Monaco, April 2010.

[16] C. R. Paul, *Inductance—Loop and Partial*, John Wiley & Sons, New York, NY, USA, 2010.

[17] "Dimatix. Fujifilm," http://www.dimatix.com/.

[18] A. Rida, L. Yang, R. Vyas, and M. M. Tentzeris, "Conductive inkjet-printed antennas on flexible low-cost paper-based substrates for RFID and WSN applications," *IEEE Antennas and Propagation Magazine*, vol. 51, no. 3, pp. 13–23, 2009.

[19] U. Karthaus and M. Fischer, "Fully integrated passive UHF RFID transponder IC with 16.7-μW minimum RF input power," *IEEE Journal of Solid-State Circuits*, vol. 38, no. 10, pp. 1602–1608, 2003.

[20] Identification cards—Physical Characteristics, *International Standard ISO 7810*.

C. Schmidt, F. Casado, A. Arriola, I. Ortego, P. D. Bradley, and D. Valderas,

Broadband UHF Implanted 3-D Conformal Antenna Design and Characterization for In-Off Body Wireless Links

IEEE Transactions on Antennas and Propagation, vol. 62, no. 3, pp. 1433–1444, Mar. 2014

IEEE TRANSACTIONS ON ANTENNAS AND PROPAGATION, VOL. 62, NO. 3, MARCH 2014 1433

Broadband UHF Implanted 3-D Conformal Antenna Design and Characterization for In-Off Body Wireless Links

Christoph Schmidt, Félix Casado, Aitor Arriola, Iñaki Ortego, Peter D. Bradley, and Daniel Valderas

***Abstract*—A broadband UHF antenna for implanted central venous catheters (CVC) is designed, implemented, and properly characterized. According to the requirements, the CVC antenna (CVCA) is low profile, surface integrated, and 3-D conformal to a 16 mm base radius, 10 mm upper radius, and 16 mm high truncated cone. It operates at the MedRadio band (401–406 MHz) for implant communication and at the ISM 2.45 GHz band for electronics wake up. A prototype implementation including a test-bed within a phantom that is representative of a body is introduced. The antenna exhibits $S_{11} < -10$ dB at the bands of interest with broadband behavior. The measured gain is −28.95 dBi in vertical and −36.9 dBi in horizontal polarization in the MedRadio band and −25.5 dBi and −19.9 dBi at 2.45 GHz. The gain is corroborated by the link characterization between an implanted node with electronics and an external base station. Base station antenna, electronics sensitivity, transmitted power, and path loss are independently measured and introduced in a broken down link budget for read range estimate. This is 18.95 m for the MedRadio band in free space conditions. By using the power saving mode at 2.45 GHz, it is reduced to an estimate of 1.88 m.**

***Index Terms*—Antenna measurements, biomedical communication, biomedical monitoring, biomedical telemetry, broadband antennas, implantable biomedical devices, monopole antennas.**

I. Introduction

TOO often, patients have a large number of consultations and/or spend long observation periods in hospitals to monitor the evolution of a certain pathology resulting in a delay in the appropriate therapy. Communication with low-cost, low-power, multifunctional small nodes may facilitate real time diagnosis and therapy on the spot in an autonomous way. This could offer savings to the health system via a reduced number of consultations and shorter observation periods in hospitals.



Fig. 1. Implanted MRI compatible CVC [8].

One common feature that makes this technology so attractive is the ability to be operated remotely, i.e. wirelessly, from outside the body. Possible applications include prosthesis control via myoelectric sensors [1], interaction with cochlear implants [2], artificial electrical stimulation of the surviving ganglion cells [3], automated drug delivery devices [4] etc. Additionally, the opportunities to perform in-vivo, in-real-time diagnosis are multiplied by implanted wireless telemetry, in which implanted sensor data is extracted for diagnostic purposes. The state of the art in this area over the last decade has been focused on developing new ways to monitor parameters such as blood pressure [5], glucose ratio for diabetes treatment [6] and intracranial pressure [7]. In all these applications, cables could be eliminated, procedures simplified and care made cost-effective by implanted wireless links.

This paper seeks to address wireless monitoring of microbial biofilm formation in implanted Central Venous Catheters (CVC), which are commonly used in clinical practice as drug delivery interfaces. The CVC is subcutaneously implanted in the chest with an offset of several centimeters with respect to its center. In this study, an MRI (bio)compatible silicon rubber truncated cone CVC is employed [8] with a base radius and height of 16 mm and an upper radius of 10 mm. The implant has an internal 14 mm base diameter and a 10 mm high cylindrical reservoir for drug injection from the outside. It is inserted into the upper part of the truncated cone (Fig. 1).

In the European framework in which this study is conducted, there are a number of standards on Electromagnetic Compatibility and Radio spectrum matters for wireless medical devices in different frequency ranges, particularly for ultralow-power active medical implants (ULP-AMI). There are two main standards in Europe: one at the 9–315 KHz band [9] for proximity magnetic coupling and another one at the 401–406 MHz band [10], which allows for an increased data rate over longer ranges.

Manuscript received August 02, 2012; revised November 04, 2013; accepted December 08, 2013. Date of publication January 14, 2014; date of current version February 27, 2014. This work was supported in part by the Spanish Ministry of Science and Innovation through the COSIMA project (TEC2010-19545-C04-02), in part by the Basque Department of Education, Universities and Research (PI-2008-26), and in part by the Catedra Telefónica. I. Ortego received a scholarship from the Department of Education of the Basque Government.

C. Schmidt, I. Ortego, and D. Valderas are with CEIT and Tecnun (University of Navarra), Manuel de Lardizábal 15, 20018 San Sebastián, Spain (e-mail: chschmidt1@web.es; iortego@ceit.es; dvalderas@ceit.es).

A. Arriola and F. Casado are with IK4-Ikerlan, P° J. M. Arizmendiarrieta, 2, 20500 Arrasate-Mondragón, Spain (e-mail: aarriola@ikerlan.es; fcasado@ikerlan.es).

P. D. Bradley is with Microsemi, San Diego, CA 92127 USA (e-mail: peter.bradley@microsemi.com).

Color versions of one or more of the figures in this paper are available online at http://ieeexplore.ieee.org.

Digital Object Identifier 10.1109/TAP.2013.2295816

0018-926X © 2013 IEEE. Personal use is permitted, but republication/redistribution requires IEEE permission.
See http://www.ieee.org/publications_standards/publications/rights/index.html for more information.

ULP-AMI communication using inductive loop techniques in the Low Frequency (LF) 9–315 KHz band has found wide acceptance as it allows easy penetration into human tissue. It was the first technology used for these purposes in the early 1970's, particularly for pacemakers [11], and it is quite often the current technology of choice. However, these communication links are mainly established in a clinical setting, which limits the autonomy of the system. In addition, communication with the implant requires the external loop antenna be placed precisely over it, which again undermines the possibility of an autonomous and sustainable scenario. Some other downsides include the exhibited low data rate.

On the other hand, the MedRadio band (401–406 MHz) has the potential for long-range communications (meters) between an external peripheral ULP-AMI-P and an ULP-AMI. The limit set for transmitted power by the ULP-AMI-P (25 μW E.R.P $= -16$ dBm [10]) is far below the ones required to wirelessly charge battery-less, state-of-the-art electronics including a sensor [12] if body losses are added. With battery assisted ULP-AMIs allocated in this band, the communication range is boosted relative to their LF counterparts, the data rate is increased and the number of potential applications multiplies. Given this scenario, it seemed reasonable to explore 401–406 MHz as the appropriate band for the communication for an estimated data throughput of 800 Kbps with a BER $< 1.5e-10$ [13]. This is compatible with the CVC application scenario, where the battery lifetime will not be a bottleneck if the CVC is implanted for several months. The implant will be inserted at a subcutaneous level, where RF body losses are kept under a certain threshold.

In this manner, the first objective of this paper is to design a MedRadio antenna that is compact, conformal to the CVC truncated cone, low profile, insulated and as efficient and directive as possible. A major requirement is that the antenna must not obstruct access to the exterior for the liquid exchange. As justified in Section II-A, the antenna should also be dual band. The radiator that meets these requirements should be chosen mainly among loop antennas [14], linear conformal antennas [15], compact multilayer helical antennas [16], stent-shape antennas [17] and microstrip antennas either in one [18] or several layers [19], [20].

The second objective of this paper is to examine a MedRadio power link budget between an ULP-AMI-P and a CVC ULP-AMI by breaking down the transmitted power, electronics sensitivity and antenna characteristics to corroborate the read range operation. Power link budgets within real human bodies are difficult to assess experimentally. Although some communication links have been studied within the body [21], [22], clear standards and procedures to define the terms at which medical implant communication tests should be standardized are still being developed. Thus, there has been little discussion about implanted antenna gain characterization. When performing radiation measurements, the feeding cables tend to mask the results due to low gain when antennas are placed in phantoms. In fact, gain measurements for implantable antennas are rare, whereas extended numerical simulations have already appeared in the literature [18], [19], [23], [24]. This makes the workflow jump, in most cases, from antenna simulation straight to transmitting implant measurements once the antenna has been integrated [16] without having feedback on proper antenna characterization.

Furthermore, other aspects, such as the minimum required human phantom size representative of a human being [25], are not usually taken into account; this means that different antennas cannot be compared for the same application when they are in different phantoms. A representative phantom size for the patient will be included in the study as a third objective.

This paper has been divided into six sections. After the introduction, the second part deals with the implanted antenna design that includes the proper phantom size definition; the third section analyzes the robustness on the matching to several parameter variations. In the fourth part, the implementation and proper characterization of the antenna are addressed. The read range in free space communication links with a ULP-AMI-P is determined by examining the components of the link budget in section fifth. The last section describes the conclusions.

II. Antenna Design

A. Requirements of the Implanted Antenna

The shape of the supporting reservoir is a truncated cone with a base radius of 16 mm and a height of 16 mm. Although the top part of the truncated cone is the surface closest to the skin, this area was discarded as the antenna locus as it must be unobstructed for liquid exchange between the implant's inner reservoir and possible external pumps, syringes, etc. As a result, the antenna was determined to be 3-D, conformal to the truncated cone, and low-profile, i.e., ideally with no extra volume added to the smart implant. The antenna required broadband behavior to avoid detuning in a changing live environment. Dual band operation in the MedRadio frequency at 401–406 MHz as well as in the global ISM band of 2.4–2.5 GHz was also required. As a basic principle, data is transferred in the MedRadio band, whereas the higher frequency is used to initiate communication and wake up the smart implant in order to enter its operating mode. A biocompatible synthetic layer made up of the same material as the CVC [8] prevents physiological interaction between the surrounding tissue and the antenna.

B. Antenna Design Process

The constraints mentioned above were taken into account when selecting a monopole-like structure as a radiating element. Its broadband impedance bandwidth [26], unlike implanted microstrip antennas [18], [19], and low-profile extension are major advantages with respect to the antenna requirements. The design needed a convenient way to mount a monopole onto the cone. The constraint of having to accommodate the radiator on the limited surface with enough length to allow the antenna to operate in the 401–406 MHz MedRadio band is set.

In order to reduce computation time, the simulation model used a body phantom that had smaller dimensions than the phantom used in the measurements. This is considered an acceptable approximation, as the impact of phantom size on the input impedance matching is mostly negligible within certain limits. The reduced cubical phantom for the simulation had a side length of 6 cm. The position of the implant in the body

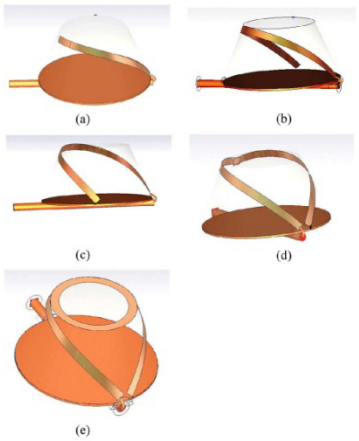

Fig. 2. Topologies used during the optimization process: (a) Short monopole. (b) Long monopole. (c) Long monopole with short circuit to ground. (d) Extended monopole with short circuit. (e) Extended monopole with short circuit and loop.

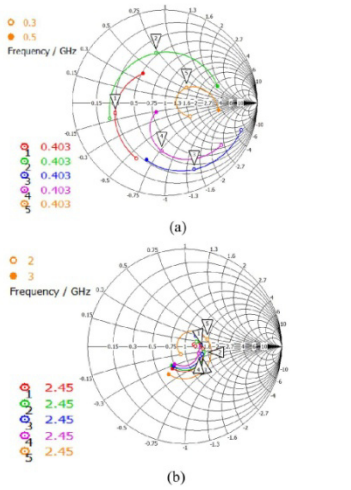

Fig. 3. Smith chart showing the complex impedance matching between (a) 0.3–0.5 GHz and (b) 2.0–3.0 GHz referring to the design steps towards the final antenna model 1) Short monopole. 2) Long monopole. 3) Long monopole with short circuit to ground. 4) Extended monopole with short circuit. 5) Extended monopole with short circuits and loop.

was replicated in the simulation by locating it at 9 mm from the phantom-air interface (subcutaneous position). The chosen antenna topology was designed with CST Microwave Studio electromagnetic simulation software.

Moreover, a single skin tissue phantom was considered to be accurate enough for the simulation for several reasons. Firstly, its properties are similar to general muscle tissue at 403 MHz ($\varepsilon_{r_skin} = 46.7, \varepsilon_{r_muscle} = 57.1; \sigma_{_skin} = 0.658, \sigma_{_muscle} = 0.623$); secondly, it represents the volume between implant and air, through which the data transmission is studied. Simulations will show that peak SAR is more critical in this area and accurate material definition should be done accordingly. The use of a more complex three-tissue phantom (skin, fat and muscle) would not significantly alter the return loss of the antenna, and it would only increase the simulation time [16], [23], [24]. The skin mimicking liquid was elaborated according to [18] and measured with a dielectric probe 85070E by Agilent Technologies. The results were gathered and compiled in a dispersion list. Prior to simulation, the dispersion list was imported into CST Microwave Studio, which in turn calculated the missing data based on a dispersion model (2nd order Debye model).

A broadband simulation type from 0 up to 4 GHz was utilized by applying a transient solver based on the Finite Integration Method. By using the Fast Perfect Boundary Approximation (FPBA), hexahedral mesh was employed without the need to resort to the subgriding technique in most cases. The absorbing boundary condition was chosen for the computation domain around the phantom. A space in the off-body direction of $\lambda/4$ for a precise far field computation was kept. An increased number of meshcells per wavelength of 35 was considered for the upper frequency limit. The "Bend sheet" feature was employed to project the antenna over the CVC truncated cone. The feeding cable was included in the model. The design was optimized with respect to a reference impedance of 50 Ω.

The design process is illustrated through the Figs. 2 and 3, where the optimization steps in Fig. 2(a)–(e) correspond to markers 1–5 shown in Fig. 3. The simulation model includes a round ground plane that covers the bottom side of the cone. The outer conductor of the coaxial feed cable was soldered to this implant's groundplane. The inner conductor was connected to the monopole, which, in turn, is attached to the cone shell. To describe the cone itself, the parameters of silicon rubber [8] based material were employed. Its relative permittivity was set to 3 according to [27].

The design process started with a single monopole [see Fig. 2(a)]. Marker 1 in the Smith chart in Fig. 3(a) shows its resistive properties around 403 MHz. The monopole is too short as the resonating frequencies are located above the MedRadio band. In this case, matching conditions are not optimal. By extending the monopole [see Fig. 2(b)], the frequency point of interest in Fig. 3(a), marker 2, moves clockwise towards the inductive part of the Smith chart. In order to take advantage of the cone surface, a short circuit implementation as a miniaturization technique is now applied [see Fig. 2(c)]. By adding a short circuit to this configuration, the graph is mirrored to the capacitive region of the diagram with respect to the center

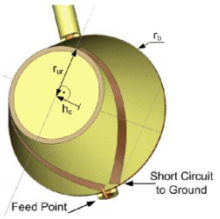

Fig. 4. Top view of the final antenna simulation model without the protection layer.

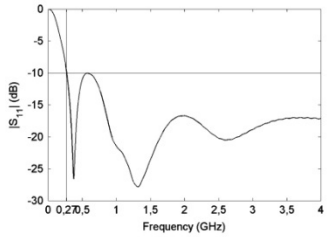

Fig. 5. Simulated $|S_{11}|_{dB}$ versus frequency of the CVCA in a 6 cm³ skin phantom.

TABLE I
FINAL GEOMETRY OF THE CVCA

Parameter	Value (mm,°)
Base radius (r_b)	16
Upper ring outside radius (r_{ur})	10
Cone height (h_c)	16
Copper strip length	33
Copper strip width at upper ring	1.5
Copper strip width at monopole	2
Angle between the monopole-to-ring connections	90

[Fig. 3(a), marker 3]. Even by adding a further extension of the monopole Fig. 2(d) the matching leaves room for improvement [see Fig. 3(a), marker 4]. By using a closed loop [see Fig. 2(e)], which can be seen as an additional inductance, the input impedance rotates clockwise from marker 4 to 5 and almost matches the desired 50 Ω [see Fig. 3(a), marker 5]. This loop is narrow enough to leave the top of the implant clear.

The Smith chart in Fig. 3(b) demonstrates the low influence of the abovementioned geometric changes of the antenna on the impedance matching for the 2–3 GHz range. This is due to the resistive properties of the lossy medium around the antenna. After applying further minor optimizations, the final topology was singled out, where the monopole extends over both sides of the truncated cone shell (see Fig. 4). The specific design parameters are displayed in Table I. The radiator is referred to as the CVC antenna (CVCA) hereafter.

The outside metal antenna parts have to be insulated to prevent interactions with the surrounding body tissue. As a design strategy, when the coating is made thinner, the antenna reduces its operating frequency (becoming more compact) due to the size-reduction effect introduced by the closer presence of the high permittivity media. At the same time, a large relative frequency bandwidth is achieved. This increases the robustness against implant environment variations [28], [29], including for example, variations in the proportion of body tissues over different patients or position variations of the implant itself. However, the radiation efficiency decreases due to the proximity of the same lossy media and a trade-off should be struck.

Therefore, the antenna was coated with a 0.2 mm biocompatible synthetic film made up of the same silicone rubber material as the CVC. In this way, the CVCA is fully integrated. This nonconductive coating has a major impact on the electromagnetic properties, as it is placed in the near field of the antenna. Commonly used coatings for implanted planar microstrip antennas include a ceramic layer with high permittivity ($\varepsilon_r \geq 10$) and low loss with at least 0.6 millimeter [18]–[20]. This solution was not feasible because of the 3-D cone-like shape of the antenna topology.

Fig. 5 depicts the simulation results of the antenna's S-parameter $|S_{11}|$ dB (reference impedance 50 Ω) with a 0.2 mm biocompatible synthetic film isolation within the 6 cm³ cube phantom.

At the reference value of $|S_{11}|$ dB < -10 dB the antenna covers the required bandwidth from 0.273 GHz to more than 4 GHz. This means that it can be operated worldwide in the MedRadio band as well as in the ISM 2.45 GHz band.

C. Phantom Size

It is known that the amount of body tissue surrounding the implanted antenna undermines its efficiency in two ways: by affecting the losses introduced by the body, and by the variation of the reflections coming back from the body-air interface.

For the measurement setup, the antenna is placed like in a typical subcutaneous case (9 mm deep from the top part) and with an offset of 6 cm with respect to the vertical center axis of a human torso, as shown in Fig. 6.

The cross section of the torso is modeled by a polystyrene tank of 355 mm × 255 mm filled with skin tissue mimicking liquid composed of 56.18% Sugar, 41.49% deionized water and 2.33% NaCl salt [18]. The liquid's properties were measured by the dielectric probe, and its permittivity and its loss tangent are shown in Fig. 7 with reference to [30]. As previously mentioned, these properties are the ones that were employed in the design process (Section II-B).

A study should set the minimum phantom height that will dramatically influence the radiation properties. Since real size human-phantoms are not often practical in terms of radiation measurements and simulation time, a phantom size representative of the whole body would depend on the operation frequency and direction of interest. The latter was specified to be on the horizontal plane for the communication link.

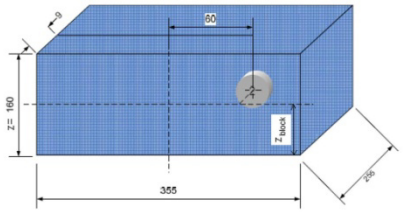

Fig. 6. Human torso-size phantom and location of the implant (dimensions in mm).

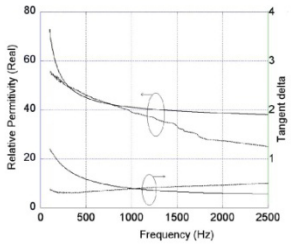

Fig. 7. Comparison of dielectric properties of dry skin and of tissue-simulating liquid (solid theory, dash experimental).

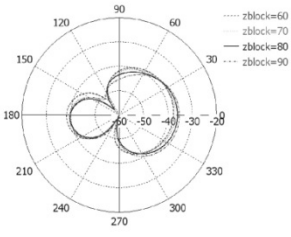

Fig. 8. Simulated antenna gain (dBi) in relation to phantom height z ($z/2 = z_\mathbf{block}$ (mm)) for 403 MHz (vertical polarization, horizontal plane).

Simulations are performed to investigate this minimum height z that the phantom should have in order to represent its impact on the gain pattern for the vertical polarization (theta-component) in the horizontal plane ($\theta = 90°$). Fig. 8 shows the change of the gain in relation to the phantom height z ($z_{\mathbf{block}}$ equals z/2) (Fig. 6). A value of $z = 160$ mm is estimated to be sufficient to account for body effects as the simulated gain patterns reasonably converge at 403 MHz below 109, million meshcells. For higher frequencies, the phantom will be electrically larger and, therefore, representative, as well. In this manner, the CVCA is placed at $z_{\mathbf{block}} = 80$ mm.

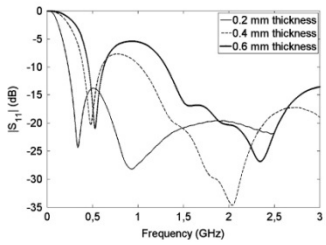

Fig. 9. Simulated $|S_{11}|_{\mathbf{dB}}$ versus frequency of the CVCA in representative skin phantom for different isolation layer thicknesses.

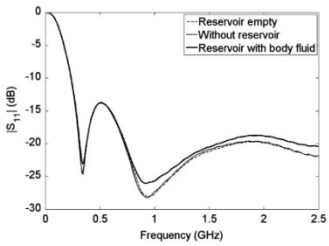

Fig. 10. Simulated $|S_{11}|_{\mathbf{dB}}$ versus frequency of the CVCA in representative skin phantom for different functional states.

III. Matching Robustness Study Against Parameter Variations

Once the basic antenna shape and an appropriate phantom size were defined, a study of the robustness of the matching against certain functional aspects was addressed. The study was performed in the 355 mm × 250 mm × 160 mm phantom.

A. Biocompatible Layer Thickness

Fig. 9 shows the impact that the biocompatible layer lateral thickness has on the CVCA matching. The lowest $|\mathbf{S_{11}}| < -10$ dB condition recorded around the MedRadio band is given at 230 MHz, 395 MHz and 452 MHz for 0.2 mm, 0.4 mm, and 0.6 mm, respectively. It is observed that from a thickness of 0.6 mm, the matching is not accomplished in the MedRadio band. The top isolation is kept to a thickness of 1 mm and its variation does not significantly affect performance (not shown for brevity).

B. Functional Operation

Computed matching against reservoir status (not present, present but empty, and filled with body liquid) was studied. The body liquid [30] was selected as being representative of functional operation, and imported in CST Microwave Studio with a 2nd order Debye model fit. Fig. 10 shows that the antenna is robust against the functional variations.

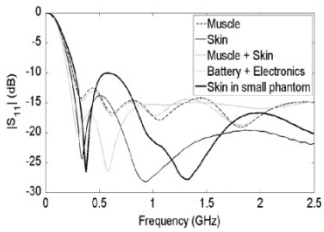

Fig. 11. Simulated $|S_{11}|_{dB}$ versus frequency of the CVCA in representative phantom for different tissue phantoms and in the presence of battery and electronics.

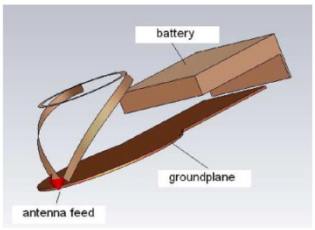

Fig. 12. CVCA along with metallic parts corresponding to the presence of the battery and electronics. The nonmetallic elements have been removed for clarity.

C. Tissue Variation

In order to analyze the impact of the variability of the surrounding tissue on the antenna matching, a muscle and a muscle-skin bilayer phantom were considered. In the latter case, the skin was considered to be between the top antenna part and the free space interface. Therefore, its thickness is 9 mm, which is the same as the CVCA insertion depth as described in Section II-C. The positioning of the antenna is also kept as described in that section. Muscle properties were extracted from [30] and imported by a 2nd Debye fitting into CST Microwave Studio. The selected antenna proves to have a robust $|S_{11}| < -10$ dB condition against tissue variability (Fig. 11) from skin to other tissues (thin solid to dash and dot lines). The performance in the small phantom (Fig. 5) has been also superimposed for comparison purposes in Fig. 11. It is observed how increasing phantom size improves the matching (thick to thin dark solid).

The robustness of the antenna against dielectric environment changes can be attributed to the short-circuit at one end, which gives the CVCA a magnetic nature.

D. Battery and Electronics Proximity

The antenna was conceived to operate in close proximity to a biofilm sensor, electronics and implanted battery Varta LPP 402025 CE [31]. The specific battery dimensions are 25.5 mm × 20.5 mm × 4.3 mm. The electronics and battery are placed alongside the truncated cone to avoid placing them beneath it and, therefore, preventing excessively long total implant height (Fig. 12). Previous cable antenna feeding running under the groundplane was substituted by a discrete port at the antenna terminals for functionality purposes.

The computed CVCA 50 Ω reflection coefficient in this situation is shown in Fig. 11 (grey solid). When the whole implant is tested with all its parts integrated—not the purpose of the present study—two matching networks in parallel should be introduced between each transceiver chip's RF ports (MICS and ISM bands) with arbitrary impedances [32], [33] and the antenna.

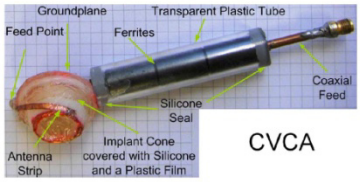

Fig. 13. Antenna prototype with detailed assembly.

IV. Antenna Characterization

A. Test-Bed Implementation

During the simulations a standing wave was observed in the stretch of the cable under the liquid level, as the wave undergoes a strong reflection due to the interface between very different permittivity media (air and skin mimicking liquid). To overcome this phenomenon, and inspired by [16] and [34], a test-bed is considered, where the cable was covered by a plastic tube and sealed at its edges with silicone as shown in Fig. 13. Magnetic beads were placed around the cable inside the plastic tube to minimize undesired currents along the outer conductor.

The antenna structure on the truncated cone was covered with silicone plus a thin plastic film protection layer. Due to prototyping limitations, the width is estimated to be between 0.2 mm and 0.4 mm. The core of a thin coax cable (RG 402) was soldered to the radiating element (monopole) while the outer conductor was soldered to the coppery ground plane of the cone. The junction at the feed point, as well as the ground plane was sealed with glue.

Once the prototype was assembled, reflection coefficient and gain characterization was conducted.

B. Reflection Coefficient

The CVCA measured reflection coefficient in the representative phantom at the MedRadio band (Fig. 17 and according to Fig. 6) is shown in Fig. 14. The $|S_{11}|_{dB}$ fits very accurately between the simulations corresponding to 0.2 mm and 0.4 mm

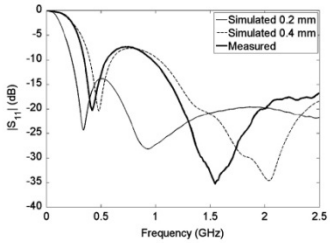

Fig. 14. Simulated with different isolation thickness and measured reflection coefficient $|S11|_{dB}$.

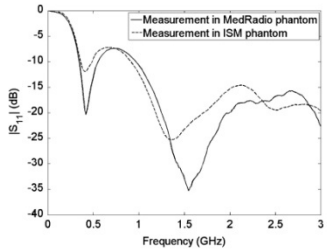

Fig. 16. Measured reflection coefficient $|S_{11}|_{dB}$ at two experimental phantoms.

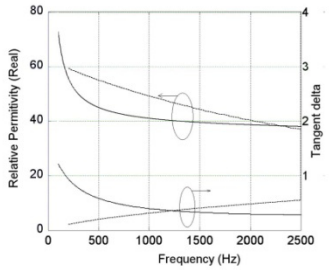

Fig. 15. Comparison of dielectric properties of dry skin and of tissue-simulating liquid at 2.45 GHz (solid theory, dash experimental).

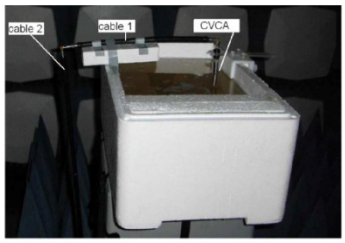

Fig. 17. Farfield measurement in the anechoic chamber showing phantom with inserted implant antenna.

film protection layers. It is below -10 dB from 345 MHz to 555 MHz and from 965 MHz onwards.

In order to disregard possible imprecise conclusions at the higher band, a phantom of the same size is realized for ISM 2.4 GHz band with 53% sugar and 47% deionized water according to [18]. The phantom properties are measured against theoretical values [30] and shown in Fig. 15. Fig. 16 shows that the $|S_{11}|_{dB} < -10$ dB broadband performance at this band is kept.

C. Gain

The antenna was placed in the specific position within the phantom as described in Section II-C. The antenna's centre was placed inside the phantom at a depth of 8 cm (half the phantom's height). This body torso section was modeled by a polystyrene tank with a 350 mm × 250 mm footprint. With an absolute height of $z = 16$ cm this resulted in 14.5 dm^3 of tissue simulating liquid.

The implant within the phantom was placed in an anechoic chamber for gain measurements in the horizontal plane at both polarizations (see Fig. 17) and placed on a plastic stand 134 cm tall. Due to the general low gain of implanted antennas, reflection from cables and mounts may affect the outcome. The antenna was mounted with the closest feeding cable in an upright position. As mentioned previously, three ferrite beads were clamped to the cable near to the antenna (Fig. 13). The next feeding cable was placed horizontally to prevent interference in the vertical predominant polarization (see Fig. 17: cable 1). To suppress further radiation coming from the outer conductor, the cable running on the top (1) and the back of the phantom (2) were covered with a synthetic semi flexible ferrite tube (Wave-X® heat shrink tube absorber WH-A750). On top of that, the feeding cables behind the phantom mount were enclosed with foam absorbers (cable 2).

The gain patterns of the horizontal plane over the 360° sweep for radiation coming from the chest are shown in Figs. 18 and 19. At 403 MHz, a VULB 9163 Log Periodic antenna by Schwarzbeck was used as a measurement antenna, and a 3146 Log Periodic antenna by EMCO was used as gain reference; at 2.45 GHz, a 3160-03 horn antenna by ETS-Lindgren was used as a measurement antenna and a SAS-581 horn antenna by AH-Systems as gain reference. The measurements included both polarizations (θ (vertical) and Φ (horizontal) component).

The attenuation dips that are observed in the measurement results and not present in simulation (e.g., at 90° in Fig. 18, vertical polarization) are interpreted as the scattered signal coming from cable 2 when it is not longer behind the phantom and facing

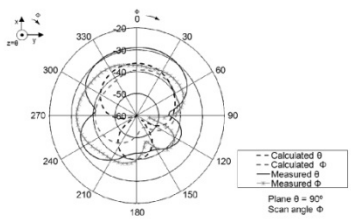

Fig. 18. Calculated versus measured results of vertical and horizontal component of gain (dBi) in the horizontal plane at 403 MHz.

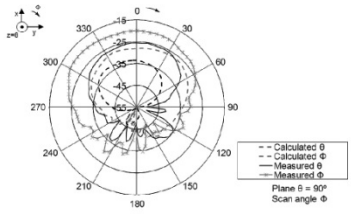

Fig. 19. Calculated versus measured results of vertical and horizontal component of gain (dBi) in the horizontal plane at 2.45 GHz.

the measurement antenna. This effect cannot be observed in simulations.

The measured gain $G_{implant_dB}$ in vertical polarization at phi $= 0°$ at 403 MHz $G_{implant_dB_v} = -28.95$ dBi whereas in the horizontal polarization $G_{implant_dB_h} = -36.9$ dBi. Simulations revealed that theta component in phi $= 0°$ $G_{implant_dB_v} = -36.1$ dBi and the phi-component is $G_{implant_dB_h} = -39.4$ dBi. The computed radiation efficiency was 0.017% and the maximum gain was -34.36 dBi.

For the 2.45 GHz frequency, the measured gain $G_{implant_dB}$ in vertical polarization at phi $= 0°$ $G_{implant_dB_v} = -25.5$ dBi whereas in the horizontal polarization $G_{implant_dB_h} = -19.9$ dBi. Simulations revealed that vertical component in phi $= 0°$ $G_{implant_dB_v} = -33.5$ dBi and the phi-component is $G_{implant_dB_h} = -28.1$ dBi. The computed radiation efficiency was 0.059% and the maximum gain was -26.14 dBi. The simulation and measurements revealed the predominant polarization changes from vertical to horizontal from 403 MHz to 2.45 GHz. Higher directivity due to the increase in electrical antenna size at this higher frequency was also observed.

It should be noted that the accuracy of the measurements in the anechoic chamber is limited by the performance of the absorbers and the gain of the measurement antennas. In this case, the chamber is covered with FS-400 hybrid absorbers by ETS-Lindgren (reflectivity -20 dB and -18 dB at 403 MHz and 2.45 GHz, respectively), and the gain of the measurement antennas is 6.6 dBi (Schwarzbeck VULB 9163) and 17 dBi (ETS-Lindgren 3160-03) at 403 MHz and 2.45 GHz, respectively. With these specifications, the accuracy of the measurements in the anechoic chamber is ± 1.75 dB at 403 MHz and ± 0.5 dB at 2.45 GHz. Therefore, it cannot cause the differences between simulated and measured results, which are 8 dB in the theta-component and 8.2 dB in the phi component at 2.45 GHz. This is due to the poor suppression properties of the current running along the external conductors of the feeding cables presented by any choke ferrites in the GHz band. This issue is particularly sensitive for low gain implanted antennas. However, simulation gives insight into this phenomenon, along with an impact estimate. In this case, the cable significantly increased the radiated energy. This is inevitable and should be taken into account by a read range uncertainty factor of 0.4 corresponding to the difference between simulations and measurements.

D. Specific Absorption Rate (SAR)

For the evaluation of performances and safety issues, the 1-g averaged SAR distributions are simulated and compared with ANSI/IEEE limitations [35]. The analysis was performed only at the frequency in which the implanted sensor node can transmit (i.e., MICS band [32], [33]). At 403 MHz, for 0.5 W (rms) input power, the maximum SAR at skin tissue was 59.1 W/Kg, for a density of 1100 kg/m^3 [36]. The transmitted power to the CVCA had to be decreased to 13.54 mW (11.32 dBm) in order to fulfill the SAR limit of 1.6 W/Kg. For a computed maximum absolute gain at 403 MHz of -34.36 dBi, this led to an ERP of -25.19 dBm that also satisfied the -16 dBm ERP allowed by MICS standard [10].

V. Free Space Link Budget

The objective of the link budget calculation is to evaluate possible application scenarios and, in particular, the maximum operating distance of the system.

A. Transmitted Power, Sensitivity and Base Station Characterization

For the measurements, two devices of the Application Development Kit (ADK) by Microsemi [37], both of them equipped with the ZL70102 transceiver chip [13], [32], [33], were employed: the implanted sensor node (SN), together with the CVCA, and the external base station (BS) with its corresponding helix antenna. Prior to the active link budget measurements, the implanted SN, the BS and its corresponding antenna had to be characterized.

A complete communication sequence involves three consecutive operations: implant search, wake-up and data exchange. In the present system, the communication can be initiated at 2.45 GHz as well as at 403 MHz. In this manner, a search operation wakes up the sensor node from its stand-by mode. Further transmission of sensor data is accomplished exclusively at the MedRadio frequency of 403 MHz and not at 2.45 GHz to avoid possible interference with unlicensed ISM bands in implanted sensitive high-end applications. During the search implant operation, the transmit power (P_{TX}) of the base station was measured at both frequencies. For this purpose, a 3 dB hybrid coupler and a spectrum analyzer were used (Fig. 20).

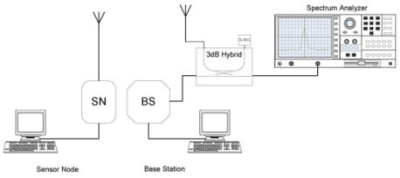

Fig. 20. Principal sketch of the measurement of the transmit power P_{TX} of the base station.

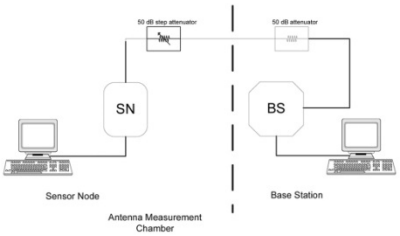

Fig. 21. Principal sketch of the measurement of the maximum sensitivity P_{RXp} of the SN.

The obtained values of the transmit power are $P_{TX} = -12.7$ dBm at 403 MHz and $P_{TX} = 17.5$ dBm at 2.45 GHz.

The sensitivity of the implanted sensor node was separately measured. This was accomplished by connecting the base station to the sensor node via cable and two calibrated attenuators, one of them adjustable (Fig. 21). The two attenuators together with cable losses represented the total gain and free space losses of both antennas. The attenuation was slowly lowered to the point where the system went into on-session. Then, the attenuation was again increased until the communication link was lost. The obtained values reflect the sensitivity (P_{RXp}) of the implanted sensor node ($P_{RXp} = -99$ dBm at 403 MHz and $P_{RXp} = -68$ dBm at 2.45 GHz). Although it is below the typical manufacturer's expectation at 2.45 GHz, the measured sensitivity is in between the expected values.

In order to characterize the base station's low profile helical antenna (shown in Fig. 24), it was mounted directly in a vertical position on a ground plane, which resembled the PCB of the base station in shape and size. The respective measurements involved gains (G_{BS}) and reflection coefficients ($|S_{11}|_{BS_dB}$) for both frequencies (see Table II). At 403 MHz the reflection coefficient is $|S_{11}|_{BS_dB} = -4.42$ dB and at 2.45 GHz it is $|S11|_{BS_dB} = -5.37$ dB (Fig. 22). This corresponds to mismatch losses of $L_{BS} = 1.92$ dB at 403 MHz and $L_{BS} = 1.48$ dB at 2.45 GHz. The predominant polarization of the helical antenna is vertical with -3.27 dBi average gain at 403 MHz and -2.71 dBi at 2.45 GHz in this horizontal plane. This is the reason why vertical polarization is considered in the link budget. The radiation pattern is omni-directional in this plane and it is not shown for brevity.

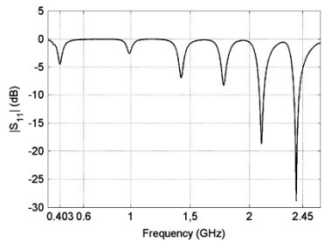

Fig. 22. Measured reflection coefficient of the base station helical antenna (S_{11BS}).

TABLE II
LINK BUDGET CALCULATION ACCORDING TO THE MEASURED RESULTS FOR LINE OF SIGHT

		Frequency (MHz)	
		403.35	2450
Transmission (Base Station)	Transmit Power, P_{TX} (dBm)	-12.7	17.5
	Gain, G_{BS} (dBi)	-3.27	-2.71
	Mismatch Loss, L_{BS} (dB)	1.92	1.48
	Free-space Loss, L_{FS} (dB) [at distance d_{set}=1.43m]	27.7	43.3
Receiving (Implant)	Gain, G_{AUT} (dBi)	-28.95	-25.5
	Mismatch Loss, L_{AUT} (dB)	0.15	0.09
	Coaxial Cable Loss, L_{cable} (dB)	2.4	8.2
	Attenuation, L_A (dB)	20	2

B. Wireless Test-Bed Setup

After completing the preceding characterizations, the active wireless link budget measurements were carried out. At one end the ADK sensor node was connected to the CVCA in the phantom by keeping the same cabling set up (Figs. 17 and 24). In the wireless measurements, only one variable attenuator was inserted between the sensor node and the CVCA. The setup was completed at the other end by the external ADK base station with its corresponding helix antenna. The base station and sensor node were controlled by a computer via USB connection (Fig. 23). This allowed the wireless link to be monitored in addition to initiating the communication process. Both antennas were positioned 1.34 m high. The whole setup was arranged in an anechoic chamber (Fig. 24).

The distance between the two antennas (d_{set}) was fixed to $d_{set} = 1.43$ m in free space. This distance was determined by approaching the base station manually to the point where the system went into on-session at the wake-up frequency of 2.45 GHz (downlink). The losses in free space (L_{FS}) are calculated according to the following (1), derived from the term $(\lambda/4\pi r)^2$ after units arrangements and dB application, for both frequencies

$$L_{FS} = 20\log_{10}(d_{set}) + 20\log_{10}(f) - 27,55 \qquad (1)$$

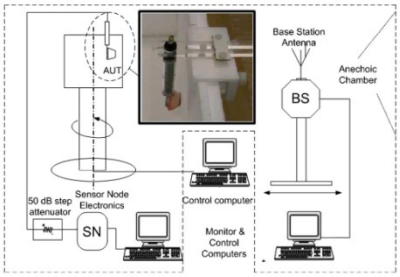

Fig. 23. Principal sketch of the measurement for maximum transmission range and detail of antenna orientation without phantom liquid.

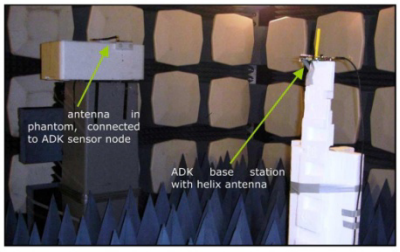

Fig. 24. Measurement setup in anechoic chamber for link budget calculation in free space.

where

f [MHz]	is center frequency of the frequency band
d_{set} [m]	distance between the two antennas, set to 1.43 m
L_{FS} [dB]	free-space loss

For f = 403 MHz free space loss resulted in $L_{FS} = 27.7$ dB and for f = 2450 MHz $L_{FS} = 43.3$ dB at $d_{set} = 1.43$ m.

The transmission of sensor data (uplink) is accomplished in the MedRadio band at 403 MHz. In order to avoid further inaccuracies in positioning, the 1.43 m separation was kept while increasing the attenuator value to emulate communication over distances longer than the chamber length. Regarding possible near-field effects, it should be noted that 1.43 m covers approximately two wavelengths at 403 MHz (free-space wavelength at 403 MHz = 0.74 m). The impact of the near field in this situation can be estimated by calculating the ratio between the near-field and far-field factors of a dipole antenna [38]; this calculation indicates an inductive near-field 22 dB below the radiated field, which implies an uncertainty of ±0.65 dB in the measurements. This accuracy was considered sufficient for the proposed experiment.

The communication link was lost at the point where attenuation value (L_A) reached 20 dB at the input of the sensor node. Table II gives a comprehensive summary of the measured results, including losses introduced by cables in the setup of Fig. 23:

TABLE III
RESULTING VALUES OF SENSITIVITY OF THE ELECTRONICS

		Frequency (MHz) 403.35	2450
in free space	Sensitivity, P_{RX} (dBm)	-97.1	-65.8
cable connection	Sensitivity, P_{RXp} (dBm), premeasured	-99	-68

Equation (2) [39] shows the link budget at both frequencies for the described setup

$$P_{RX} = P_{TX} - L_{BS} + G_{BS} - L_{FS} + G_{AUT} - L_{AUT} - L_{cable} - L_A \quad (2)$$

where

P_{RX} [dBm]	is the receiver sensitivity of the sensor node
P_{TX} [dBm]	the transmit power of the base station
L_{BS} [dB]	the mismatch loss of the helix antenna
G_{BS} [dBi]	the gain of the base station antenna
L_{FS} [dB]	the free space loss at the given frequency f[MHz] and distance d_{set} [m] (see (1))
G_{AUT} [dBi]	gain of the CVCA under test
L_{AUT} [dB]	mismatch loss of the CVCA under test
L_{cable} [dB]	losses of the coaxial cable
L_A [dB]	value of the attenuator losses

By applying (2) and the data provided in Table II a new value of sensitivity of the electronics is achieved, now in the wireless setup, for comparison with the conducted wired measurement in Section V-A. The results are compared in Table III. There is a good agreement between the sensitivity values in the conducted (wired) and wireless measurements.

C. Range Estimate Calculation

In this manner, (3) describes the maximum distance d_{max} that can be reached in an ideal free-space scenario, where feeding cables and the attenuator are not included

$$20\log_{10}(d_{max}) = L_{cable} + L_A + 20\log_{10}(d_{set}). \quad (3)$$

The losses in the cable L_{cable} and attenuation L_A were different at the different frequencies (see Table II). They effectively represent the respective free space loss for a specific additional distance.

Therefore, in an ideal environment, such as an anechoic chamber without cables and attenuators, the system attains in free space a maximum operating distance of $d_{max_INI} = 4.72$ m for communication initiation at 2.45 GHz and $d_{max_DATA} = 18.95$ m for data exchange in the MedRadio band. The value of d_{max_INI} is an overestimate due to the

radiating effect of the feeding cable. By applying the uncertainty factor of 0.4 for the 2.45 GHz frequency defined in Section IV-C, the best estimate for d_{max_INI} is 1.88 m.

VI. Conclusion

A low profile, broadband UHF antenna has been integrated on the surface of a Central Venous Catheter (CVC) implant with a truncated cone shape (base radius and height of 16 mm and upper radius of 10 mm) for wireless interaction with an external base station. The 3-D antenna exhibits compact and broadband features due to the application of short circuit and inductive loading techniques. It operates in the MedRadio band (401–406 MHz) for communication and the ISM 2.45 GHz band for electronic wake up. After a characterization that included proper phantom dimensioning, the antenna gain in vertical polarization is -28.95 dBi and -25.5 dBi at the respective frequencies. An uncertainty provided by the combination of simulation and measurements is estimated for the upper frequency, in which test-bed limitation is discussed. After thorough characterization of the base station antenna, path loss, transmitted power and sensitivity of the electronics involved in the link, a communication distance of 18.95 m is estimated for communication and 1.88 m for wake up operation in free space. This analysis sets an estimate of the limits and potentials for implanted medical application range within current regulation framework.

Acknowledgment

The authors would like to thank J. L. Moreno of R.C. Microelectrónica, S.A., and ARC Technologies, Inc., for providing samples of the Wave-X® absorber WH-A750c, as well as B. Sedano and M. Alonso for configuring the ADK.

References

[1] R. F. ff Weir, P. R. Troyk, G. De Michele, and T. Ku:ken, "Implantable myoelectric sensors (IMES) for upper-E:xtremity prosthesis control—Preliminary work," in *Proc. 25th Annu. Inf. Conf. IEEE EMBS*, Cancun, Mexico, Sep. 17–21, 2003.

[2] J. A. Moore, "An introduction to cochlear implant technology, activation, and programming," 2002.

[3] J. G. Hollyfield, R. E. Anderson, and M. M. LaVail, "Retinal degenerative diseases and experimental therapy," in *Electrical Stimulation of the Human Retina*. New York, NY, USA: Springer, 1999.

[4] D. A. LaVan, T. McGuire, and R. Langer, "Small-scale systems for in vivo drug delivery," *Nat. Biotechnol.*, vol. 21, no. 10, pp. 1184–1191, Oct. 2003.

[5] P. Cong, D. J. Young, B. Hoit1, and W. H. Ko, "Novel long-term implantable blood pressure monitoring system with reduced baseline drift," in *Proc. 28th IEEE EMBS Annu. Int. Conf.*, New York, NY, USA, Aug. 30–Sept. 3 2006.

[6] Y. Zhao, S. Li, A. Davidson, B. Yang, Q. Wang, and Q. Lin, "A MEMS viscometric sensor for continuous glucose monitoring," *J. Micromech. Microeng.*, vol. 17, pp. 2528–2537, 2007.

[7] M. N. Ericson, T. E. McKnight, S. F. Smith, and J. O. Hylton, "Implantable Device for In-Vivo Intracranial and Cerebrospinal Fluid Pressure Monitoring," United States Patent and Trademark Office granted patent, 2003, US6533733.

[8] [Online]. Available: http://www.bardaccess.com/port-mri-port.php?section=FeaturesAccessed, Apr. 16, 2013

[9] ETSI EN 302 195-1.

[10] ETSI TR 102 343, EN 301 839.

[11] Magjarevic, Ratko, Ferek-Petric, Bozidar. Implantable Cardiac Pacemakers-50 Years from the First Implantation, 2010.

[12] J. Yin, J. Yi, M. K. Law, Y. Ling, M. C. Lee, K. P. Ng, B. Gao, H. C. Luong, A. Bermak, U. Chan, W.-H. Ki, C.-Y. Tsui, and M. Yuen, "A system-on-chip EPC gen-2 passive UHF RFID tag with embedded temperature sensor," *IEEE J. Solid-State Circuits*, vol. 45, no. 11, pp. 2404–2419, Nov. 2010.

[13] Zarlink Semiconductors, ZL70102 Datasheet [Online]. Available: http://www.microsemi.com/ultra-low-power-wireless/implantable-medical-transceivers/zl70102#docs-amp-specs Accessed, Apr. 22, 2013

[14] F. Po, E. De Foucauld, and J. David, An Efficient Adaptive Antenna-Impedance Tuning Unit Designed for Wireless Pacemaker Telemetry [Online]. Available: http://www.intechopen.com/books/modern-telemetry/an-efficient-adaptive-antenna-impedance-tuning-unit-designed-for-wireless-pacemaker-telemetry, p. 24, 2010. Accessed, Apr. 22, 2013

[15] A. J. Johansson, "Wireless communication with medical implants: Antennas and propagation," in *Competence Centre for Circuit Design*. Lund, Sweden: Lund Univ., 2004.

[16] F. Merli, L. Bolomey, J.-F. Zürcher, G. Corradini, E. Meurville, and A. K. Skrivervik, "Design, realization and measurements of a miniature antenna for implantable wireless communication systems," *IEEE Trans. Antennas Propag.*, vol. 59, no. 10, pp. 3544–3555, Oct. 2011.

[17] C. Occhiuzzi, G. Contri, and G. Marrocco, "Design of implanted RFID tags for passive sensing of human body: The STENTag," *IEEE Trans. Antennas Propag.*, vol. 60, no. 6, pp. 3146–3154, Jun. 2012.

[18] T. Karacolak, A. Z. Hood, and E. Topsakal, "Design of a dual-band implantable antenna and development of skin mimicking gels for continuous glucose monitoring," *IEEE Trans. Microw. Theory Tech.*, vol. 56, no. 4, pp. 1001–1008, Apr. 2008.

[19] W. C. Liu, F. M. Yeh, and M. Ghavami, "Miniaturized implantable broadband antenna for biotelemetry communication," *Microw. Opt. Technol. Lett.*, vol. 50, no. 9, pp. 2407–2409, Sep. 2008.

[20] C.-M. Lee, T.-C. Yo, and C.-H. Luo, "Compact broadband stacked implantable antenna for biotelemetry with medical devices," in *Proc. IEEE Annual Wireless and Microwave Technology Conf.*, Dec. 2006, pp. 1–4.

[21] A. Alomainy and Y. Hao, "Modelling and characterisation of biotelemetric radio channel from ingested implants considering organ contents," *IEEE Trans. Antennas Propag.*, vol. 57, no. 4, pp. 999–1005, Apr. 2009, Special Issue on Body-Centric Wireless Communications.

[22] K. Sayrafian-Pour, W.-B. Yang, J. Hagedorn, J. Terrill, and K. Y. Yazdandoost, "A statistical path loss model for medical implant communication channels," in *Proc. IEEE 20th Int. Symp. Personal, Indoor and Mobile Radio Communications*, Sep. 13–16, 2009, pp. 2995–2999.

[23] J. Kim and Y. Rahmat-Samii, "Implanted antennas inside a human body: Simulations, designs, and characterizations," *IEEE Trans. Microw. Theory Tech.*, vol. 52, no. 8, pp. 1934–1943, Aug. 2004.

[24] M. Z. Azad and M. Ali, "A miniature implanted inverted-F antenna for GPS application," *IEEE Trans. Antennas Propag.*, vol. 57, no. 6, pp. 1854–1858, Jun. 2009.

[25] J. Garcia, A. Arriola, G. Sasiain, D. Valderas, J. I. Sancho, and X. Chen, "Characterization of phantom size and link budget for off-body communications," presented at the EuCAP, Barcelona, Spain, Apr. 12–16, 2010.

[26] D. Valderas, C. Schmidt, and X. Chen, "Broadband implanted UHF RFID antenna," in *Proc. IEEE APS Int. Symp. Antennas and Propagation and CNC/USNC/URSI Radio Science Meet.*, Toronto, ON, Canada, Jul. 11–17, .

[27] B. G. Babu, D. E. Selvaraj, R. Srinivas, B. G. Prakash, R. V. Prakash, E. Muthupandi, and R. Balakumar, "Analysis of relative permittivity and tan delta characteristics of silicone rubber based nano-composites," *Int. J. Sci. Eng. Technol.*, vol. 1, no. 5, pp. 201–206.

[28] P. S. Hall and Y. Hao, *Antennas and Propagation for Body-Centric Wireless Communications*. Norwood, MA, USA: Artech House, 2006, ch. 9.

[29] F. Merli, B. Fuchs, J. R. Mosig, and A. K. Skrivervik, "The effect of insulating layers on the performance of implanted antennas," *IEEE Trans. Antennas Propag.*, vol. 59, no. 1, pp. 21–31, Jan. 2011.

[30] Dielectric Properties of Body tissues in the frequency range 10 Hz–100 GHz, Institute For Applied Physics, Florence/Italy, 2010. [Online]. Available: [Online]. Available: http://niremf.ifac.cnr.it/tissprop/, Oct. 03, 2009

[31] [Online]. Available: http://www.varta-microbattery.com/applications/mb_data/documents/data_sheets/DS56416.pdfApr. 07, 2013

[32] P. D. Bradley, "An ultra low power, high performance medical implant communication system (MICS) transceiver for implantable devices," in *Proc. IEEE Biomedical Circuits and Systems Conference BioCAS*, Nov. 2006, pp. 158–161.
[33] P. D. Bradley, "Implantable ultralow-power radio chip facilitates in-body communications," RF Design (Online Magazine) 2007 [Online]. Available: http://rfdesign.com/next_generation_wireless/short_range_wireless/706RFDF1.pdf
[34] F. Merli and A. K. Skrivervik, "Design and measurement considerations for implantable antennas for telemetry applications," presented at the 4th Eur. Conf. Antennas and Propagation, Barcelona, Spain, Apr. 12–16, 2010.
[35] *IEEE Recommended Practice for Measurements and Computations of Radio Frequency Electromagnetic Fields With Respect to Human Exposure to Such Fields, 100 kHz–300 GHz.*, IEEE Std. C95.3™-2002.
[36] A. Christ, A. Klingenböck, T. Samaras, C. Goiceanu, and N. Kuster, "The dependence of electromagnetic far-field absorption on body tissue composition in the frequency range from 300 MHz to 6 GHz," *IEEE Trans. Microw. Theory Tech.*, vol. 54, no. 5, pp. 2188–2195, May 2006.
[37] ZL70102 Application Development Kit (ADK), accessed, [Online]. Available: http://www.zarlink.com/zarlink/hs/82_ZLE70102.htm, Apr. 21, 2013
[38] L. Hemming, *Electromagnetic Anechoic Chambers: A Fundamental Design and Specification Guide*. Hoboken, NJ, USA: Wiley, 2002.
[39] C. A. Balanis, *Antenna Theory, Analysis and Design*, 3rd ed. Hoboken, NJ, USA: Wiley, 2005.



Christoph Schmidt received the degree in electrical and electronics engineering (specialized in high frequency technology) from the University of Erlangen-Nuremberg (FAU), Germany, in 2001. He is currently pursuing the Ph.D. degree in the Electronics and Communication Department, CEIT and Tecnun (University of Navarra), San Sebastián, Spain.

He was a research and development engineer within the Department for High Frequency Electronics, Fraunhofer Institute for Integrated Circuits (IIS), Erlangen, Germany. In 2007, he joined CEIT in Donostia—San Sebastián, Spain, as a junior researcher. He has been working on projects for navigation applications like Galileo and digital satellite radio broadcasting receivers. His current research interests include ultralow power medical transceivers (smart implants), high-frequency electronics and antennas, especially compact antennas for wireless body applications, and antenna interactions with the human body.

Mr. Schmidt has published and presented many papers in a number of established international conferences.



Félix Casado received the B.Sc. degree in telecommunications engineering (electronic systems specialty) from the Universitat Autònoma de Barcelona (UAB), Spain, in 2008; the M.Sc. degree in telecommunications engineering from Universitat Autònoma de Barcelona (UAB), Spain, in 2010; and the M.Sc. degree in applied engineering from the University of Navarra, Spain, in 2012. He is currently pursuing the Ph.D. degree in antennas and microwaves at IK4-IKERLAN Technological Research Center, Arrasate-Mondragón, Spain, together with the University of Navarra.

His research interests include reconfigurable antennas and matching networks for reliable communication links.



Aitor Arriola received the M.S. degree in telecommunications engineering from the University of the Basque Country (UPV/EHU), Bilbao, Spain, in 1999, and the Ph.D. degree from the University of Navarra, San Sebastian, Spain, in 2011.

Since 1999, he has been with the Communications Department of IK4-IKERLAN Technological Research Center, Arrasate-Mondragón, Spain. From 2006 to 2008, he was with the RF Component Design and Modeling (RFCDM) Group of Imec, Leuven, Belgium, as visiting researcher. He has participated in several national and international research projects involving the design, measurement, and integration of planar antennas into products. His research interests include reconfigurable antennas and antennas for body area networks.



Iñaki Ortego received the degree in telecommunications engineering from Tecnun, University of Navarra, Spain, in 2010. He is currently pursuing the Ph.D. degree at Tecnun-CEIT (Investigaciones Técnicas de Gipuzkoa), San Sebastián, Spain, on a fellowship from the Basque Government. His Ph.D. is focused on the design, simulation, fabrication, and measurement of different implanted radiating structures.

He is with the Electronics and Communication Department, Antennas for Communication and Monitoring Systems Group, Tecnun-CEIT. He is a specialist in Inkjet Printing Technology.



Peter D. Bradley received the B.E. degree in electrical engineering with first class honors in 1987 and the M.E. degree in biomedical engineering in 1996, both from the University of New South Wales, Sydney, Australia. He received the Ph.D. degree in medical physics from the University of Wollongong, Australia, in 2000.

He has over 20 years experience in medical device design and analysis, including implantable devices such as implantable cardiac defibrillators and pacemakers. Early research work included the first extensive analysis of the effects of cosmic radiation on implantable devices. Since 2000, he has worked with Zarlink/Microsemi, San Diego, CA, USA, developing integrated circuits for medical applications and particularly ultralow power medical communications. He is currently a medical device systems consultant. He was the system architect for several of Zarlink-Microsemi's medical transceivers which dominate the implanted medical transceiver market, including the EEtimes product of the year in 2008. His interest areas include low-power radio transceivers, integrated circuits for biomedical instrumentation and system analysis, semiconductor radiation detectors, microdosimetry, and the effects of ionizing radiation on implantable medical devices. He has published over 20 papers and holds six patents on low-power transceiver techniques.



Daniel Valderas received the M.Sc. and the Ph.D. degrees from Tecnun, University of Navarra, Spain, in 1998 and 2006, respectively.

He is a researcher with the Electronics and Communications Department of the Centro de Estudios e Investigaciones Técnicas de Gipuzkoa (CEIT) and a lecturer with Tecnun, University of Navarra, Spain. He was an Academic Visitor at Florida Atlantic University, Boca Raton, FL, in 2003, at Imperial College, London, U.K., in 2007, and at Queen Mary, University of London, London, U.K., in 2008. He has participated in many different research projects on antenna and electromagnetic fields. His research interests focus on UWB and broadband antennas, RFID antennas, and antennas for body applications.

I. Ortego, D. Valderas,

Potentials and Comparison between Subtractive Etching and Inkjet Printing Technology for the Fabrication of NFC Coil Antennas

Proceedings of the XVIII Conference on the Design of Circuits and Integrated Systems, Donostia, San-Sebastian, November 2014

Proceedings of the XVIII Conference on the Design of Circuits and Integrated Systems Donostia - San Sebastián, Nov. 2013

Potentials and Comparison between Subtractive Etching and Inkjet Printing Technology for the Fabrication of NFC Coil Antennas

Iñaki Ortego
Electronics and Communication Department
CEIT and Tecnun University of Navarra
Manuel de Lardizabal 15, 20018 San Sebastián, Spain
Email: iortego@tecnun.es

Daniel Valderas
Electronics and Communication Department
CEIT and Tecnun University of Navarra
Manuel de Lardizabal 15, 20018 San Sebastián, Spain
Email: dvalderas@tecnun.es

Abstract—The aim of this paper is to examine the advantages, limitations and potentials of subtractive etching technique and inkjet printing technology for the fabrication of Near Field Communication (NFC) coil antennas. Two different prototypes made by these two technologies are presented and the main features and differences are analyzed. Subtractive etching is a repeatable method in which very low input resistance and very high quality factor (Q) antennas may be fabricated, requiring usually a damping resistor in order to increase the bandwidth of the coil. Inkjet printing technology enables an accurate adjustment of thickness of the printed conductive tracks and the conductivity of silver ink, giving a wide range of degree of freedom in the design of NFC antennas. The input resistance and quality factor can be finely tuned as long as skin depth is not surpassed while keeping same inductance levels. Typically, the obtained Q values are around 4-10, much lower than subtractive etching that could be above 120. Therefore, the manufacturing technique that is going to be used should be taken into account in the design process of the antenna since very different input impedance and quality factor can be obtained for the same structure.

Keywords—near field communication; subtractive etching; inkjet printing technology; quality factor; input impedance

I. INTRODUCTION

Near Field Communication (NFC) is an emerging and promising technology that enables the exchange of data wirelessly in a short range. It is a set of short-range wireless technologies evolved from RFID, typically requiring a distance of 10 cm or less that operates mainly at 13.56MHz. Therefore, NFC is compatible with almost all existing RFID solutions, increasing its potential use with already installed commercial deployments. As the size and cost of NFC technology continue to decrease, more interesting applications become feasible, especially when used in combination with a mobile phone. It is estimated that this system will be used in more than 1.2 billion smartphones by 2015 [1].

In this context, there are so different applications in which this technology could be helpful that the cost of the different manufacturing processes is essential. There are a number of approaches to implement and NFC antenna layout onto a selected substrate. Depending on the application the requirement for the antenna will be different.

In this paper a comparison between two different manufacturing processes will be realized, comparing the obtained input impedance values and quality factors. The remainder of this paper is organized as follows. In section II, a description of the two manufacturing processes will be done, explaining its main characteristics. Section III deals with the implementation and obtained results. Lastly, in section IV the conclusions are stated.

II. MANUFACTURING PROCESS

A. Subtractive etching

The earliest and most cumbersome method of antenna fabrication has been subtractive etching on a metal-plated laminate (e.g. FR4). Etching is the process of using strong acid or mordant to cut into the unprotected parts of a metal surface to create a certain design in the metal.

Subtractive etching has matured to the point where it has became a low-tech process requiring inexpensive off-the-shelf materials and equipment. However, for larger production runs, etching creates significant amounts of metal salt and chemical waste products, incurring increased costs due to regulatory fees.

The most typical substrate and the one that will be used in this study is FR4. This substrate is a composite material composed of woven fiberglass cloth with an epoxy resin binder that is flame resistant (self-extinguishing). The metal is usually copper. In Table I the typical commercial and standard thickness of FR4 & copper is shown.

TABLE I. STANDARD MATERIALS USED IN SUBTRACTIVE ETCHING

Material	Thickness
Copper	18 µm, 35 µm
FR4	0.5 mm, 0.8 mm, 1.5 mm

ISBN 978-84-8081-401-0

B. Inkjet Printing Technology

Inkjet printing is a direct-write technology by which the designed pattern is transferred directly to the substrate, and there is no requirement of masks contrary to the traditional etching technique [2]. This additive method provides a low cost, environmentally friendly manufacturing process on flexible materials.

About 1500 worldwide research units working on various aspects of flexible electronics are estimated [3]. The parameters that affect the final performance of the printed samples have been recently investigated extensively [4][5].

In the fabrication process several parameters are involved, such as, size of ink nano-particles, substrate, surface tension of the particle and of the substrate, time and temperature of the ink sintering, among others [6], which provide a wide range of degree of freedom for circuit designs, and particularly for antennas, on flexible substrates. A deep study of the effect of these parameters is out of the scope of this article. There are three main factors in this technology: the substrate, the ink and the printer.

1) Substrate: One of the main advantages of this technology is that it allows printing different patterns in to a flexible substrate, usually plastic or different polyimides. There is a wide range of available types of polyimides that varies in density, coating, thickness, texture and dielectric properties. It is important to characterize correctly the properties of the substrate, since it can affect the final system performance. There are different methods for high frequency dielectric characterization such as ring resonators [7][8], parallel plate resonators [9] and cavity resonators [10][11]. In this article, a common polyimide film will be used: Dupont Kapton. It exhibits an excellent balance of physical, chemical, and electrical properties over a wide temperature range.

2) Ink: Up to date, inks made of silver conductive nanoparticles with diameters ranging from just 2nm to above 50nm, encapsulated with a protective shell and dispersed in a liquid solvent have been used. In this study, Suntronic Jettable Silver U5714 ink by Sunjet has been used as conductive ink. It is a solvent-based silver nano-particle inkjet ink and 20% of its weight is due to silver particles. Once it is printed, a continuous conducting structure can be obtained by sintering, that is by increasing the temperature of the structure so that separated nanoparticles melt together. In this work, a sintering process of 30min at 200ºC has been selected for all the prototypes.

3) Printer: Dimatix Materials Printer DMP-2831 (Fig. 1) has been used. It is a laboratory and limited production tool that enables to evaluate the use of inkjet printing technology for new manufacturing and analytical processes. In this work, DMC-11610 cartridge which has 16 nozzles, 254 µm spaced with a nominal opening of 21 µm, and a 10 pL drop

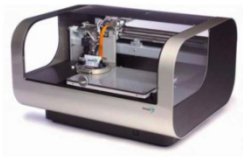

Fig. 1. Dimatix Materials Printer DMP-2831 [12]

volume capacity has been employed. Only two nozzles with 16-17V applied voltage and 40ºC of temperature have been used at a height of 0,5mm with a drop spacing of 20µm.

III. Implementation And Results

A five turn rectangular planar spiral inductor at 13.56 MHz that fulfils the ISO7810 standard [13] that defines the physical characteristics of identification cards has been designed with 1mm track width (Table II).

The methodology of inductive calculations using an analytical approach may be found in [14]. Numerical computation of the presented coil is made by CST MICROWAVE STUDIO simulation software. Frequency domain solver with hexahedral mesh is used and local mesh refinement strategy is adopted within the coil conductive track.

The measurement of the input impedance was realized using a standard VNA according to the setup shown in Fig. 2. A FTB-1-6 balun by Mini-Circuits is employed between the feeding cable and the fabricated prototype.

Two different prototypes have been studied (Table III, Fig. 3) and the obtained results are shown in Table IV.

TABLE II. Nominal Dimensions of ID-1 Card Type

Width (mm)	Height (mm)
85.6	53.98



Fig. 2. Measurement set up

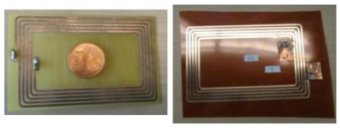

Fig. 3. Fabricated prototypes: inkjet printed antenna (right) and same antenna with subtractive etching (left)

ISBN 978-84-8081-401-0

Proceedings of the XVIII Conference on the Design of Circuits and Integrated Systems Donostia - San Sebastián, Nov. 2013

TABLE III. FABRICATED PROTOTYPES

Name	Technique	Substrate	Antenna
Prototype 1	Substractive etching	FR4 (0.8 mm)	Copper (18 µm)
Prototype 2	Inkjet	Kapton (127 µm)	Silver ink (5 µm)

TABLE IV. OBTAINED RESULTS: ANALYTICAL (A), SIMULATION (S) AND MEASUREMENT (M) AT 13.56 MHZ

Name	Parameter	A	S	M
Prototype 1	R [Ω]	1.5	1.6	1.6
	L [µH]	2,80	2,78	2,96
	Q	159	148	157
Prototype 2	R [Ω]	31	35,12	32,35
	L [µH]	2,82	2,79	2,94
	Q	7,75	6,77	7,76

It can be observed that the obtained inductance value is the same for both technologies but there is a considerable change in terms of input resistance and therefore, in the quality factor. This is due to the differences in the conductivity and thickness of the conductive track (antenna).

On the one hand, the conductivity of the copper is fixed. However, the ink's conductivity depends on the sintering process; the obtained conductivity values are shown in Table V. It can be seen that, as the conductivity is lower, the input resistance of the inkjet printed prototype will be higher. In constrast to subtractive etching technique, inkjet printing technology allows accurate adjustment of the electrical properties of the antenna, and therefore offers the opportunity to fulfill different requirements keeping the same geometry.

On the other hand, the thickness of the two prototypes are different and this parameter affects directly to the input resistance. Inkjet printing technology allows varying the thickness of the printed layers with approximately 1µm resolution. As the obtained thickness is below the skin depth, a change on the track thickness directly affects both the input impedance and the quality factor. For thicknesses far deeper than skin depth, input resistance and Q factor are no longer adjustable by this degree of freedom.

Theoretically the thickness could be increased up to 48µm to get higher Q values by decreasing the input resistance. Nevertheless, in practice, it is not feasible to fabricate printed coil antennas with such a high thicknesses due to the ink spilling over the track when too many layers are mounted on it.

Typical coil antenna manufactured by inkjet printing technology exhibits small Q factors of around 4-10 [15] [16]. The fabricated printed prototype was made with 6 layers which correspond with 6µm thickness. Another prototype was manufactured with 10 layers (10µm thickness) to check the aforementioned capability of inkjet printed technology to vary the input resistance with the thickness. This last prototype is a reasonable trade off between delivered performance in terms of Q values and complexity of the manufacturing process due to the number of layers.

TABLE V. CONDUCTIVITY AND SKIN DEPTH CALCULATION FOR THE USED MATERIALS

Material	Conductivity [S/m]	Skin depth at 13.56MHz [µm]
Pure silver	$63.01 \cdot 10^6$	17.2
Silver ink	$8 \cdot 10^6$	48.3
Copper	$59.6 \cdot 10^6$	17.7

A measured inductance value of 2.9µH, a resistance of 23.5Ω and a Q factor of 10.5 are obtained in perfect accordance with the above considerations.

The Q factor required for the antenna is directly related to the read range to be achieved by the technology. For example, in a typical RFID system for a distance of 38cm, Q factors close to 40 are required [17]. NFC allows for shorter distances and consequently restrictions on tag Q factors are relaxed to get the same voltage to energize the RFID tag integrated circuit. Therefore, the obtained Q values for inket printed coil is good enough.

With copper-etched antennas, quality factors of more than 120 could be realized. The obtained value are in concordance with previous studies [18]. For NFC applications, the bandwitdh is not critical however usually damping resistors are used in order to obtain broader bandwidth decreasing at the same time the Q value.

Regarding the obtained results, the manufacturing process that is used should be taken into account in the design of the antenna since the obtained input resistance and quality factor for a certain designed structure are very different depending the manufacturing process that is used.

IV. CONCLUSIONS

An exploration of the potentials, advantages and limitations of subtractive etching technique and inkjet printing technology for NFC applications have been successfully conducted. Two different prototypes have been presented and the main differences between them have been studied.

With subtractive etching technique, coils with very low input resistance and very high quality factors can be obtained. Usually, damping resistors are necessary in order to get lower Q values and higher bandwidth. The main advantage of this technology is that the manufacturing process is very repeatable; however, it creates waste of material and the substrate is rigid.

In contrast, inkjet printing technology offers great degree of freedom for the fabrication of NFC coil antennas. The resistance can be controlled by the capability of this technology of varying the track thickness and therefore the Q factor can be finely tuned as long as the skin depth is not surpassed. This also allows the removal of the typical damping resistors that are usually used in current NFC inductors. The obtained Q values, compared with the ones obtained by subtractive etching technique are one order of magnitude lower; however, they are enough for NFC

ISBN 978-84-8081-401-0

applications. Besides, the conductivity of the silver ink may be controlled with the sintering process. Inkjet printing technology is a promising technique that is suitable for the fabrication of low cost, environmentally friendly NFC coils on flexible substrates.

As final remark, the manufacturing technique and the electrical properties of the materials that will be used must be taken into account in the design process of the antenna right from the beginning, since very different antenna characteristics are obtained for a certain structure.

ACKNOWLEDGMENT

Iñaki Ortego's scholarship has been granted by the Department of Education of the Basque Government. The authors would like to thank the collaboration agreement between Tecnun and CST that has made possible the achievements of this research.

REFERENCES

[1] "Device Solutions." [Online]. Available: http://www.device-solutions.com/downloads/NFC Enabling Technology Final.pdf.
[2] T. H. J. van Osch, J. Perelaer, a. W. M. de Laat, and U. S. Schubert, "Inkjet Printing of Narrow Conductive Tracks on Untreated Polymeric Substrates," Advanced Materials, vol. 20, no. 2, pp. 343–345, Jan. 2008.
[3] Jupiter Hu (Industrial Technology Research Institute (ITRI)), "Overview of Flexible Electronics from ITRI ' s Viewpoint," Symposium A Quarterly Journal In Modern Foreign Literatures, pp. 6650–6650, 2010.
[4] M. L. Allen, K. Jaakkola, K. Nummila, and H. Seppa, "Applicability of Metallic Nanoparticle Inks in RFID Applications," IEEE Transactions on Components and Packaging Technologies, vol. 32, no. 2, pp. 325–332, Jun. 2009.
[5] S. H. Yoon, J. H. Lee, P. C. Lee, and J. Do Nam, "Sintering and Consolidation of Silver Nanoparticles Printed on Polyimide Substrate Films," Macromolecular Research, vol. 17, no. 8, pp. 568–574, 2009.
[6] R. E. S. Mancosu, R. D. Quintero, J. A. Q. Azevedo, "Sintering, in Different Temperatures, of traces of Silver Printed in Flexible Surfaces," 11th. Int. Conf, on Thermal, Mechanical and Multiphysics Simulation and Experiments in Micro-Electronics and Micro-Systems, 2010.
[7] N. K. I. Wolff, "Microstrip Ring Resonator and Dispersion Measurement on Microstrip Lines," Electronics Letters, vol. 7, pp. 779–781, 1971.
[8] P. A. Bernard and J. M. Gautray, "Measurement of Dielectric Constant Using a Microstrip Ring Resonator," IEEE Transactions on Microwave Theory and Techniques, vol. 39, no. 3, pp. 592–595, 1991.
[9] J. Yoon, J. Kwon, and H. Lee, "The Microwave Measurement of the Dielectric Properties by the Parallel Plate Resonator and Ceramic Cavity Method," Proceedings of 5th International Conference on Properties and Applications of Dielectric Materials, vol. 2, pp. 964–968, 1997.
[10] U. Arz, J. Leinhos, and M. D. Janezic, "Broadband Dielectric Material Characterization : A Comparison of On-Wafer and Split-Cylinder Resonator Measurements," Proceedings of the 38th European Microwave Conference, no. October, pp. 913–916, 2008.
[11] J. Baker, R. G. Geyer, J. H. Grosvenor, M. D. Janezic, C. A. Jones, B. Riddle, and C. M. Weil, "Dielectric Characterization of Low-loss Materials: A Comparison of Techniques," IEEE Transactions on Dielectrics and Electrical Insulation, vol. 5, no. 4, pp. 571–577, 1998.
[12] "Dimatix. Fujifilm." [Online]. Available: http://www.dimatix.com/.
[13] Identification cards - Physical Characteristics, International Standard ISO 7810. .
[14] C. R. Paul, Inductance - Loop and Partial. John Wiley & Sons, Inc, 2010.
[15] A. Rida, R. Vyas, and M. M. Tentzeris, "Conductive Inkjet-Printed Antennas on Flexible Low-Cost Paper-Based Substrates for RFID and WSN Applications," IEEE Antennas and Propagation Magazine, vol. 51, no. 3, pp. 13–23, Jun. 2009.
[16] E. Ramon and E. Diaz, "Inkjet Printed Antennas for NFC systems," pp. 1220–1223, 2010.
[17] A. L. Scholtz and R. Weigel, "Antenna design for future multi-standard and multi-frequency RFID systems," 2009.
[18] M. Gebhart and R. Szoncso, "Optimizing Design of Smaller Antennas for Proximity Transponders," 2010 Second International Workshop on Near Field Communication, pp. 77–82, 2010.

ISBN 978-84-8081-401-0

C. Schmidt, D. Valderas, J. García, I. Ortego, and X. Chen,

Passive UHF RFID Near Field Link Budget for Implanted Sensors

European Conference on Antennas and Propagation (EUCAP), pp. 3479–3483, 2011

EuCAP 2011 - Convened Papers

Passive UHF RFID Near Field Link Budget for Implanted Sensors

Christoph Schmidt[1], Daniel Valderas[1], Joseba García[1], Iñaki Ortego[1], Xiaodong Chen[2]

[1]CEIT and Tecnun (University of Navarra), Pº Manuel Lardizábal 15
20018 San Sebastián, Spain
cschmidt@ceit.es; dvalderas@ceit.es; jgmiranda@ceit.es; iortego@ceit.es

[2]Dept of Electronic Eng, Queen Mary, University of London
London E1 4NS, UK
xiaodong.chen@elec.qmul.ac.uk

Abstract: **The precise estimation of the communication range for a passive wireless implanted sensor is an essential system design parameter in medical telemetry research. Path loss measurements between an RFID reader antenna and an implanted biosensor at UHF band were performed in an anechoic chamber representing two scenarios: depending on whether the reader is worn by a medic within 1 meter distance from the implant or by the patient in a shirt pocket.**
Near-field measurements in the first scenario proved that a passive RFID communication link can be established within 0.46 m for the considered subcutaneous implant. As the gain of the implanted antenna is quite low, the impact of the feeding cables on the results of the second scenario have been estimated by simulations of the measurement set up embedded. This uncertainty is due to the radiation and reflection coming from the feeding cables and it increases with the distance between the two antennas. A methodology is presented to estimate this uncertainty for a proper link-budget estimate.

I. Introduction

Researchers have recently shown an increased interest in short range telemetry networks which are placed directly on or near the human body [1]. In order to include implanted sensors in this so called Personal Area Network (PAN) it is necessary to have a communication link between a transceiver located in the human body and another outside but near it. This requires antennas which have a broadside radiation pattern and operate near or into the human body. Particularly, passive or semi passive sensors rely on a good estimate of the link budget.

This paper is aimed at studying the reliability of the wireless link between an implanted chip and a UHF-RFID reader near the human body. Special interest will be focused on the uncertainty introduced by the set up, respectively feeding cables, for a RFID-UHF 865-868MHz near field link measurements.

II. Range Measurements

A. Implanted and base station antennas employed

The implanted antenna consists of a broadband monopole-like structure in a circular arrangement. A specific designed structure helps to match the small monopole to the desired frequency [2]. A ground plane and short circuits are avoided to improve radiation efficiency. The complete antenna is sealed by a high permittivity substrate and superstrate made out of Rogers RO3210 (ε_r=10) laminate for compact design. The whole radiator is bounded by a circumference of 20 mm diameter.

Fig. 1 shows the top view of the layout along with the feeding set up. The reflection coefficient is below -10 dB at the frequency of interest [2].

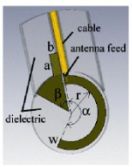

Fig. 1 Implant test antenna

As RFID reader antenna we utilized a conventional PIFA that is employed to probe the field within a short distance from the implanted antenna. The antenna is designed with a low profile (3 mm) [3]. The radiating plate has the dimensions of a portable handset (79 mm x 49 mm) over a slightly larger ground plane (106 mm x 61 mm). Antenna gain along the broadside direction was found to be 0 dBi (Fig. 2).



Fig. 2 Probe antenna – PIFA

B. Read range perpendicularly to the chest

The reader antenna is placed as it were worn in a shirt pocket of a standing medic and facing the implant at different distances for both PIFA orientations, vertical and horizontal. These are representative positions for vertical and horizontal polarizations for handset antennas.

The entire setup to measure path loss is shown in Fig. 3. The implanted antenna is placed inside a polystyrene tank filled with skin mimicking gel, 9 mm away from the phantom interface to simulate a subcutaneous insertion into a human torso. The wall thickness of the phantom is 2 cm as it represents the patient's clothing. The size of the phantom is the minimum representative for the whole body for far field communication at the frequency of interest (350 x 250 x 165 mm) [4].



Fig. 3 Near-field measurements set up for reader to implant communications

Path loss measurements (S_{12}) were performed in anechoic chamber from distance d=0m (PIFA probe antenna located on phantom surface) up to a distance of d=1m. As the PIFA is facing the phantom, a mismatch is observed, falling from free-space conditions (-17 dB) to the d=0 m situation (-4.7 dB) due to the phantom proximity (Fig. 4). This influence is implicitly considered in the path loss when it is measured. As the distance is kept under near field conditions, multipath and fading are not considered in the scenario's link budget.

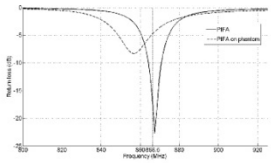

Fig. 4 return loss of the reader antenna placed on the chest phantom and in free air

Once path loss is obtained, the power that is received by the implant and by the reader is calculated according to the link budgets defined in (1) and (2) respectively. They are related to the RFID uplink and downlink budgets. The power received by the reader P_{reader_dB} is the one backscattered by the implant within the torso. Both reader and tag antennas are matched to 50Ω. $EIRP_{dB}$ is 35,15 dBm due to regulation constraints.

$$P_{reader_dB} = EIRP_{dB} - 2P_{Loss_dB} \quad (1)$$

$$P_{implant_dB} = EIRP_{dB} - P_{Loss_dB} \quad (2)$$

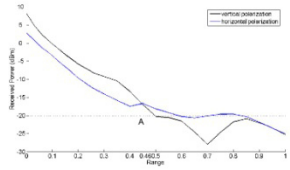

Fig. 5 Power received by the implanted tag from a reader placed perpendicularly to the chest for vertical and horizontal PIFA as reader antenna (ref. (Fig. 3)). Point A (0.46 m, -20 dBm)

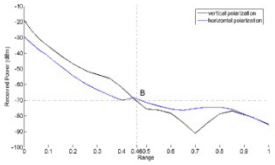

Fig. 6 Power received by the reader from the implanted-tag backscattered signal for vertical and horizontal PIFA as reader antenna (ref. (Fig. 3)) Point B (0.46 m, -70 dBm)

Application-oriented conditions are considered for an implanted passive RFID transceiver: power consumption is assumed to be $P_{implant_dB}$=-20 dBm and reader sensitivity P_{reader_dB}=-70 dBm. As can be seen in Fig. 5 and Fig. 6, a communication link can be reliably established within distance of 0.46 m for both polarizations.

C. On-chest measurement

Once passive communication has been validated in a broadside link, the case of different reader locations on the chest is contemplated. This is the case, e.g., of a reader located in patient's shirt pocket.



Fig. 7 Measurement set up for on-chest measurement

Path loss (S_{12}) measurements were taken at the position showed in Fig. 8, where the PIFA antenna is attached to the phantom. The PIFA antenna is moved along the *x* axis for two different heights *y*. Vertical and horizontal PIFA orientations

are considered in each case. As the PIFA antenna is placed facing the phantom, a mismatch occurs (Fig. 4). Its impact is again embedded into the path loss measurements.

Fig. 9 and Fig. 10 show the power received by the implant and the handset with horizontal distance x along the chest for the two different heights y, namely top and bottom. They correspond again to expression (1) and (2) respectively. If no further losses are considered, the link is assured when the reader is around the chest as in all cases ($P_{implant}$ >-20 dBm and P_{reader} >-70 dBm).

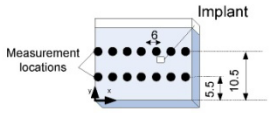

Fig. 8 Positions for on-chest measurements on phantom (dimensions in cm)

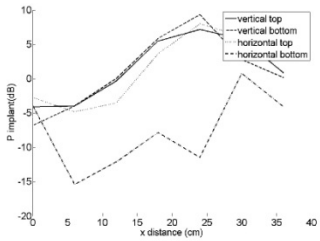

Fig. 9 Power received by the implanted-tag from a reader placed on the chest at positions given by Fig. 7 and Fig. 8

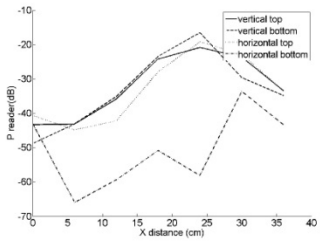

Fig. 10 Power received by the reader placed on the chest at positions given by Fig. 7 & Fig. 8 from the back scattered signal by the implanted-tag

III. Validation

Presumed that the implant exhibits a very low gain due to the lossy material surrounding it, it is important to check the impact of the radiation coming from the cables that could mask the results. This impact has been studied closer in detailed simulations. The comparison between simulations of the whole set up (including cables) with the measurements will give an estimate of uncertainty for the latter.

A. Simulation

By using CST Microwave Studio 2010, a detailed and realistic reproduction of the measurement environment in the anechoic chamber has been modelled. Models of both antennas, including their antenna feed, were integrated. These feeds were represented by long (≈1,5 m) and bent coaxial cables going down to the chamber floor.

Frequency Solver simulations have been performed according to the measurement set up on each position (Fig. 11). Path loss is in this fashion represented by the logarithmic transmission coefficient $|S_{21}|$dB at 868 MHz.

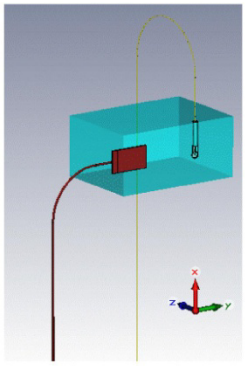

Fig. 11 Simulation arrangement with long cables (main section)

Furthermore, the simulation has been repeated at every position of the reader antenna without the cables in place for comparison purposes.

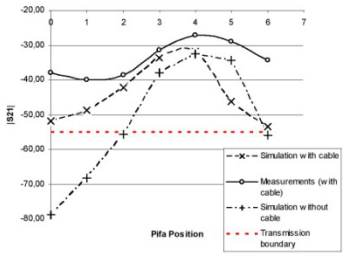

Fig. 12 Comparison of the transmission coefficient for the same set of positions and horizontally oriented PIFA, top line

The P_{Loss_dB} threshold for reliable communication is P_{Loss_dB} ≤-55,15 dB and it is calculated from formula (2) (EIRP = 35,15 dBm and P_{tag}=-20 dBm).

Fig. 12 shows the results for the top line (Fig. 8) with the reader antenna in horizontal position. In the diagram, horizontal axis represents the 7 registered positions along the torso. The results show a good agreement only near the implanted antenna (position 3-5) when cables are considered

both for simulation and measurements (inevitably in the latter). Further away from the implant, the simulated transmission coefficient drops significantly, especially in the case of the simulation without the cables included. In the rest of cases (horizontal PIFA bottom line, vertical PIFA top and bottom lines), the results are similar and omitted for brevity.

B. Uncertainty calculation

The simulations without cables have shown a higher degradation of $|S_{21}|$ with distance between antennas. This demonstrates the significant influence of the cables on the validity of the results. Please notice that the position of the cables are not exactly the same in both measurement and simulated set ups.

Obviously, performing measurements without cables is as desirable as impossible. A way to get around this constraint is to add an uncertainty value to the simulations without cable. This is shown in Fig. 13, Fig. 14, Fig. 15 and Fig. 16. An estimate of this uncertainty can be extracted by the difference between the simulations with cable and measurements. The range of uncertainty is an estimate of the impact of the cables on the results of the measurement.

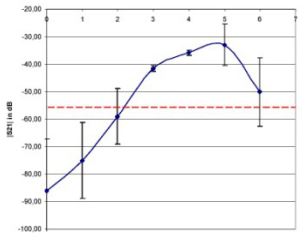

Fig. 13 Simulated transmission coefficient for bottom line, measurement uncertainty included, reader antenna horizontally oriented

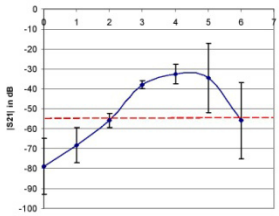

Fig. 14 Simulated transmission coefficient for top line, measurement uncertainty included, reader antenna horizontally oriented

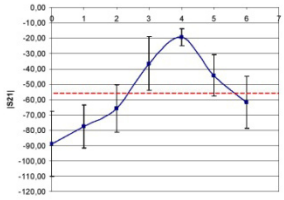

Fig. 15 Simulated transmission coefficient for top line, measurement uncertainty included, reader antenna vertically oriented

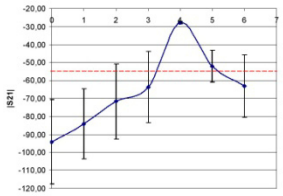

Fig. 16 Simulated transmission coefficient for bottom line, measurement uncertainty included, reader antenna vertically oriented

The further away the reader is placed on the chest, the higher is the impact that is observed due to the small signal to noise ratio at these points.

The proposed method indicates that a communication link can only be assured within a much smaller area in comparison to the one provided only by the measurements (namely the whole torso (Fig. 9 and Fig. 10)). Fig 17 and 18 show three different concentric areas in the torso that represent reliable, uncertain, and impossible communication respectively.

It is noteworthy, that for greater distance the polarisation match of the antennas is not directly correlated with the transmission coefficient.

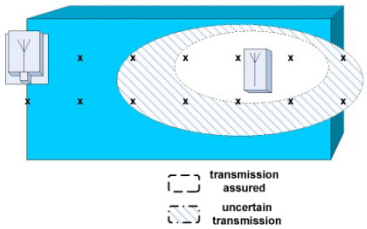

Fig. 17 Characterization of zones with different transmission reliability, reader antenna PIFA vertically oriented

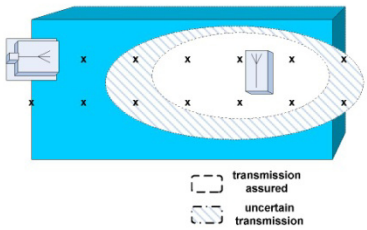

Fig. 18 Characterization of zones with different transmission reliability, reader antenna PIFA horizontally oriented

IV. Conclusion

Near-field measurements have shown that an RFID passive link is likely to be set when the reader is within 0.46 m from the torso with an implanted antenna inside at UHF band in broadside direction.

Furthermore the results demonstrate that an UHF terminal worn on the chest can surely communicate with the implant within a decent region. A method that defines this region has been presented. It includes measurement set up uncertainties. Those are due to the radiation and reflection coming from the feeding cables. The uncertainty increases with the distance between the two antennas. The results show that the suppression of leakage current of the cable is a key parameter to precise link-budget estimation for antennas worn on the chest. Further investigations are directed to practical solutions for wireless transmission measurements.

Acknowledgment

This work was supported in part by the Cátedra Telefónica of the University of Navarra and by the Spanish Ministry of Science and Innovation through the COSIMA project (TEC2010-19545-C04-02). The authors appreciate the University agreement with CST that has enabled the fulfilment of this project.

References

[1] P.S. Hall and Y. Hao, eds. Antennas and Propagation for Body-Centric Wireless Communications, London, UK: Artech House, 2006

[2] D. Valderas, C. Schmidt, X. Chen, "Broadband implanted RFID antenna", IEEE APS/URSI Radio Science Meeting, Toronto 2010

[3] J. Garcia, A. Arriola, G. Sasiain, D. Valderas, Jl. Sancho, X.Chen, "Characterization of phantom size and link budget for off-body communications", Antennas and Propagation (EuCAP), Barcelona, 2010

[4] D. Valderas, C. Schmidt, X. Chen, "RF Implanted Antenna Gain Characterization: Procedures and Challenges", IEEE APS/URSI Radio Science Meeting, Toronto 2010

I. Ortego, N. Sanchez, J. Garcia, F. Casado, D. Valderas, and J. I. Sancho,

Inkjet Printed Flexible Antenna Analysis for Near Field Communication Systems

50th Anniversary Conference - Engineering: Science and Technology, p. 5, 2012

Inkjet Printed Flexible Antenna Analysis for Near Field Communication Systems

I. Ortego[1], N. Sanchez[1], J. Garcia[1], F. Casado[2], D. Valderas[1], J.I. Sancho[1]

[1] CEIT and Tecnun (University of Navarra), Spain

[2] IKERLAN-IK4, Spain

1 Objectives

- Examination of the potential of Inkjet Printing Technology for the fabrication of Near Field Communication (NFC) coil antennas.
- Definition of a general methodology including design, simulation, fabrication and measurement for rectangular, planar-spiral inductors working at 13.56 MHz.

2 Analytical approach

- Inductance calculation

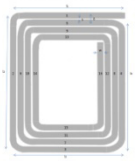

$$L = 0,002l\left\{\ln\left(\frac{2l}{w+t}\right) + 0.50049 + \frac{w+t}{3l}\right\}\ [\mu m]$$

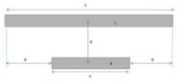

$$M = 2lF[nH]$$

$$M_{k+p} = 2l_{k+p}F_{k+p}$$

$$F = \ln\left\{\left(\frac{l}{d}\right) + \left[1+\left(\frac{l}{d}\right)^2\right]^{1/2}\right\} - \left[1+\left(\frac{d}{l}\right)^2\right]^{1/2} + \left(\frac{d}{l}\right)$$

$$L_T = L_0 + M_+ - M_-\ [\mu m]$$

where $M_{k,p} = \frac{1}{2}\left[\left(M_{k+p} + M_{k+q}\right) - \left(M_p + M_q\right)\right]$

- Resistance and Q calculation

$$R = \frac{1}{\sigma}\cdot\frac{L}{S} = \frac{1}{\sigma}\cdot\frac{L}{t\cdot w} \qquad Q = \frac{L\omega}{R}$$

The skin effect at 13,56MHz is approximately 47µm

3 Simulation and Fabrication

- Computer Simulation Technology (CST).
- Inkjet Printing Technology:

Direct-write technology by which the designed pattern is transferred directly to the substrate.

Substrate: Dupont Kapton® polyimide film 127µm thick

Ink: SunTronic Jettable Silver U5714 ink by Sunjet



Dimatix Materials Printer 2800

Sintering process: A continuous conducting structure can be obtained by increasing the temperature of the structure so that the separate nanoparticles melt together.

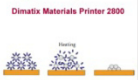

Sintering process

Nominal dimensions of the coil antenna

Width (mm)	Height (mm)	Thickness (mm)
85.6	53.98	0.76

These dimensions have been selected to fulfil the ISO7810 standard



Fabricated prototype

4 Measurements

- Thickness and conductivity of printed traces

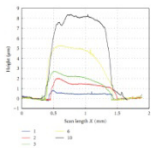

Obtained profiles for different number of printed layers

Obtained conductivity values with 30min@200°C sintering process

Material: silver	Conductivity ($(\Omega m)^{-1}$)	Conductivity with respect to pure silver (%)
Pure	$63.01 \cdot 10^6$	100
One layer	$8 \cdot 10^6$	12.8
Two layers	$9 \cdot 10^6$	14.3
Three layers	$7.9 \cdot 10^6$	12.5
Six layers	$8.5 \cdot 10^6$	13.5

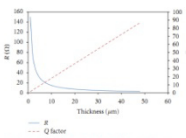

Calculation of R and Q for different thickness

- The conductivity of the ink is 10% to 20% of the the pure silver.
- A thickness of 0.8µm for each layer can be assumed.
- Inkjet printing technology allows to vary the thickness of the printed layers with approximately 1µm resolution all the way from 0µm to the skin depth
- A Q value up to 90 can be theoretically achieved by this technology as long as the thickness is kept below the skin depth (47µm).

5 Results and validation

Obtained results of the two prototypes: Analytical (A), Simulation (S) and Measured (M)

		A	S	M
4 layers	$R\ [\Omega]$	46,58	51,13	50,25
	$L\ [\mu H]$	2,82	2,79	2,9
	Q	5,16	4,64	4,91
6 layers	$R\ [\Omega]$	31	35,118	32,35
	$L\ [\mu H]$	2,82	2,79	2,947
	Q	7,75	6,77	7,76

Methodology validation

The reflection coefficient will be used as figure of merit to estimate the correlation between the results obtained by analytical formulas, computed numerical models and measurements.

$$|\Gamma| = 20\log\left(\left|\frac{Z_1 - Z_2^*}{Z_1 + Z_2}\right|\right)$$

If the reflection coefficient is below −10dB, a good correlation is achieved.

Results validation

	Comparison		$\|\Gamma\|$ (dB)
4 layers	A	S	−25.16
	A	M	−21.94
	S	M	−20.35
6 layers	A	S	−22.78
	A	M	−15.39
	S	M	−14.08

6 Conclusions

- The resistance can be controlled by the capability of this technology of varying the track thickness, which prevents from extra damping resistor implementations.
- Q values ranging from 4 to 10 (which agree NFC requirements) can be obtained while keeping the same inductance value.
- Inkjet printing technology is therefore a promising technique for the fabrication of NFC coil antennas. Moreover, due to its low cost manufacturing process and substrate flexibility, it is a perfect candidate for the implementation of environmentally friendly NFC terminals into flexible substrates.